Search for Microscopic Black Holes in Multi-Jet Final-States using Multiple Single-Jet Triggers with ATLAS Detector with 8 TeV Proton-Proton Collisions at the Large Hadron Collider

by

Aatif Imtiaz Butt

A thesis submitted in partial fulfillment of the requirements for the degree of

Doctor of Philosophy

Department of Physics
University of Alberta

This thesis is dedicated to Late Mr. Karamat Ullah Dar
who donated generously to help pay my tuition fee for M.Sc Physics
at Quaid-e-Azam University, Islamabad in 2000-02.

Abstract

Higher dimensional microscopic black holes may be produced in particle accelerators at high energies which will emit a high multiplicity of Standard Model (SM) particles via thermal decay. This thesis documents a search for higher dimensional microscopic black holes in multi-jet final-states using six single-jet triggers with the ATLAS detector with 8 TeV proton-proton collisions at the Large Hadron Collider. The ATLAS 2012 data corresponds to a total integrated luminosity of 20.3 fb^{-1}. The background topology in this search consists of all multi-jet final-states from all SM processes. Quantum Chromodynamics (QCD) processes contribute maximally to the SM multi-jet final-states and dominate this background topology. The invariant mass (M) and scalar sum of transverse momenta of all jets (H_T) in events are used as analysis variables. The M and H_T distributions for ATLAS data are consistent with QCD predictions of two well known hadronization models (PYTHIA8 and HERWIG++) for each single-jet trigger. Counting experiments are performed to set model-independent upper limits (at 95% confidence level) on the production cross section times acceptance times efficiency of new physics in multi-jet events. The model-independent upper limit on the production cross section times acceptance times efficiency is 0.15 fb^{-1} for the threshold mass $M_{th} > 4.5$ TeV. Model-dependent production cross section limits (at 95% confidence level) are also calculated versus M_{th} and fundamental Planck mass M_D for non-rotating and rotating black holes for two, four and six large extra dimensions.

Acknowledgements

I would like to take the opportunity to thank professor Douglas M. Gingrich for his supervision, guidance, academic feedback and moral support. He provided excellent research environment which helped me become better at working in large collaboration like CERN. He encouraged me to work independently at the same time which helped produce this thesis.

I am thankful to Physics Department at University of Alberta for providing me with research and teaching assistantships during my PhD study. I would like to thank Pakistan Atomic Energy Commission for providing partial financial support during my studies.

I am grateful to Asif Saddique, Logan Sibley, Francesc Vives Vaque, Nitesh Soni, Halasya Siva Subramania and Seema Bahinipati for their technical support. Long discussions with these fine researchers put me back on track on multiple occasions after I had committed a scientific blunder. I have better understanding of my research field as the result of these useful discussions.

Last but not the least, I would like to thank my family and close friends in Pakistan, Switzerland and Canada for moral support and wonderful company during PhD studies.

Table of Contents

List of Tables

List of Figures

List of Abbreviations and Symbols

ADD Model	A model introduced by Arkani-Hamed, Savas Dimopoulos and Gia Dvali in 1998
ALICE	A Large Ion Collider Experiment
ATLAS	A Toroidal LHC ApparatuS
CERN	Conseil Europen pour la Recherche Nuclaire
CMS	Compact Muon Solenoid
CP	Charge Parity
EF	Event Filter
EFE	Einsteins Field Equations
EM	Electromagnetic
GR	The General Theory of Relativity
H_T	Scalar sum of transverse momenta of all jets in an event
ID	Inner Detectors
IP	Interaction Point
L1	Level-1
L2	Level-2
LAr	Liquid Argon
LHC	Large Hadron Collider
LHCb	LHC beauty
LHCf	LHC forward
MBH	Microscopic Black Holes
M_D	Fundamental Planck Scale Mass in D dimensions
M	Invariant mass of an event
M_{Pl}	Fundamental Planck Scale Mass in 4 dimensions
M_{th}	Threshold mass for production of microscopic black hole
Pb-Pb	Lead-Lead
pPb	Proton-Lead
pp	Proton-Proton
p_T	Transverse momentum of a jet
PS	Proton Synchrotron
QCD	Quantum Chromodynamics
QED	Quantum Electrodynamics
RoI	Region of Interest
RS Model	A model introduced by Lisa Randall and Raman Sundrum in 1999
SCT	Semiconductor Tracker
SM	The Standard Model
SSB	Spontaneous Symmetry Breaking
SUSY	Supersymmetry
TOTEM	TOTal Elastic cross section and diffractive dissociation Measurement
TRT	Transition Radiation Tracker
η	Pseudorapidity

Chapter 1

Introduction

Physicists have observed four fundamental forces to date. The Standard Model (SM) is a theoretical framework based on quantum field theory which successfully describes the strong, electromagnetic and weak interactions. The gravitational interaction is the weakest among all interactions and is not included in the SM since little is known about gravity at the quantum level. The huge difference between the strengths of the electroweak and gravitational interactions is called the aesthetic hierarchy problem. The ADD model introduced by Arkani-Hamed, Savas Dimopoulos and Gia Dvali is a model of large extra spatial dimensions which argues that gravity appears to be weak in the 4-dimensional universe and the TeV scale is the fundamental scale of gravity in D-dimensions [1]. Creation of microscopic black holes is a possibility under models of large extra dimensions at the Large Hadron Collider (LHC). The decay of microscopic black holes could be detected with the ATLAS detector at the LHC.

Chapter 2 briefly reviews theories and models that serve as motivation to this thesis. This includes the Standard Model of particle physics, the theory of general relativity, the hierarchy problem, theories of supersymmetry and theories of extra spatial dimensions.

Chapter 3 covers the physics of black holes. Different types of classical black hole are briefly discussed in this chapter. Higher dimensional black holes are discussed in detail with emphasis on the production and decay mechanism at the LHC.

Chapter 4 is dedicated to the description of the LHC machine and ATLAS detector. Various sub-detectors of the ATLAS detector are discussed in detail according to their functionality.

Finally, chapter 5 is about the physics analysis. It describes the procedure adopted and results of the search for microscopic black holes in multi-jet final-states using multiple single-jet triggers with the ATLAS detector with 8 TeV proton-proton collisions at the LHC. The analysis is concluded by setting a model independent upper limit on production cross section for new physics and model dependent lower limits on threshold mass for a model of non-rotating and rotating black holes decaying to multi-jet final-states. The results are compared with other similar searches.

Chapter 2

A Theoretical Review

There are four fundamental interactions known to mankind in nature that influence us and the matter we observe in our daily lives. Strong nuclear, electromagnetic and weak nuclear interactions are described in a theoretical framework called the Standard Model (SM). The general theory of relativity (GR) is essentially the theory of gravity, however a quantum theory of gravitation is yet to be discovered. The huge disparity between the electroweak energy scale $m_{EW} \sim 0.1$ TeV[1] and Planck scale $M_{Pl} \sim 10^{16}$ TeV is called the hierarchy problem and restricts us from combining all four interactions effectively in one theoretical framework. The Kaluza-Klein theory was the first attempt to combine electromagnetic interactions with gravity using the concept of extra dimensions in space. In recent years, the ADD model introduced by Arkani-Hamed, Savas Dimopoulos and Gia Dvali and the RS models given by Lisa Randall and Raman Sundrum are notable attempts to address the hierarchy problem by incorporating large extra spatial dimensions and a warped extra dimension, respectively. This chapter provides the reader with a brief review of theories and models mentioned above that can most easily be described as the foundation and motivation for this doctoral work. The formation of micro black holes (MBH) at the Large Hadron Collider (LHC) is possible if extra spatial dimensions exist in nature. Chapter 3 is dedicated to black hole physics with emphasis on MBH.

2.1 The Standard Model

The Standard Model is an elegant theoretical framework which explains most experimental observations in particle physics and has had enormous success in predicting potential discoveries over the past few decades. Elementary particles that carry half-integral spin are called fermions. Elementary particles that carry integral spin are called bosons. Fermions are divided in two families: leptons and quarks, each have three generations. Particles differ by their flavour and mass between generations. The down (d), up (u), strange (s), charm (c), bottom (b) and top (t) quarks with their anti-particles make up the quark family. The electron (e), muon (μ), tau (τ) and their respective neutrinos along with their anti-particles constitute the lepton family. The up and down quarks and the electrons constitute atoms. The remaining leptons and quarks have been observed experimentally in particle accelerators and elsewhere.

[1]Natural units are used throughout this thesis. We take $4\pi G = c = \hbar = \epsilon_\circ = 1$.

A global symmetry does not depend on spacetime. In contrast, a local symmetry depends on spacetime. A gauge theory is a theory where the action is invariant under local symmetry. The local symmetry introduces gauge fields which mediate a force via gauge bosons. The SM is a gauge theory of a symmetry group $SU(3)_C \otimes SU(2)_L \otimes U(1)_Y$ describing strong nuclear, weak nuclear and electromagnetic interactions of matter through the exchange of corresponding spin-1 gauge bosons: eight massless gluons for the strong nuclear interaction, three massive bosons ($W^{\pm}$ and Z) for the weak nuclear interaction and one massless photon for the electromagnetic interaction. The subscripts C, L and Y represent colour, left-handedness and hypercharge, respectively.

Quantum electrodynamics (QED) is relativistic quantum field theory of electrodynamics and is the simplest piece in SM framework. It describes the interaction mechanism between electrically charged elementary fermions by means of the exchange of gauge photons.

Quantum chromodynamics (QCD) describes the interaction mechanism of colour charge: an extra quantum number carried by all quarks in order to satisfy Fermi-Dirac statistics in hadrons. Each quark species can have three different colours, i.e., red, green or blue. Mesons are colourless states of one quark and one anti-quark. Baryons are colourless states of three quarks or anti-quarks. Together, mesons and baryons are called hadrons. The confinement hypothesis postulates that all observable states are colourless and forbids the observability of free quarks since they carry colour charge.

A set of quantum states which yield the same energy upon measurement is called a degenerate set of quantum states. A Lagrangian function of a system summarizes its dynamics in a simple expression which involves kinetic and potential energy of the system. If a Lagrangian is invariant under a group of transformations and has degenerate set of states with minimal energy which transform as the members of given multiplet, arbitrary selection of one such state as the ground state of the system is called spontaneous symmetry breaking (SSB). The vacuum is the ground state in quantum field theory and SSB mechanism takes place when the Lagrangian is symmetric but the vacuum is non-symmetric. The existence of massless degrees of freedom connecting the degenerate states of minimal energy is a general property of the SSB of continuous symmetries.

The electroweak section has symmetry group $SU(2)_L \otimes U(1)_Y$ with four gauge fields. If the Lagrangian is invariant under a continuous symmetry group G but the vacuum is only invariant under a subgroup $H \subset G$ then there exist as many massless spin-0 particles called Nambu-Goldstone bosons as number of broken generators. This general result is called Goldstone theorem [2–4]. The $SU(2)_L \otimes U(1)_Y$ theory interacts with a complex doublet which has four real scalar field components. The SSB mechanism breaks the electroweak symmetry to produce three Goldstone bosons which are eaten by three gauge fields to acquire mass. These massive gauge fields are $W^{\pm}$ and Z whereas the massless gauge field is the photon. One massive scalar field of the complex doublet remains after SSM. This field is called Higgs field and the associated particle is called Higgs boson with mass equal to 125 GeV [5–7].

The SM enjoys great success in predicting potential discoveries. However there are problems that the

model fails to address successfully. The hierarchy problem, strong CP problem, neutrino oscillations, matter-antimatter asymmetry in the universe, nature of dark matter and dark energy are few prime examples.

2.2 The General Theory of Relativity

In 1915, Albert Einstein gave a relativistic theory of gravity in which he established that the curvature of spacetime is directly related to energy and momentum of matter present. This relationship is specified by a system of non linear partial differential equations also known as Einstein's field equations (EFE)

$$R_{\mu\nu} - \frac{1}{2} g_{\mu\nu} R = 8\pi T_{\mu\nu}, \tag{2.1}$$

where $R_{\mu\nu}$ is the second rank Ricci tensor, $g_{\mu\nu}$ is the metric tensor and $T_{\mu\nu}$ is stress-energy tensor of second rank.

The metric tensor is the fundamental object of study in general relativity which defines the geometric and casual structure of spacetime. The trivial solution to EFE is the Minkowski or flat spacetime metric tensor:

$$g_{\mu\nu} = \begin{pmatrix} 1 & 0 & 0 & 0 \\ 0 & -1 & 0 & 0 \\ 0 & 0 & -1 & 0 \\ 0 & 0 & 0 & -1 \end{pmatrix}, \tag{2.2}$$

which represents a spacetime void of mass and energy. In 1916, Karl Schwarzschild gave a non trivial exact solution to EFE outside a neutral, non rotating spherical body of mass M and radial distance r as

$$g_{\mu\nu} = \begin{pmatrix} 1 - \frac{2M}{r} & 0 & 0 & 0 \\ 0 & -(1 - \frac{2M}{r})^{-1} & 0 & 0 \\ 0 & 0 & -r^2 & 0 \\ 0 & 0 & 0 & -r^2 \sin^2\theta \end{pmatrix}, \tag{2.3}$$

which is called the Schwarzschild metric . The structure of spacetime outside an electrically charged and non rotating spherical body is described by the Reissner-Nordström metric, whereas that outside an electrically neutral and rotating spherical body is represented by the Kerr metric [8]. The Kerr-Newman metric describes the spacetime structure outside an electrically charged and rotating spherical body [9, 10]. We shall discuss these solutions in Chapter 3.

2.3 Hierarchy Problem

The Planck mass scale is 17 orders of magnitude greater than the electroweak mass scale. The SM predicts no new physics in this enormously large region which is aesthetically unappealing to high energy physicists and is called the mass hierarchy problem. A unified theory of everything would require all the fundamental scales to be of same order.

In the perturbative theory of quantum mechanics, one-loop radiative corrections to the Higgs boson mass due to a fermion anti-fermion pair can be written as

$$\Delta m_{Hf}^2 = \frac{|\lambda_f|^2}{16\pi^2} \Big[-2\Lambda^2 + 6m_f^2 \ln\left(\frac{\Lambda}{m_f}\right) + ... \Big], \tag{2.4}$$

where λ_f is fermion-Higgs Yukawa coupling, m_f is fermion mass and Λ is an ultraviolet cut-off. The one-loop Feynman diagram for the fermion-Higgs interaction is shown in Figure 2.1. The ultraviolet cut-off for the SM is the Planck scale and the radiative correction to Higgs boson mass is extremely large. This requires incredible fine tuning cancellation between different radiative corrections and bare mass of Higgs boson to yield the observed Higgs mass.

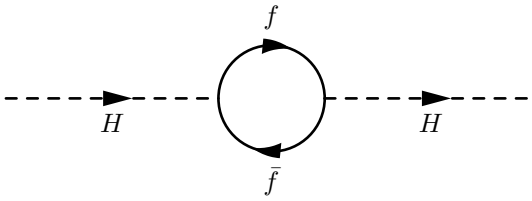

Figure 2.1: Feynman diagram for fermion one-loop correction for Higgs boson mass.

2.4 Supersymmetry

Theories of supersymmetry (SUSY) [11] provide a solution to the hierarchy problem and address several limitations of the SM. SUSY suggests that every particle has a supersymmetric partner which differs in spin by 1/2. The supersymmetric partner of a fermion is a boson called sfermion. SUSY is a spontaneously broken symmetry and supersymmetric partners are much heavier than the corresponding SM partners.

The one-loop radiative correction to the Higgs boson mass due to the sfermion-Higgs interaction can be written as

$$\Delta m_{Hs}^2 = \frac{\lambda_s}{16\pi^2}\left[\Lambda^2 - 2m_s^2 \ln\left(\frac{\Lambda}{m_s}\right) + ...\right], \tag{2.5}$$

where λ_s is sfermion-Higgs coupling and m_s is sfermion mass. The one-loop Feynman diagram for sfermion-Higgs interaction is shown in Figure 2.2. In a scenario where $\lambda_s = |\lambda_f|^2$, two sfermions will effectively cancel the quadratic term in Λ in the one-loop radiative correction due to the pair of fermion anti-fermion.

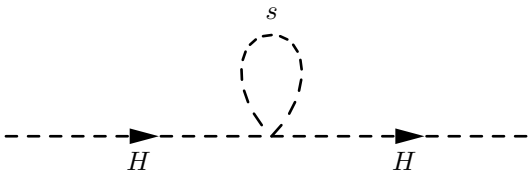

Figure 2.2: Feynman diagram for scalar one-loop correction for Higgs boson mass.

2.5 Theories of Extra Spatial Dimensions

The concept of extra spatial dimensions in physics was initiated by Gunnar Nordström in 1914 in his attempt to deliver a higher dimensional theory of gravitation whose four-dimensional projection would yield Maxwell's equations and Newton's law of gravitation. The Kaluza-Klein (KK) theory developed by Theodore Kaluza and Oskar Klein in 1926 , the ADD model introduced by Arkani-Hamed, Savas Dimopoulos and Gia Dvali in 1998 [1, 12] and Randall-Sundrum (RS) models given by Lisa Randall and Raman Sundrum in 1999 [13, 14] are notable theoretical frameworks that incorporate the concept of extra spatial dimensions. The exciting thing about the later two models is that the cut-off length scale of these types of solutions for the hierarchy problem is placed just below 10^{-16} cm which is easily accessible at LHC. Validation of any such models will serve to figure out the framework of quantum gravity besides successfully addressing the long-standing hierarchy problem.

2.5.1 The Kaluza-Klein Theory

Kaluza pursued Nordström's idea of extra dimensions shortly after and successfully showed in 1921 that a five-dimensional general relativity with a circular fifth dimension yields Einstein's theory of general relativity and Maxwell's equations if we impose the condition that the circular dimension has small radius. Kaluza's work was in classical regime. Klein gave quantum interpretation to Kaluza's work in 1926 and a refined form of this theory is called the Kaluza-Klein (KK) theory.

All fields of the KK theory satisfy periodic boundary condition for the fifth spatial dimension which is compactified on a very small circle of radius R comparable to the Planck length. The momentum component in the fifth dimension is quantized and appears as a tower of infinite states of increasing masses when viewed from four-dimensional perspective. This tower of states is called a KK tower of mass states. At the Planck length, excited mass states are heavy and do not represent electromagnetism. This conclusion led to abandonment of the KK theory for many decades to come.

2.5.2 The ADD Model

The framework of the ADD model allows us to address the hierarchy problem without relying on the principle of supersymmetry [1]. The Planck scale and electroweak scale are considered two fundamental energy scales. The enormous desert between the two fundamental scales has been the driving force behind the construction of theories beyond SM. The ADD model assumes that the true Planck scale is close to the electroweak scale. The apparent enormity of the Planck scale is a consequence of large size of compact extra spatial dimensions compared to the fundamental electroweak scale.

Let us consider a D-dimensional space-time where $D = n+4$ with n compactified extra spatial dimensions with the same radius R. Using Gauss's law, the gravitational potential $V(r)$ between two test masses of mass m_1 and m_2 within a distance $r \ll R$ in $(n+4)$ dimensions is given by

$$V(r) \sim \frac{m_1 m_2}{M_D^{n+2}} \frac{1}{r^{n+1}}, \quad (r \ll R), \tag{2.6}$$

where M_D is fundamental Planck scale in D dimensions. The gravitational flux lines at $r \ll R$ enter n extra spatial dimensions and contribute significantly to the gravitational potential between the two masses. However, the contribution to gravitational flux due to n extra spatial dimensions becomes constant at $r \gg R$. The gravitational potential in this case is

$$V(r) \sim \frac{m_1 m_2}{M_D^{n+2} R^n} \frac{1}{r}, \quad (r \gg R), \tag{2.7}$$

which is the usual four-dimensional Newton's law of gravitation and the effective four-dimensional Planck scale is

$$M_{Pl}^2 \sim M_D^{n+2} R^n. \tag{2.8}$$

The assumption that the electroweak and the fundamental Planck scales are close to each other essentially means

$$M_D \sim m_{EW}. \tag{2.9}$$

Using Equation 2.9 in Equation 2.8 and requiring that R be chosen to reproduce the observed M_{Pl}, we get

$$R \sim 10^{\frac{30}{n}-17} \text{cm} \times \left(\tfrac{1 \text{ TeV}}{m_{EW}}\right)^{1+\frac{2}{n}}. \tag{2.10}$$

The approximate values of R for $n = 1 \to 7$ large extra spatial dimensions are tabulated in Table 2.1 using Equation 2.10. For $n = 1$ case, the size of large extra dimension is comparable to that of our solar system. We omit $n = 1$ case since we don't observe deviation from Newton's inverse-square law of gravitation in our daily lives. The $n = 2$ case has been omitted by performing torsion balance experiment to test inverse-square law at $r = 56 \times 10^{-4}$cm [15], putting an upper limit on $R \leq 44 \times 10^{-4}$cm. This is the most direct way of measuring deviation from inverse-squared law of gravitation.

The SM gauge forces have been accurately measured at $1/m_{EW}$ scale distances. The framework of the ADD model is consistent with this observation since it requires all SM fields to be strictly localized in usual 4 dimensional submanifold. The gravitons are free to propagate in all D dimensions, however their couplings are suppressed by $1/M_D$. The task of localizing all SM fields is completed by embedding this framework in string theory [12]. The SM fields consist of open strings and are confined on 4-dimensional submanifold called D3-brane. The gravitational sector consists of closed strings which are free to propagate in D dimensional bulk.

2.5.3 The Randall-Sundrum Models

Lisa Randall and Raman Sundrum presented two models in an attempt to solve the hierarchy problem using a single warped extra spatial dimension. The first model is called RS1 model which assumes that two brane worlds are embedded in a five-dimensional geometry [13]. The brane where gravity is strong is called Planck-brane while the second brane is called TeV-brane. All SM fields live in TeV-brane. Gravity in TeV-brane is weak because the graviton probability function decreases exponentially as one moves from Planck-brane to TeV-brane through warped extra dimension. The second model is called RS2 which puts

n	R (cm)
1	10^{13}
2	10^{-2}
3	10^{-7}
4	10^{-9}
5	10^{-11}
6	10^{-12}
7	10^{-13}

Table 2.1: Estimates of compactification radius R for $n = 1 \rightarrow 7$ large extra spatial dimensions are given based on ADD model.

the two Planck-branes at infinite distance from each other via fifth dimension [14]. The scenario of MBH production at the LHC is only possible in RS1 model since there is no TeV-brane in RS2 model.

Chapter 3

Physics of Black Holes

This chapter reviews the physics of black holes in moderate detail. We discuss different types of classical black holes in general relativity and their properties. We generalize the discussion to higher spatial dimensions. We discuss the formation of MBH, their decay mechanism and signatures to look for at the LHC.

3.1 Classical Black Holes

The general theory of relativity describes the force of gravity as the spacetime curvature. This curvature is caused by matter and energy distributions in spacetime and affects the paths of particles. Sufficiently dense matter forms a region of space called black hole where the gravity becomes so strong that the escape velocity for outward moving particle becomes greater than the speed of light. The boundary of a black hole is called the event horizon. We review different black hole solutions in following subsections.

3.1.1 Schwarzschild Black Hole

Karl Schwarzschild found the first exact solution to EFE in 1916. The metric describes the spacetime curvature in vacuum due to a static, spherically symmetric and electrically neutral object of mass M

$$ds^2 = -\left(1 - \frac{2M}{r}\right)dt^2 + \left(1 - \frac{2M}{r}\right)^{-1} dr^2 + r^2 d\Omega_2^2, \tag{3.1}$$

is called Schwarzschild metric where

$$d\Omega_2^2 = d\theta^2 + \sin^2\theta d\phi^2 \tag{3.2}$$

is the metric on a 2-sphere. The Schwarzschild metric becomes singular when $r = 2M$ and when $r = 0$. The $r = 2M$ singularity is called coordinate singularity and can be removed by changing to an alternative coordinate system. The $r = 0$ singularity is called curvature singularity and cannot be removed by change of coordinate system.

The spacetime region around the object can be divided into two regions if all of its mass M resides within the spherical surface of radius r. The trajectory of light ray or any massive particle inside the region $r \leq 2M$ must hit the singularity at $r = 0$ and thus the object is called a black hole. The spherical surface $r_H = 2M$ is called the event horizon and the length $r_S = 2M$ is called Schwarzschild radius of the black hole.

3.1.2 Reissner-Nordström Black Hole

The metric describing the spacetime curvature due to a static and spherically symmetric object of mass M which carries an electric charge Q is called Reissner-Nordström metric and is given as

$$ds^2 = -\left(1 - \frac{2M}{r} + \frac{Q^2}{r^2}\right)dt^2 + \left(1 - \frac{2M}{r} + \frac{Q^2}{r^2}\right)^{-1} dr^2 + r^2 d\Omega_2^2. \tag{3.3}$$

The curvature singularity is at $r = 0$. For $M > |Q|$, the location of the event horizon is given by $r_H = M + \sqrt{M^2 - Q^2}$. In addition to this, we have a new type of horizon called inner horizon which is given by $r- = M - \sqrt{M^2 - Q^2}$. For $M = |Q|$, event and inner horizons merge and the black hole is called extremal black hole. There is a mathematical singularity for $M < |Q|$ in Equation 3.3 at $r = 0$ which is not enclosed by an event horizon.

3.1.3 Kerr-Newman Black Hole

The Kerr-Newman metric [9,10] is the solution to EFE for a rotating spherical object of mass M and electric charge Q and is given as

$$ds^2 = -\frac{\Delta}{\Sigma}\left[dt - a\sin^2\theta d\phi\right]^2 + \frac{\Delta}{\Sigma}dr^2 + \Sigma d\theta^2 + \frac{\sin^2\theta}{\Sigma}\left[\left(r^2 + a^2\right)d\phi - adt\right]^2 \tag{3.4}$$

where

$$\Delta = r^2 - 2Mr + a^2 + Q^2 \text{ and } \Sigma = r^2 + a^2\cos^2\theta. \tag{3.5}$$

The angular momentum of the object is $J = aM$ where $a > 0$ is a constant and $\theta = 0$ is the axis of rotation. The metric has a curvature singularity when $\Sigma = 0$. If $M^2 > a^2 + Q^2$, the event horizon is given by $r_H = M + \sqrt{M^2 - Q^2 - a^2}$ and inner horizon is given by $r- = M - \sqrt{M^2 - Q^2 - a^2}$.

The event horizon is a rotating surface in this case and its angular speed is given by

$$\Omega_H = \frac{a}{r_H^2 + a^2}. \tag{3.6}$$

Change of coordinate system introduces a new surface $r_S = M + \sqrt{M^2 - a^2\cos^2\theta - Q^2}$ which is called stationary limit surface and lies outside the event horizon. The region between event horizon and the stationary limit surface is called ergosphere.

An electrically neutral, rotating spherical object of mass M is called Kerr black hole whose metric can be obtained by putting $Q = 0$ in Equation 3.4. Higher dimensional version of Kerr black holes are most relevant to this study as we shall discuss in Section 3.3.3.

3.2 Higher Dimensional Black Holes

Higher dimensional black holes are complex objects in general. In this section, we will briefly discuss generalization of four dimensional Schwarzschild and Kerr black holes to higher dimensions.

The Schwarzschild-Tangherlini metric [16] describes a static, non-rotating spherically symmetric and electrically neutral black hole in higher dimensions $D = n + 4$ and is given as

$$ds^2 = -\left[1 - \left(\frac{r_H}{r}\right)^{n+1}\right]dt^2 + \left[1 - \left(\frac{r_H}{r}\right)^{n+1}\right]^{-1} dr^2 + r^2 d\Omega^2_{n+2}, \tag{3.7}$$

where r_H is the higher dimensional event horizon, n is the number of extra spatial dimensions and $d\Omega^2_{n+2}$ is the metric on $(n+2)$-sphere. The mass M of Tangherlini black hole is

$$M = \frac{1}{16\pi}(n+2) r_H^{n+1} A_{n+2}, \tag{3.8}$$

where A_{n+2} is the area of a unit $(n+2)$-sphere which contains Γ-function

$$A_{n+2} = \frac{2\pi^{\frac{n+3}{2}}}{\Gamma\left(\frac{n+3}{2}\right)}. \tag{3.9}$$

The higher dimensional counterpart of neutral Kerr metric is Myers-Perry metric [17]. A $(n+4)$-dimensional Myers-Perry black hole has N_r independent axis of rotation where $N_r = (n+2)/2$ if n is even or else $N_r = (n+3)/2$ if n is odd. This makes Myers-Perry metric much complicated. Singly-rotating Myers-Perry black hole is simplified version of a general Myers-Perry black hole which has only one axis of rotation on 3-brane. The metric for singly-rotating Myers-Perry black hole is

$$\begin{aligned} ds^2 = &-\left(1 - \frac{\mu}{\Sigma r^{n-1}}\right)dt^2 - \frac{2a\mu \sin^2\theta}{\Sigma r^{n-1}} dt d\phi + \frac{\Sigma}{\Delta} dr^2 + \Sigma d\theta^2 \\ &+ \left(r^2 + a^2 + \frac{a^2 \mu \sin^2\theta}{\Sigma r^{n-1}}\right) \sin^2\theta d\phi^2 + r^2 \cos^2\theta d\Omega_n^2, \end{aligned} \tag{3.10}$$

where

$$\Delta = r^2 + a^2 - \frac{\mu}{r^{n-1}} \text{ and } \Sigma = r^2 + a^2 \cos^2\theta. \tag{3.11}$$

The mass M and angular momentum J of singly rotating Myers-Perry black hole are given by

$$M = \frac{1}{16\pi}(n+2) A_{n+2} \mu, \quad J = \frac{2}{n+2} aM, \tag{3.12}$$

where $\mu > 0$ and $a > 0$ are the parameters which govern the mass and angular momentum of the black hole, respectively. For any value of n, the Myers-Perry black hole has an event horizon only and no inner horizon.

3.3 Microscopic Black Holes at the LHC

In this section, we will discuss the main assumptions and criteria for creation of microscopic black holes (MBH) at the LHC in the context of theories of large extra dimensions. Hawking radiation is an important observable effect associated with the decay of MBH. We will discuss Hawking radiation and different phases in decay mechanism in detail. We will also discuss observable signatures to identify MBH events at the LHC.

3.3.1 Creation of Microscopic Black Holes

According to low-scale gravity models [1, 12, 13], creation of MBH [18] at the LHC is possible if the available energy is greater than M_D. The Schwarzschild radius depends on the centre-of-mass energy E of the colliding particles and is denoted by $r_H(E)$. The impact parameter b is the perpendicular distance between the paths of the colliding particles. MBH will be formed according to Thorne's Hoop Conjecture [19] if $b < r_H(E)$ and the colliding particles will disappear forever behind the event horizon. Numerical results [20, 21] show that

$$b \leq b_{max} \simeq 1.5 \times 2^{-1/n+1} r_H(E), \tag{3.13}$$

for MBH to form in case of grazing collision of energetic particles and the ratio $b_{max}/r_H(E)$ approaches unity as D increases.

The MBH formed is a higher dimensional object created on 3-brane and will extend to the bulk. The simplest case of higher dimensional black holes is Schwarzschild-Tangherlini black hole whose metric is described in Equation 3.7. The relationship between r_H, M and M_D in D dimensions in this case [17] is given by

$$r_H = \left(\frac{8\Gamma(\frac{n+3}{2})}{(n+2)\sqrt{\pi}^{(n+1)}} \right)^{\frac{1}{n+1}} \frac{1}{M_D} \left(\frac{M}{M_D} \right)^{\frac{1}{n+1}}. \tag{3.14}$$

The Compton wavelength of a particle is equivalent to the wavelength of a photon whose energy is equal to the rest mass energy of the particle. The MBH will form in classical regimn if the Compton wavelength λ_C of the colliding particles is much less than the corresponding $r_H(E)$

$$\frac{4\pi}{E} \ll \left(\frac{8\Gamma(\frac{n+3}{2})}{(n+2)\sqrt{\pi}^{(n+1)}} \right)^{\frac{1}{n+1}} \frac{1}{M_D} \left(\frac{E}{M_D} \right)^{\frac{1}{n+1}}. \tag{3.15}$$

The inequality 3.15 is solved to estimate the ratio $x_{min} = E/M_D$ for different values of n and is tabulated in Table 3.1. The LHC smashed proton beams at 8 TeV centre-of-mass energy in 2012. The E is always less than 8 TeV since it is the parton energy. It is obvious that value of fundamental Planck scale decreases as number of extra spatial dimensions increase.

n	2	3	4	5	6	7
x_{min}	8.0	9.5	10.4	10.9	11.1	11.2

Table 3.1: The values of the ratio $x_{min} = E/M_D$ are presented as a function of n to describe the criterion for creation of MBH.

3.3.2 Production Cross Section of Microscopic Black Holes

Production of MBH is a classically allowed process. The production cross section of MBH is geometric in nature and depends on r_H

$$\sigma_{\text{production}} \propto \pi r_H^2 = \pi \left(\frac{8\Gamma(\frac{n+3}{2})}{(n+2)\sqrt{\pi}^{(n+1)}} \right)^{\frac{2}{n+1}} \frac{1}{M_D^2} \left(\frac{E}{M_D} \right)^{\frac{2}{n+1}}, \tag{3.16}$$

when two high energy elementary particles collide. The cross section increases with the centre-of-mass energy of colliding elementary particles as well as with the increase in D.

The LHC collides two high energy protons which are composite particles. In this case, the production cross section of MBH is calculated [22] by properly summing over all pairs of partons that carry enough energy to produce MBH:

$$\sigma^{pp\to\text{MBH}}_{\text{production}} = \sum_{ij} \int_{\tau_m}^{1} d\tau \int_{\tau}^{1} \frac{dx}{x} f_i(x) f_j(\tau/x) \sigma^{ij\to MBH}_{\text{production}}, \tag{3.17}$$

where x is the parton momentum fraction, $\tau = x_i x_j$ is the parton-parton centre-of-mass energy squared fraction, $\sqrt{\tau_m s}$ is the minimum centre-of-mass energy for MBH production and $f_i(x)$ are the parton distribution functions (PDF) which determine the fraction of the centre-of-mass energy carried by the partons. The sum over all initial parton pairings represents an enhancement in MBH production cross section at a given centre-of-mass energy for pp collisions relative to collision between elementary particles in an accelerator. The parton-parton cross section increases with E unlike other conventional hard perturbative processes however the PDFs decrease rapidly with increase in E due to availability of more virtual quarks and gluons and the fraction of energy passed to individual partons decreases.

3.3.3 Properties of Microscopic Black Holes

We understand MBH fairly well in the context of general relativity when $M \gg M_D$ since they resemble thermal black holes in their properties. In the limit $M \sim M_D$, a quantum theory of gravity is required to understand the properties of MBH. A MBH with $M \gg M_D$ will most probably be a singly-rotating Myer-Perry black hole and will go through different phases of decay [22] during its lifetime. They are briefly described here in chronological order.

Balding Phase

The newly formed MBH is highly asymmetric and carries quantum gauge charges of the initial state parton pair. These gauge charges are shed rapidly through the emission of small number of quanta on the brane. Emission of gravitational radiation in bulk is dominant in this phase. At the end of transient balding phase, a MBH is characterized only by its mass and angular momentum.

Mass and Angular Momentum Loss Phase

The MBH can generally be described by Myer-Perry metric in Equation 3.10 at the end of the balding phase. The MBH decays slowly via semi-classical Hawking evaporation process [23]. The mass of a highly rotating black hole drops to about $60-70\%$ in an initial period of $10-15\%$ of total decay time [24]. The angular momentum also drops to about 20% its initial value during this early time. This phase is often referred as spin-down phase. The decay of MBH beyond this point resembles the decay of a non-rotating black hole which can be described by Schwarzschild-Tangherlini metric in Equation 3.7. The mass and angular momentum decrease approximately linearly with time except for the last $10-20\%$ when they drop faster. This is known as Schwarzschild phase.

Planck Phase

The MBH enters quantum regime once $M \sim M_D$ and its properties are governed by quantum theory of gravitation. It will either continue to decay and vanish completely or will become a stable remnant in D dimensions. The fate of MBH remnant is unknown at this moment.

A non-zero value of the impact parameter between the two colliding partons at the LHC will result in the formation of a rotating MBH in the higher dimensions with a single axis of rotation on the brane. Since the balding phase is very short-lived, the formed MBH quickly becomes a singly-rotating Myer-Perry black hole which is an extension of neutral Kerr black hole in the higher dimensions.

Temperature and Lifetime

The temperature of the MBH depends on its mass, angular momentum, Planck scale and dimensionality. The mathematical expression for MBH's temperature [22] can be written in term of the radius of its event horizon as

$$T_H = \frac{(n+1)+(n-1)a_*^2}{4\pi r_H(1+a_*^2)} \xrightarrow{J\to 0} \frac{(n+1)}{4\pi r_H}, \tag{3.18}$$

where a_* is a dimensionless rotation parameter and is equal to $(n+2)J/2Mr_H$. The temperature of MBH increases with its dimensionality and decreases with its mass.

The lifetime of a classical MBH is defined as the time required to complete the spin-down and Schwarzschild phases. The expression for lifetime of a D-dimensional MBH [22] is given as

$$\tau_D = \frac{C}{M_D}\left(\frac{M}{M_D}\right)^{\frac{n+3}{n+1}} \tag{3.19}$$

where C is a constant which depends on dimensionality and initial angular momentum of the MBH. The balding phase is generally believed to be relatively short-lived [24] and is often omitted from calculation of lifetime.

3.3.4 Hawking Evaporation Process

Black holes are prohibited to emit particles in the general theory of relativity. S.W. Hawking showed [23] that quantum mechanical effects in curved spacetime allow black holes to create and emit particles like a hot object in thermal equilibrium with a temperature. A quantum fluctuation is the temporary appearance of a particle-antiparticle pair in the vacuum for a time allowed by the uncertainty principle. When these virtual pairs are created near the event horizon of a black hole, the antiparticle (or particle) crosses the event horizon and enters the black hole while the particle (or antiparticle) escapes to infinity. The black hole converts the virtual pair into real particle (or antiparticle) with a reduction in its mass. An observer at infinity receives a flux of incoming particles emitted from the black hole which is called Hawking radiation. The mass of the black hole keeps on decreasing as the result of discrete emission of particles (antiparticles).

In the case of D-dimensional MBH, Hawking radiation is emitted on brane as well as into the bulk. The Hawking radiation emitted on brane consists of SM modes whereas that emitted into the bulk consists of

gravitational modes, called gravitons and scalar fields which carry no quantum numbers under the SM gauge group. The radiation spectrum for a MBH [25] in spin-down and Schwarzschild phases nearly matches a black-body spectrum. The fluxes of particles N and energy E emitted by a rotating MBH and measured by an observer at infinity, along with rate of loss of angular momentum J are given by expressions [26]

$$\frac{d^2}{dtd\omega}\begin{pmatrix}N\\E\\J\end{pmatrix} = \frac{1}{2\pi}\sum_{l,m,j\ldots}\frac{|\mathscr{A}(\omega)|^2}{\exp(\tilde{\omega}/T_H)\mp 1}\begin{pmatrix}1\\\omega\\m\end{pmatrix}, \tag{3.20}$$

where l, m, j in the summation are azimuthal, magnetic and total angular momentum quantum numbers, respectively. The $|\mathscr{A}(\omega)|^2$ is the transmission (or absorption) probability, also called gray-body factor and depends on angular momentum, spin and dimensionality in general. The parameter $\tilde{\omega}$ is defined as:

$$\tilde{\omega} = \omega - m\Omega_H = \omega - m\frac{a}{r_H^2 + a^2}, \tag{3.21}$$

and T_H is the Hawking temperature of the MBH. The ∓ 1 factor represents bosons and fermions, respectively.

The emission of a particular species of particle in Hawking radiation is directly related to its degrees of freedom (dof). For SM particles, degrees of freedom is calculated [25] as:

$$\text{dof} = n_Q \times n_S \times n_F \times n_C, \tag{3.22}$$

where n_Q is the number of charge states, n_S is number of spin states, n_F is number of flavours and n_C is the number of color states. Table 3.2 shows number of degrees of freedom for all particles in SM. The MBH will emit all 118 SM degrees of freedom with equal probability except for gray-body effects via Hawking radiation since gravitational coupling is blind to charge, spin, flavour and color. The probabilities of emission for different particles is given as

$$P_i = \frac{\epsilon_i \times \text{dof}_i}{\sum_j \epsilon_j \times \text{dof}_j}, \tag{3.23}$$

where ϵ_i is the emission rate of particle i and can be calculated using Equation 3.20 with complete knowledge of greybody factor for a given species. The greybody factors have been calculated for various types of black holes using analytical and numerical techniques. For non-rotating and neutral higher dimensional MBH, P. Kanti and J. March-Russell presented analytical calculations of greybody factors using a low-energy approximation for Higgs bosons [27], and fermions and gauge bosons [28]. C.M. Harris and P. Kanti performed exact numerical calculations [29] of greybody factors for all SM particles for non-rotating and neutral higher dimensional MBH. D. Ida, K. Y. Oda and S. C. Park analytically calculated [30] greybody factors of all SM particles for a rotating neutral higher dimensional MBH, neglecting the balding phase. V. Cardoso, M. Cavaglià, and L. Gualtieri provided exact numerical calculations [31] of greybody factor for gravitons in the bulk. Table 3.3 shows fractional emission rates per degree of freedom relative to Higgs boson emission rate for a non-rotating and neutral MBH in various dimensions using results from Ref. [29, 31]. The emission probability of different SM particles and gravitons for a non-rotating and neutral MBH in various dimensions [25] is given in Table 3.4. This shows that emission of hadrons (composite particles made up of quarks and gluons) is significantly high in Hawking evaporation during Schwarzschild phase in the LHC.

This also shows that MBH will prefer to evaporate on brane however significant graviton emission occurs in bulk as dimensionality increases.

Particle Type	Charge State	Spin State	Flavour State	Colour State	dof
Quarks	2	2	6	3	72
Charged leptons	2	2	3		12
Neutrinos	2	1	3		6
Gluons	1	2		8	16
Photon	1	2			2
Z boson	1	3			3
W bosons	2	3			6
Higgs boson	1				1

Table 3.2: Number of degrees of freedom (dof) of the SM particles.

D	4	5	6	7	8	9	10	11
Higgs Boson	1.00	1.00	1.00	1.00	1.00	1.00	1.00	1.00
Fermions	0.37	0.70	0.77	0.78	0.76	0.74	0.73	0.71
Gauge Bosons	0.11	0.45	0.69	0.83	0.91	0.96	0.99	1.01
Gravitons	0.02	0.20	0.60	0.91	1.90	2.50	5.10	7.60

Table 3.3: Fractional emission rates per degree of freedom relative to Higgs boson are tabulated for a non-rotating and neutral MBH in various dimensions [29, 31].

D	4	5	6	7	8	9	10	11
Quarks	0.71	0.66	0.62	0.59	0.57	0.55	0.53	0.51
Charged Leptons	0.12	0.11	0.10	0.10	0.10	0.09	0.09	0.09
Neutrinos	0.06	0.06	0.05	0.05	0.05	0.05	0.04	0.04
Gluons	0.05	0.09	0.12	0.14	0.15	0.16	0.16	0.16
Photon	0.01	0.01	0.02	0.02	0.02	0.02	0.02	0.02
EW Bosons	0.03	0.05	0.07	0.08	0.09	0.09	0.09	0.09
Higgs Boson	0.03	0.01	0.01	0.01	0.01	0.01	0.01	0.01
Graviton	0.00	0.00	0.01	0.01	0.02	0.03	0.05	0.08

Table 3.4: Emission probability of SM particles and graviton for a non-rotating and neutral MBH in different dimensions [25].

3.3.5 Detection Signatures

Emission of quarks and gluons is dominant as MBH continues to decay on brane. Observed deviations from anticipated behaviour of QCD events could point towards the formation of MBH in the detector. QCD events with high transverse momentum gradually decrease due to falling PDFs as collision energy increases [32]. We expect MBH events with higher transverse momentum to dominate over the QCD events as the collision energy increases [33]. In a standard QCD process, typical back-to-back di-jet production is dominant for pp collisions. Multi-jet events will exceed QCD di-jet events since MBH decays mainly through the emission of

Hawking radiation to partons [33,34]. Neutrino emission on the brane and graviton emission in the bulk will result in the observation of missing energy in the detector.

3.3.6 Current Limits on M_D

Measuring M_D in the context of theories of higher dimensions is our main goal if MBH are discovered at the LHC. Observation of MBH decay in the detector would help determining the value of M_D. Searches have been made at various experimental facilities and have put model-dependent limits on M_D. Lower limits on M_D with 95% confidence level for direct graviton emission searches at LEP (ALEPH and DELPHI experiments), Tevatron (CDF and DØ experiments) and LHC (CMS and ATLAS experiments) have been summarized in Ref. [35] and are reproduced here in Table 3.5. Lower limits on M_D have been set in MBH decay channels like $\gamma + \text{jets}$, $e^{\pm} + \text{jets}$, $\mu^{\pm} + \text{jets}$, e^+e^-, $\mu^+\mu^-$, $e^{\pm}\mu^{\mp}$, $e^{\pm}\tau^{\mp}$, $\mu^{\pm}\tau^{\mp}$ and multi-jets, however these limits are less stringent because of the relation of measurement quantities to quantities in theory.

D	M_D [TeV]						
	Mono-photon		Mono-jet	Mono-photon		Mono-jet	
	LEP	CDF	DØ	ATLAS	CMS	ATLAS	CMS
6	1.60	1.40	0.884	2.17		5.25	5.61
7	1.20	1.15	0.864	2.12	2.30	4.11	4.38
8	0.94	1.04	0.836	2.13	2.70	3.57	3.86
9	0.77	0.98	0.820	2.14	2.20	3.27	3.55
10	0.66	0.94	0.797	2.17	2.00	3.06	3.26
11			0.797				
12			0.778				

Table 3.5: Lower limits on M_D at the 95% confidence level from direct graviton emission searches at LEP, Tevatron and LHC [35].

Chapter 4

ATLAS Detector at the Large Hadron Collider

The CERN laboratory in Geneva, Switzerland is the mecca for experimental high energy physicists for decades to come. The Large Hadron Collider (LHC) at CERN is currently the world's largest accelerator and collider for pp, p-Pb and Pb-Pb collisions [36]. Six notable detector experiments reside at the LHC: ATLAS [37], CMS [38], LHCb [39], LHCf [40], TOTEM [41] and ALICE [42]. ATLAS and CMS are general purpose giant detectors. LHCb is dedicated to precision measurements of CP violation and rare decays of B hadrons. LHCf conducts measurements of very energetic neutral particles in the very forward region to help understand the ultra high energy cosmic rays. TOTEM is dedicated to measure the total cross section, elastic scattering and diffractive processes for pp collisions at the LHC. ALICE is designed to study short-lived quark-gluon plasma formed as a result of colliding Pb-Pb nuclei.

This chapter in its subsequent sections presents a brief yet comprehensive account of the LHC machine and ATLAS detector. Emphasis is on the design of the LHC machine and ATLAS detector. We shall also discuss the trigger sequence and mechanism to select events of interest.

4.1 The Large Hadron Collider

The LHC is a 26.7 km two-ring superconducting hadron accelerator installed in a previously existing tunnel between 45 m and 175 m below ground that housed the LEP machine [36]. It is composed of eight arcs, each 2987 m long, which are connected through eight straight sections of length 528 m each. Four octants are equipped with beam interaction points whereas the remaining four octants are used by accelerator equipment. ATLAS and LHCf are installed at Point 1, ALICE at Point 2, CMS and TOTEM at Point 5 whereas LHCb is situated at Point 7. A layout of the LHC machine and positions of six detector experiments are shown in Figure 4.1.

The LHC machine is designed to collide protons with unprecedented 14 TeV centre-of-mass energy and design luminosity of 10^{34} cm^{-2}s^{-1}. The nominal design number of bunches per beam are 2808 with bunch spacing of 24.95 ns and 1.15×10^{11} protons/bunch. There are approximately 20 pp interactions per bunch

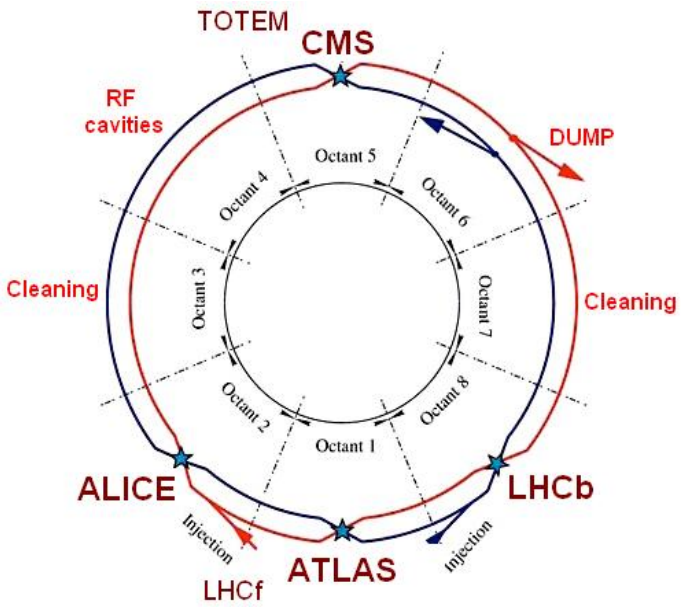

Figure 4.1: A layout of the LHC showing all eight octants and location of six detector experiments [36].

crossing on average. These additional *pp* interactions are unwanted for physics study and are referred to as pileup effects.

In 2012, the LHC machine collided protons with 8 TeV energy and delivered a total integrated luminosity of 23.3 fb^{-1} with instantaneous luminosity reaching as high as 7.7×10^{33} $\text{cm}^{-2}\text{s}^{-1}$. The nominal bunch spacing of 25 ns was achieved while filling a record number of 2748 bunches per beam.

4.1.1 Injection Chain

The LHC doesn't accelerate the proton bunches to the required energy in one go. In fact, accelerating protons to the designed collision energy of 7 TeV per beam is a five stage process with stringent requirements at each phase. The LHC chain is shown in Figure 4.2. Starting at LINAC2, the protons are accelerated to the energy of 50 MeV with 20 μs pulse length. The protons are injected into proton synchrotron booster (PS Booster) in its four rings where they form one bunch per ring and achieve energy of 1.4 GeV. The PS Booster injects the proton bunches to the Proton Synchrotron (PS) where an energy of 25 GeV with bunch spacing of 25 ns is achieved in its single ring, hence a proton bunch train is formed. This proton bunch train is passed to Super Proton Synchrotron (SPS) which further accelerates the protons to 450 GeV. The proton bunch train finally splits into two, and each is fed to the LHC in opposite directions where they are accelerated to the required energy per beam in radio frequency cavities. LINAC2, PS Booster, PS and SPS have been used by previous experiments in CERN for decades.

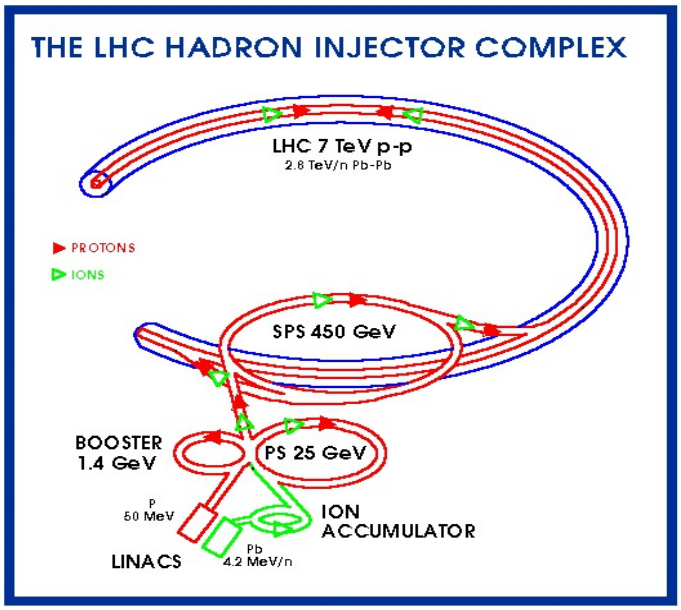

Figure 4.2: The LHC Injector Complex [36].

4.2 ATLAS Detector

ATLAS is a perfect example of a hermetic detector. It comprises a series of concentric cylinders with total length of 44 m and diameter of 25 m, weighs about 7000 tons and is installed 100 m underground [37].

A common coordinate system is used throughout ATLAS. The point where two proton beams collide is called interaction point (IP). The IP is the origin of the coordinate system. The z-axis runs along the beam line. The xy plane is perpendicular to the beam line and is called the transverse plane. Particle momentum measured in xy-plane is called the transverse momentum, p_T. The positive x-axis points from the interaction point to the centre of the LHC ring and the positive y-axis points upward to the surface of the earth. The detector half at positive z-values is referred to as the A-side while the other half is called C-side. The transverse plane is described in terms of $r\phi$ coordinates. The azimuthal angle ϕ is measured from the x-axis. The radial dimension r measures the distance from the beam line. The polar angle θ is defined as the angle from the positive z-axis. The polar angle is often reported in terms of pseudorapidity, defined as $\eta = -\ln(\tan\theta/2)$ and is a preferred angular coordinate to work with in experimental high energy physics.

We divide the ATLAS detector into four major components based on their purpose and measurements they perform:

1. Inner Detectors
2. Calorimeters
3. Muon Spectrometers
4. Superconducting Magnet Systems.

Each component and its sub-components are further divided into two sections: barrel and end-cap sections mainly because of cylindrical geometry of ATLAS as shown in Figure 4.3. The only exception is the superconducting solenoid, one of the two magnetic systems in ATLAS which has no end-cap sections. We discuss the technical aspects of ATLAS detector components in moderate detail in the following subsections. Further details can be found in Ref. [37].

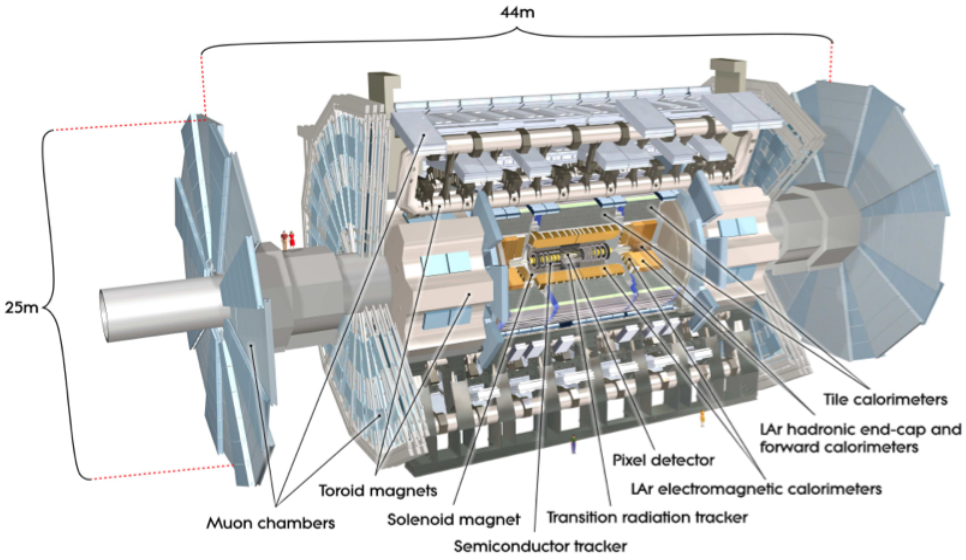

Figure 4.3: The cut-away view of ATLAS detector [37].

4.2.1 Inner Detectors

The inner detectors (IDs) are the most compact yet very sophisticated in their construction and are responsible for high precision measurements of the impact parameter, vertex position and momenta of charged particles produced by pp collisions at the IP. The IDs are 7 m in length with 1.15 m radius. The IDs are divided into three sub-components based on different detection methods as shown in Figure 4.4. These sub-components are pixel detectors, semiconductor tracker (SCT) and transition radiation tracker (TRT). The barrel and end-cap sections combined for all three sub-components ensure $|\eta| < 2.5$ coverage. The final momentum of a passing track through the IDs is determined by 43 precise momentum measurements taken along its path.

Pixel Detectors

Closest to the IP, pixel detectors consist of 80 million very minute semiconductor segments called pixels that provide high granularity and precision tracking. A module, formed by combining 46080 pixels, has dimensions of 62.4×21.4 mm^2 and is divided into 16 chips for distinct read-outs. Each chip is an array of 18×160 pixels. These chips are designed to operate for 10 years in the intense radiation environment of 300 kGy of ionization radiation and fluence of 5×10^{14} neutrons/cm^2.

The pixel detectors in the barrel consist of three concentric cylinders with radii 5 cm, 9 cm and 12 cm.

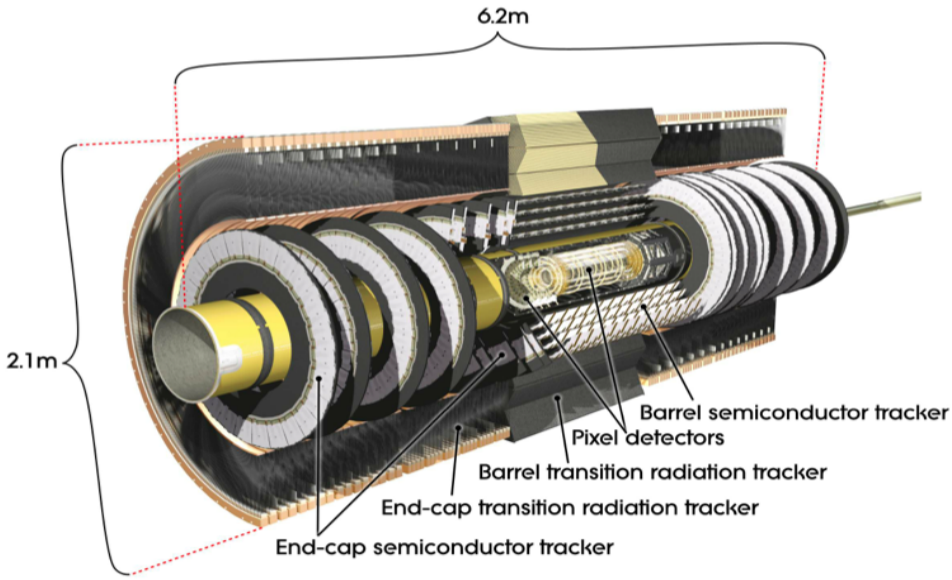

Figure 4.4: The cut-away view of ID [37].

Altogether, they hold 1456 modules. The two end-cap pixel detectors consist of three discs each. Each disc has 288 modules with inner radius of 9 cm and outer radius of 15 cm. Each layer is 2.5% of a radiation length in thickness at track normal incidence and all three layers are typically crossed by each track.

Semiconductor Tracker

The semiconductor tracker (SCT) presents eight layers of silicon microstrip detectors to a track coming from the IP thus yielding eight precise measurements in the $r\phi$ dimension, incorporating small angle stereo to provide z measurement. A silicon detector is a wafer of 6.36×6.4 cm^2 with 768 readout strips and pitch size 80 μm. Pitch size is the distance between identical features in an array. A module is formed when two wafers are aligned together to form a 12.8 cm long strip, on top of which another strip is placed with an inclined angle of 40 mrad. A heat transport plate is introduced between the two strips to conduct heat produced by the electronics through the module thus ensuring its cold operation. For each module, the spatial resolution in the $r\phi$ dimension is 16 μm and 580 μm in z direction. Tracks can be distinguished if separated by 200 μm. The SCT presents an integrated area of 61 m^2 with a total of 6.2 million readout channels.

In the barrel SCT, the modules are mounted on the inner and outer surfaces of four carbon fibre cylinders with radii 30 cm, 37.3 cm, 44.7 cm and 52 cm thus forming eight layers. In each end-cap SCT, nine discs host up to a maximum of three rings of modules each. Each disc also ensures $|\eta| < 2.5$ coverage.

Transition Radiation Tracker

The transition radiation tracker (TRT) is a huge assembly of straw detectors, each with 4 mm diameter, gold plated W-Re wire of 30 μm diameter stretched along its axis and maximum length of 144 cm. Each straw is

filled with a mixture of Xe (70%), CO_2 (27%) and O_2 (3%), which along with its small diameter, ensures an exceptionally high rate of operation, fair tracking of particles and detection of associated transition radiation with trigger timing of 1 ns. Addition of Xe makes the TRT capable of distinguishing between relativistic electrons and hadrons. The TRT provides 36 position measurements for each track.

The barrel TRT is a module with the number of straws varying from 329 to 793 per module. A total of 50000 straws are installed along the axial direction in the barrel TRT. To reduce occupancy near the IP, each straw is divided into two equal halves, each having an independent readout channel. Thus, there are 100000 readout channels for the barrel TRT. The radial range also varies from 56 cm to 107 cm. The first six layers are inactive for 40 cm on either sides of the IP to reduce occupancy.

Each end-cap TRT consists of 18 concentric wheels with modules of straw detectors arranged in the radial direction. All wheels have an outer radius of 103 cm, the first 14 wheels have an inner radius of 64 cm while the outer four wheels have an inner radius of 48 cm. The two end-cap TRT combined contain 320000 straws and hence the same amount of readout channels.

4.2.2 Calorimeters

The ATLAS calorimeters are an assembly of electromagnetic (EM) and hadronic calorimeters based on the sampling technique with an overall coverage of $|\eta| < 4.9$. Table 4.1 gives an overview of η coverage for the various components of ATLAS calorimeters which are shown in Figure 4.5 and categorized below according to their working principle and requirements in radiation tolerance.

Calorimeters	Sections	η coverage
EM calorimeter	EM barrel	$\|\eta\| < 1.475$
	EM end-cap	$1.375 < \|\eta\| < 3.2$
Hadronic tile calorimeter	Main barrel	$\|\eta\| < 1.0$
	Extended barrel	$0.8 < \|\eta\| < 1.7$
LAr hadronic calorimeter	End-cap only	$1.5 < \|\eta\| < 3.2$
Forward calorimeter	End-cap only	$3.1 < \|\eta\| < 4.9$

Table 4.1: The η coverage of ATLAS calorimeters.

EM Calorimeter

An accordion geometry is adopted to ensure full coverage, avoid dead regions, provide efficient energy resolution and position measurement of electrons and photons. Lead and LAr are used as passive and active mediums, respectively. The low radiation length in Pb adds to the compactness of EM calorimeter in the barrel and end-cap regions. The barrel and end-cap sections are divided into three longitudinal sampling layers for position measurement, containment of EM shower energy and to distinguish hadronic showers from EM showers. In the barrel section, the LAr gap is kept constant at 2.1 mm but this gap increases in the end-cap sections as the accordion wave increases in the r direction.

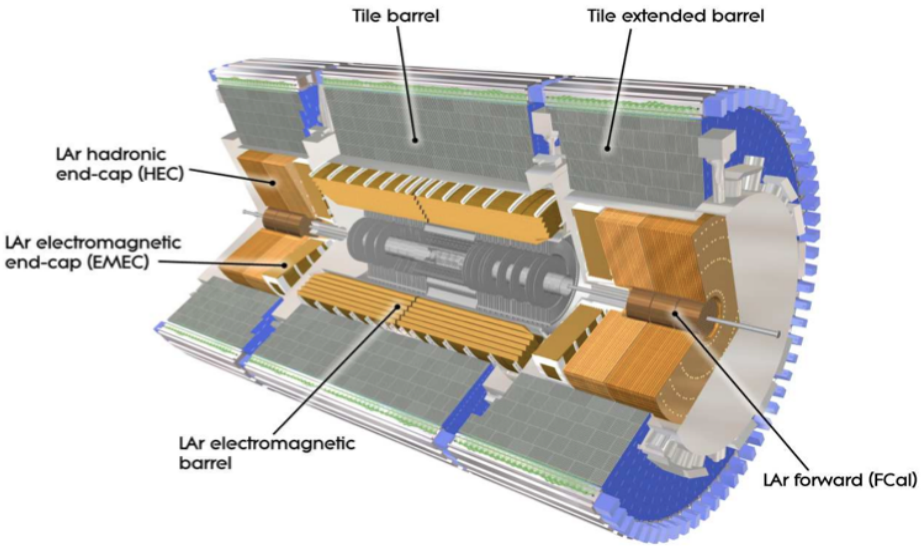

Figure 4.5: The cut-away view of ATLAS calorimeters [37].

Hadronic Tile Calorimeter

An extended barrel section is placed on either side of the main barrel section with a radial gap of 68 cm. Each such section is a combination of 64 independent wedges fixed along ϕ direction. Each wedge is made of steel which acts as passive medium for high energy hadrons. Scintillating plastic is affixed to two of its rectangular sides. The radial gap between the extended barrel sections and the main barrel section serves for cabling space. It also hosts the intermediate tile calorimeter to maximize volume of active material in the region.

LAr Hadronic Calorimeter

The LAr hadronic calorimeter has a conventional geometry of copper plates and LAr. Each end-cap has two wheels and each wheel contains 32 identical modules. The front wheel module has 24 copper plates whereas the back wheel module has only 16 copper plates. In each case, separation between the plates is 8.5 mm. Three electrodes are introduced between the two plates such that LAr is virtually divided into four compartments which adds to the fast response of ATLAS detector.

Forward Calorimeter

The forward calorimeter uses LAr as active medium but is divided into one EM module and two hadronic modules. The EM module has copper sheets while the hadronic module has Tungsten sheets. The use of Tungsten sheets adds compactness due to its high density and better ability to produce showers in limited space. The LAr gap size is 250 μm in the case of the EM module whereas for the two hadronic modules it is 375 μm and 500 μm, respectively. The smaller gap size for LAr ensures efficient collection of large ion buildups due to relatively higher intensities in forward region.

4.2.3 Muon Spectrometers

The muon spectrometers are the largest component of the ATLAS detector and is shown in Figure 4.6. It contains monitored drift tubes (MDT), cathode strip chambers (CSC), resistive plate chambers (RPC) and thin gap chambers (TGC) in its barrel and two end-cap sections at different η ranges. A module based on any of the four detectors is called a chamber. The barrel chambers form three cylindrical layers at 5 m, 7.5 m and 10 m from beam axis and cover the region of $|\eta| < 1.0$. The barrel chambers are arranged in projective towers for alignment purposes due to the huge size of spectrometers. Alignment is ensured using optical instrumentation. The inner cylinder has projective towers of 2×4 chambers optically aligned on either sides of the cylinder. Two outer cylinders carry projective towers of 2×3 chambers on either side of both cylinders. The end-cap sections contain four disks each at 7 m, 10 m, 14 m, and 21 m from the IP covering $1.4 < |\eta| < 2.7$ with chambers arranged in trapezoidal shape. The relative position of the discs is monitored instead of the individual chambers.

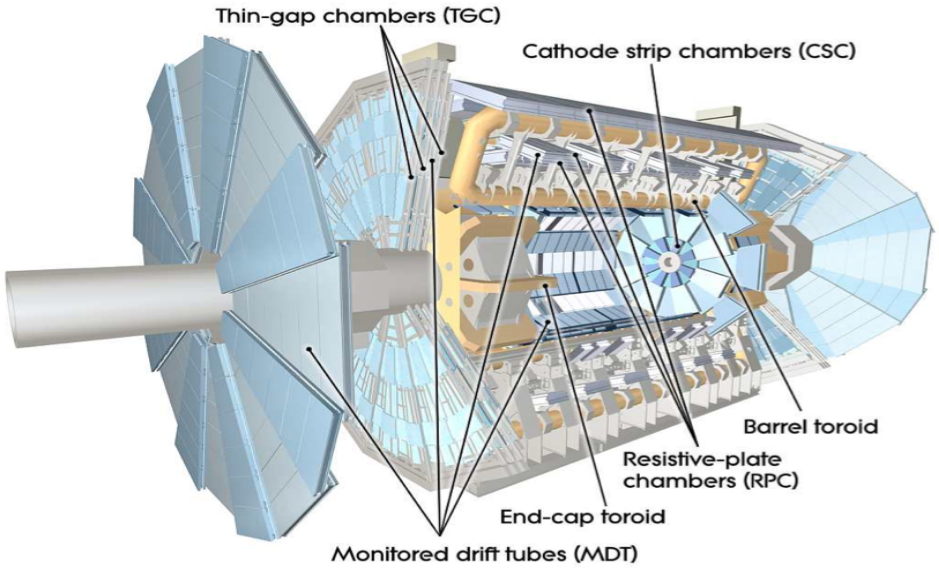

Figure 4.6: The cut-away view of muon spectrometers [37].

In the barrel and the end-cap sections, 16 fold segmentation is adopted in the ϕ direction to cover the eight fold toroidal superconducting barrel and end-cap magnets. Eight segments between the two magnet coils are relatively larger in size and are called large sectors. The segments around individual magnet coils are called the small sectors.

The MDTs are used for precise track measurement of muons in the barrel region where the muon flux is relatively low. The CSCs are installed near the IP and in the forward region for precise track measurement. The RPCs in the barrel and the TGCs in the end-cap sections serve as bunch crossing identifiers because of their time resolution of less than 25 ns.

4.2.4 Superconducting Magnet Systems

The superconducting magnetic system of the ATLAS detector consists of a central solenoid (CS), one large air-core barrel toroid (BT) and two end-cap toroids (ECT). An Al-Cu-NbTi alloy with varying composition is used for flat superconducting cables of the three magnetic systems. A geometric representation of the magnetic system is shown in Figure 4.7.

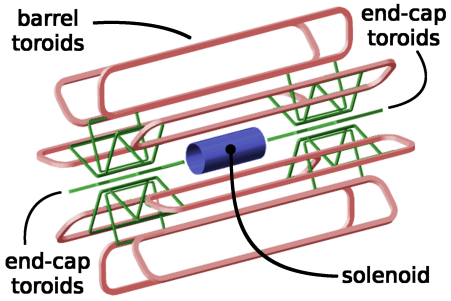

Figure 4.7: Geometric representation of ATLAS magnet systems [43].

The CS is 5.3 m in length with a bore of 2.4 m and provides a strong magnetic field of 2 T. It bends charged particles coming from the IP in the IDs and the EM calorimeter in opposite directions. The BT is 26 m in length and 20 m in outer diameter. It has eight coils assembled symmetrically in r direction around z axis and provides a bending power ranging from 2 Tm to 6 Tm in $|\eta| < 1.3$. The ECT is 5 m in length with an inner bore of 1.65 m and an outer bore of 10.7 m. It has eight coils as well but rotated by 22.5° in ϕ direction with respect to BT to provide radial overlap of magnetic field and optimize the bending power in the interface region of BT and ECT. The bending power of ECT ranges from 4 Tm to 8 Tm in $1.6 < |\eta| < 2.7$. Two ECTs are inserted in the BT and are aligned with the CS. Each magnet system requires operation at low temperature. The CS and eight coils of the BT are provided with an independent helium based cooling mechanism. All eight coils of each ECT have only one cooling mechanism.

4.3 Trigger Mechanism

An event is recorded by the ATLAS detector as a result of colliding pp beams at the IP. The event rate is 40 MHz for the nominal value of instantaneous luminosity [44]. Recording all the events is simply impossible because of the limited response time of the ATLAS detector. It will also require an enormous amount of computing and storage resources to reconstruct all the the events and save them for physics analyses. We select events based on physics interests.

Selection of an event in the ATLAS detector is a three phase sequential triggering process [37]. The first trigger stage is called Level-1 (L1), the second trigger stage is called Level-2 (L2) and the third trigger stage is called Event Filter Level (EF).

The L1 triggers are implemented using custom made electronics, capable of identifying particles with high transverse momenta in different parts of the detector. The L1 trigger decisions are made by the central

triggering processor using different detectors in calorimeters, muon spectrometers and other dedicated detectors in the forward region. The L1 calorimeter triggers use the LAr and Tile calorimeters to identify electrons, photons, tau, single hadron and jet signatures and calculates missing and total transverse energy sums. The L1 muon triggers uses RPC in the barrel and TGC in the end-caps to identify muons of different threshold energies. The acceptance rate of the L1 trigger stage is 75 kHz. The decision is passed to front-end electronics within 2.5 μs of associated bunch crossing.

The L2 trigger system is an extensive array of commercially available computers and networking hardware. The L2 triggers analyze Regions-of-Interest (RoI) in different parts of the detector identified by the L1 triggers and store information on coordinates, energy and particle types provided by the RoI. The L2 triggers process an event in an average time of 40 ms. The selection criteria of the L2 triggers reduces the event rate to just below 3.5 kHz.

The EF trigger system use offline analysis procedures on fully built events at the L2 stage. The algorithms used and the tools adapted for the EF triggers are more sophisticated compared to the L2 triggers. A more complete and detailed calibration is performed at the EF level to reconstruct the events. The event acceptance rate at the EF level is 300 Hz with an average processing time of 40 s per event. Only the events passed by the EF triggers are used for subsequent physics analyses.

The efficiency of a given trigger for a particular physics process is calculated with respect to a reference trigger. The trigger is used in its fully efficient region to avoid working with varying efficiencies in a physics analysis. The efficiency of the trigger is also calculated for the same physics process using a Monte Carlo simulated sample. The trigger is considered fit for the physics analysis if the fully efficient region calculated using data matches with that calculated using the Monte Carlo sample [45]. More about the efficiency of the trigger will be discussed in detail in Section 5.2.

Event reconstruction at the EF level for a given trigger is truncated if the processing time is too long. Such events are stored in debug stream [45] for reconstruction offline.

Chapter 5

Analysis

This chapter presents an analysis of the data in the context of low-scale gravity models. A search for MBH with the ATLAS detector using pp collisions at 8 TeV centre-of-mass energy at the LHC is presented. The study scans ATLAS 2012 data using six triggers in their fully efficient regions to search for possible low-scale gravity signatures, compares the results with two Monte Carlo QCD samples (namely PYTHIA8 and HERWIG++), and sets model-independent upper limits on production cross section times acceptance for new physics in multi-jet final-states. Model-dependent upper limits on the production cross section are also calculated for non-rotating and rotating black holes with no graviton emission for two, four and six large extra dimensions.

5.1 Introduction

Low-scale gravity models [1, 12–14, 46] are considered as a potential solution to the long standing hierarchy problem in high energy particle physics, as discussed in Section 2.5. This is achieved by lowering the fundamental gravity scale to few TeV thus making it comparable to the electroweak scale. The production of MBH at the LHC is possible for ADD and RS1 models. The MBH are very short-lived and decay instantly and democratically in all SM degrees of freedom, thus emitting energetic particles with high multiplicity through Hawking mechanism [23]. QCD processes are the most significant background for this analysis. Quarks and gluons form hadrons and appear as jets coming from IP due to confinement hypothesis. We look for final-states with three or more jets with high transverse momentum in the central region of ATLAS calorimeters which exceed QCD background prediction.

The invariant mass of the final-state is chosen as an analysis variable and is denoted by M in this analysis. We chose M because it is the main observable variable for the classical black holes in MBH theory. The transverse momentum of a jet is a selection cut variable in this analysis and is denoted by p_T. The scalar sum of transverse momenta of all jets in the final-state is denoted by H_T. The p_T and H_T are well measured variables in ATLAS detector.

The M and H_T variables are strongly correlated by kinematics. Fully efficient regions in M and H_T domains are estimated for six single-jet triggers. We check for strong correlation between M and H_T variables

for all six triggers in their fully efficient regions after event reconstruction. We use these triggers to look for possible MBH signal in ATLAS data.

We use M to define control regions (CRs) and signal regions (SRs). A multi-jet event whose M qualifies for a given CR (or a given SR) is also required to have H_T greater than the lower edge of the given CR (or the given SR).

Two normalized Monte Carlo QCD samples, PYTHIA8 and HERWIG++, are used to predict QCD background in all SRs. Statistical uncertainties associated with MC samples are calculated for all SRs. Systematic uncertainties like jet energy scale, jet energy resolution and choice of control regions for the purpose of normalization are also calculated for all SRs.

We gear our efforts towards potential discovery beyond SM If ATLAS data significantly exceeds the MC prediction for QCD background in any given SR after all uncertainties are taken into account. If and only if there is no hint for potential discovery beyond SM in all SRs, we calculate model-independent upper limits on production cross section for new physics beyond SM in multi-jet final-states and model-dependent upper (and lower) limits on production cross section (and threshold mass) of MBH in the M domain using statistical and systematic uncertainties.

The analysis is performed in the `ROOT` environment. `ROOT` is a data analysis framework designed for high energy particle physics. The LHC and ATLAS detector use software based on `ROOT` because it provides the required functionalities to handle big data processing, perform statistical analysis, optimized visualization and efficient storage.

5.2 Triggers

A physics analysis in experimental high energy physics starts with a careful selection of triggers. We are interested in events which contain multiple highly energetic QCD jets. Virtually all QCD jets deposit their energy in ATLAS calorimeters. We select EF-j110-a4tchad, EF-j145-a4tchad, EF-j180-a4tchad, EF-j220-a4tchad, EF-j280-a4tchad and EF-j360-a4tchad for this study. The acronym "a4tchad" stands for the procedure of reconstructing hadronic (had) jets using topological clusters (tc) [47] of calorimeter cells and the anti-kt algorithm [48] with a cone-base radius of 0.4 mm (a4) [49] in η-ϕ space. Topological clusters (also called topoclusters) are arbitrary groups of calorimeter cells in three dimensions which follow the shower development taking advantage of the fine segmentation of the ATLAS calorimeters. A topocluster formation algorithm starts with a seed cell whose signal-to-noise ratio is above 4. Neighbouring cells with signal-to-noise ratio of 2 and above are added to the topocluster. A topocluster has an energy equal to the sum of energies of all included calorimeter cells and a reconstructed direction originating from the center of the ATLAS coordinate system. Topological clusters efficiently suppress calorimeter noise. A leading order jet in the p_T domain is the jet which has largest p_T magnitude in an event. EF-j110-a4tchad, EF-j145-a4tchad, EF-j180-a4tchad, EF-j220-a4tchad, EF-j280-a4tchad and EF-j360-a4tchad record events

whose leading order jet has p_T greater than 110 GeV, 145 GeV, 180 GeV, 220 GeV, 280 GeV and 360 GeV, respectively at the EF level based on calorimeter information.

A physics analysis should use a trigger in its fully efficient region in the domain of the variable of choice. This helps to avoid working with varying trigger efficiency and its associated uncertainty. Working with an under-efficient trigger can be very cumbersome. Trigger efficiency at the EF level should be calculated using a reference trigger which has different triggers at L1 and L2 stages, and lower threshold [50]. The efficiency of a trigger A with respect to a reference trigger B as a function of a variable x is given as:

$$\text{Efficiency of } A \text{ w.r.t. } B = \frac{A(x) \cap B(x)}{B(x)}, \tag{5.1}$$

where the numerator represents events recorded by both triggers and the denominator represents events recorded only by the reference trigger. Table 5.1 shows all six triggers and corresponding reference triggers used in this study. We calculate the efficiencies of EF-j110-a4tchad with respect to EF-j80-a4tchad as separate functions of M and H_T. Similarly, we calculate the efficiencies of EF-j145-a4tchad, EF-j180-a4tchad, EF-j220-a4tchad, EF-j280-a4tchad and EF-j360-a4tchad with respect to EF-j110-a4tchad as separate functions of M and H_T. We consider a trigger fully efficient in M or H_T domain when its efficiency reaches the 99.9% plateau.

We can define fully efficient region of a trigger only if the reference trigger is a proper subset of that trigger. The first five triggers shown in Table 5.1 are highly pre-scaled at L1, L2 and EF stages. Pre-scaling is random data recording for a given trigger. The reference trigger is not a proper subset of the trigger in this case which makes it difficult to find fully efficient regions of these triggers as functions of M and H_T using Equation 5.1. We emulate pre-scaled triggers at L1, L2 and EF stages using the complete information stored for non physics purposes to eliminate pre-scaling effects and restore the required relationship between the two triggers. Emulation enables us to declare fully efficient regions of the triggers as functions of M and H_T, separately. We also emulate EF-j360-a4tchad and EF-j460-a4tchad to compare and validate the emulation method. The threshold values of M and H_T at which six triggers are fully efficient are shown in Table 5.2. The recorded luminosity of each trigger is also presented in the same table. The efficiency plots for the six triggers are shown in Figures 5.1 and 5.2 as functions of M and H_T.

Trigger Chain			Reference Trigger Chain		
Event Filter	Level-2	Level-1	Event Filter	Level-2	Level-1
EF-j110-a4tchad	L2-j105-c4cchad	L1-J50	EF-j80-a4tchad	L2-j75-c4cchad	L1-J30
EF-j145-a4tchad	L2-j140-c4cchad	L1-J75	EF-j110-a4tchad	L2-j105-c4cchad	L1-J50
EF-j180-a4tchad	L2-j165-c4cchad	L1-J75	EF-j110-a4tchad	L2-j105-c4cchad	L1-J50
EF-j220-a4tchad	L2-j165-c4cchad	L1-J75	EF-j110-a4tchad	L2-j105-c4cchad	L1-J50
EF-j280-a4tchad	L2-j165-c4cchad	L1-J75	EF-j110-a4tchad	L2-j105-c4cchad	L1-J50
EF-j360-a4tchad	L2-j165-c4cchad	L1-J75	EF-j110-a4tchad	L2-j105-c4cchad	L1-J50

Table 5.1: Chain of triggers at the Event Filter, Level-2 and Level-1 stages along with the corresponding chain of reference triggers.

Trigger	Reference Trigger	M (TeV)	H_T (TeV)	Luminosity (fb^{-1})
EF-j110-a4tchad	EF-j80-a4tchad	0.6	0.4	9.84×10^{-3}
EF-j145-a4tchad	EF-j110-a4tchad	0.9	0.6	3.64×10^{-2}
EF-j180-a4tchad	EF-j110-a4tchad	1.0	0.8	7.90×10^{-2}
EF-j220-a4tchad	EF-j110-a4tchad	1.2	1.0	2.62×10^{-1}
EF-j280-a4tchad	EF-j110-a4tchad	1.3	1.0	1.20×10^{0}
EF-j360-a4tchad	EF-j110-a4tchad	1.8	1.3	2.03×10^{1}

Table 5.2: All six triggers are shown with their respective reference triggers. The third and fourth columns show threshold values of M and H_T at which corresponding trigger is fully efficient with respect to the reference trigger as functions of M and H_T, respectively. The last column shows the integrated recorded luminosity for each trigger.

As discussed briefly in Section 4.3, the efficiency of a trigger used in a physics analysis should also be calculated using a Monte Carlo sample for the same physics process. The trigger is declared fit for physics analysis if the 99.9% efficiency plateaux for data and the Monte Carlo sample are reached within 100 GeV difference of each other. However, we didn't calculate the efficiency of the six triggers used in this search using the Monte Carlo QCD samples. A similar search for MBH [45] with the ATLAS detector at $\sqrt{8}$ TeV calculated the efficiency of EF-j170-a4tchad-ht700 with respect to the p_T of the leading jet (p_T^{leading}) and the H_T using the same Monte Carlo sample that we used in this analysis. The 99% plateaux for p_T^{leading} and H_T for the Monte Carlo sample were slightly below the corresponding 99% plateaux for data in that search. Since the triggers used in this search are similar to EF-j170-a4tchad-ht700, we expect that all six triggers will follow the same trend.

Only 18 events were found in the debug stream for EF-j170-a4tchad-ht700 in the similar search [45] mentioned in above paragraph. The H_T of 13 events was below 2.0 TeV. The H_T of four events was between 2.0 TeV and 2.4 TeV. Only one event had H_T equal to 2.97 TeV with multiplicity equal to three. Based on this observation, we do not expect significant number of events in the debug stream with high H_T and high multiplicity for all six triggers in this analysis.

Inaccuracies in the reconstruction procedure of hadronic jets can assign wrong energy and p_T to jets. This can significantly change the M and H_T distributions and alter the strong correlation between the two variables. Two quantities are said to be highly correlated if the correlation coefficient is close to unity. Since we choose to work with M and H_T, we show in Figure 5.3 that the two variables are strongly correlated after jet reconstruction procedure. The correlation coefficient, $r_{(M,H_T)}$, between M and H_T is greater than 0.93 for all six triggers.

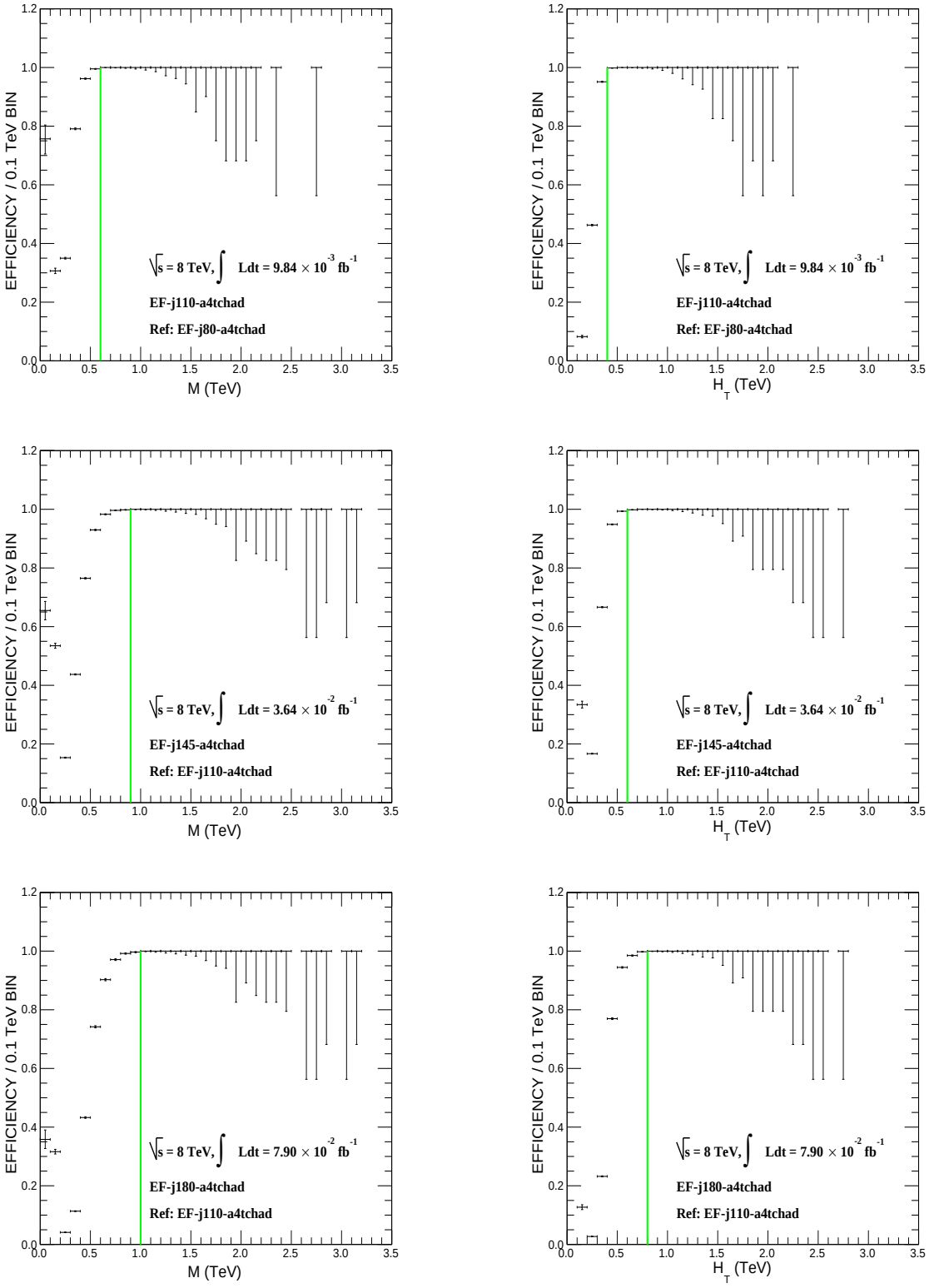

Figure 5.1: Efficiency of the EF-j110-a4tchad, EF-j145-a4tchad and EF-j180-a4tchad triggers at the EF level as functions of M and H_T with respect to corresponding reference triggers mentioned in Table 5.1. The vertical green lines show threshold values of M and H_T when the 99.9% plateau is reached.

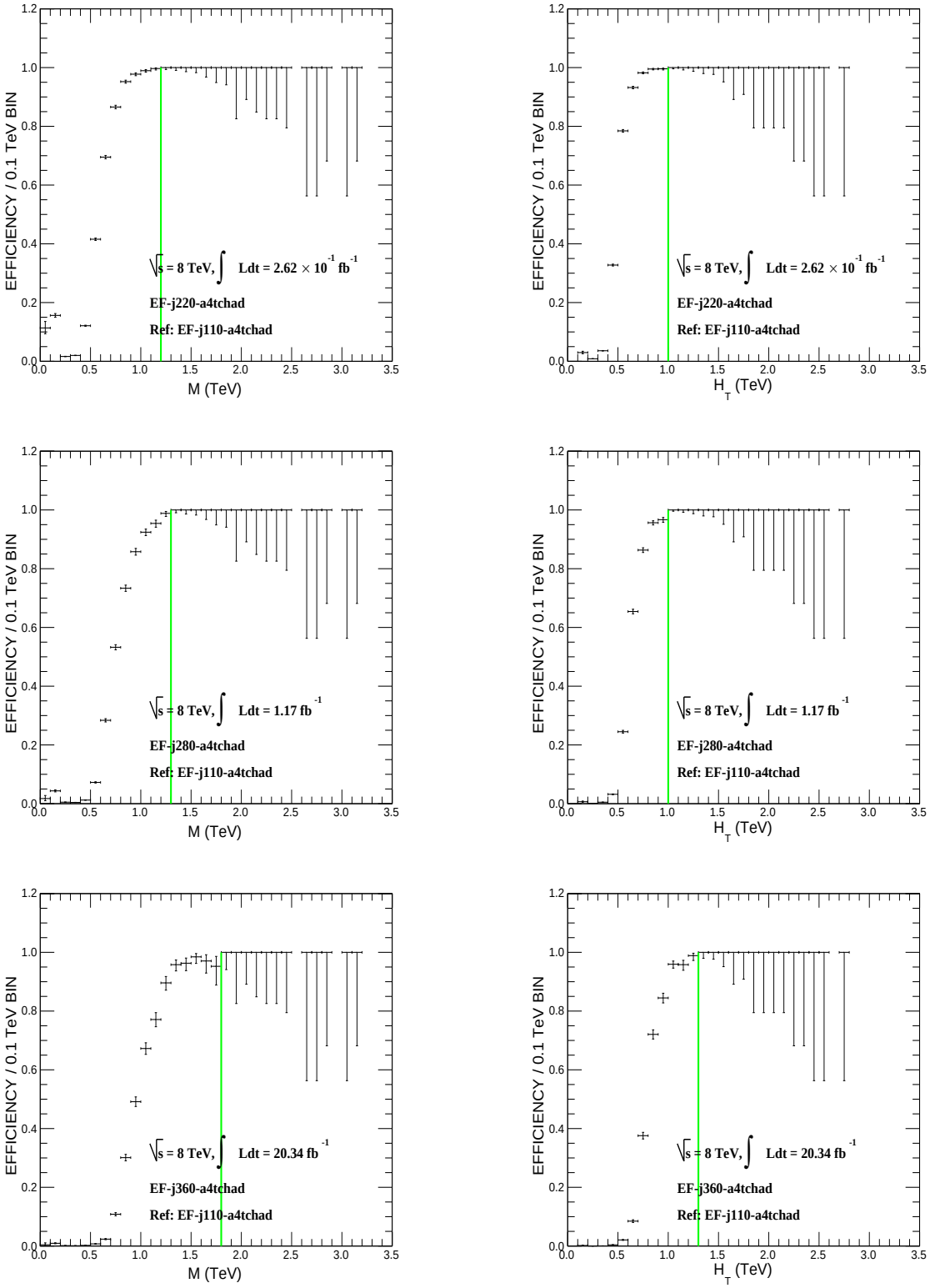

Figure 5.2: Efficiency of the EF-j220-a4tchad, EF-j280-a4tchad and EF-j360-a4tchad triggers at the EF level as functions of M and H_T with respect to corresponding reference triggers mentioned in Table 5.1. The vertical green lines show threshold values of M and H_T when the 99.9% plateau is reached.

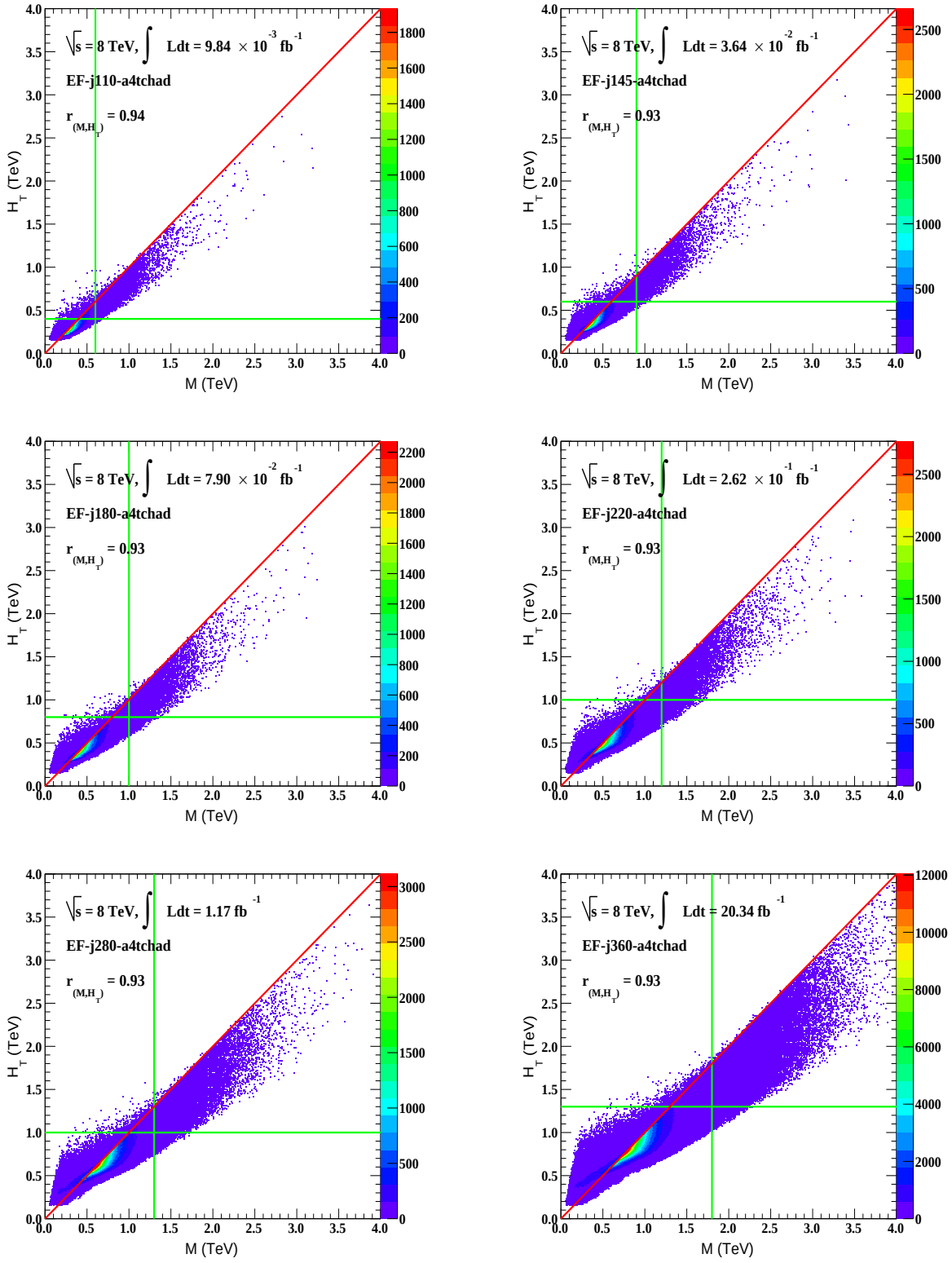

Figure 5.3: Scatter plots of M and H_T for all six triggers. The vertical and horizontal green lines show threshold values of M and H_T, respectively when the 99.9% plateau is reached. The values of correlation coefficient $r_{(M,H_T)}$ are also shown. The red line denotes $r_{(M,H_T)} = 1$ for reference.

5.3 Monte Carlo Samples

All SM physics processes are considered background to this search for MBH at the LHC. QCD jet production is the dominant background since the decay of a MBH on the brane is democratic in all SM degrees of freedom, and quarks and gluons have most degrees of freedom. Within QCD jet production however, contribution from mechanisms like $t\bar{t} \to$ jets, $W \to \ell\nu +$ jets, $Z \to \ell\ell +$ jets, $ZZ \to$ jets, $WW \to$ jets, $WZ \to$ jets and $\gamma\gamma \to$ jets is considerably small. This contribution is significantly suppressed by requiring three or more jets in an event for this analysis.

PYTHIA8 [51] and HERWIG++ [52] are both general-purpose, standalone MC event generators which perform $2 \to 2$ matrix element calculations. The mechanism to form hadrons from colour-carrying final-state partons in hard scattering processes is called hadronization. PYTHIA8 adopts the Lund string fragmentation framework [53, 54] for hadronization process. HERWIG++ uses the cluster model [55] for hadronization of final-state partons. Our lack of complete understanding of physics processes is represented by many parameters in both generators. A set of parameters with optimized values to best describe a given physics data is called a tune. The momentum distribution functions of partons within a hadron are collectively called parton distribution functions (PDF). We use PYTHIA8 with the AU2 [56] tune and CT10 [57] PDF to simulate QCD background. HERWIG++ is used with the EE3 [58] tune and CTEQ6L1 [59] PDF to simulate QCD background. A summary of different features like ATLAS tune and PDF used in PYTHIA8 and HERWIG++ is shown in Table 5.3. Both PYTHIA8 and HERWIG++ are extensively tuned and tested to match with data within ATLAS collaboration. Monte Carlo event generators like Sherpa 2.2.0 [60], POWHEG [61], MadGraph [62] and ALPGEN [63] perform $2 \to n$ matrix element calculations which resemble our need to simulate multi-jet SM QCD background more closely. However these event generators have not been extensively tuned and tested within ATLAS collaboration.

We use PYTHIA8 and HERWIG++ samples to estimate QCD multi-jet background which are centrally produced by ATLAS collaboration, passed through a full simulation of ATLAS detector [64] using GEANT4 [65] and corrected for average pile-up effects at 8 TeV centre-of-mass energy. Each MC sample is divided into eight subsamples, i.e., "JZXW" where X={0,1,2,...,7}, based on p_T of the reconstructed leading order jet emerged from hard scattering of initial patrons. The total number of events, p_T range of leading order jet, cross section and filter efficiency of each subsample for PYTHIA8 and HERWIG++ are shown in Tables 5.4 and 5.5 respectively. Filter efficiency is the fraction of events in the initial sample that are selected in the final simulated sample based on p_T cuts. A weighting factor is associated with each subsample which is applied to simulate the correct shape of p_T distribution when all subsamples are combined. This weighting factor is calculated using cross section σ, filter efficiency ϵ as:

$$W_{\mathrm{JZXW}} = \frac{W^{\mathrm{MC}}_{\mathrm{JZXW}} \times \sigma \times \epsilon \times W^{\mathrm{pileup}}_{\mathrm{JZXW}}}{\text{Total events in JZXW}}, \tag{5.2}$$

where $W^{\mathrm{MC}}_{\mathrm{JZXW}}$ is the MC weighting factor associated with each subsample and $W^{\mathrm{pileup}}_{\mathrm{JZXW}}$ is pileup reweighing factor required due to the differences of pileup conditions at the time of MC simulation and actual data taking.

Generator	PYTHIA8	HERWIG++
ATLAS Tune	AU2	EE3
PDF Set	CT10	CTEQ6L1

Table 5.3: Summary of ATLAS tune and parton distribution function (PDF) set for PYTHIA8 and HERWIG++ MC samples.

PYTHIA8				
Subsample	Events	p_T (TeV)	Cross Section (fb)	Filter Efficiency
$JZ0W$	1500000	0−0.02	7.2850×10^{13}	9.8554×10^{-1}
$JZ1W$	1599994	0.02−0.08	7.2850×10^{13}	1.2898×10^{-4}
$JZ2W$	5999034	0.08−0.2	2.6359×10^{10}	3.9939×10^{-3}
$JZ3W$	5977254	0.2−0.5	5.4419×10^{8}	1.2187×10^{-3}
$JZ4W$	5997214	0.5−1.0	6.4453×10^{6}	7.0821×10^{-4}
$JZ5W$	2996082	1.0−1.5	3.9740×10^{4}	2.1521×10^{-3}
$JZ6W$	2993651	1.5−2.0	4.1609×10^{2}	4.6843×10^{-4}
$JZ7W$	2991955	2.0−8.0	4.0636×10^{1}	1.4600×10^{-2}

Table 5.4: Total number of events, p_T range of leading jet, cross section and filter efficiency of each subsample for PYTHIA8 are shown.

HERWIG++				
Subsample	Events	p_T (TeV)	Cross Section (fb)	Filter Efficiency
$JZ0W$	1399998	0−0.02	1.1860×10^{8}	9.9231×10^{-1}
$JZ1W$	1399897	0.02−0.08	3.6012×10^{12}	1.4607×10^{-3}
$JZ2W$	1399993	0.08−0.2	1.9038×10^{10}	2.5568×10^{-3}
$JZ3W$	1399680	0.2−0.5	3.6224×10^{8}	8.5373×10^{-4}
$JZ4W$	1399665	0.5−1.0	4.1655×10^{6}	5.4308×10^{-4}
$JZ5W$	399490	1.0−1.5	8.3181×10^{4}	5.4903×10^{-4}
$JZ6W$	1389845	1.5−2.0	5.7850×10^{3}	1.9889×10^{-4}
$JZ7W$	1396932	2.0−8.0	6.5251×10^{2}	5.6710×10^{-4}

Table 5.5: Total number of events, p_T range of leading jet, cross section and filter efficiency of each subsample for HERWIG++ are shown.

5.4 ATLAS Data

We use the complete ATLAS dataset from *pp* collisions at 8 TeV centre-of-mass energy collected using Jet-Tau-E_T^{miss} triggering stream which is a good choice for exotic searches beyond SM physics with dominant QCD background. The recorded luminosity varies from 9.84 pb^{-1} to 20.3 fb^{-1} for this study and depends on which trigger is used in the M and H_T domains. The data recorded in real time is organized in periods. There are 10 available periods for use in physics studies, alphabetically named from A to J. Period F is not recommended for physics studies. Beam conditions at the LHC and ATLAS detector may remain stable and unaltered from a few minutes to a few hours. The amount of data recorded during this time is called a run. Each period contains several runs. A run further consists of lumi-blocks. Instantaneous luminosity of colliding *pp* beams is constant for a given lumi-block. A lumi-block is tagged "good" for certain physics if the beam conditions are stable and corresponding components of ATLAS detector are recording data with optimal performance. Each lumi-block, good or bad, contains several thousand events.

5.5 Selection Cuts and Jet Calibration

Selection cuts in this analysis can be divided into two categories. The cuts applied to discriminate good data from bad are collectively called event cleaning cuts. All ATLAS analyses follow standard guidelines and recommendations for event cleaning cuts. Jet calibration is performed for all clean events for correct measurement of energy in the ATLAS calorimeters. The cuts specific to this analysis are called physics cuts and are applied on calibrated jets.

5.5.1 Event Cleaning Cuts

An event has to pass a sequence of six cuts to get accepted for this analysis as a clean event. These cuts are discussed below.

Good Run List

A complete list of all physics runs containing only good lumi-blocks is called good run list (GRL). We apply GRL cut on ATLAS data to select only good events. Approximately 94% events in Jet-Tau-E_T^{miss} triggering stream pass through GRL cut.

LAr and Tile Errors

LAr error and tile error are two cuts of same type. Noise bursts in LAr or tile calorimeters cause data integrity problem. These cuts are applied to drop corrupt events which were recorded by LAr or tile calorimeters during noise bursts.

CoreFlag Error

A few events were recorded partially because of unavailability of a certain component of the ATLAS detector. CoreFlag error ensures removal of such events.

Primary Vertex Requirement

An event must have at least one primary vertex reconstructed offline using two or more associated tracks in the ATLAS detector. A track is the trajectory of a particle moving in a detector which is used to calculate charge and momentum of that particle. Requirement of two or more associated tracks with a primary vertex ensures that the recorded event is formed directly due to colliding protons and is not from pileup effects.

Jet Cleaning

A bad jet is an indication of fake energy deposited in ATLAS calorimeter mainly due to cosmic-ray showers or LHC beam conditions. A jet emerging from the IP occasionally fails to deposit energy in the ATLAS calorimeters due to hardware malfunction or transition regions between barrel and end-caps and is called the ugly jet. Two different cuts are applied to drop events which have bad or ugly jets with $p_T \geq 20$ GeV and are called jet cleaning cuts.

The cut flow for ATLAS data and cumulative percentage corresponding to the selection cuts are shown in Table 5.6. Approximately 92.5% events pass event cleaning cuts. Event cleaning cuts are also applied to PYTHIA8 and HERWIG++ samples. No considerable drop in event statistics is observed for both MC samples.

Cuts	Events Passed	Cumulative %
Jet-Tau-E_T^{miss} Stream	748831957	100
Good Run List	704045336	94.02
LAr Error	702298202	93.79
Tile Error	702298159	93.79
CoreFlag	702297682	93.79
Good Vertex	702242634	93.78
Ugly or Bad Jets	692846272	92.52

Table 5.6: Events passed and cumulative percentages corresponding to six sequential event cleaning cuts are shown for ATLAS data.

5.5.2 Jet Calibration

We search for a MBH signal in multi-jet events in this analysis. Jet calibration ensure correct measurement of average energy across the whole detector, independent of *pp* collision events produced in addition to the event of interest. ATLAS has developed several schemes of varying complexity to calibrate jets [66]. The local cluster weighting (LCW) calibration method clusters together topologically connected calorimeter cells and classifies these clusters as either electromagnetic or hadronic. Energy corrections are derived from single pion Monte Carlo simulations for the non-compensation effects, signal losses due to noise threshold effects, and energy lost in non-instrumented regions. LCW calibration is performed on all jets in this study. However, we do not distinguish between electromagnetic and hadronic jets since a MBH decays predominately to all SM particles.

In addition to LCW calibration, we perform recommended offline jet calibration on all jets for pileup correction, vertex correction and jet energy correction. For pileup correction, average energy due to additional pp interactions is subtracted from the energy measured in the ATLAS calorimeters using correction constants from in situ measurements. The jet direction is corrected in such a way that it originates from the primary vertex instead of the geometric centre of the detector. The jet energy is corrected using reconstructed jets from MC simulations. LCW and offline jet calibrations are also applied to PYTHIA8 and HERWIG++ samples.

5.5.3 Physics Cuts

Physics cuts are applied to select interesting events for this analysis from MBH physics perspective. These are discussed below in the sequence they are applied.

Trigger Cut

We require a clean event in ATLAS data to pass through at least one of the six single-jet triggers described in section 5.2. A clean event can qualify to pass through multiple triggers. We intend to use only one trigger for a given SR based on the highest statistics.

Transverse Momentum Cut

We prefer to minimize pileup effects as much as possible. The number of reconstructed primary vertices and average number of interactions per bunch crossing are directly related to pileup effects in an event. The study in Ref. [67] shows that selecting jets with $p_T \geq 50$ GeV minimizes pileup effects in 2012. In a multi-jet event, we select those jets for analysis whose $p_T \geq 50$ GeV after performing offline jet calibration. The p_T cut does not affect threshold values of the six triggers in M and H_T domains.

Three Jets Cut

We require events to have at least three reconstructed jets with $p_T \geq 50$ GeV after offline jet calibration. The requirement of three or more high p_T jets discriminates against QCD di-jet background.

Pseudorapidity Cut

The η and ϕ distributions of all jets with $p_T \geq 50$ GeV are shown in Figures 5.4 and 5.5, respectively for all six triggers for ATLAS data, PYTHIA8 and HERWIG++. MC samples are normalized to match the number of data events. We observe that η distributions for MC samples fluctuate wildly with respect to ATLAS data for $|\eta| > 1.4$ for all six triggers. This region of bad agreement corresponds to LAr hadronic calorimeter, forward calorimeter, end-cap EM calorimeter and hadronic tile calorimeter in its extended barrel region. This bad agreement is also reflected in M distributions shown in Figures 5.6 and 5.7 for all triggers when $|\eta| < 2.8$ is applied. The H_T distributions are also plotted alongside for $|\eta| < 2.8$ which behave fairly well. We restrict this search for MBH to a narrower central region of ATLAS detector by selecting jets with $|\eta| < 1.2$ and use only barrel sections of ATLAS calorimeters.

We use clean events in ATLAS data and search for MBH signal in events which have at least three jets with $p_T \geq 50$ GeV and $|\eta| < 1.2$. Physics cut flow statistics for clean events are presented in Table 5.7. Physics cuts are also applied to PYTHIA8 and HERWIG++ samples.

Jet-Tau-E_T^{miss} Stream	748831957		
Clean Events	692846272 93%		
Trigger	EF-j110-a4tchad 3699844 0.49%	EF-j145-a4tchad 3717314 0.50%	EF-j180-a4tchad 3026557 0.40%
$p_T \geq 50$ GeV	3606153 0.48%	3646119 0.49%	2982603 0.40%
Three Jets	853464 0.11%	1374701 0.18%	1396926 0.19%
$\|\eta\| < 2.8$	749712 0.10%	1252432 0.17%	1305444 0.17%
$\|\eta\| < 1.2$	181943 0.02%	344871 0.05%	398490 0.05%
Trigger	EF-j220-a4tchad 3694759 0.49%	EF-j280-a4tchad 4624607 0.62%	EF-j360-a4tchad 20324235 2.71%
$p_T \geq 50$ GeV	3639982 0.49%	4566385 0.61%	20102089 2.68%
Three Jets	1957813 0.26%	2726767 0.36%	12788627 1.71%
$\|\eta\| < 2.8$	1869562 0.25%	2648976 0.35%	12540407 1.67%
$\|\eta\| < 1.2$	652304 0.09%	1090402 0.15%	6092883 0.81%

Table 5.7: Reduction in events after applying requirements for all six triggers are shown here. Statistics after p_T, three jets requirement and η cuts are also shown along with cumulative percentages.

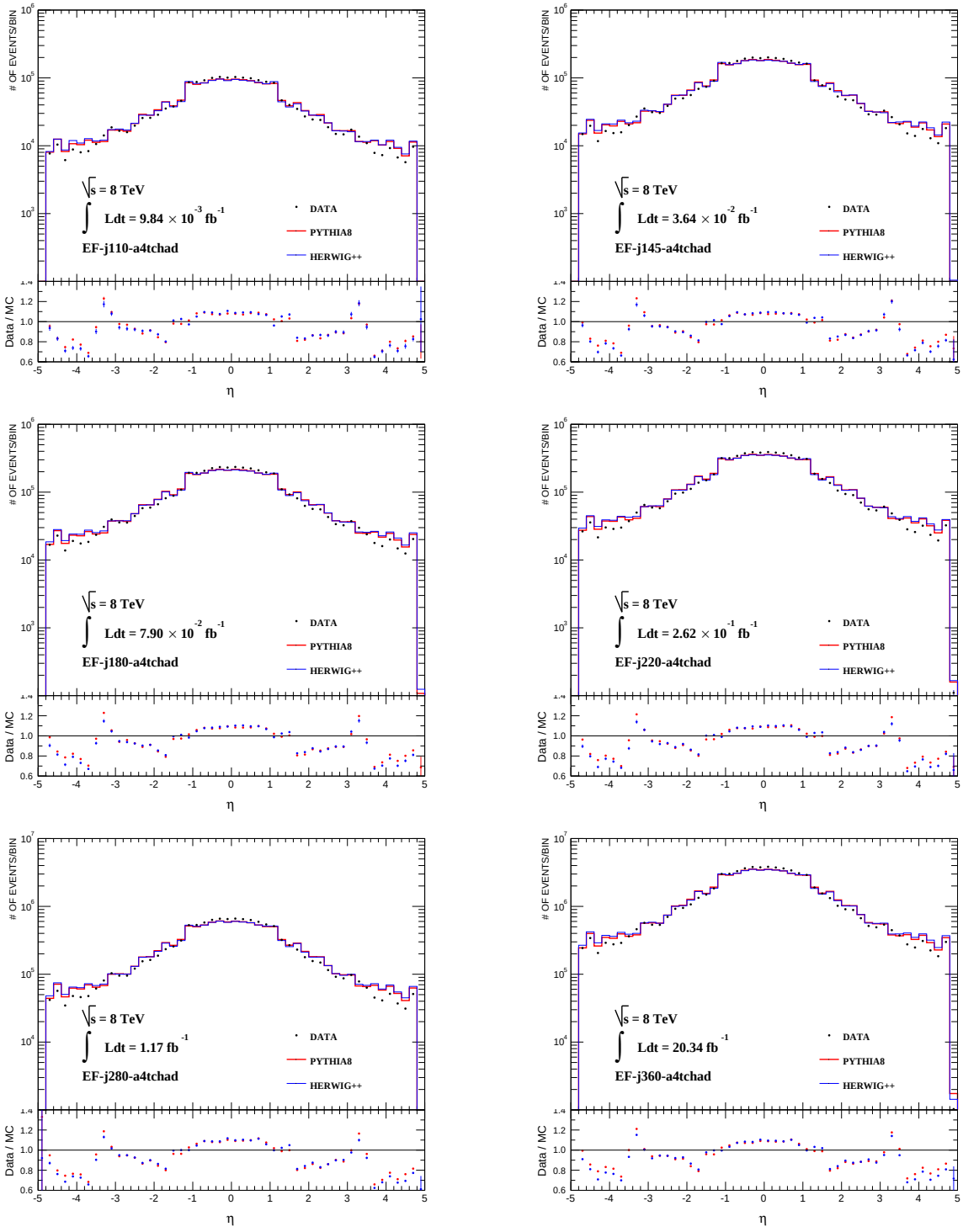

Figure 5.4: η distributions of jets with $p_T \geq 50$ GeV for all six triggers for ATLAS data, PYTHIA8 and HERWIG++ simulated samples. The ratios of ATLAS data with PYTHIA8 and HERWIG++ are shown at the bottom of each plot in red and blue colours respectively.

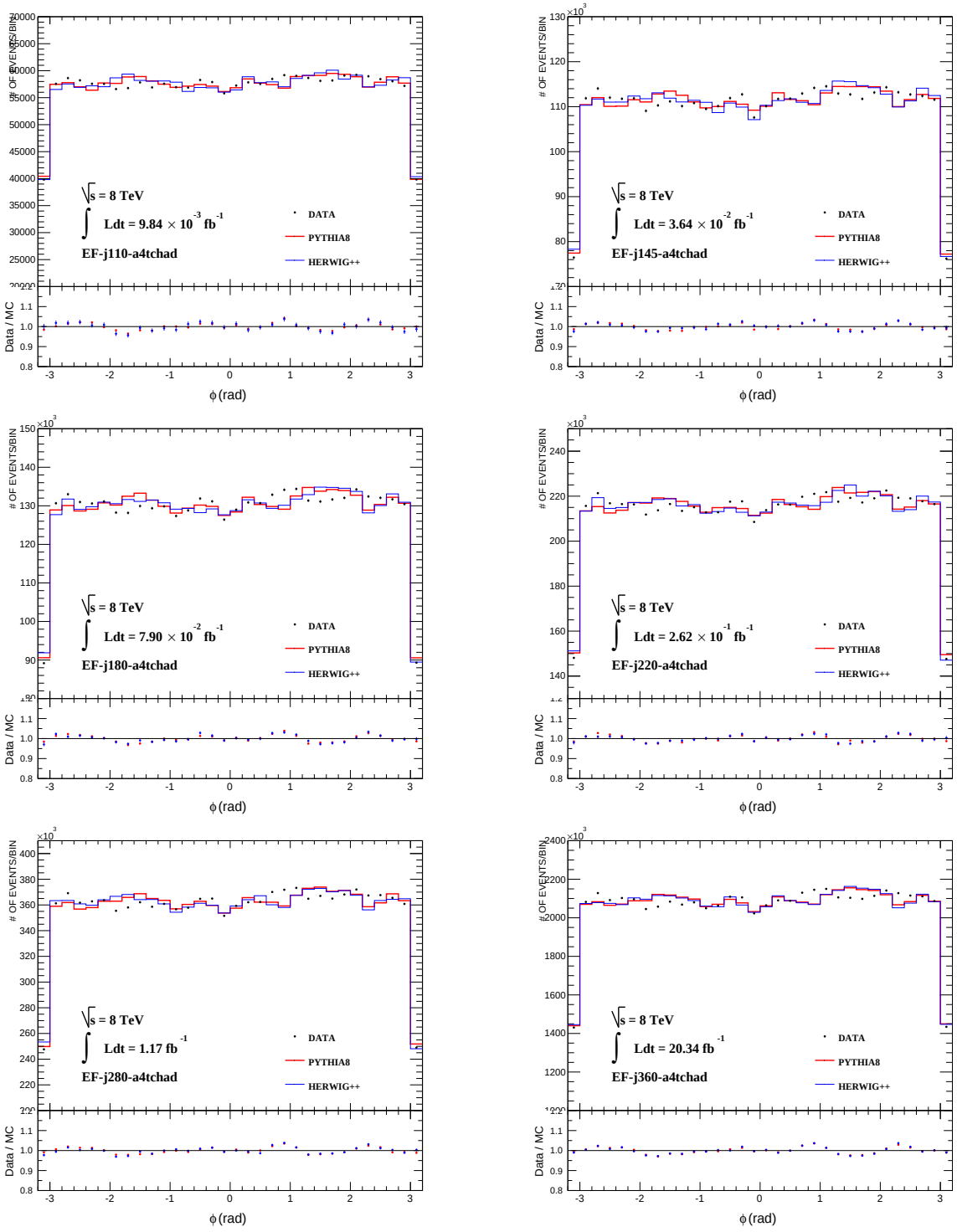

Figure 5.5: ϕ distributions of jets with $p_T \geq 50$ GeV for all six triggers for ATLAS data, PYTHIA8 and HERWIG++ simulated samples. The ratios of ATLAS data with PYTHIA8 and HERWIG++ are shown at the bottom of each plot in red and blue colours respectively.

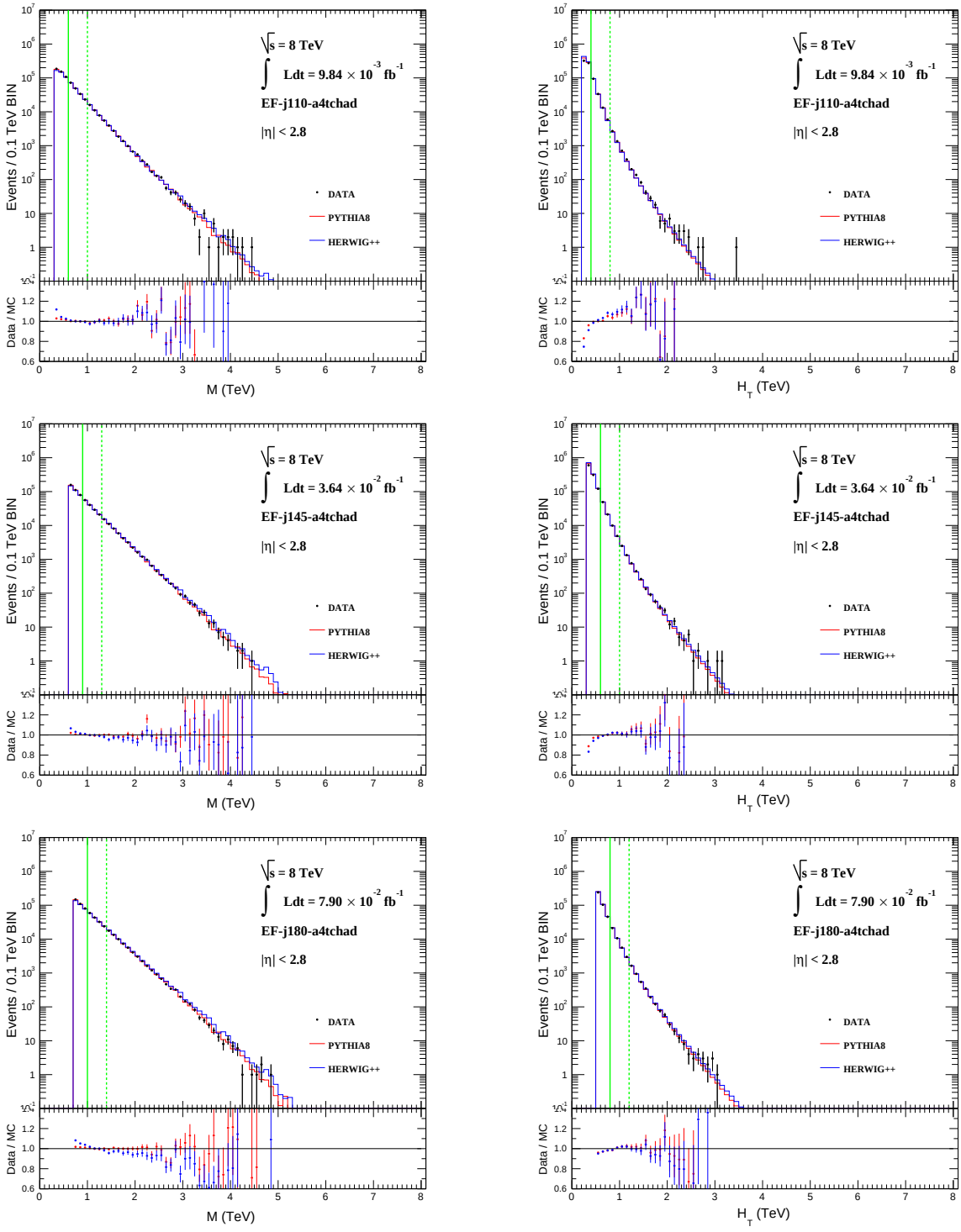

Figure 5.6: M and H_T distributions are plotted for EF-j110-a4tchad, EF-j145-a4tchad and EF-j180-a4tchad for ATLAS data, PYTHIA8 and HERWIG++ with $|\eta| < 2.8$. Solid vertical green line in each plot shows threshold value of corresponding trigger. The region between solid and broken vertical lines shows the normalization region. The ratio of ATLAS data with PYTHIA8 and HERWIG++ is shown at the bottom of each plot.

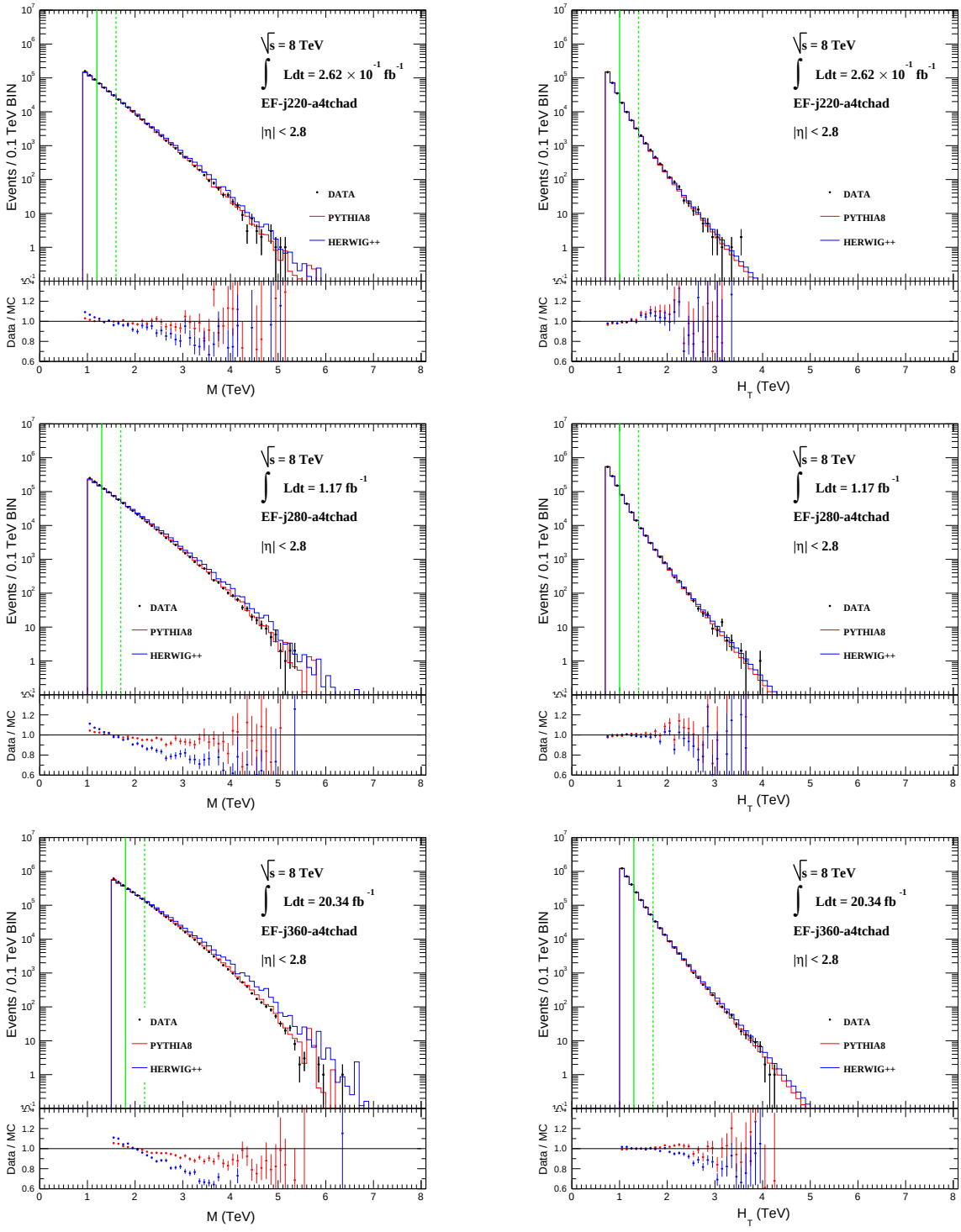

Figure 5.7: M and H_T distributions are plotted for EF-j220-a4tchad, EF-j280-a4tchad and EF-j360-a4tchad for ATLAS data, PYTHIA8 and HERWIG++ with $|\eta| < 2.8$. Solid vertical green line in each plot shows threshold value of corresponding trigger. The region between solid and broken vertical lines shows the normalization region. The ratio of ATLAS data with PYTHIA8 and HERWIG++ is shown at the bottom of each plot.

5.6 Refined Definitions of M and H_T

As discussed earlier in Section 5.1, we choose to work with M and H_T as analysis and control variables, respectively. The definitions of M and H_T modify with physics cuts to describe data characteristics in a better way. The mass of a multi-jet event is defined as

$$M = \sqrt{\sum_{\geq 3 \text{ jets}} p_\mu p^\mu}, \quad p_T \geq 50 \text{ GeV and } |\eta| < 1.2, \tag{5.3}$$

where p_μ is four-momentum vector of a jet in multi-jet event and $p_\mu p^\mu = E^2 - p^2$ with E and p being reconstructed energy and momentum of the jet. The H_T of the multi-jet event is defined as

$$H_T = \sum_{\geq 3 \text{ jets}} p_T, \quad p_T \geq 50 \text{ GeV and } |\eta| < 1.2. \tag{5.4}$$

The M and H_T distributions for ATLAS data, PYTHIA8 and HERWIG++ for all six triggers using Equations 5.3 and 5.4 are shown in Figures 5.8 and 5.9. A green vertical line in each plot shows the threshold of a given trigger in respective M or H_T domain. PYTHIA8 and HERWIG++ distributions are normalized with respect to ATLAS data. Normalization regions for M and H_T distributions are 0.4 TeV wide and start at the threshold value of a given trigger in the respective domain. Table 5.8 shows normalization regions for M and H_T distributions are shown for all six triggers. For example, the threshold of the EF-j110-a4tchad in the M and H_T domains is 0.6 TeV and 0.4 TeV, respectively. We normalized M and H_T distributions for MC samples with respect to ATLAS data in regions [0.6 TeV, 1.0 TeV] and [0.4 TeV, 0.8 TeV], respectively.

The M and H_T distributions for ATLAS data, PYTHIA8 and HERWIG++ for EF-j110-a4tchad for multiplicities five and above are shown in Figure 5.10. The kinematic thresholds for M and H_T are below trigger cut from five-jet multiplicity onwards. The event statistics in normalization region are low for multiplicities five and greater for ATLAS data. We drop EF-j110-a4tchad from this study since PYTHIA8 and HERWIG++ QCD predictions for higher multiplicity events can be misleading.

Triggers	Normalization Regions (TeV)	
	M	H_T
EF-j110-a4tchad	$0.6 \longleftrightarrow 1.0$	$0.4 \longleftrightarrow 0.8$
EF-j145-a4tchad	$0.9 \longleftrightarrow 1.3$	$0.6 \longleftrightarrow 1.0$
EF-j180-a4tchad	$1.0 \longleftrightarrow 1.4$	$0.8 \longleftrightarrow 1.2$
EF-j220-a4tchad	$1.2 \longleftrightarrow 1.6$	$1.0 \longleftrightarrow 1.4$
EF-j280-a4tchad	$1.3 \longleftrightarrow 1.7$	$1.0 \longleftrightarrow 1.4$
EF-j360-a4tchad	$1.8 \longleftrightarrow 2.2$	$1.3 \longleftrightarrow 1.7$

Table 5.8: Normalization regions used for M and H_T distributions in Figures 5.8 and 5.9 are shown for all triggers.

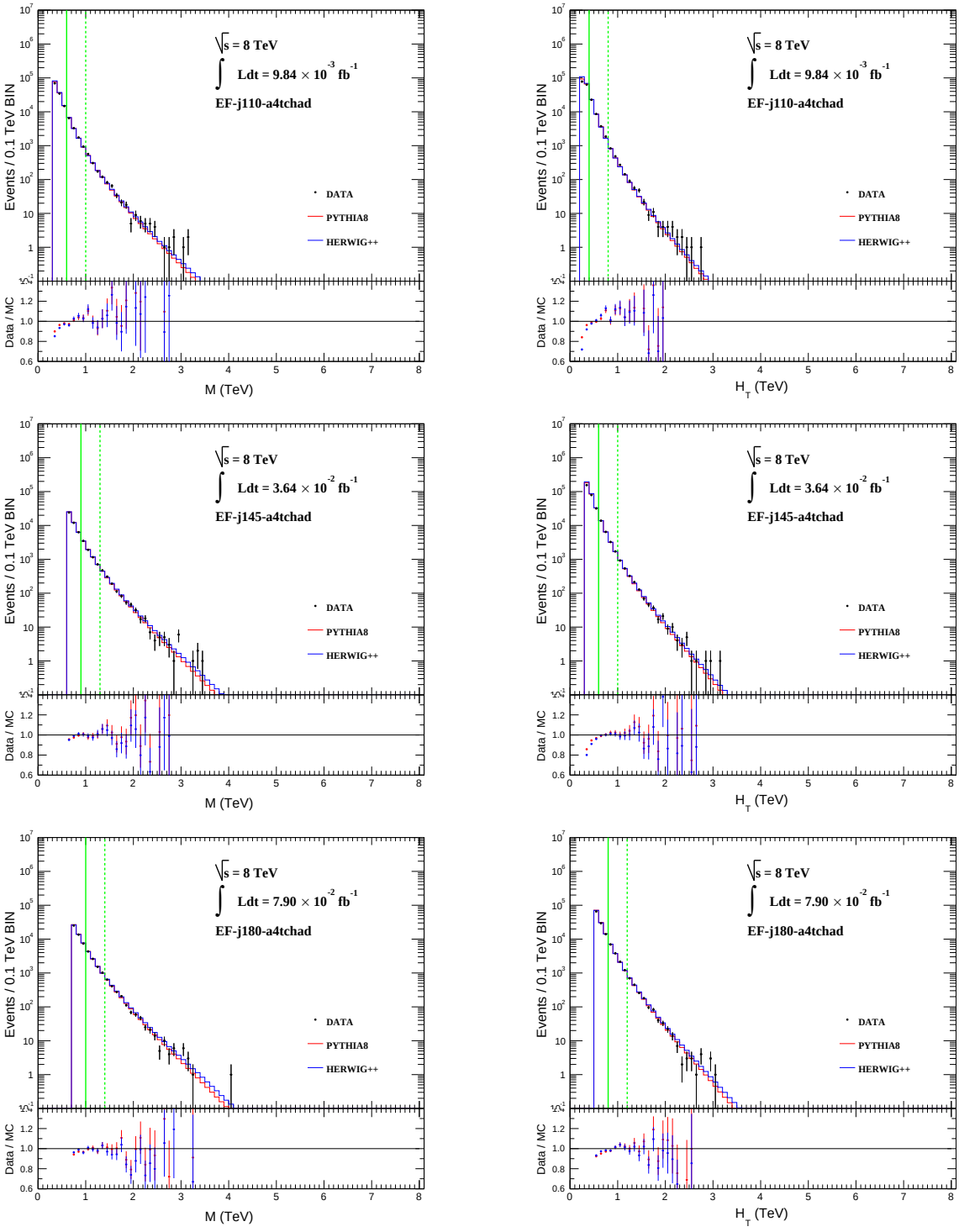

Figure 5.8: M and H_T distributions are plotted for EF-j110-a4tchad, EF-j145-a4tchad and EF-j180-a4tchad for ATLAS data, PYTHIA8 and HERWIG++ with $|\eta| < 1.2$. Solid vertical green line in each plot shows threshold value of corresponding trigger. The region between solid and broken vertical lines shows the normalization region. The ratio of ATLAS data with PYTHIA8 and HERWIG++ is shown at the bottom of each plot.

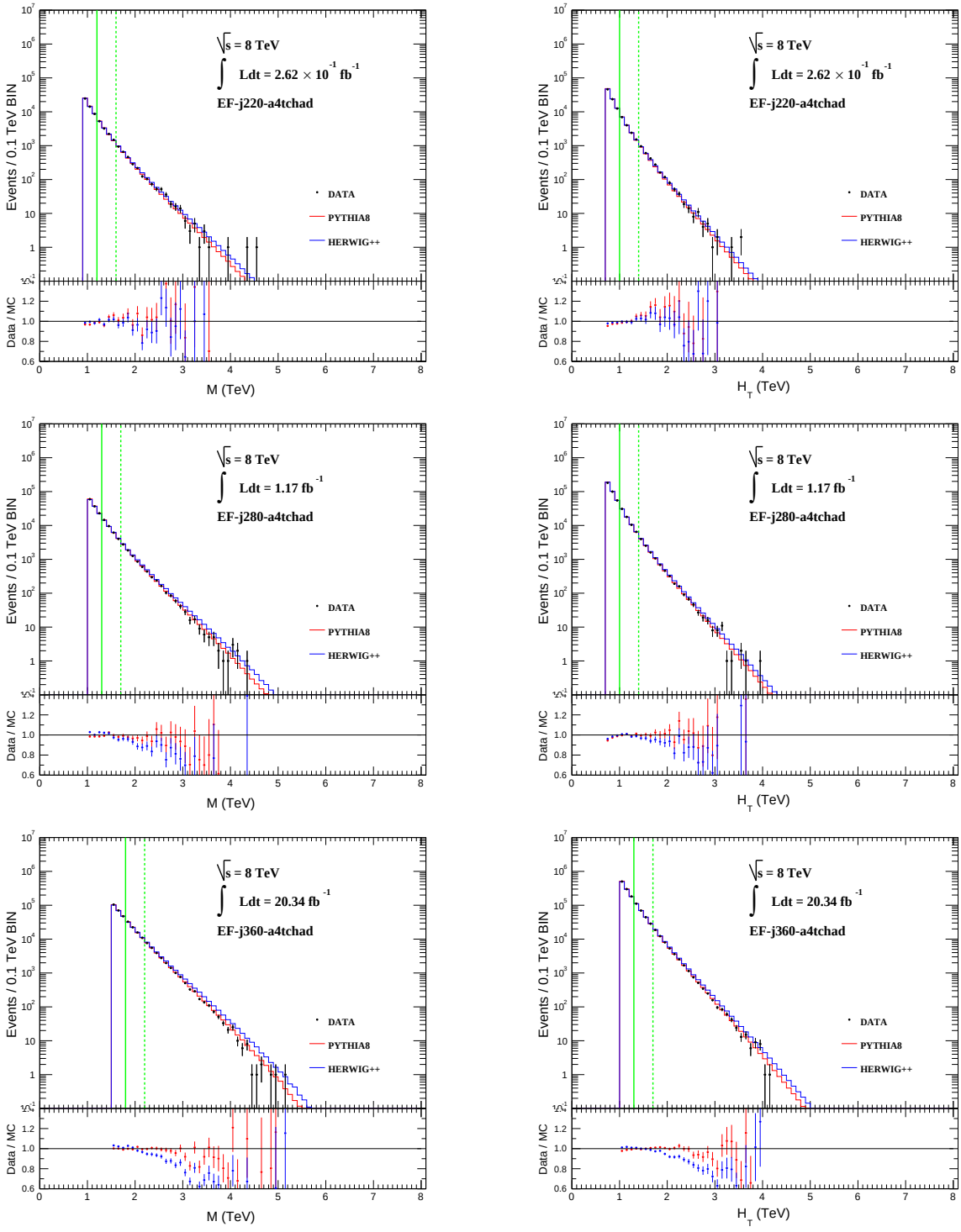

Figure 5.9: M and H_T distributions are plotted for EF-j220-a4tchad, EF-j280-a4tchad and EF-j360-a4tchad for ATLAS data, PYTHIA8 and HERWIG++ with $|\eta| < 1.2$. Solid vertical green line in each plot shows threshold value of corresponding trigger. The region between solid and broken vertical lines shows the normalization region. The ratio of ATLAS data with PYTHIA8 and HERWIG++ is shown at the bottom of each plot.

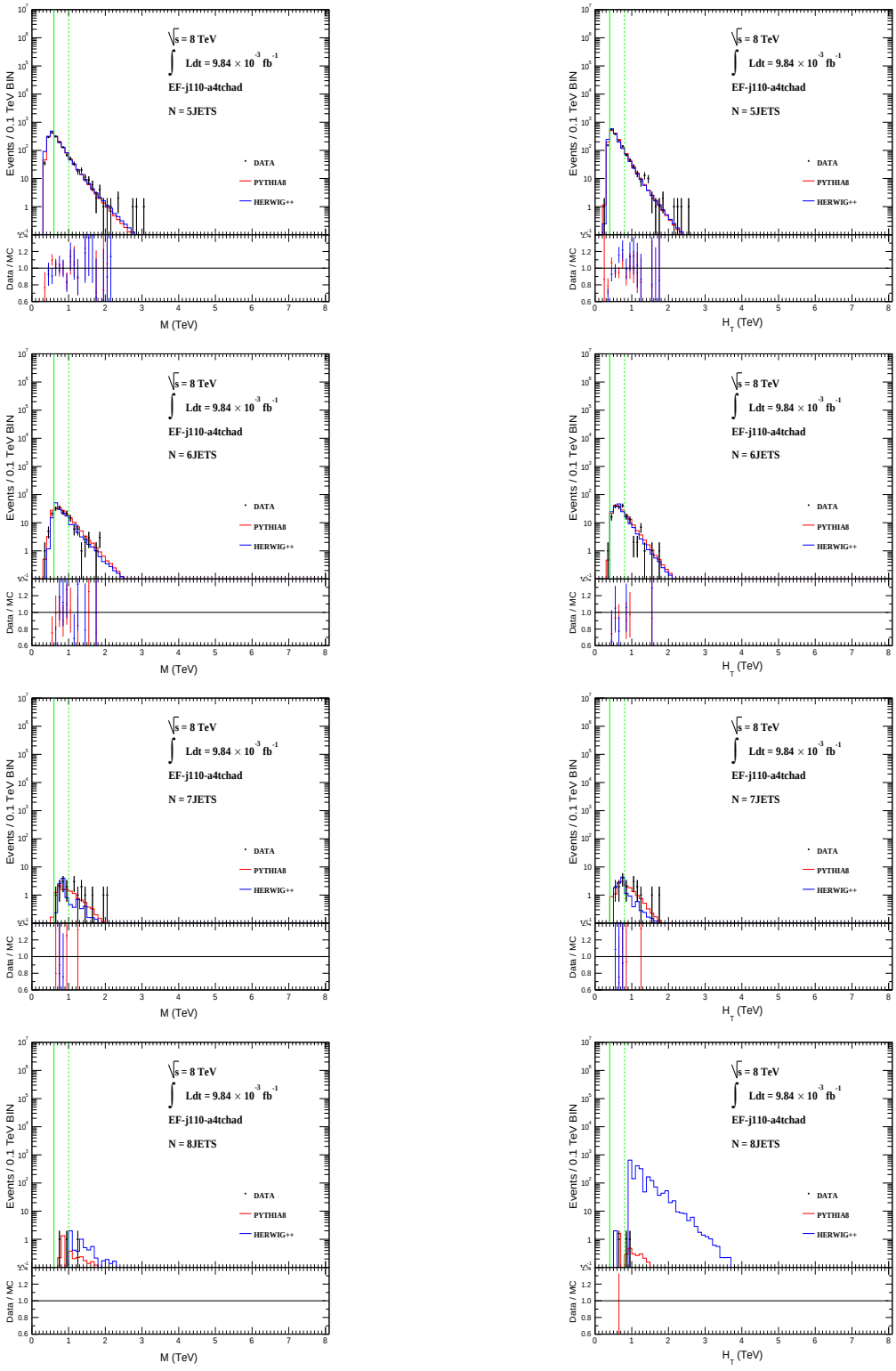

Figure 5.10: M and H_T distributions are plotted for EF-j110-a4tchad for multiplicities five and above for ATLAS data, PYTHIA8 and HERWIG++ with $|\eta| < 1.2$ and $p_T > 50$ GeV. Solid vertical green line in each plot shows threshold value of EF-j110-a4tchad. The region between solid and broken vertical lines shows the normalization region. The ratio of ATLAS data with PYTHIA8 and HERWIG++ is shown at the bottom of each plot.

5.7 Control and Signal Regions

We define a control region (CR) in the mass domain with its lower bound laying in the fully efficient region of lowest p_T trigger. All physics processes are well understood in the CR. A signal region (SR) starts where the CR ends and goes all the way to 8 TeV. The purpose of defining a CR is to normalize MC samples with respect to data and use normalization factors to predict background in SR. The data shows no obvious enhancement and matches with MC prediction in SR. We assume that there is no new physics near the lower bound of SR and slide the CR by 0.1 TeV towards higher mass while keeping the width of CR constant. MC samples are normalized again in new CR and recalculated normalization factors predict background in corresponding SR. Lack of signal enhancement in a SR allows repeating the whole procedure again. The event statistic continues to drop significantly in newly defined SR for a given trigger as we keep sliding the CR towards higher masses. We switch working with next available trigger when the new CR lays in its fully efficient region.

The width of the CR is 0.4 TeV in this analysis. This width is chosen to enable us to work with maximum possible triggers. If we choose to work with 0.5 TeV wide CR, we loose EF-j145-a4tchad and EF-j220-a4tchad. If we choose to define a 0.3 TeV wide CR, the normalization factors in higher masses show considerable fluctuation due to low statistics in the CR which affects background prediction in the SR.

Although CR and SR are defined in M domain, we use H_T to impose additional requirement on events for better control. An event is said to be in the CR if its M and H_T satisfy following conditions,

$$\text{CR}: \quad M^{low} < M < M^{high} \quad \text{and} \quad H_T > M^{low}. \tag{5.5}$$

The SR with M^{min} as lower bound is defined such that $M^{min} = M^{high}$. An event qualifies to be in the SR if M and H_T satisfy following conditions,

$$\text{SR}: \quad M^{min} \leq M \quad \text{and} \quad H_T > M^{min}. \tag{5.6}$$

PYTHIA8 and HERWIG++ are normalized to data in a CR. The normalization factors f_{MC} for two MC samples are calculated as

$$f_{\text{MC}} = \frac{N^{\text{CR}}_{\text{data}}}{N^{\text{CR}}_{\text{MC}}}, \tag{5.7}$$

where $N^{\text{CR}}_{\text{data}}$ and $N^{\text{CR}}_{\text{MC}}$ are the number of events for the ATLAS data and MC in a CR, respectively. We use f_{MC} to normalize PYTHIA8 and HERWIG++ events in SR using

$$N^{n\text{SR}}_{\text{MC}} = f_{\text{MC}} \times N^{\text{SR}}_{\text{MC}}, \tag{5.8}$$

where $N^{n\text{SR}}_{\text{MC}}$ and $N^{\text{SR}}_{\text{MC}}$ are normalized and unnormalized MC predictions in a SR, respectively. The statistical uncertainty for MC samples in SR is given by

$$\Delta^{\text{STAT.}}_{\text{MC}} = \sqrt{\left\{ \left(\frac{e f_{\text{MC}}}{f_{\text{MC}}} \right)^2 + \left(\frac{\sqrt{\alpha}}{N^{\text{SR}}_{\text{MC}}} \right)^2 \right\} \times f_{\text{MC}}}\ , \tag{5.9}$$

where

$$ef_{\mathrm{MC}} = \sqrt{\left(f_{\mathrm{MC}}\right)^2 \times \left\{\frac{1}{N^{\mathrm{CR}}_{\mathrm{data}}} + \left(\frac{\sqrt{\beta}}{N^{\mathrm{CR}}_{\mathrm{MC}}}\right)^2\right\}} \tag{5.10}$$

is the error in f_{MC}, α is sum of the square of the weights associated with $N^{\mathrm{SR}}_{\mathrm{MC}}$ and β is sum of the square of the weights associated with $N^{\mathrm{CR}}_{\mathrm{MC}}$.

A comparison of ATLAS data with PYTHIA8 and HERWIG++ in each SR along with statistical uncertainties for all triggers is shown in Table 5.9. Normalization factors for PYTHIA8 and HERWIG++ show the ratio of events in the corresponding CRs for data and MC samples and are shown in the table as well. Figure 5.11 plots $N^{\mathrm{SR}}_{\mathrm{data}}$, $N^{n\mathrm{SR}}_{\mathrm{P}}$ and $N^{n\mathrm{SR}}_{\mathrm{H}}$ versus M^{min} of all defined SRs for all triggers. $\Delta^{\mathrm{STAT.}}_{\mathrm{data}}$, $\Delta^{\mathrm{STAT.}}_{\mathrm{P}}$ and $\Delta^{\mathrm{STAT.}}_{\mathrm{H}}$ are also plotted along side. Ratios of data to PYTHIA8 and HERWIG++ in each SR are also shown for each trigger. We observe that PYTHIA8 consistently shows better agreement with data.

The evidence for new physics in the multi-jet final-states is not statistically significant since ATLAS data in all SRs is approximately equal to MC QCD predictions. As a result, systematic uncertainties are studied and an upper limit on production cross section times detector acceptance times efficiency for new physics is calculated for each SR for all triggers in this study.

M^{min} (TeV)	$N_{\mathrm{data}}^{\mathrm{SR}}$	f_{P}	$N_{\mathrm{P}}^{n\mathrm{SR}}$	$\Delta_{\mathrm{P}}^{\mathrm{STAT.}}$	f_{H}	$N_{\mathrm{H}}^{n\mathrm{SR}}$	$\Delta_{\mathrm{H}}^{\mathrm{STAT.}}$
EF-j145-a4tchad							
1.3	566	0.75	531.7	24.0	1.74	578.2	11.6
EF-j180-a4tchad							
1.4	749	0.80	786.9	31.8	1.86	868.6	15.7
1.5	492	0.79	505.9	27.0	1.84	562.5	13.3
EF-j220-a4tchad							
1.6	1211	0.83	1140.8	43.1	1.90	1278.5	22.1
EF-j280-a4tchad							
1.7	3188	0.79	3281.7	78.2	1.79	3699.8	43.5
1.8	2117	0.78	2176.3	65.0	1.77	2466.1	35.1
1.9	1429	0.79	1475.9	54.9	1.77	1689.9	29.3
2.0	969	0.79	1000.5	46.5	1.76	1157.4	24.7
2.1	649	0.80	687.4	39.2	1.75	793.3	20.9
EF-j360-a4tchad							
2.2	7713	0.82	8211.8	149.5	1.80	9584.1	91.6
2.3	5190	0.82	5640.0	121.2	1.76	6496.0	73.3
2.4	3514	0.83	3905.7	100.5	1.75	4511.5	59.8
2.5	2367	0.84	2729.5	84.5	1.78	3183.6	48.8
2.6	1624	0.85	1899.9	70.8	1.80	2273.5	41.1
2.7	1112	0.82	1260.8	57.3	1.73	1526.6	33.8
2.8	767	0.80	838.9	46.5	1.67	1035.4	27.9
2.9	518	0.79	566.2	37.9	1.63	708.7	23.1
3.0	360	0.80	394.1	30.7	1.60	488.6	19.1
3.1	264	0.81	273.1	25.3	1.60	342.3	16.1
3.2	180	0.79	185.0	20.3	1.51	227.6	13.1
3.3	119	0.74	120.5	16.2	1.41	148.6	10.6
3.4	77	0.71	79.5	13.1	1.33	98.6	8.7
3.5	53	0.82	63.5	11.5	1.50	77.6	7.7
3.6	40	0.90	47.6	9.7	1.62	58.1	6.6
3.7	25	0.73	26.4	7.2	1.30	32.7	4.9
3.8	19	0.78	19.3	5.9	1.37	23.8	4.1
3.9	10	0.85	14.2	4.9	1.47	17.8	3.6
4.0	2	1.17	13.3	4.7	2.03	17.0	3.5
4.1	1	1.12	8.5	3.6	1.92	11.0	2.8
4.2	0	1.43	7.3	3.3	2.40	9.4	2.5
4.3	0	1.20	4.1	2.3	1.94	5.2	1.8
4.4	0	0.44	1.0	1.1	0.70	1.3	0.9
4.5	0	0.32	0.5	0.8	0.50	0.6	0.6

Table 5.9: Number of events for ATLAS data ($N_{\mathrm{data}}^{\mathrm{SR}}$) and normalized number of events for PYTHIA8 ($N_{\mathrm{P}}^{n\mathrm{SR}}$) and HERWIG++ ($N_{\mathrm{H}}^{n\mathrm{SR}}$) are shown in each SR along with statistical uncertainty in PYTHIA8 ($\Delta_{\mathrm{P}}^{\mathrm{STAT.}}$) and HERWIG++ ($\Delta_{\mathrm{H}}^{\mathrm{STAT.}}$) for all triggers. f_{P} and f_{H} are normalization factors for PYTHIA8 and HERWIG++.

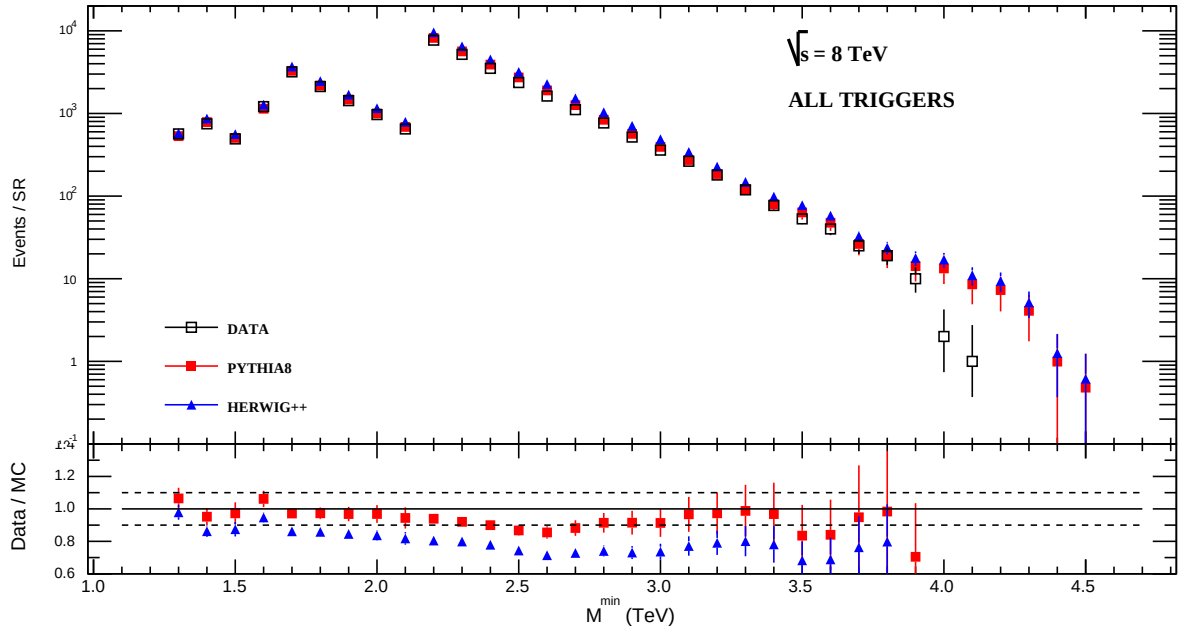

Figure 5.11: Number of events for ATLAS data and normalized number of events for PYTHIA8 and HERWIG++ in each SR are plotted along with statistical uncertainties in ATLAS data, PYTHIA8 and HERWIG++ for all triggers.

5.8 Systematic Uncertainties

Four kinds of systematic uncertainties are attributed to this study that significantly affect the production cross section limits for MBH. These are jet energy scale (JES), jet energy resolution (JER), choice of CR width and choice of MC samples. The uncertainties in jet energy measurement are usually the dominant experimental uncertainty for analyses which search for new physics with the requirement of high p_T jets in the final-state. The uncertainty due to choice of CR width is introduced due to the analysis procedure while the other three uncertainties are associated with MC samples used for background prediction. We quantify the effect of each uncertainty in SRs for all triggers in subsequent subsections.

5.8.1 Jet Energy Scale

The reconstructed jet energy with ATLAS calorimeters is not exactly equal to that of collimated spray of energetic hadrons which initiated the jet from IP. Dedicated analysis [66] suggests that pileup conditions, bad and dead calorimeter regions, leakage, out of calorimeter jet cone and non-compensative responses of calorimeters primarily result in the mismatch among measured energies of final-state hadrons and corresponding reconstructed jets in ATLAS calorimeters. This mismatch of reconstructed jet energy between ATLAS data and MC samples can be on either side of the hadron energy. The degree of mismatch varies in different regions of ATLAS calorimeters. To compensate for this energy mismatch, we scale the energy of clean reconstructed jets up and down for PYTHIA8 and HERWIG++ using η, ϕ, p_T, E_T, number of primary vertices (NPV) and average number of interactions per bunch crossing (μ) in accordance with standard ATLAS recommendations. The upward jet energy scaling may allow more jets to satisfy the analysis cuts in a given event, hence raising its M and H_T. This may result in predicting more events in a given SR. Some events may qualify for higher SRs as a result of upward jet energy scaling. Similarly, the downward jet energy scaling may lead to predicting fewer events in a given SR. Events can be dropped from the analysis or they may qualify for the lower SRs.

A set of 100 pseudo-experiments are performed to look for JES effects in each SR for all triggers. JESup and JESdown are two scaling functions which depend on η, ϕ, p_T and E of the jets. JESup raises the p_T and E of a given jet by some fixed fraction whereas JESdown lowers the p_T and E of a jet in an event. The p_T and E of each jet in an event is scaled by the same fraction of JESup or JESdown to obtain M and H_T distributions for one pseudo-experiment. A selection of 99 equidistant steps between JESup and JESdown provides with a total of one hundred M and H_T distributions for each trigger in which JES effect has been propagated. The CRs and SRs are redefined for all 100 pseudo-experiments for all triggers. For any given SR, the pseudo-experiment giving the maximum upward deviation in SR QCD prediction from nominal value is chosen to report upward systematic uncertainty due to JES and is called JES+. Similarly, the pseudo-experiment giving the maximum downward deviation in SR QCD prediction from nominal value is chosen to report downward systematic uncertainty due to JES and is called JES−. The percent deviation in SR QCD prediction of all 100 pseudo-experiments from nominal QCD prediction in each SR is shown in Appendix A in Figures A.1, A.2 and A.3 for all triggers. Table 5.10 quantifies the asymmetric effects of JES

for each SR for all triggers. The maximum upward JES uncertainty for any SR for PYTHIA8 (HERWIG++) is 16% (15%). The maximum downward JES uncertainty for any SR for PYTHIA8 (HERWIG++) is 14% (13%).

M^{min} (TeV)	$SU_{\mathrm{P}}^{n\mathrm{SR}}$ %	$SD_{\mathrm{P}}^{n\mathrm{SR}}$ %	$SU_{\mathrm{H}}^{n\mathrm{SR}}$ %	$SD_{\mathrm{H}}^{n\mathrm{SR}}$ %
EF-j145-a4tchad				
1.3	0.40	−0.47	0.51	−0.27
EF-j180-a4tchad				
1.4	0.56	−0.58	0.35	−0.44
1.5	1.03	−1.03	0.93	−1.08
EF-j220-a4tchad				
1.6	1.43	−1.27	1.32	−1.82
EF-j280-a4tchad				
1.7	1.66	−1.94	1.23	−1.69
1.8	1.85	−1.98	2.17	−1.50
1.9	2.09	−2.26	1.73	−1.99
2.0	2.19	−2.28	2.04	−2.05
2.1	2.30	−2.31	2.51	−2.58
EF-j360-a4tchad				
2.2	2.54	−2.64	2.15	−2.94
2.3	3.02	−3.08	3.33	−2.78
2.4	3.60	−3.80	3.60	−3.00
2.5	4.08	−3.91	3.83	−3.08
2.6	3.95	−4.19	3.10	−4.12
2.7	4.75	−4.66	3.58	−4.08
2.8	4.88	−4.82	3.85	−4.55
2.9	5.08	−5.30	3.83	−4.82
3.0	5.10	−4.93	5.43	−4.08
3.1	5.17	−4.32	5.04	−5.13
3.2	4.85	−4.84	5.28	−4.36
3.3	5.39	−5.34	5.32	−4.48
3.4	5.81	−5.92	5.77	−6.06
3.5	5.84	−7.54	7.33	−7.21
3.6	8.02	−9.10	7.98	−7.91
3.7	8.93	−9.98	7.53	−10.52
3.8	11.21	−11.78	10.11	−10.76
3.9	12.70	−12.75	9.53	−10.72
4.0	13.43	−13.56	11.01	−13.19
4.1	15.95	−13.36	13.99	−12.51
4.2	15.80	−13.48	14.29	−12.97
4.3	14.47	−12.96	15.29	−12.14
4.4	15.88	−12.96	14.75	−10.82
4.5	14.72	−12.19	13.06	−11.61

Table 5.10: Systematic uncertainty due to JES for PYTHIA8 and HERWIG++ is tabulated in percentage difference from nominal MC predictions for SRs for all triggers. $SU_{\mathrm{P}}^{n\mathrm{SR}}$ ($SU_{\mathrm{H}}^{n\mathrm{SR}}$) is the normalized number of events in SRs for PYTHIA8 (HERWIG++) when JES is randomly fluctuated upwards. $SD_{\mathrm{P}}^{n\mathrm{SR}}$ ($SD_{\mathrm{H}}^{n\mathrm{SR}}$) is the normalized number of events in SRs for PYTHIA8 (HERWIG++) when JES is randomly fluctuated downwards.

5.8.2 Jet Energy Resolution

ATLAS calorimeters will reconstruct jets which will differ slightly in terms of reconstructed energies when the measurement is repeated several times with precisely known constant hadron energy. The variation in reconstructed jet energies is random in nature and follows a Gaussian distribution. This uncertainty is called jet energy resolution (JER) uncertainty.

We generated 500 samples for PYTHIA8 and HERWIG++ to study the effect of JER in M and H_T distributions by randomly fluctuating p_T and E_T of reconstructed jets in an event in accordance with ATLAS 2012 guidelines for all triggers. The relative difference between the simple average of 500 JER driven M distributions and nominal M distributions for all triggers is shown in Appendix A in Figure A.4 and is less than 2% in the region between minimum M threshold and 5 TeV. Similarly, relative difference between simple average of 500 JER driven H_T distributions and nominal H_T distributions for all triggers is shown in Appendix A in Figure A.5 and is less than 1% in the region between minimum H_T threshold and 5 TeV. The region between solid and broken green lines represents first CR for a given trigger.

The generated 500 samples for PYTHIA8 and HERWIG++ are used to study the effect of JER in all SR for all triggers. Let $N_{\rm MC}^{\rm SR\_JER_i}$ be the MC prediction in SR for $i^{\rm th}$ JER sample where $i = 1, 2, 3, ..., 500$. The relative differences of all JER samples from corresponding nominal MC predictions are given as,

$$\Delta{\rm JER}_i = \frac{N_{\rm MC}^{\rm SR\_JER_i} - N_{\rm MC}^{\rm SR}}{N_{\rm MC}^{\rm SR}}, \tag{5.11}$$

which give a distribution in each SR for a given trigger. The 68% area about maximum of a JER distribution in any SR is used to report asymmetric JER uncertainty on nominal SR prediction. A non-zero upper value of JER (JER+) is associated with a SR if the right edge of the 68% region is positive. Similarly, we associate a non-zero lower value of JER (JER−) with a SR if the left edge of the 68% region is negative. These distributions are shown in Appendix A in Figures A.6, A.7 and A.8 for each SR for all triggers along with corresponding maximum and both edges of the 68% region. The asymmetric JER percentage uncertainties for PYTHIA8 and HERWIG++ for all triggers in their SR are presented in Table 5.11 and is less than 2% for all SRs.

M^{min} (TeV)	$RU_{\mathrm{P}}^{n\mathrm{SR}}$ %	$RD_{\mathrm{P}}^{n\mathrm{SR}}$ %	$RU_{\mathrm{H}}^{n\mathrm{SR}}$ %	$RD_{\mathrm{H}}^{n\mathrm{SR}}$ %
EF-j145-a4tchad				
1.3	0.00	−0.27	0.23	−0.22
EF-j180-a4tchad				
1.4	0.13	−0.12	0.23	−0.32
1.5	0.00	−0.22	0.00	−0.38
EF-j220-a4tchad				
1.6	0.23	0.00	0.00	−0.67
EF-j280-a4tchad				
1.7	0.18	−0.12	0.00	−0.52
1.8	0.08	−0.17	0.48	0.00
1.9	0.08	−0.12	0.18	−0.32
2.0	0.13	−0.17	0.28	−0.22
2.1	0.13	−0.12	0.38	−0.17
EF-j360-a4tchad				
2.2	0.13	−0.12	0.00	−0.67
2.3	0.23	0.00	0.83	0.00
2.4	0.13	−0.12	0.58	0.00
2.5	0.28	−0.27	0.98	0.00
2.6	0.63	0.00	0.00	−0.47
2.7	0.38	0.00	0.23	−0.22
2.8	0.38	0.00	0.13	−0.42
2.9	0.28	0.00	0.33	−0.17
3.0	0.33	0.00	0.72	0.00
3.1	0.83	0.00	0.38	0.00
3.2	0.58	0.00	0.93	0.00
3.3	0.38	−0.22	1.38	0.00
3.4	0.88	0.00	0.33	−0.17
3.5	0.18	−0.52	0.72	0.00
3.6	0.53	0.00	0.78	0.00
3.7	0.72	0.00	0.00	−0.72
3.8	0.58	0.00	0.72	0.00
3.9	0.63	0.00	0.48	−0.42
4.0	0.43	0.00	0.33	−0.27
4.1	1.03	0.00	1.08	0.00
4.2	0.72	0.00	1.48	0.00
4.3	0.88	0.00	1.08	0.00
4.4	0.53	0.00	0.88	0.00
4.5	0.53	0.00	0.58	0.00

Table 5.11: Systematic uncertainty due to JER for PYTHIA8 and HERWIG++ predictions is tabulated for all SRs for all triggers. $RU_{\mathrm{P}}^{n\mathrm{SR}}$ ($RU_{\mathrm{H}}^{n\mathrm{SR}}$) is $+1\sigma$ deviation of 500 JER samples above the scaled nominal value of PYTHIA8 (HERWIG++) in each SR. $RD_{\mathrm{P}}^{n\mathrm{SR}}$ ($RD_{\mathrm{H}}^{n\mathrm{SR}}$) is -1σ deviation of 500 JER samples below the scaled nominal value of PYTHIA8 (HERWIG++) in each SR.

5.8.3 Choice of CR width

We chose the width of CR to be 0.4 TeV which allows us to work with maximum number of available triggers. Predictions of PYTHIA8 and HERWIG++ in SRs are normalized using a scale factor derived from comparing MC events with ATLAS data events in CRs. Changes in the width of the CRs effect the prediction of PYTHIA8 and HERWIG++ in the SRs. This introduces systematic uncertainty due to the choice of CR width. We vary the width of the CRs to 0.3 TeV and 0.5 TeV by stretching the lower edge of each CR towards lower mass region and observe the change in predictions in corresponding SR for all triggers. Since we want to define each CR in the fully efficient region of a given trigger, we cannot widen the first CR of each trigger to 0.5 TeV. The predicted number of events in SR for varied widths of CR are given in Table 5.12 for PYTHIA8 and HERWIG++ in percentage relative difference from nominal values. The maximum upward and downward uncertainty in PYTHIA8 (HERWIG++) predictions due to CRW for any SR are 50% (50%) and 30% (30%), respectively.

M^{min} (TeV)	$\Delta N^{n\mathrm{SR}}_{\text{P-300}}$ %	$\Delta N^{n\mathrm{SR}}_{\text{P-500}}$ %	$\Delta N^{n\mathrm{SR}}_{\text{H-300}}$ %	$\Delta N^{n\mathrm{SR}}_{\text{H-500}}$ %
EF-j145-a4tchad				
1.3	−0.94	0.00	0.54	0.00
EF-j180-a4tchad				
1.4	1.05	0.00	2.22	0.00
1.5	1.71	−0.16	2.40	−1.03
EF-j220-a4tchad				
1.6	5.63	0.00	5.88	0.00
EF-j280-a4tchad				
1.7	0.86	0.00	1.55	0.00
1.8	2.61	−0.68	3.14	−1.55
1.9	1.58	−2.07	1.75	−2.51
2.0	3.64	−1.39	3.55	−1.84
2.1	4.29	−2.61	4.50	−2.73
EF-j360-a4tchad				
2.2	1.23	0.00	0.14	0.00
2.3	2.03	−1.06	1.65	−0.47
2.4	3.69	−1.77	3.74	−1.54
2.5	5.34	−2.46	5.99	−2.96
2.6	1.13	−3.52	1.03	−4.43
2.7	−0.96	0.44	−0.84	−0.32
2.8	0.19	1.12	0.47	0.77
2.9	1.31	−0.66	−0.86	−1.13
3.0	2.54	−2.34	2.54	−0.61
3.1	5.74	−2.56	3.51	−2.40
3.2	−8.55	−3.12	−8.89	−1.45
3.3	−1.74	6.65	−2.32	6.88
3.4	11.34	0.93	10.40	1.22
3.5	9.63	−8.72	9.53	−8.17
3.6	−6.36	−2.69	−5.33	−2.42
3.7	−21.52	13.36	−22.66	11.83
3.8	4.51	2.72	5.50	3.73
3.9	46.60	−6.38	49.01	−7.05
4.0	−10.11	−29.52	−10.75	−30.22
4.1	49.73	2.92	49.58	3.13
4.2	9.58	−28.57	7.83	−28.65
4.3	−72.86	4.71	−72.86	6.20
4.4	8.80	163.21	8.45	162.43
4.5	−100.00	5.30	−100.00	4.93

Table 5.12: Systematic uncertainty associated with choice of CR width to normalize PYTHIA8 and HERWIG++ predictions in each SR with respect to ATLAS data is shown for all triggers. $\Delta N^{n\mathrm{SR}}_{\text{P-300}}$ ($\Delta N^{n\mathrm{SR}}_{\text{H-300}}$) and $\Delta N^{n\mathrm{SR}}_{\text{P-500}}$ ($\Delta N^{n\mathrm{SR}}_{\text{H-500}}$) are % difference from nominal predictions of PYTHIA8 (HERWIG++) in coresponding SR when CR are 0.3 TeV and 0.5 TeV wide, respectively.

5.8.4 Choice of MC

PYTHIA8 and HERWIG++ are two SM MC generators which differ in the way they simulate QCD multi-jet processes. We discussed some of the differences in Section 5.3. We observe in Table 5.13 that different PYTHIA8 subsamples have 7% to 87% more events in comparison to corresponding HERWIG++ subsamples. We also observed in Table 5.9 that PYTHIA8 predictions in most CR are in better agreement with data. We decide to use PYTHIA8 predictions to estimate QCD multi-jet background for calculation of upper limit on production cross section times detector acceptance of MBH. We use the difference of PYTHIA8 and HERWIG++ predictions in each SR to quantify the uncertainty associated with choice of Monte Carlo (UCMC). This automatically incorporates uncertainties involved due to choice of hadronization schemes adopted, use of a specific ATLAS tune and PDF sets.

Subsample	PYTHIA8	HERWIG++	% Difference
JZ0W	1500000	1399998	6.7
JZ1W	1599994	1399897	12.5
JZ2W	5999034	1399993	76.7
JZ3W	5977254	1399680	76.6
JZ4W	5997214	1399665	76.7
JZ5W	2996082	399490	86.7
JZ6W	2993651	1389845	53.6
JZ7W	2991955	1396932	53.3

Table 5.13: Number of events for different subsamples of PYTHIA8 and HERWIG++ are shown along with % relative difference of events for corresponding subsamples.

5.9 Comparison between ATLAS Data and Monte Carlo

We compare ATLAS data with PYTHIA8 prediction for QCD background in all SRs. Statistical and systematic uncertainties associated with PYTHIA8 prediction are taken into account. We consider all four systematic uncertainties discussed in Section 5.8 to be uncorrelated since we do not see a correlation between any two of the four reported systematic uncertainties. Table 5.14 summarizes these uncertainties in relative percentage of nominal PYTHIA8 prediction in all SRs for all triggers. The nominal PYTHIA8 prediction is presented in third column and associated statistical uncertainty in fourth column. Uncertainties due to JES and JER are presented in fifth and sixth columns, respectively. There is a maximum of 16% upward fluctuation due to JES in PYTHIA8 prediction. The maximum downward fluctuation due to JES is 14%. Systematic uncertainty in PYTHIA8 prediction due to JER is least among the four systematic uncertainties and amounts to a maximum of 1.3% (0.5%) in upward (downward) direction. Uncertainty due to choice of CR width for normalization purposes is denoted by CRW and is presented in seventh column. The maximum upward and downward uncertainty due to CRW for any SR are 50% and 30%, respectively. The uncertainty due to choice of MC sample is denoted by UCMC and is presented in eighth column. We take the difference of PYTHIA8 and HERWIG++ predictions for the QCD background to amount for UCMC. We note that HERWIG++ predictions are overestimated with reference to PYTHIA8 predictions for all SRs. This implies that we should only take upwards UCMC for PYTHIA8. However assuming zero downwards UCMC for PYTHIA8 is not a sensible choice either. We assume that a symmetric UCMC about PYTHIA8 prediction would automatically account for differences of any well-tuned QCD event generator that would underestimate the QCD background with respect to PYTHIA8. The maximum fluctuation in UCMC is 29% for any SR. We add all upward uncertainties in quadrature to give the overall upward fluctuation in PYTHIA8 prediction for a SR. This is denoted by $N^{n\text{SR}}_{\text{P-MAX}}$. The overall downward fluctuation in PYTHIA8 prediction for a SR is denoted by $N^{n\text{SR}}_{\text{P-MIN}}$ and is obtained by adding all downward uncertainties in quadrature. $N^{n\text{SR}}_{\text{P-MAX}}$ and $N^{n\text{SR}}_{\text{P-MIN}}$ can be considered to form upper and lower bounds of a closed interval which contains nominal value of PYTHIA8 prediction for QCD background. ATLAS data and PYTHIA8 prediction along with the total uncertainty in each SR are plotted in Figure 5.12 for all triggers.

In a scenario where MBH start to form above certain production threshold, we expect to see continuous increase in disparity between ATLAS data and PYTHIA8 QCD prediction in all subsequent SR. However, we see from Table 5.14 that ATLAS data for any SR lays in corresponding PYTHIA8 QCD background prediction interval which indicates that no significant access for production of MBH are observed in this data. Based on this finding, we calculate exclusion limits on production cross section of MBH as a function of M^{min} in next section.

M^{min} (TeV)	$N_{\text{data}}^{\text{SR}}$	$N_{\text{P}}^{n\text{SR}}$	$\Delta_{\text{P}}^{\text{STAT.}}$ %	JES+ JES− %	JER+ JER− %	CRW+ CRW− %	UCMC %	$\delta_{\text{total}}^{+}$ $\delta_{\text{total}}^{-}$ %	$N_{\text{P-MAX}}^{n\text{SR}}$ $N_{\text{P-MIN}}^{n\text{SR}}$
EF-j145-a4tchad									
1.3	566	531.7	±4.51	+0.40 −0.47	0.00 −0.27	0.00 −0.94	±8.75	9.85 −9.90	584.0 479.0
EF-j180-a4tchad									
1.4	749	786.9	±4.04	+0.56 −0.58	0.13 −0.12	1.05 0.00	±10.39	11.22 −11.17	875.1 699.0
1.5	492	505.9	±5.34	+1.03 −1.03	0.00 −0.22	1.71 −0.16	±11.19	12.56 −12.45	569.5 442.9
EF-j220-a4tchad									
1.6	1211	1140.8	±3.77	+1.43 −1.27	0.23 0.00	5.63 0.00	±12.08	13.92 −12.72	1299.6 995.7
EF-j280-a4tchad									
1.7	3188	3281.7	±2.38	+1.66 −1.94	0.18 −0.12	0.86 0.00	±12.74	13.10 −13.11	3711.5 2851.5
1.8	2117	2176.3	±2.99	+1.85 −1.98	0.08 −0.17	2.61 −0.68	±13.32	14.02 −13.81	2481.4 1875.9
1.9	1429	1475.9	±3.72	+2.09 −2.26	0.08 −0.12	1.58 −2.07	±14.50	15.20 −15.28	1700.2 1250.4
2.0	969	1000.5	±4.65	+2.19 −2.28	0.13 −0.17	3.64 −1.39	±15.69	16.90 −16.58	1169.6 834.6
2.1	649	687.4	±5.70	+2.30 −2.31	0.13 −0.12	4.29 −2.61	±15.42	17.15 −16.80	805.2 571.8
EF-j360-a4tchad									
2.2	7713	8211.8	±1.82	+2.54 −2.64	0.13 −0.12	1.23 0.00	±16.71	17.05 −17.02	9611.6 6814.5
2.3	5190	5640.0	±2.15	+3.02 −3.08	0.23 0.00	2.03 −1.06	±15.18	15.76 −15.67	6528.7 4756.2
2.4	3514	3905.7	±2.57	+3.60 −3.80	0.13 −0.12	3.69 −1.77	±15.51	16.55 −16.27	4552.0 3270.2
2.5	2367	2729.5	±3.10	+4.08 −3.91	0.28 −0.27	5.34 −2.46	±16.64	18.21 −17.54	3226.5 2250.6
2.6	1624	1899.9	±3.73	+3.95 −4.19	0.63 0.00	1.13 −3.52	±19.67	20.44 −20.75	2288.3 1505.6
2.7	1112	1260.8	±4.54	+4.75 −4.66	0.38 0.00	0.44 −0.96	±21.08	22.09 −22.08	1539.3 982.3
2.8	767	838.9	±5.54	+4.88 −4.82	0.38 0.00	1.12 0.00	±23.43	24.59 −24.55	1045.2 632.9
2.9	518	566.2	±6.69	+5.08 −5.30	0.28 0.00	1.31 −0.66	±25.17	26.57 −26.59	716.6 415.6
3.0	360	394.1	±7.78	+5.10 −4.93	0.33 0.00	2.54 −2.34	±23.97	25.84 −25.79	496.0 292.5
3.1	264	273.1	±9.28	+5.17 −4.32	0.83 0.00	5.74 −2.56	±25.33	28.08 −27.44	349.8 198.2
3.2	180	185.0	±10.97	+4.85 −4.84	0.58 0.00	0.00 −8.55	±23.00	25.94 −27.31	233.0 134.5
3.3	119	120.5	±13.46	+5.39 −5.34	0.38 −0.22	6.65 −1.74	±23.29	28.23 −27.48	154.5 87.4
3.4	77	79.5	±16.41	+5.81 −5.92	0.88 0.00	11.34 0.00	±23.92	31.70 −29.61	104.8 56.0
3.5	53	63.5	±18.06	+5.84 −7.54	0.18 −0.52	9.63 −8.72	±22.29	30.82 −30.92	83.0 43.8
3.6	40	47.6	±20.37	+8.02 −9.10	0.53 0.00	0.00 −6.36	±22.01	31.05 −31.98	62.4 32.4
3.7	25	26.4	±27.14	+8.93 −9.98	0.72 0.00	13.36 −21.52	±24.24	39.79 −43.44	36.8 14.9
3.8	19	19.3	±30.40	+11.21 −11.78	0.58 0.00	4.51 0.00	±23.21	40.12 −40.03	27.1 11.6
3.9	10	14.2	±34.65	+12.70 −12.75	0.63 0.00	46.60 −6.38	±25.66	64.75 −45.41	23.4 7.7
4.0	2	13.3	±35.38	+13.43 −13.56	0.43 0.00	0.00 −29.52	±27.94	47.04 −55.56	19.6 5.9
4.1	1	8.5	+68.9 −53.4	+15.95 −13.36	1.03 0.00	49.73 0.00	±28.84	91.14 −62.16	16.3 3.2
4.2	0	7.3	+80.4 −54.9	+15.80 −13.48	0.72 0.00	9.58 −28.57	±28.83	87.37 −69.57	13.7 2.2
4.3	0	4.1	+123.8 −66.5	+14.47 −12.96	0.88 0.00	4.71 −72.86	±26.56	127.55 −102.97	9.3 −0.1
4.4	0	1.0	+202.4 −100.0	+15.88 −12.96	0.53 0.00	163.21 0.00	±26.86	261.86 −104.35	3.6 −0.0
4.5	0	0.5	+524.5 −100.0	+14.72 −12.19	0.53 0.00	5.30 −100.00	±28.40	525.47 −144.76	3.0 −0.2

Table 5.14: Systematic uncertainties due to JES, JER, choice of CR width (CRW) and choice of Monte Carlo (UCMC) are presented for each SR in relative percentage of nominal prediction of PYTHIA8. $N_{\text{P-MAX}}^{n\text{SR}}$ ($N_{\text{P-MIN}}^{n\text{SR}}$) is the upper (lower) bound on PYTHIA8 prediction in each SR when all five uncertainties are added in quadrature to obtain the total upward uncertainty $\delta_{\text{total}}^{+}$ (total downward uncertainty $\delta_{\text{total}}^{-}$). ATLAS data events in each SR are denoted by $N_{\text{data}}^{\text{SR}}$. PYTHIA8 prediction and corresponding statistical uncertainty are denoted by $N_{\text{P}}^{n\text{SR}}$ and $\Delta_{\text{P}}^{\text{STAT.}}$, respectively.

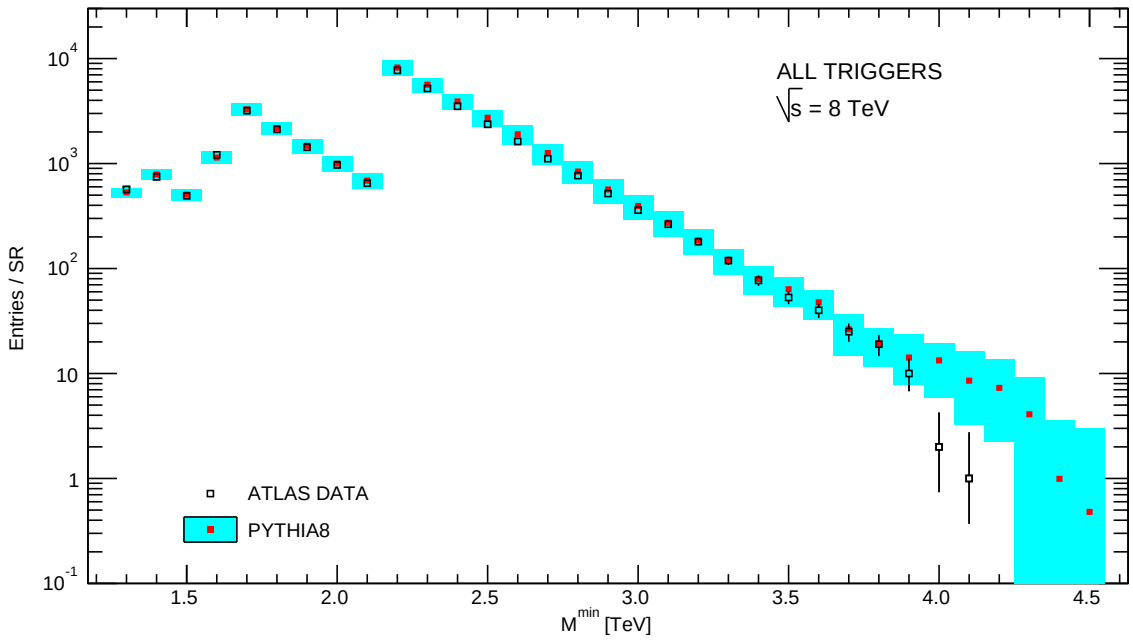

Figure 5.12: Number of events for ATLAS data and predicted number of events for PYTHIA8 along with the total uncertainty for all triggers.

5.10 Model-Independent Limits

Upper limits are calculated for the production cross section times acceptance times efficiency as a function of threshold mass M_{th} in all signal regions using all four systematic uncertainties collectively presented in Table 5.14 for all triggers. A frequentist CL_s method [68] is used to calculate upper limits at the 95% confidence level (CL). All four systematic uncertainties are considered to be uncorrelated for this calculation. The uncertainty in luminosity is 2.8% which is derived by ATLAS collaboration following the same methodology as that detailed in reference [69]. This uncertainty is also incorporated in the limit calculation. The results are presented in Table 5.15. The observed upper limits on the production cross section times detector acceptance times efficiency are calculated for ATLAS data using a background-only hypothesis. With each observed upper limit, an expected upper limit is calculated. The expected upper limit is the mean value of 2500 pseudo datasets generated by randomly fluctuating the estimated background and performing the counting experiment repeatedly. The $\pm 1\sigma$ and $\pm 2\sigma$ bands represent 68% and 95% confidence level on either sides of the expected upper limit. Figure 5.13 shows observed and expected upper limits as solid and dotted lines respectively with $\pm 1\sigma$ band in yellow and $\pm 2\sigma$ band in green.

The observed upper limits for the EF-j145-a4tchad and EF-j220-a4tchad triggers are above the corresponding expected upper limits. This is because the number of events are greater in data than in the PYTHIA8 background prediction in the SRs for these triggers. The observed upper limits for the EF-j180-a4tchad, EF-j280-a4tchad and EF-j360-a4tchad triggers are below the corresponding expected limits because the PYTHIA8 background prediction is higher than the observed number of events in data in the SRs for these triggers. The observed upper limits for all SRs are always within $\pm 2\sigma$ of expected upper limits and are typically within $\pm 1\sigma$.

M^{min} (TeV)	Observed UL (fb)	Expected UL (fb)	-1σ	$+1\sigma$	-2σ	$+2\sigma$
EF-j145-a4tchad						
1.3	3473.942	2736.677	694.967	1062.801	986.531	2181.575
EF-j180-a4tchad						
1.4	1777.021	2001.898	510.945	665.228	793.606	1483.260
1.5	1281.804	1401.759	306.575	474.503	638.417	1075.528
EF-j220-a4tchad						
1.6	1282.188	1144.719	309.499	346.110	507.055	748.776
EF-j280-a4tchad						
1.7	615.026	652.943	163.653	192.840	250.617	416.650
1.8	448.950	460.378	87.570	143.349	186.061	287.300
1.9	308.327	345.776	84.632	98.370	118.695	203.053
2.0	239.296	245.057	56.274	80.863	96.318	157.932
2.1	149.730	173.085	44.674	43.845	72.590	100.486
EF-j360-a4tchad						
2.2	101.935	121.317	30.933	39.885	51.679	65.959
2.3	61.718	72.138	17.342	21.908	26.349	45.955
2.4	42.469	51.570	13.719	16.904	23.646	31.800
2.5	28.825	37.374	9.991	9.992	12.866	22.414
2.6	21.350	29.054	6.734	8.610	10.480	16.247
2.7	18.793	20.763	4.709	6.545	6.116	12.004
2.8	14.202	16.117	4.771	4.012	7.124	8.025
2.9	10.457	11.713	2.733	2.716	3.904	6.042
3.0	6.881	7.771	1.652	2.307	2.732	4.209
3.1	6.091	6.224	1.323	1.343	2.069	3.465
3.2	3.920	4.155	0.910	1.024	1.506	2.321
3.3	2.681	2.739	0.551	0.895	1.009	1.798
3.4	1.847	1.943	0.474	0.632	0.787	1.313
3.5	1.214	1.365	0.249	0.498	0.483	1.015
3.6	0.912	1.164	0.326	0.369	0.503	0.902
3.7	0.887	0.900	0.172	0.318	0.372	0.648
3.8	0.672	0.675	0.140	0.247	0.283	0.500
3.9	0.426	0.506	0.131	0.202	0.206	0.415
4.0	0.211	0.345	0.111	0.134	0.152	0.304
4.1	0.174	0.262	0.078	0.119	0.110	0.244
4.2	0.328	0.274	0.090	0.102	0.141	0.235
4.3	0.156	0.164	0.015	0.086	0.024	0.179
4.4	0.148	0.150	0.003	0.021	0.016	0.073
4.5	0.152	0.153	0.003	0.029	0.020	0.072

Table 5.15: Model-independent observed and expected upper limits (UL) (at 95% confidence level) on the production cross section (σ) times acceptance (A) times efficiency (ϵ) in fb for ATLAS data for counting experiments with $M > M^{min}$ as a function of M^{min} for each trigger. The $\pm1\sigma$ and $\pm2\sigma$ values represent 68% and 95% confidence intervals on either sides of the expected upper limit. The luminosities for EF-j145-a4tchad, EF-j180-a4tchad, EF-j220-a4tchad, EF-j280-a4tchad and EF-j360-a4tchad are 3.6×10^{-2} fb^{-1}, 7.9×10^{-2} fb^{-1}, 2.6×10^{-1} fb^{-1}, 1.2 fb^{-1} and 20.3 fb^{-1}, respectively.

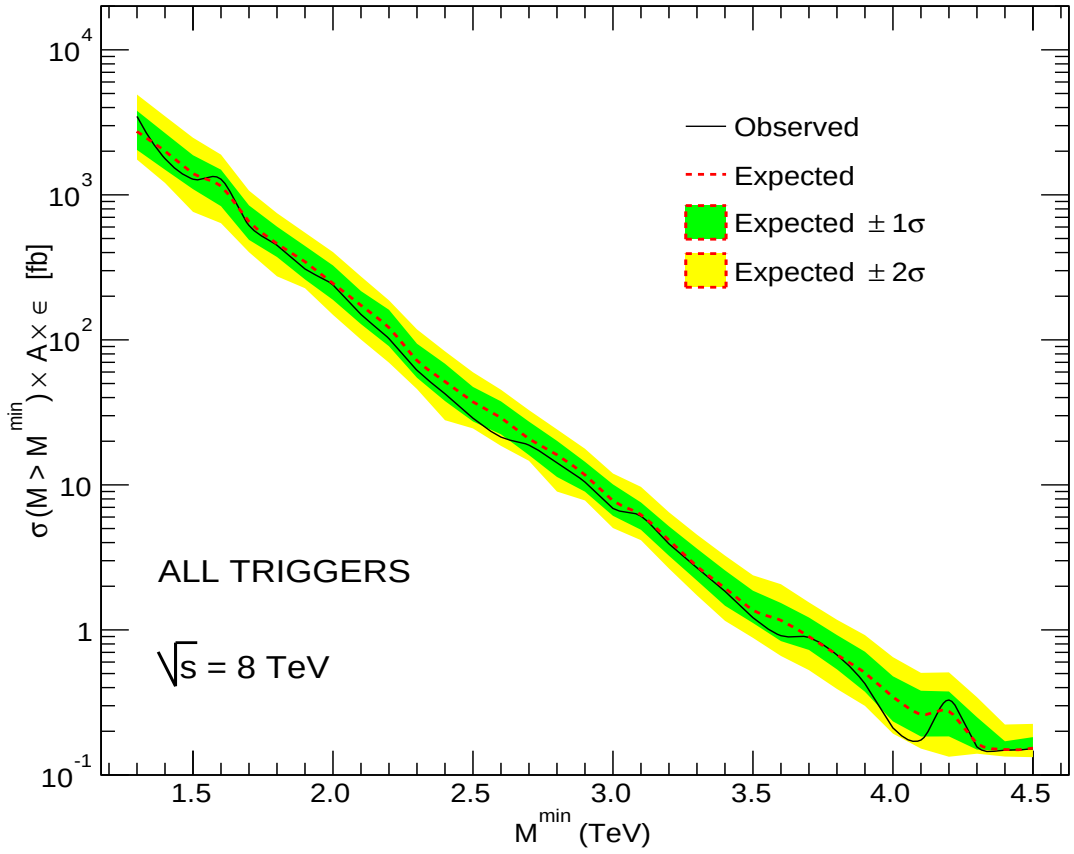

Figure 5.13: Model-independent observed and expected upper limits on the production cross section (σ) times acceptance (A) times efficiency (ϵ) for ATLAS data at the 95% confidence level for counting experiments with $M > M^{min}$ as a function of M^{min} for all triggers. The luminosities for EF-j145-a4tchad, EF-j180-a4tchad, EF-j220-a4tchad, EF-j280-a4tchad and EF-j360-a4tchad are 3.6×10^{-2} fb^{-1}, 7.9×10^{-2} fb^{-1}, 2.6×10^{-1} fb^{-1}, 1.2 fb^{-1} and 20.3 fb^{-1}, respectively.

5.11 Model-Dependent Limits

The CHARYBDIS2 program [24] simulates the production and decay of microscopic black holes with large extra dimensions in pp collisions. The models used here can be identified as non-rotating or rotating black holes. Each model is further parameterized based on values of the fundamental Planck scale M_D, threshold production mass M_{th} and number of large extra dimensions n. The threshold mass needs to be greater than the fundamental Planck scale for these models since the black hole production mechanism is governed by classical physics. The decay mechanism is essentially dominated by emission of Hawking radiation. CHARYBDIS2 conserves angular momentum, electric charge and baryon number while simulating the decay. Greybody factors are used. Lepton number may not be conserved. The complete lists of parameters used with the CHARYBDIS2 program to produce non-rotating and rotating black holes are given in Appendix B.

Signal samples of 10000 events are produced with a unique set of (n, M_D, M_{th})−values. The number of extra dimensions are two, four or six. The fundamental Planck scale M_D ranges from 1.5 TeV to 4.0 TeV in 0.5 TeV steps. The threshold mass M_{th} ranges from 4.0 TeV to 6.0 TeV in 0.5 TeV steps.

Signal sample events are generated using the CHARYBDIS2 program and processed for hadronization using the PYTHIA8 program. These simulated events are passed through AtlFast-II detector simulation and then reconstructed. The reconstruction efficiency of a signal sample for a given SR is defined as the ratio of the number of reconstructed events to the number of hadronized events which satisfy the SR cuts. The acceptance is defined as the ratio of the number of hadronized events which satisfy the SR cuts to the total number of events generated for a given signal sample. We calculate reconstruction efficiencies and acceptances in the SRs for all signal samples in this study. It is possible to set exclusion limits on the production cross section versus M_{th} for any model since the reconstruction efficiency and acceptance have been determined. The statistical uncertainty on the product of reconstruction efficiency and acceptance is typically two orders of magnitude less than the product value ($\sim$1) and is neglected in setting limits on the production cross section.

Model-dependent exclusion limits are calculated using microscopic black hole models for the two scenarios. Analysis cuts described in Section 5.5 are applied on the signal samples. The signal samples are added on top of PYTHIA8 background prediction. Uncertainties on signal predictions due to jet energy scale and jet energy resolution are considered correlated with uncertainties on SM background prediction due to jet energy scale and jet energy resolution, respectively. Uncertainty in the integrated luminosity, and the remaining two systematic uncertainties on SM background prediction described in Section 5.8 are also taken into account. Exclusion limits on the production cross section versus M_{th} are calculated using the frequentist CL_s method in SRs which contain zero data events. These SRs are defined with the EF-j360-a4tchad trigger.

5.11.1 Non-Rotating Black Holes

In this scenario, CHARYBDIS2 is used to simulate the production of non-rotating black holes which decay via Hawking radiation in SM modes. There are a total of 52 AltFast-II samples which are parametrized in (n, M_D, M_{th})−values such that $n = \{2, 4, 6\}$, $M_D = \{1.5, 2.0, 2.5, 3.0, 3.5, 4.0\}$ and $M_{th} = \{4.5, 5.0, 5.5, 6.0\}$.

All 52 AltFast-II signal samples are passed through the requirement cuts as described in Section 5.5. The cut flow statistics for all samples are shown in Table 5.16 along with respective cumulative percentages in parentheses. Typically, 98% of the events pass jet cleaning cuts, the EF-j360-a4tchad trigger requirement and the $p_T > 50$ GeV cut for the leading jet. A significant drop in events passed is observed when requirements of three jets with $p_T > 50$ GeV and $|\eta| < 1.2$ are invoked for samples having M_D values close to M_{th} values. This is because of the requirements of high multiplicity. The available phase-space is not sufficient enough to produce multiple high p_T jets in the very central region of the ATLAS calorimeters.

The M and H_T distributions for non-rotating black hole signal samples added on top of the SM background PYTHIA8 prediction for $n = \{2, 4, 6\}$ and $M_D = \{1.5, 2.0, 2.5, 3.0, 3.5, 4.0\}$ are shown in Figures C.1, C.2, C.3, C.4, C.5 and C.6, respectively, for different values of M_D. The reconstruction efficiencies per 0.1 TeV bin for M and H_T distributions for all 52 AltFast-II signal samples in the corresponding fully efficient regions of the EF-j360-a4tchad trigger are shown in Figures C.7, C.8, C.9, C.10, C.11 and C.12. The reconstruction efficiencies for lower M and H_T regions are typically less than unity. For higher M and H_T regions, we observe an upward migration of events after reconstruction which results in reconstruction efficiencies greater than unity.

The reconstruction efficiencies and acceptances in the last four SRs defined using the EF-j360-a4tchad trigger are presented in Table 5.17 for all 52 AltFast-II signal samples. The reconstruction efficiencies for all four SRs fluctuate about unity. The acceptances for signal samples typically show a monotonically increasing trend with increasing M_{th} values while keeping n and M_D unchanged. This is because the farther the M_{th} value from a given M_D value, the higher the multiplicity and hence the higher the number of signal events in a given SR. The product of reconstruction efficiency and acceptance is also presented in Table 5.17 along with the uncertainty in the product.

The upper limits on the production cross section are calculated (at 95% confidence level) for all 52 AltFast-II signal samples using a frequentist CL_s method and are plotted as solid lines versus corresponding M_{th} values for given sets of (n, M_D)−values in Figure 5.14. The expected upper limit on the production cross section for each AltFast-II signal sample is the mean value of 2500 pseudo datasets generated by randomly fluctuating the signal and estimated background within systematic and statistical uncertainties, and performing the counting experiment repeatedly. The expected limits on the production cross section versus M_{th} are plotted as dotted-broken lines. Corresponding limits on the theoretical production cross section versus M_{th} are plotted as broken lines. For a given set of (n, M_D)−values, the production cross section limit curve typically intersects the theoretical production cross section curve. The M_{th} values lower than the point of intersection are excluded for that given set of (n, M_D)−values. Since the AltFast-II signal samples vary in

M_{th} by a stepsize of 0.5 TeV, the uncertainty in obtaining the point of intersection via interpolation between the cross section limit curve and the cross section curve can be significant. To minimize the uncertainty in obtaining the point of intersection via interpolation, truth samples are locally generated which vary in the M_{th} domain by a stepsize of 0.1 TeV for all sets of (n, M_D)−values. These samples are not passed through AltFast-II simulation. As a result, the truth samples do not contain reconstructed events which means that the reconstruction efficiency is not calculable. However, the acceptance is calculable for all truth samples and is used to calculate upper limits on the production cross section. Scale-factors are calculated to take into account the differences (for instance the inability to calculate reconstruction efficiency in the case of truth samples) between AltFast-II and truth samples and are shown in Table 5.18. A scale-factor is the ratio of upper limit on the production cross sections derived using an AltFast-II sample and a truth sample with same (n, M_D, M_{th})−values. For a given set of (n, M_D)−values, the truth samples are scaled using the scale-factor that is derived from a truth/AltFast-II sample pair that is closest in M_{th} value.

The production cross section curve varies smoothly in M_{th} domain by a stepsize of 0.1 TeV from 4.5 TeV to 6.5 TeV. For a few sets of (n, M_D)−values, the cross section limit curves for AltFast-II signal samples do not intersect the corresponding cross section curve. The truth samples are used to extrapolate the cross section limit curve for higher M_{th} values until the point of intersection is obtained. Figures C.13, C.15 and C.15 show separate plots of upper limit on observed and expected production cross sections for each set of (n, M_D)−values. The $\pm1\sigma$ and $\pm2\sigma$ confidence intervals about the expected upper limits are also drawn. Table 5.19 presents lower limits on observed and expected M_{th} values for all sets of (n, M_D)−values. The $\pm1\sigma$ and $\pm2\sigma$ values of M_{th} about the expected values are also presented.

Exclusion contour plots in the M_{th}-M_D plane for two, four and six extra dimensions for AltFast-II and truth samples are presented in Figure 5.15. The models with M_{th} values laying under the observed limit curves are excluded at 95% CL for a particular set of (n, M_D)−value.

n	M_D (TeV)	M_{th} (TeV)	Total Events	Clean Events	Trigger Cut	$p_T \geqslant 50$ GeV	Three Jets	$\|\eta\| < 1.2$
2	3.5	4.5	10000	9866 (98.7%)	9815 (98.2%)	9764 (97.6%)	8464 (84.6%)	6882 (68.8%)
2	4.0	4.5	10000	9839 (98.4%)	9773 (97.7%)	9718 (97.2%)	7975 (79.8%)	6393 (63.9%)
2	2.5	5.0	10000	9874 (98.7%)	9845 (98.5%)	9829 (98.3%)	9333 (93.3%)	8364 (83.6%)
2	3.0	5.0	10000	9870 (98.7%)	9840 (98.4%)	9800 (98.0%)	8988 (89.9%)	7673 (76.7%)
2	3.5	5.0	10000	9840 (98.4%)	9794 (97.9%)	9751 (97.5%)	8572 (85.7%)	7058 (70.6%)
2	4.0	5.0	10000	9845 (98.5%)	9815 (98.2%)	9762 (97.6%)	8406 (84.1%)	6803 (68.0%)
2	1.5	5.5	10000	9892 (98.9%)	9882 (98.8%)	9882 (98.8%)	9868 (98.7%)	9719 (97.2%)
2	2.0	5.5	10000	9863 (98.6%)	9847 (98.5%)	9845 (98.5%)	9721 (97.2%)	9250 (92.5%)
2	2.5	5.5	10000	9872 (98.7%)	9861 (98.6%)	9852 (98.5%)	9454 (94.5%)	8631 (86.3%)
2	3.0	5.5	10000	9839 (98.4%)	9817 (98.2%)	9796 (98.0%)	9126 (91.3%)	8055 (80.5%)
2	3.5	5.5	10000	9847 (98.5%)	9826 (98.3%)	9776 (97.8%)	8729 (87.3%)	7337 (73.4%)
2	4.0	5.5	10000	9844 (98.4%)	9816 (98.2%)	9766 (97.7%)	8473 (84.7%)	6976 (69.8%)
2	1.5	6.0	9000	8902 (98.9%)	8897 (98.9%)	8897 (98.9%)	8891 (98.8%)	8817 (98.0%)
2	2.0	6.0	10000	9848 (98.5%)	9843 (98.4%)	9841 (98.4%)	9757 (97.6%)	9375 (93.8%)
2	2.5	6.0	10000	9854 (98.5%)	9848 (98.5%)	9836 (98.4%)	9549 (95.5%)	8792 (87.9%)
4	3.0	4.5	10000	9869 (98.7%)	9825 (98.2%)	9796 (98.0%)	9089 (90.9%)	7879 (78.8%)
4	3.5	4.5	10000	9861 (98.6%)	9825 (98.2%)	9794 (97.9%)	8851 (88.5%)	7527 (75.3%)
4	4.0	4.5	10000	9862 (98.6%)	9826 (98.3%)	9792 (97.9%)	8709 (87.1%)	7183 (71.8%)
4	1.5	5.0	10000	9899 (99.0%)	9886 (98.9%)	9885 (98.8%)	9864 (98.6%)	9693 (96.9%)
4	2.0	5.0	10000	9885 (98.8%)	9871 (98.7%)	9869 (98.7%)	9735 (97.3%)	9247 (92.5%)
4	2.5	5.0	10000	9882 (98.8%)	9860 (98.6%)	9847 (98.5%)	9524 (95.2%)	8828 (88.3%)
4	3.0	5.0	10000	9868 (98.7%)	9848 (98.5%)	9836 (98.4%)	9216 (92.2%)	8218 (82.2%)
4	3.5	5.0	10000	9870 (98.7%)	9842 (98.4%)	9819 (98.2%)	8988 (89.9%)	7661 (76.6%)
4	4.0	5.0	10000	9883 (98.8%)	9862 (98.6%)	9826 (98.3%)	8748 (87.5%)	7322 (73.2%)
4	1.5	5.5	9000	8891 (98.8%)	8883 (98.7%)	8882 (98.7%)	8866 (98.5%)	8773 (97.5%)
4	2.0	5.5	9000	8904 (98.9%)	8897 (98.9%)	8895 (98.8%)	8803 (97.8%)	8475 (94.2%)
4	2.5	5.5	10000	9874 (98.7%)	9866 (98.7%)	9857 (98.6%)	9621 (96.2%)	9012 (90.1%)
4	3.0	5.5	10000	9860 (98.6%)	9849 (98.5%)	9834 (98.3%)	9319 (93.2%)	8418 (84.2%)
4	3.5	5.5	10000	9835 (98.3%)	9808 (98.1%)	9780 (97.8%)	9061 (90.6%)	7933 (79.3%)
4	4.0	5.5	10000	9829 (98.3%)	9815 (98.2%)	9785 (97.8%)	8858 (88.6%)	7537 (75.4%)
4	1.5	6.0	10000	9890 (98.9%)	9878 (98.8%)	9877 (98.8%)	9864 (98.6%)	9804 (98.0%)
4	2.0	6.0	10000	9866 (98.7%)	9859 (98.6%)	9856 (98.6%)	9799 (98.0%)	9524 (95.2%)
4	2.5	6.0	10000	9856 (98.6%)	9844 (98.4%)	9834 (98.3%)	9638 (96.4%)	9071 (90.7%)
4	3.0	6.0	10000	9839 (98.4%)	9834 (98.3%)	9822 (98.2%)	9460 (94.6%)	8662 (86.6%)
6	1.5	5.0	10000	9921 (99.2%)	9909 (99.1%)	9907 (99.1%)	9873 (98.7%)	9685 (96.8%)
6	2.0	5.0	10000	9883 (98.8%)	9857 (98.6%)	9847 (98.5%)	9693 (96.9%)	9233 (92.3%)
6	2.5	5.0	10000	9877 (98.8%)	9860 (98.6%)	9852 (98.5%)	9556 (95.6%)	8807 (88.1%)
6	3.0	5.0	10000	9867 (98.7%)	9848 (98.5%)	9839 (98.4%)	9339 (93.4%)	8303 (83.0%)
6	3.5	5.0	10000	9859 (98.6%)	9843 (98.4%)	9816 (98.2%)	9113 (91.1%)	7910 (79.1%)
6	4.0	5.0	10000	9869 (98.7%)	9842 (98.4%)	9817 (98.2%)	8851 (88.5%)	7504 (75.0%)
6	1.5	5.5	9000	8906 (99.0%)	8889 (98.8%)	8888 (98.8%)	8873 (98.6%)	8798 (97.8%)
6	2.0	5.5	10000	9885 (98.8%)	9878 (98.8%)	9875 (98.8%)	9780 (97.8%)	9429 (94.3%)
6	2.5	5.5	10000	9875 (98.8%)	9865 (98.7%)	9853 (98.5%)	9614 (96.1%)	8968 (89.7%)
6	3.0	5.5	10000	9857 (98.6%)	9844 (98.4%)	9824 (98.2%)	9378 (93.8%)	8468 (84.7%)
6	3.5	5.5	10000	9860 (98.6%)	9849 (98.5%)	9823 (98.2%)	9179 (91.8%)	8169 (81.7%)
6	4.0	5.5	10000	9866 (98.7%)	9856 (98.6%)	9822 (98.2%)	8938 (89.4%)	7695 (77.0%)
6	1.5	6.0	10000	9881 (98.8%)	9875 (98.8%)	9875 (98.8%)	9871 (98.7%)	9806 (98.1%)
6	2.0	6.0	10000	9877 (98.8%)	9868 (98.7%)	9866 (98.7%)	9818 (98.2%)	9530 (95.3%)
6	2.5	6.0	10000	9872 (98.7%)	9861 (98.6%)	9857 (98.6%)	9661 (96.6%)	9143 (91.4%)
6	3.0	6.0	10000	9855 (98.5%)	9842 (98.4%)	9836 (98.4%)	9473 (94.7%)	8719 (87.2%)
6	3.5	6.0	10000	9835 (98.3%)	9812 (98.1%)	9781 (97.8%)	9230 (92.3%)	8253 (82.5%)
6	4.0	6.0	10000	9823 (98.2%)	9814 (98.1%)	9785 (97.8%)	9033 (90.3%)	7878 (78.8%)

Table 5.16: Reduction of events after applying requirement cuts for EF-j360-a4tchad for non-rotating black hole samples parameterized by n, M_D and M_{th}. Cumulative percentage is also shown.

n	M_D (TeV)	M_{th} (TeV)	$M^{min} > 4.2$ TeV			$M^{min} > 4.3$ TeV			$M^{min} > 4.4$ TeV			$M^{min} > 4.5$ TeV		
			ϵ	A	$\epsilon \times A$	ϵ	A	$\epsilon \times A$	ϵ	A	$\epsilon \times A$	ϵ	A	$\epsilon \times A$
2	3.5	4.5	1.009	0.116	1.019±0.0041	1.025	0.095	1.051±0.0037	1.017	0.073	1.035±0.0032	1.049	0.053	1.101±0.0027
2	4.0	4.5	1.011	0.140	1.022±0.0045	1.029	0.112	1.059±0.0040	1.010	0.088	1.020±0.0035	1.091	0.061	1.190±0.0030
2	2.5	5.0	0.999	0.187	0.997±0.0053	0.999	0.161	0.999±0.0048	0.997	0.138	0.994±0.0044	1.004	0.114	1.009±0.0040
2	3.0	5.0	1.003	0.199	1.007±0.0055	0.997	0.172	0.994±0.0050	0.999	0.149	0.998±0.0047	0.998	0.127	0.996±0.0042
2	3.5	5.0	0.995	0.195	0.991±0.0054	1.011	0.169	1.022±0.0050	1.018	0.147	1.036±0.0047	1.011	0.128	1.022±0.0043
2	4.0	5.0	0.993	0.204	0.987±0.0056	0.988	0.183	0.976±0.0052	0.986	0.162	0.972±0.0049	1.013	0.138	1.027±0.0045
2	1.5	5.5	0.993	0.223	0.987±0.0058	1.002	0.189	1.004±0.0053	1.000	0.159	1.000±0.0048	0.995	0.129	0.989±0.0043
2	2.0	5.5	0.991	0.266	0.981±0.0065	0.982	0.235	0.965±0.0060	0.994	0.202	0.989±0.0055	0.983	0.174	0.967±0.0050
2	2.5	5.5	0.994	0.283	0.989±0.0068	0.990	0.259	0.980±0.0064	0.986	0.230	0.972±0.0059	0.999	0.201	0.998±0.0055
2	3.0	5.5	0.999	0.299	0.998±0.0070	0.996	0.275	0.992±0.0066	0.993	0.252	0.986±0.0063	0.998	0.224	0.997±0.0059
2	3.5	5.5	0.987	0.291	0.974±0.0068	1.006	0.266	1.011±0.0066	0.998	0.241	0.995±0.0061	1.001	0.219	1.002±0.0058
2	4.0	5.5	0.990	0.276	0.979±0.0066	0.988	0.254	0.977±0.0063	0.987	0.235	0.975±0.0060	0.991	0.213	0.981±0.0057
2	1.5	6.0	1.009	0.326	1.017±0.0076	0.989	0.295	0.978±0.0071	0.996	0.256	0.993±0.0065	1.008	0.220	1.016±0.0060
2	2.0	6.0	0.995	0.361	0.990±0.0078	0.989	0.330	0.978±0.0074	0.982	0.300	0.965±0.0069	0.994	0.267	0.988±0.0065
2	2.5	6.0	0.987	0.375	0.974±0.0080	0.986	0.346	0.972±0.0076	0.986	0.319	0.973±0.0072	0.990	0.293	0.980±0.0069
4	3.0	4.5	1.037	0.102	1.075±0.0038	1.022	0.080	1.044±0.0033	1.065	0.058	1.134±0.0029	1.073	0.040	1.151±0.0024
4	3.5	4.5	1.008	0.123	1.016±0.0042	1.022	0.096	1.044±0.0037	1.079	0.072	1.164±0.0033	1.065	0.052	1.134±0.0027
4	4.0	4.5	1.010	0.118	1.020±0.0041	1.057	0.092	1.118±0.0037	1.024	0.071	1.048±0.0031	1.054	0.052	1.111±0.0027
4	1.5	5.0	0.996	0.114	0.993±0.0040	1.005	0.089	1.011±0.0035	1.039	0.066	1.079±0.0031	1.047	0.051	1.096±0.0027
4	2.0	5.0	1.019	0.157	1.038±0.0048	1.015	0.130	1.030±0.0043	1.025	0.104	1.051±0.0039	1.011	0.082	1.022±0.0033
4	2.5	5.0	1.011	0.185	1.021±0.0053	1.012	0.154	1.024±0.0048	0.982	0.130	0.965±0.0043	1.031	0.102	1.064±0.0038
4	3.0	5.0	0.997	0.193	0.995±0.0054	0.994	0.166	0.987±0.0049	0.996	0.142	0.991±0.0045	0.995	0.119	0.990±0.0041
4	3.5	5.0	1.000	0.207	1.000±0.0056	0.995	0.181	0.990±0.0052	0.996	0.158	0.992±0.0048	1.006	0.133	1.012±0.0044
4	4.0	5.0	0.991	0.213	0.981±0.0057	1.000	0.187	1.000±0.0053	1.006	0.162	1.012±0.0049	0.998	0.137	0.996±0.0044
4	1.5	5.5	0.997	0.218	0.993±0.0059	0.993	0.185	0.986±0.0054	1.016	0.153	1.031±0.0049	0.994	0.127	0.989±0.0043
4	2.0	5.5	0.989	0.259	0.978±0.0065	0.993	0.226	0.986±0.0060	0.983	0.200	0.967±0.0056	1.013	0.170	1.026±0.0052
4	2.5	5.5	1.001	0.281	1.003±0.0067	0.996	0.254	0.992±0.0063	1.001	0.223	1.002±0.0059	0.987	0.196	0.974±0.0054
4	3.0	5.5	0.987	0.293	0.974±0.0069	0.995	0.264	0.990±0.0065	1.000	0.235	1.000±0.0061	0.986	0.210	0.972±0.0056
4	3.5	5.5	0.988	0.302	0.977±0.0070	0.994	0.274	0.988±0.0066	0.994	0.250	0.987±0.0063	1.002	0.226	1.004±0.0059
4	4.0	5.5	0.989	0.303	0.977±0.0070	0.992	0.278	0.984±0.0067	0.992	0.252	0.983±0.0063	0.992	0.231	0.985±0.0060
4	1.5	6.0	1.004	0.318	1.008±0.0073	0.993	0.284	0.987±0.0067	1.000	0.249	1.000±0.0063	0.990	0.219	0.980±0.0058
4	2.0	6.0	0.983	0.366	0.967±0.0079	0.996	0.331	0.991±0.0074	1.004	0.297	1.009±0.0070	1.005	0.265	1.009±0.0065
4	2.5	6.0	0.993	0.366	0.986±0.0079	0.987	0.338	0.974±0.0075	0.994	0.307	0.988±0.0071	0.998	0.280	0.995±0.0067
4	3.0	6.0	0.984	0.394	0.968±0.0083	0.986	0.365	0.973±0.0079	0.987	0.337	0.974±0.0075	0.981	0.310	0.963±0.0071
6	1.5	5.0	1.001	0.125	1.002±0.0042	1.008	0.100	1.015±0.0037	1.013	0.076	1.027±0.0032	1.078	0.056	1.162±0.0028
6	2.0	5.0	1.010	0.155	1.021±0.0048	1.020	0.128	1.040±0.0043	1.035	0.104	1.072±0.0039	1.030	0.081	1.061±0.0034
6	2.5	5.0	1.003	0.187	1.006±0.0053	1.002	0.159	1.004±0.0049	1.008	0.132	1.016±0.0044	1.006	0.109	1.011±0.0039
6	3.0	5.0	0.993	0.202	0.987±0.0055	0.997	0.172	0.994±0.0050	0.995	0.147	0.989±0.0046	0.986	0.125	0.972±0.0042
6	3.5	5.0	0.994	0.207	0.988±0.0056	0.979	0.183	0.959±0.0052	1.009	0.156	1.019±0.0048	1.011	0.134	1.023±0.0044
6	4.0	5.0	0.991	0.229	0.981±0.0060	0.988	0.203	0.976±0.0055	1.002	0.175	1.003±0.0051	0.994	0.149	0.988±0.0046
6	1.5	5.5	1.002	0.223	1.005±0.0060	1.012	0.188	1.024±0.0055	1.013	0.156	1.026±0.0049	0.995	0.130	0.989±0.0044
6	2.0	5.5	0.998	0.257	0.995±0.0064	0.985	0.227	0.970±0.0059	1.006	0.194	1.013±0.0054	0.993	0.168	0.986±0.0049
6	2.5	5.5	0.997	0.272	0.995±0.0066	1.001	0.243	1.001±0.0062	1.007	0.212	1.014±0.0057	0.987	0.187	0.974±0.0052
6	3.0	5.5	0.990	0.287	0.981±0.0068	0.989	0.260	0.978±0.0064	0.993	0.236	0.986±0.0061	1.005	0.207	1.010±0.0056
6	3.5	5.5	0.995	0.293	0.990±0.0069	0.994	0.268	0.988±0.0065	0.997	0.242	0.994±0.0061	0.994	0.218	0.987±0.0058
6	4.0	5.5	0.991	0.300	0.982±0.0070	0.986	0.276	0.972±0.0066	0.991	0.251	0.983±0.0063	1.003	0.226	1.007±0.0059
6	1.5	6.0	1.001	0.331	1.002±0.0074	1.003	0.291	1.006±0.0069	0.999	0.259	0.999±0.0064	1.004	0.225	1.008±0.0059
6	2.0	6.0	0.991	0.356	0.982±0.0078	0.997	0.322	0.994±0.0073	0.998	0.288	0.997±0.0068	0.996	0.258	0.993±0.0064
6	2.5	6.0	0.989	0.373	0.977±0.0080	0.981	0.346	0.963±0.0076	0.998	0.314	0.996±0.0072	1.001	0.286	1.002±0.0068
6	3.0	6.0	0.994	0.380	0.987±0.0081	0.987	0.357	0.975±0.0078	0.993	0.329	0.986±0.0074	0.989	0.300	0.978±0.0070
6	3.5	6.0	0.985	0.372	0.971±0.0080	0.987	0.348	0.974±0.0076	0.989	0.323	0.977±0.0073	0.982	0.300	0.965±0.0070
6	4.0	6.0	0.991	0.382	0.982±0.0081	0.989	0.358	0.979±0.0078	0.990	0.335	0.980±0.0075	0.989	0.311	0.977±0.0071

Table 5.17: The reconstruction efficiency (ϵ) and acceptance (A) in SRs for EF-j360-a4tchad trigger for non-rotating black hole samples parameterized by n, M_D and M_{th}. The product of ϵ and A is also shown along with uncertainty on the product.

n	M_D (TeV)	M_{th} (TeV)	Upper Limit on Cross Section (fb)		Scale-Factors
			AltFast-II	Truth	
2	1.5	5.5	0.8977	0.9064	0.990
2	1.5	6.0	0.3446	0.3015	1.143
2	2.0	5.5	0.5387	0.4598	1.172
2	2.0	6.0	0.2059	0.2172	0.948
2	2.5	5.5	0.3842	0.3788	1.014
2	2.5	6.0	0.1856	0.1860	0.998
2	3.0	5.5	0.2844	0.3002	0.947
2	3.5	5.5	0.3118	0.3070	1.016
2	4.0	5.0	0.7537	0.8483	0.888
2	4.0	5.5	0.3256	0.3295	0.988
4	1.5	6.0	0.3129	0.3614	0.866
4	2.0	6.0	0.2054	0.2094	0.981
4	2.5	5.5	0.3901	0.3828	1.019
4	2.5	6.0	0.1826	0.1728	1.056
4	3.0	5.5	0.3434	0.3248	1.057
4	3.0	6.0	0.1774	0.1783	0.995
4	3.5	5.5	0.3026	0.3148	0.961
4	4.0	5.5	0.2807	0.2972	0.944
6	1.5	6.0	0.3075	0.2868	1.072
6	2.0	6.0	0.2332	0.2439	0.956
6	2.5	6.0	0.1859	0.1813	1.025
6	3.0	6.0	0.1748	0.1773	0.986
6	3.5	5.5	0.3351	0.3163	1.059
6	3.5	6.0	0.1687	0.1470	1.147
6	4.0	5.5	0.2766	0.3086	0.896
6	4.0	6.0	0.1535	0.1620	0.948

Table 5.18: Scale-Factors for truth samples are calculated with respect to the corresponding AltFast-II samples for non-rotating black holes.

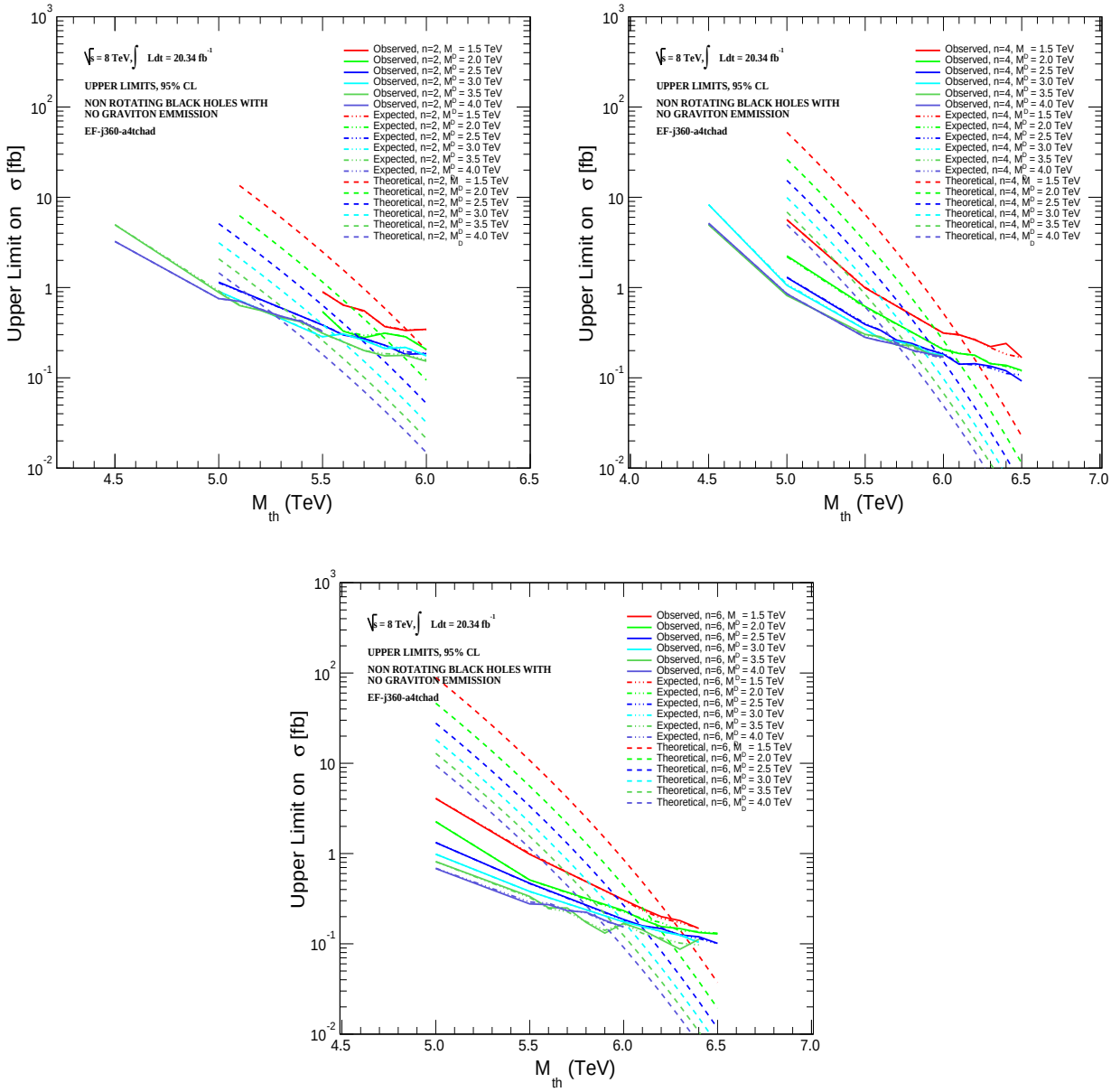

Figure 5.14: Upper limits on the observed and expected production cross sections (σ) at the 95% confidence level (CL) (solid lines and dotted-broken lines, respectively) for extra dimensions n={2,4,6} and fundamental Planck scale M_D={1.5, 2.0, 2.5, 3.0, 3.5, 4.0} are compared with theoretical production cross sections from CHARYBDIS2 black hole generator (broken lines), as a function of threshold mass M_{th} for non-rotating black holes.

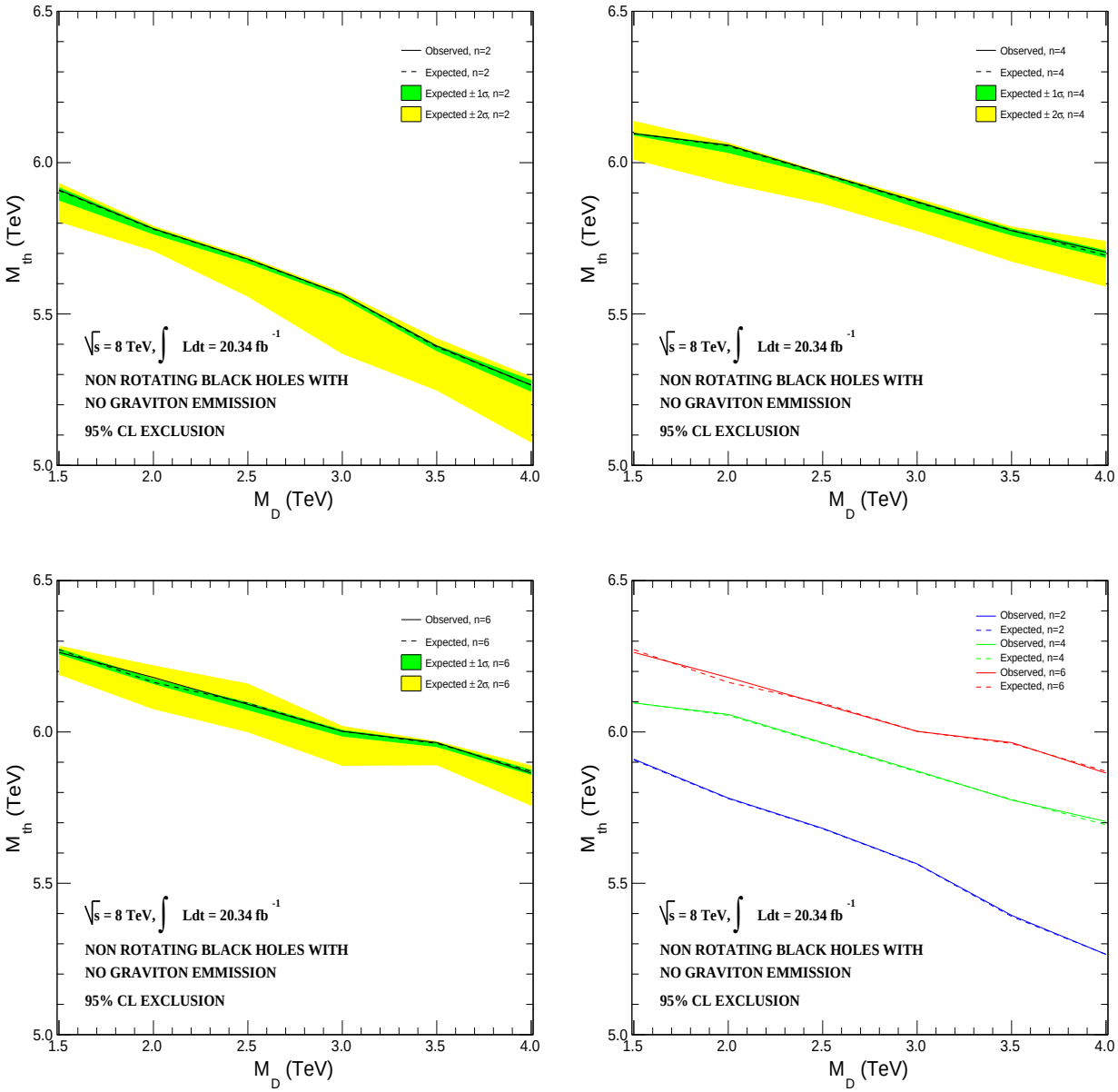

Figure 5.15: Exclusion contours in M_{th}-M_D plane in two, four and six extra dimensions for non-rotating black holes. The solid (broken) lines represent observed (expected) limits on M_{th} at the 95% confidence level versus (n, M_D)−values. The green and yellow regions show $\pm 1\sigma$ and $\pm 2\sigma$ variation in expected limits on M_{th}, respectively.

n	M_D (TeV)	M_{th} (TeV)					
		Observed UL	Expected UL	-1σ	$+1\sigma$	-2σ	$+2\sigma$
2	1.5	5.910	5.907	+0.011	−0.032	+0.026	−0.103
2	2.0	5.782	5.780	+0.005	−0.017	+0.011	−0.072
2	2.5	5.681	5.680	+0.003	−0.013	+0.009	−0.123
2	3.0	5.564	5.563	+0.004	−0.011	+0.009	−0.195
2	3.5	5.394	5.391	+0.006	−0.014	+0.029	−0.144
2	4.0	5.265	5.265	+0.017	−0.022	+0.028	−0.190
4	1.5	6.096	6.096	+0.003	−0.006	+0.042	−0.086
4	2.0	6.058	6.055	+0.005	−0.023	+0.011	−0.125
4	2.5	5.965	5.962	+0.003	−0.007	+0.006	−0.098
4	3.0	5.871	5.868	+0.006	−0.018	+0.014	−0.094
4	3.5	5.775	5.777	+0.005	−0.018	+0.012	−0.104
4	4.0	5.704	5.693	+0.017	−0.008	+0.049	−0.103
6	1.5	6.263	6.272	+0.004	−0.016	+0.013	−0.083
6	2.0	6.180	6.164	+0.012	−0.006	+0.056	−0.089
6	2.5	6.091	6.095	+0.003	−0.023	+0.065	−0.096
6	3.0	6.002	6.002	+0.005	−0.017	+0.018	−0.114
6	3.5	5.965	5.962	+0.004	−0.012	+0.008	−0.072
6	4.0	5.864	5.870	+0.005	−0.012	+0.020	−0.114

Table 5.19: Observed and expected upper limits on M_{th} for two, four and six extra dimensions for non-rotating black hole versus (n, M_D)−values. The $\pm1\sigma$ and $\pm2\sigma$ represent 68% and 95% confidence intervals on either sides of the expected limits on M_{th}.

5.11.2 Rotating Black Holes

The calculations performed for rotating black holes are identical with non-rotating black holes and are discussed in detail in the previous section. There are a total of 49 AltFast-II signal samples available for rotating black holes. The cut flow statistics for all signal samples are shown in Table 5.20 along with respective cumulative percentages in parentheses.

The M and H_T distributions for rotating black hole signal samples added on top of SM background PYTHIA8 prediction for $n = \{2, 4, 6\}$ and $M_D = \{1.5, 2.0, 2.5, 3.0, 3.5, 4.0\}$ are shown in Figures D.1, D.2, D.3, D.4, D.5 and D.6, respectively, for different values of M_D. The reconstruction efficiencies per 0.1 TeV bin for M and H_T distributions for all 49 AltFast-II signal samples in corresponding fully efficient regions of the EF-j360-a4tchad trigger are shown in Figures D.7, D.8, D.9, D.10 and D.11.

The reconstruction efficiencies and acceptances in the last four SRs defined using EF-j360-a4tchad trigger are presented in Table 5.21 for all 49 AltFast-II signal samples. The reconstruction efficiencies for all four SRs fluctuate about unity. The acceptances for signal samples typically show a monotonically increasing trend with increasing M_{th} values while keeping n and M_D unchanged. This is because of higher multiplicity.

The limits on the production cross section are calculated (at 95% confidence level) for all 49 AltFast-II signal samples using a frequentist CL_s method and are plotted as solid lines versus the corresponding M_{th} values for a unique set of (n, M_D)−values in Figure 5.16. The expected upper limit on the production cross section for each AltFast-II signal sample is the mean value of 2500 pseudo datasets generated by randomly fluctuating the signal and estimated background within systematic and statistical uncertainties, and performing the counting experiment repeatedly. The expected limits on the production cross section versus M_{th} are plotted as dotted-broken lines. The production cross section curves are plotted as broken lines. For a given set of (n, M_D)−values, the production cross section limit curve typically intersects the production cross section curve. The M_{th} values lower than the point of intersection are excluded for that particular set of (n, M_D)−values. To minimize the uncertainty in obtaining the point of intersection via interpolation, truth samples are locally generated which vary in the M_{th} domain by a stepsize of 0.1 TeV for all sets of (n, M_D)−values. These samples are not passed through AltFast-II simulation. Scale-factors are calculated to take account of the differences between AltFast-II and truth samples and are shown in Table 5.22. For a given set of (n, M_D)−values, the truth samples are scaled using the scale-factor that is derived from a truth/AltFast-II sample pair that is closest in M_{th} value.

The production cross section curve varies smoothly in the M_{th} domain by a stepsize of 0.1 TeV from 4.5 TeV to 6.5 TeV. For a few sets of (n, M_D)−values, the cross section limit curves for AltFast-II signal samples do not intersect the corresponding theoretical cross section limit curve. The truth samples are used to extrapolate the cross section limits for higher M_{th} values until the point of intersection is obtained. Figures D.12, D.14 and D.14 show separate plots for the observed upper limit and expected upper limit on the production cross sections for each set of (n, M_D)−values. The $\pm 1\sigma$ and $\pm 2\sigma$ confidence intervals about the expected upper limits are also drawn. Table 5.23 presents lower limits on the observed and expected M_{th}

values for all sets of (n, M_D)−values. The $\pm1\sigma$ and $\pm2\sigma$ values of M_{th} about the expected values are also presented.

Exclusion contour plots in the M_{th}-M_D plane for two, four and six extra dimensions for AltFast-II and truth samples are presented in Figure 5.17. The models with M_{th} values laying under the observed limit curves are excluded at 95% CL for a particular set of (n, M_D)−value.

n	M_D (TeV)	M_{th} (TeV)	Total Events	Clean Events	Trigger Cut	$p_T \geqslant 50$ GeV	Three Jets	$\|\eta\| < 1.2$
2	3.5	4.5	9000	8871 (98.6%)	8741 (97.1%)	8700 (96.7%)	7299 (81.1%)	5776 (64.2%)
2	4.0	4.5	10000	9824 (98.2%)	9712 (97.1%)	9617 (96.2%)	7148 (71.5%)	5458 (54.6%)
2	3.0	5.0	10000	9831 (98.3%)	9729 (97.3%)	9682 (96.8%)	8278 (82.8%)	6495 (65.0%)
2	1.5	5.5	10000	9847 (98.5%)	9799 (98.0%)	9784 (97.8%)	9226 (92.3%)	8012 (80.1%)
2	2.0	5.5	10000	9808 (98.1%)	9741 (97.4%)	9710 (97.1%)	8886 (88.9%)	7381 (73.8%)
2	2.5	5.5	5000	4914 (98.3%)	4876 (97.5%)	4864 (97.3%)	4314 (86.3%)	3552 (71.0%)
2	3.0	5.5	10000	9817 (98.2%)	9739 (97.4%)	9689 (96.9%)	8401 (84.0%)	6731 (67.3%)
2	3.5	5.5	10000	9805 (98.0%)	9732 (97.3%)	9678 (96.8%)	8196 (82.0%)	6402 (64.0%)
2	4.0	5.5	10000	9820 (98.2%)	9747 (97.5%)	9685 (96.8%)	8061 (80.6%)	6357 (63.6%)
2	1.5	6.0	9500	9343 (98.3%)	9308 (98.0%)	9286 (97.7%)	8909 (93.8%)	7805 (82.2%)
2	2.0	6.0	10000	9798 (98.0%)	9751 (97.5%)	9718 (97.2%)	8918 (89.2%)	7482 (74.8%)
2	2.5	6.0	10000	9811 (98.1%)	9755 (97.5%)	9714 (97.1%)	8634 (86.3%)	7055 (70.5%)
4	3.0	4.5	10000	9854 (98.5%)	9756 (97.6%)	9720 (97.2%)	8877 (88.8%)	7252 (72.5%)
4	3.5	4.5	10000	9865 (98.7%)	9783 (97.8%)	9754 (97.5%)	8801 (88.0%)	7079 (70.8%)
4	4.0	4.5	10000	9861 (98.6%)	9752 (97.5%)	9722 (97.2%)	8604 (86.0%)	6940 (69.4%)
4	1.5	5.0	10000	9864 (98.6%)	9850 (98.5%)	9846 (98.5%)	9727 (97.3%)	9030 (90.3%)
4	2.0	5.0	10000	9859 (98.6%)	9810 (98.1%)	9801 (98.0%)	9467 (94.7%)	8303 (83.0%)
4	2.5	5.0	10000	9843 (98.4%)	9784 (97.8%)	9768 (97.7%)	9170 (91.7%)	7749 (77.5%)
4	3.0	5.0	10000	9843 (98.4%)	9790 (97.9%)	9755 (97.5%)	9035 (90.3%)	7483 (74.8%)
4	3.5	5.0	10000	9847 (98.5%)	9779 (97.8%)	9745 (97.5%)	8852 (88.5%)	7220 (72.2%)
4	4.0	5.0	10000	9834 (98.3%)	9776 (97.8%)	9754 (97.5%)	8791 (87.9%)	7293 (72.9%)
4	1.5	5.5	10000	9867 (98.7%)	9854 (98.5%)	9850 (98.5%)	9780 (97.8%)	9248 (92.5%)
4	2.0	5.5	10000	9840 (98.4%)	9815 (98.2%)	9811 (98.1%)	9620 (96.2%)	8618 (86.2%)
4	2.5	5.5	9999	9825 (98.3%)	9789 (97.9%)	9776 (97.8%)	9366 (93.7%)	8100 (81.0%)
4	3.0	5.5	10000	9852 (98.5%)	9797 (98.0%)	9775 (97.8%)	9099 (91.0%)	7565 (75.7%)
4	3.5	5.5	10000	9819 (98.2%)	9755 (97.5%)	9728 (97.3%)	8874 (88.7%)	7311 (73.1%)
4	4.0	5.5	10000	9833 (98.3%)	9774 (97.7%)	9741 (97.4%)	8782 (87.8%)	7231 (72.3%)
4	1.5	6.0	10000	9877 (98.8%)	9870 (98.7%)	9866 (98.7%)	9801 (98.0%)	9417 (94.2%)
4	2.0	6.0	10000	9845 (98.5%)	9833 (98.3%)	9826 (98.3%)	9663 (96.6%)	8702 (87.0%)
4	2.5	6.0	10000	9832 (98.3%)	9806 (98.1%)	9789 (97.9%)	9381 (93.8%)	8114 (81.1%)
4	3.0	6.0	10000	9812 (98.1%)	9766 (97.7%)	9742 (97.4%)	9171 (91.7%)	7779 (77.8%)
6	1.5	5.0	10000	9905 (99.0%)	9891 (98.9%)	9891 (98.9%)	9862 (98.6%)	9619 (96.2%)
6	2.0	5.0	10000	9878 (98.8%)	9857 (98.6%)	9854 (98.5%)	9777 (97.8%)	9157 (91.6%)
6	2.5	5.0	10000	9847 (98.5%)	9813 (98.1%)	9806 (98.1%)	9604 (96.0%)	8663 (86.6%)
6	3.0	5.0	10000	9862 (98.6%)	9826 (98.3%)	9816 (98.2%)	9502 (95.0%)	8341 (83.4%)
6	3.5	5.0	10000	9853 (98.5%)	9812 (98.1%)	9791 (97.9%)	9336 (93.4%)	7982 (79.8%)
6	4.0	5.0	10000	9848 (98.5%)	9793 (97.9%)	9771 (97.7%)	9179 (91.8%)	7837 (78.4%)
6	1.5	5.5	10000	9901 (99.0%)	9896 (99.0%)	9894 (98.9%)	9872 (98.7%)	9663 (96.6%)
6	2.0	5.5	10000	9845 (98.5%)	9831 (98.3%)	9829 (98.3%)	9763 (97.6%)	9318 (93.2%)
6	2.5	5.5	10000	9841 (98.4%)	9825 (98.2%)	9823 (98.2%)	9670 (96.7%)	8813 (88.1%)
6	3.0	5.5	10000	9841 (98.4%)	9813 (98.1%)	9807 (98.1%)	9548 (95.5%)	8447 (84.5%)
6	3.5	5.5	10000	9818 (98.2%)	9778 (97.8%)	9762 (97.6%)	9309 (93.1%)	7996 (80.0%)
6	4.0	5.5	10000	9885 (98.8%)	9848 (98.5%)	9824 (98.2%)	9381 (93.8%)	8176 (81.8%)
6	1.5	6.0	10000	9884 (98.8%)	9876 (98.8%)	9876 (98.8%)	9861 (98.6%)	9714 (97.1%)
6	2.0	6.0	10000	9863 (98.6%)	9856 (98.6%)	9854 (98.5%)	9793 (97.9%)	9352 (93.5%)
6	2.5	6.0	10000	9849 (98.5%)	9836 (98.4%)	9831 (98.3%)	9708 (97.1%)	8997 (90.0%)
6	3.0	6.0	10000	9816 (98.2%)	9793 (97.9%)	9785 (97.8%)	9522 (95.2%)	8479 (84.8%)
6	3.5	6.0	9999	9815 (98.2%)	9792 (97.9%)	9781 (97.8%)	9483 (94.8%)	8292 (82.9%)
6	4.0	6.0	10000	9830 (98.3%)	9808 (98.1%)	9785 (97.8%)	9306 (93.1%)	8025 (80.2%)

Table 5.20: Reduction of events after applying requirement cuts for EF-j360-a4tchad for rotating black hole samples parameterized by n, M_D and M_{th}. Cumulative percentage is also shown.

n	M_D (TeV)	M_{th} (TeV)	$M^{min} > 4.2$ TeV			$M^{min} > 4.3$ TeV			$M^{min} > 4.4$ TeV			$M^{min} > 4.5$ TeV		
			ϵ	A	$\epsilon \times A$	ϵ	A	$\epsilon \times A$	ϵ	A	$\epsilon \times A$	ϵ	A	$\epsilon \times A$
2	3.5	4.5	0.982	0.220	0.964±0.0059	0.977	0.187	0.954±0.0054	1.018	0.150	1.037±0.0049	1.048	0.111	1.099±0.0042
2	4.0	4.5	0.981	0.211	0.961±0.0057	0.974	0.183	0.949±0.0052	0.993	0.153	0.987±0.0047	0.997	0.125	0.994±0.0042
2	3.0	5.0	0.982	0.327	0.965±0.0074	0.979	0.302	0.958±0.0070	0.992	0.272	0.985±0.0066	0.995	0.243	0.989±0.0062
2	1.5	5.5	0.981	0.388	0.963±0.0082	0.986	0.360	0.972±0.0078	0.980	0.331	0.961±0.0074	0.976	0.306	0.952±0.0070
2	2.0	5.5	0.975	0.404	0.951±0.0084	0.977	0.378	0.954±0.0080	0.977	0.353	0.954±0.0077	0.978	0.328	0.956±0.0074
2	2.5	5.5	0.990	0.400	0.981±0.0118	0.989	0.378	0.977±0.0114	0.992	0.353	0.984±0.0109	0.981	0.331	0.962±0.0104
2	3.0	5.5	0.979	0.405	0.958±0.0084	0.983	0.384	0.967±0.0081	0.982	0.362	0.964±0.0078	0.983	0.341	0.966±0.0076
2	3.5	5.5	0.985	0.408	0.970±0.0085	0.983	0.389	0.967±0.0082	0.982	0.365	0.964±0.0079	0.982	0.344	0.965±0.0076
2	4.0	5.5	0.980	0.415	0.960±0.0085	0.979	0.391	0.958±0.0082	0.981	0.368	0.962±0.0079	0.982	0.346	0.963±0.0076
2	1.5	6.0	0.980	0.459	0.961±0.0094	0.981	0.435	0.962±0.0091	0.982	0.410	0.964±0.0087	0.984	0.385	0.969±0.0084
2	2.0	6.0	0.976	0.472	0.953±0.0093	0.974	0.452	0.949±0.0090	0.980	0.429	0.961±0.0087	0.977	0.406	0.955±0.0084
2	2.5	6.0	0.977	0.457	0.954±0.0091	0.982	0.438	0.964±0.0088	0.980	0.418	0.960±0.0086	0.977	0.401	0.954±0.0083
4	3.0	4.5	1.009	0.192	1.018±0.0054	1.019	0.156	1.038±0.0049	1.008	0.123	1.017±0.0042	1.051	0.089	1.104±0.0036
4	3.5	4.5	1.002	0.207	1.004±0.0057	0.990	0.170	0.981±0.0050	0.991	0.133	0.981±0.0044	1.038	0.096	1.078±0.0038
4	4.0	4.5	0.996	0.202	0.991±0.0056	0.989	0.168	0.979±0.0050	1.002	0.133	1.004±0.0044	1.041	0.099	1.083±0.0038
4	1.5	5.0	0.981	0.255	0.963±0.0063	0.985	0.220	0.971±0.0058	1.005	0.183	1.009±0.0052	1.007	0.151	1.015±0.0047
4	2.0	5.0	0.978	0.296	0.957±0.0069	0.980	0.264	0.960±0.0064	0.990	0.230	0.980±0.0059	0.978	0.201	0.956±0.0055
4	2.5	5.0	0.984	0.312	0.969±0.0072	0.981	0.278	0.963±0.0066	1.001	0.243	1.001±0.0062	1.005	0.207	1.009±0.0057
4	3.0	5.0	0.981	0.316	0.963±0.0072	0.986	0.282	0.973±0.0067	0.982	0.254	0.964±0.0063	0.991	0.220	0.983±0.0058
4	3.5	5.0	0.983	0.324	0.966±0.0073	0.980	0.296	0.961±0.0069	0.994	0.260	0.989±0.0064	0.986	0.230	0.972±0.0059
4	4.0	5.0	0.983	0.340	0.967±0.0075	0.982	0.312	0.965±0.0071	0.976	0.280	0.952±0.0066	0.984	0.241	0.969±0.0061
4	1.5	5.5	0.973	0.360	0.947±0.0077	0.981	0.326	0.962±0.0073	0.971	0.295	0.944±0.0068	0.992	0.259	0.984±0.0064
4	2.0	5.5	0.977	0.399	0.954±0.0083	0.982	0.368	0.963±0.0079	0.974	0.339	0.949±0.0075	0.990	0.304	0.981±0.0071
4	2.5	5.5	0.980	0.427	0.961±0.0087	0.981	0.398	0.963±0.0083	0.982	0.371	0.964±0.0079	0.983	0.345	0.966±0.0076
4	3.0	5.5	0.973	0.413	0.948±0.0084	0.973	0.389	0.946±0.0081	0.973	0.363	0.946±0.0078	0.977	0.331	0.955±0.0074
4	3.5	5.5	0.983	0.421	0.967±0.0087	0.978	0.398	0.956±0.0083	0.982	0.372	0.965±0.0080	0.978	0.346	0.956±0.0076
4	4.0	5.5	0.985	0.432	0.971±0.0088	0.984	0.408	0.969±0.0084	0.981	0.383	0.963±0.0081	0.986	0.355	0.972±0.0077
4	1.5	6.0	0.986	0.444	0.973±0.0089	0.986	0.413	0.973±0.0085	0.981	0.383	0.962±0.0081	0.976	0.353	0.953±0.0076
4	2.0	6.0	0.980	0.470	0.960±0.0092	0.980	0.444	0.960±0.0089	0.974	0.419	0.949±0.0085	0.977	0.393	0.955±0.0082
4	2.5	6.0	0.989	0.483	0.978±0.0094	0.985	0.461	0.970±0.0091	0.981	0.438	0.963±0.0088	0.981	0.416	0.962±0.0085
4	3.0	6.0	0.976	0.486	0.952±0.0094	0.976	0.467	0.952±0.0092	0.978	0.445	0.956±0.0089	0.987	0.419	0.974±0.0086
6	1.5	5.0	0.988	0.221	0.976±0.0058	0.984	0.188	0.968±0.0053	1.005	0.152	1.009±0.0047	1.000	0.121	1.000±0.0041
6	2.0	5.0	0.976	0.274	0.952±0.0065	0.982	0.232	0.964±0.0059	0.983	0.193	0.966±0.0053	1.004	0.155	1.009±0.0048
6	2.5	5.0	0.981	0.299	0.962±0.0069	0.979	0.264	0.959±0.0064	0.988	0.228	0.977±0.0059	0.977	0.192	0.956±0.0053
6	3.0	5.0	0.984	0.329	0.967±0.0074	0.990	0.291	0.980±0.0069	0.992	0.253	0.983±0.0063	1.005	0.215	1.010±0.0058
6	3.5	5.0	0.989	0.325	0.978±0.0073	0.997	0.290	0.994±0.0069	1.002	0.255	1.004±0.0064	1.004	0.220	1.007±0.0058
6	4.0	5.0	0.993	0.334	0.986±0.0075	0.991	0.302	0.982±0.0070	0.995	0.269	0.991±0.0066	1.007	0.232	1.015±0.0061
6	1.5	5.5	0.985	0.323	0.969±0.0073	0.993	0.285	0.986±0.0068	0.975	0.253	0.950±0.0062	0.992	0.218	0.984±0.0057
6	2.0	5.5	0.974	0.386	0.948±0.0081	0.975	0.351	0.950±0.0076	0.976	0.314	0.953±0.0071	0.978	0.280	0.956±0.0066
6	2.5	5.5	0.980	0.412	0.960±0.0085	0.986	0.380	0.972±0.0081	0.986	0.344	0.972±0.0076	0.998	0.307	0.996±0.0071
6	3.0	5.5	0.981	0.420	0.963±0.0086	0.980	0.388	0.961±0.0082	0.979	0.360	0.958±0.0078	0.979	0.327	0.959±0.0073
6	3.5	5.5	0.976	0.429	0.952±0.0087	0.974	0.403	0.949±0.0083	0.966	0.374	0.933±0.0079	0.970	0.344	0.940±0.0075
6	4.0	5.5	0.987	0.433	0.975±0.0088	0.994	0.406	0.988±0.0085	0.997	0.375	0.993±0.0081	0.996	0.346	0.993±0.0076
6	1.5	6.0	0.994	0.410	0.989±0.0085	0.991	0.374	0.982±0.0080	0.995	0.339	0.989±0.0075	0.992	0.306	0.985±0.0071
6	2.0	6.0	0.980	0.456	0.961±0.0090	0.981	0.427	0.963±0.0087	0.975	0.396	0.951±0.0082	0.977	0.366	0.954±0.0078
6	2.5	6.0	0.979	0.501	0.959±0.0096	0.979	0.474	0.958±0.0093	0.977	0.448	0.954±0.0089	0.974	0.423	0.948±0.0086
6	3.0	6.0	0.976	0.500	0.953±0.0096	0.979	0.477	0.958±0.0093	0.975	0.451	0.951±0.0090	0.979	0.425	0.958±0.0087
6	3.5	6.0	0.975	0.520	0.950±0.0098	0.975	0.497	0.950±0.0096	0.980	0.471	0.961±0.0093	0.981	0.445	0.963±0.0089
6	4.0	6.0	0.984	0.513	0.968±0.0098	0.980	0.489	0.961±0.0095	0.983	0.466	0.967±0.0092	0.979	0.439	0.958±0.0088

Table 5.21: The reconstruction efficiency (ϵ) and acceptance (A) in SRs for EF-j360-a4tchad trigger for rotating black hole samples parameterized by n, M_D and M_{th}. The product of ϵ and A is also shown along with uncertainty on the product.

n	M_D (TeV)	M_{th} (TeV)	Upper Limit on Cross Section (fb)		Scale-Factors
			AltFast-II	Truth	
2	1.5	6.0	0.1174	0.0955	1.229
2	2.0	5.5	0.1556	0.1529	1.018
2	2.0	6.0	0.1048	0.0895	1.171
2	2.5	5.5	0.2753	0.1325	2.078
2	2.5	6.0	0.1049	0.0951	1.103
2	3.0	5.5	0.1513	0.1315	1.151
2	3.5	5.5	0.1319	0.1229	1.074
2	4.0	5.5	0.1237	0.1278	0.968
4	1.5	6.0	0.1308	0.1171	1.117
4	2.0	6.0	0.1057	0.0958	1.103
4	2.5	6.0	0.0891	0.0885	1.007
4	3.0	6.0	0.0915	0.0851	1.076
4	3.5	5.5	0.1203	0.1245	0.966
4	4.0	5.5	0.1258	0.1270	0.991
6	1.5	6.0	0.1687	0.1451	1.163
6	2.0	6.0	0.1126	0.1032	1.091
6	2.5	6.0	0.0992	0.0937	1.059
6	3.0	6.0	0.0843	0.0818	1.031
6	3.5	6.0	0.0745	0.0774	0.963
6	4.0	6.0	0.0865	0.0645	1.341

Table 5.22: Scale-Factors for truth samples are calculated with respect to the corresponding AltFast-II samples for rotating black holes.

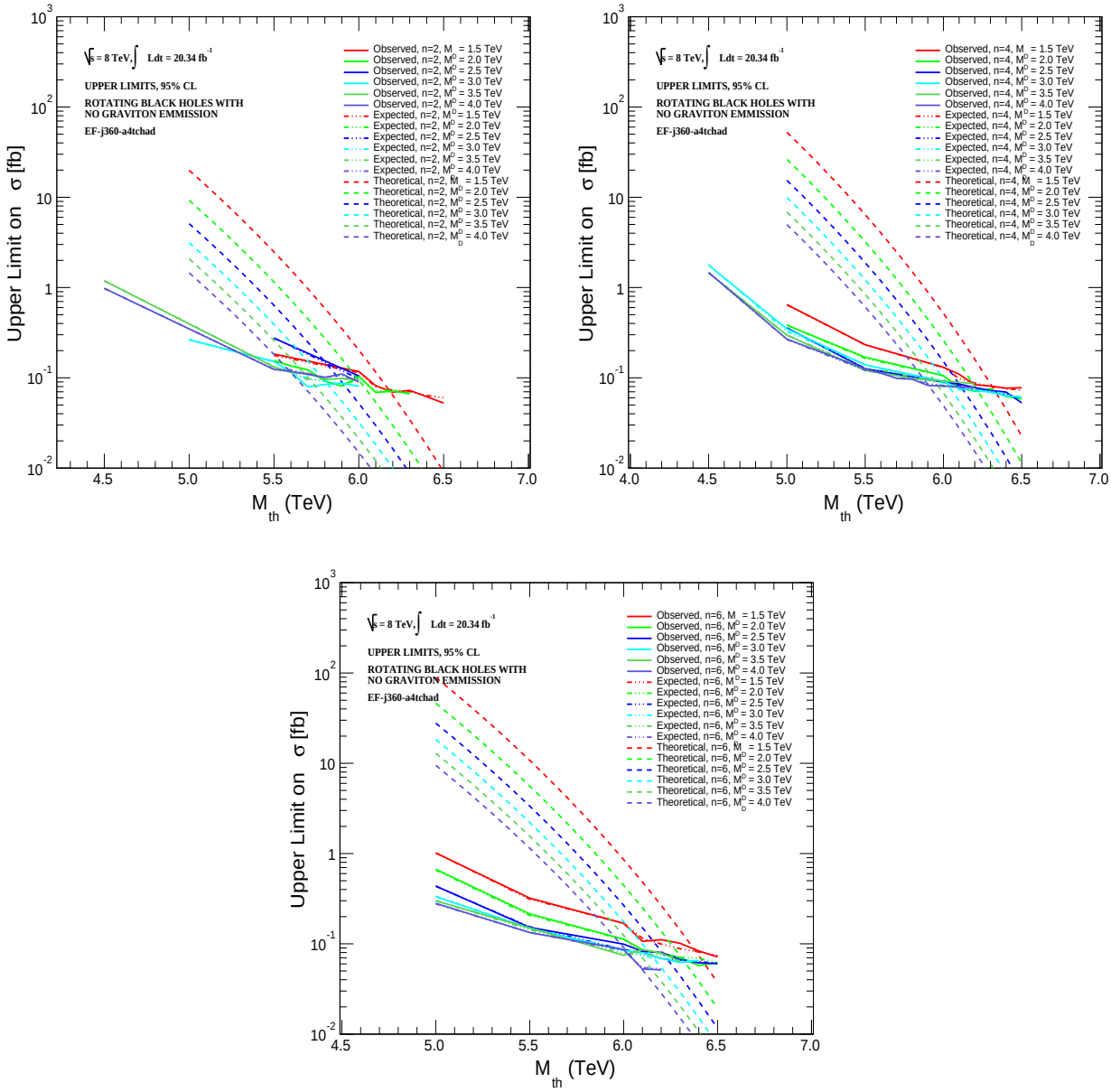

Figure 5.16: Upper limits on the observed and expected production cross sections (σ) at the 95% confidence level (CL) (solid lines and dotted-broken lines, respectively) for extra dimensions n={2,4,6} and fundamental Planck scale M_D={1.5, 2.0, 2.5, 3.0, 3.5, 4.0} are compared with theoretical production cross sections from CHARYBDIS2 black hole generator (broken lines), as a function of threshold mass M_{th} for rotating black holes.

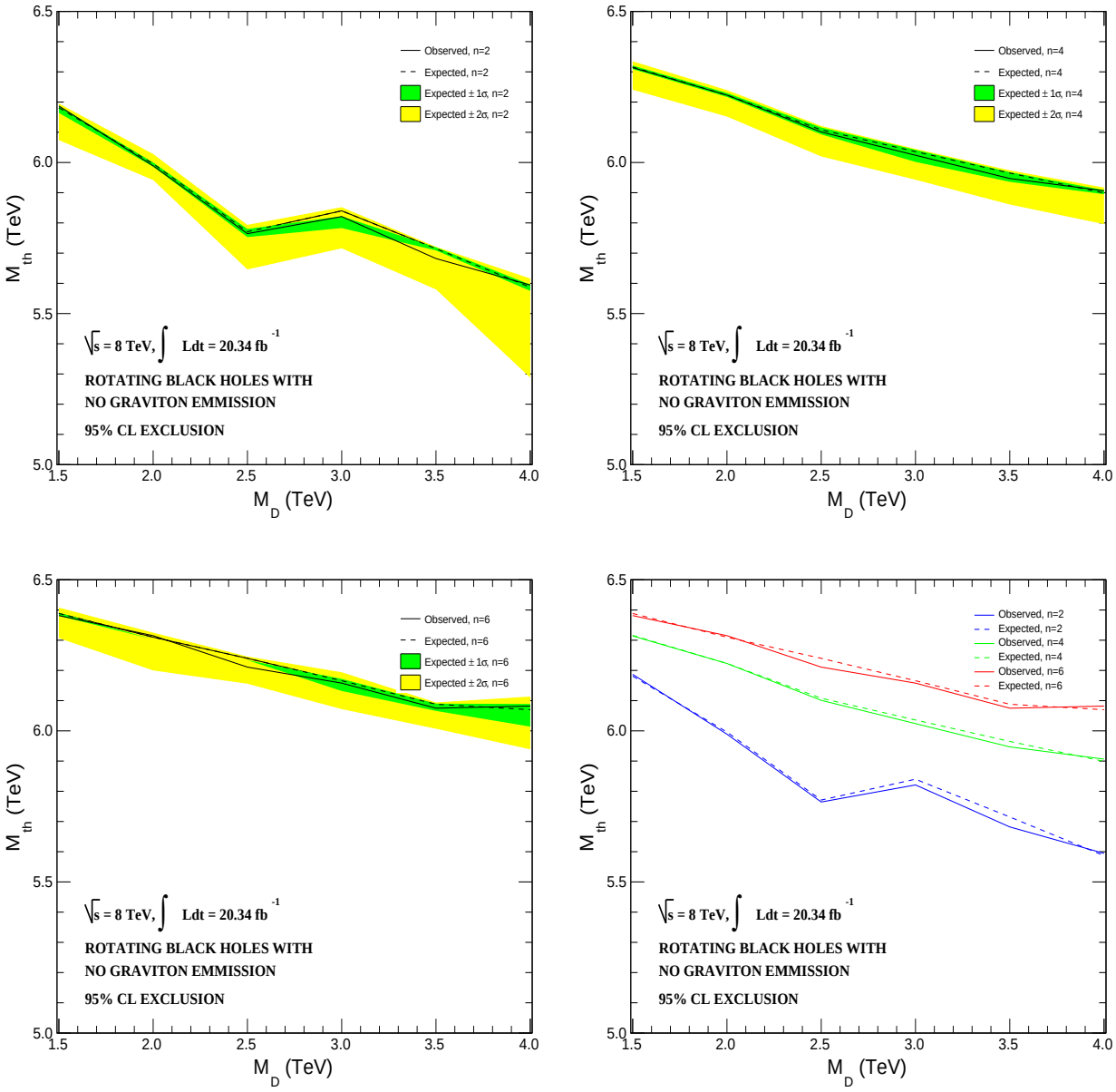

Figure 5.17: Exclusion contours in M_{th}-M_D plane in two, four and six extra dimensions for rotating black holes. The solid (broken) lines represent observed (expected) limits on M_{th} at the 95% confidence level versus $(n,\ M_D)-$values. The green and yellow regions show $\pm 1\sigma$ and $\pm 2\sigma$ variation in expected limits on M_{th}, respectively.

The -2σ band for n=2 at $M_D = 4.0$ TeV is unrealistically wide because one truth sample job namely $(n = 2,\ M_D = 4.0,\ M_{th} = 5.4)$ crashed repeatedly while in production phase. The interpolation for -2σ band is between $M_{th} = 5.3$ and $M_{th} = 5.5$ which widens the band.

n	M_D (TeV)	M_{th} (TeV)					
		Observed UL	Expected UL	-1σ	$+1\sigma$	-2σ	$+2\sigma$
2	1.5	6.187	6.181	+0.006	−0.017	+0.014	−0.107
2	2.0	5.989	5.996	+0.004	−0.010	+0.032	−0.054
2	2.5	5.764	5.771	+0.009	−0.018	+0.022	−0.125
2	3.0	5.821	5.840	+0.018	−0.057	+0.012	−0.124
2	3.5	5.682	5.715	+0.004	−0.006	+0.006	−0.135
2	4.0	5.595	5.587	+0.009	−0.012	+0.029	−0.299
4	1.5	6.314	6.316	+0.005	−0.007	+0.019	−0.075
4	2.0	6.223	6.223	+0.007	−0.006	+0.016	−0.071
4	2.5	6.101	6.108	+0.008	−0.015	+0.013	−0.088
4	3.0	6.024	6.036	+0.006	−0.034	+0.009	−0.093
4	3.5	5.947	5.965	+0.003	−0.029	+0.009	−0.104
4	4.0	5.907	5.899	+0.010	−0.004	+0.018	−0.103
6	1.5	6.381	6.388	+0.003	−0.008	+0.020	−0.081
6	2.0	6.315	6.310	+0.007	−0.007	+0.015	−0.110
6	2.5	6.211	6.240	+0.006	−0.006	+0.006	−0.084
6	3.0	6.158	6.166	+0.006	−0.034	+0.028	−0.094
6	3.5	6.075	6.088	+0.002	−0.022	+0.006	−0.081
6	4.0	6.082	6.070	+0.019	−0.056	+0.043	−0.131

Table 5.23: Observed and expected upper limits on M_{th} for two, four and six extra dimensions for rotating black hole versus (n, M_D)−values. The $\pm1\sigma$ and $\pm2\sigma$ represent 68% and 95% confidence intervals on either sides of the expected limits on M_{th}.

5.12 Discussion

The model-independent upper limit on the production cross section for new physics in multi-jet final-states in this study improves on the CMS [70] result and is comparable with the ATLAS [71] result. These results are also at $\sqrt{s} = 8$ TeV but use H_T as the analysis variable. The CMS result is higher mainly due to their lower luminosity. A comparison at $M_{th} = H_T^{min} > 4.3$ TeV and $M_{th} = H_T^{min} > 4.5$ TeV is shown in Table 5.24. The comparison is not exact because $M_{th} > H_T^{min}$. The theoretical best limit on the production cross section for new physics for a total integrated luminosity of 20.3 fb^{-1} is 0.148 at 95% confidence level in the absence of background, or and uncertainties.

Model-Independent Upper Limits on $\sigma \times A \times \epsilon$ at $\sqrt{s} = 8$ TeV			
CMS [70] (for 12.1 fb^{-1})	ATLAS [71] (for 20.3 fb^{-1})	This Study (for 20.3 fb^{-1})	This Study (for 20.3 fb^{-1})
$H_T^{min} > 4.5$ TeV	$H_T^{min} > 4.3$ TeV	$M_{th} > 4.3$ TeV	$M_{th} > 4.5$ TeV
0.20	0.16	0.16	0.15

Table 5.24: Model-independent observed upper limit (at 95% confidence level) on the production cross section (σ) times acceptance (A) times efficiency (ϵ) in fb for CMS [70], ATLAS [71] and this study for $M^{min} = H_T^{min} > 4.3$ TeV and $M^{min} = H_T^{min} > 4.5$ TeV at $\sqrt{s} = 8$ TeV.

For the model-dependent limits, the exclusion limits on M_{th} are higher for higher n values due to higher cross sections. For higher values of M_D, the ratio M_{th}/M_D is closer to unity which indicates that the semi-classical decay assumptions are least valid. For such models, the exclusion limits on M_{th} are lower due to fewer Hawking emissions. The exclusion limits on M_{th} for rotating black holes are higher compared to non-rotating black holes when all parameters are identical. One reason is higher acceptance for rotating black holes which lowers the observed upper limit on production cross section and subsequently raises the lower limit on M_{th}. The exclusion limits on M_{th} are slightly higher in this study when compared to other ATLAS [71] results. The ATLAS result [72] at $\sqrt{s} = 13$ TeV exclude the production of rotating black holes with n equal to two, four and six up to M_{th} values equal to 9.2 TeV, 9.6 TeV and 9.7 TeV, respectively in the M_D domain ranging from 2.0 TeV to 5.5 TeV using pp collision data corresponding to a total integrated luminosity of 3.0 fb^{-1}.

We suggest that M is a better analysis variable to set upper limits on the production cross section. It gives an accurate comparison with microscopic black hole theory since mass is the main independent variable in theory.

Chapter 6

Summary

This study was carried out to search for higher dimensional microscopic black holes in multi-jet final-states using five single-jet triggers with the ATLAS detector for 8 TeV pp collisions at the LHC. The ATLAS data corresponds to a total integrated luminosity of 20.3 fb^{-1}. QCD multi-jet final-states are the main background for this search.

The analysis procedure carries two-fold distinction over similar 8 TeV searches [70, 71] at the LHC. First, it uses multiple single-jet triggers in contrast to using only one multi-jet trigger. This allows for the search for new physics beyond the SM at much lower thresholds. For example, a multi-jet trigger EF-j170-a4tchad-ht700 used in ATLAS study [71] is fully efficient at $H_T > 0.8$ TeV whereas EF-j110-a4tchad, EF-j145-a4tchad and EF-j180-a4tchad used in this study are fully efficient at $H_T = 0.4$, 0.6 and 0.8, respectively. Second, it uses M as a discriminating variable instead of H_T for the search of microscopic black holes. The advantage of using M is that Schwarzschild radius, temperature, etc. are functions of M and not H_T. However, H_T is used in this study as a control variable since it is a well measured variable with the ATLAS detector.

Five single-jet triggers are used in this study. Four triggers are pre-scaled at the EF level. These triggers are bootstrapped to obtain their un-prescaled versions. The bootstrap method is cross-checked for accuracy with two un-prescaled triggers. Trigger efficiencies are calculated with respect to M and H_T, separately. Triggers are used only in their fully efficient regions in both variables.

PYTHIA8 samples are chosen to estimate the SM QCD multi-jet background for this search. Characteristics of kinematic variables like p_T, η and ϕ are studied for data and PYTHIA8 samples which help determine analysis cuts on kinematic variables. A requirement of three jets with $p_T > 50$ GeV and $|\eta| < 1.2$ in a given multi-jet final-state is imposed in this search to suppress QCD di-jet background and to use the central region of the ATLAS calorimeters. The M and H_T distributions for data are consistent with PYTHIA8 QCD predictions for all triggers.

The CRs and SRs are defined in the M domain for six triggers. The H_T is used as a control variable in the CRs and SRs. A given CR and SR uses only the trigger with the maximum statistics available. PYTHIA8 QCD multi-jet background estimates are calculated in all SRs. Four systematic uncertainties associated with

PYTHIA8 predictions are calculated for all SRs. These are the uncertainties in jet energy scale and jet energy resolution, uncertainty due to the choice of CR width and uncertainty due to choice of background model.

Counting experiments are performed to set model-independent upper limits for new physics in multi-jet final-states at the 95% confidence level using the CL_s frequentist approach for each SR. The model-independent upper limit on the observed production cross section times acceptance times efficiency at the 95% confidence level is 0.15 fb^{-1} for $M_{th} > 4.5$ TeV. Upper limits on model-dependent production cross sections are calculated with 95% confidence interval using the frequentist CL_s approach for non-rotating and rotating black holes for two, four and six large extra dimensions, M_{th} ranging from 4.5 TeV to 6.5 TeV and M_D ranging from 1.5 TeV to 4.0 TeV. Lower limits on M_{th} for given sets of (n, M_D)−values are also calculated for non-rotating and rotating black holes.

Bibliography

[1] N. Arkani-Hamed, S. Dimopoulos, and G. Dvali, "The hierarchy problem and new dimensions at a millimeter,"
Physics Letters B 429 (1998) .

[2] Y. Nambu, "Quasiparticles and Gauge Invariance in the Theory of Superconductivity,"
Physical Review 117 (1960) .

[3] J. Goldstone, "Field Theories with Superconductor Solutions,"
Nuovo Cimento 19 (1961) .

[4] J. Goldstone, A. Salam, and S. Weinberg, "Broken Symmetries,"
Physical Review 127 (1962) .

[5] ATLAS Collaboration, "Observation of a new particle in the search for the Standard Model Higgs boson with the ATLAS detector at the LHC,"
Physics Letters B 716 (2012) .

[6] ATLAS Collaboration, "Evidence for the spin-0 nature of the Higgs boson using ATLAS data,"
Physics Letters B 726 (2013) .

[7] CMS Collaboration, "Observation of a new boson at a mass of 125 GeV with the CMS experiment at the LHC,"
Physics Letters B 716 (2012) .

[8] R. Kerr, "Gravitational field of a spinning mass as an example of algebraically special metrics,"
Physical Review Letters (1963) .

[9] E. T. Newman and A. Janis, "Note on the Kerr Spinning-Particle Metric,"
Journal of Mathematical Physics 6 (1965) .

[10] E. T. Newman, E. Couch, K. Chinnapared, A. Exton, A. Prakash, and R. Torrence, "Metric of a rotating, charged mass,"
Journal of Mathematical Physics 6 (1965) .

[11] S. P. Martin, "A Supersymmetry Primer,"
arXiv:hep-ph/9709356 [hep-ph]. http://arxiv.org/abs/hep-ph/9709356v6.

[12] I. Antoniadis, N. Arkani-Hamed, S. Dimopoulos, and G. Dvali, "New dimensions at a millimeter to a fermi and superstrings at a TeV,"
Physics Letters B 436 (1998) .

[13] L. Randall and R. Sundrum, "Large Mass Hierarchy from a Small Extra Dimension," Physical Review Letters 83 (1999) .

[14] L. Randall and R. Sundrum, "An Alternative to compactification," Physical Review Letters 83 (1999) .

[15] D. Kapner, T. Cook, E. Adelberger, J. Gundlach, B. R. Heckel, C. Hoyle, and H. Swanson, "Tests of the Gravitational Inverse-Square Law below the Dark-Energy Length Scale," Physical Review Letters 98 (2007) .

[16] F. R. Tangherlini, "Schwarzschild field in n dimensions and the dimensionality of space problem," Nuovo Cimento 27 (1963) .

[17] R. C. Myers and M. J. Perry, "Black holes in higher dimensional space-times," Annals of Physics 172 (1986) .

[18] P. C. Argyres, S. Dimopoulos, and J. March-Russell, "Black holes and sub-millimeter dimensions," Physics Letters B 441 (1998) .

[19] K. S. Thorne, "Nonspherical gravitational collapse–a short review," Magic Without Magic: John Archibald Wheeler 1 (1972) .

[20] H. Yoshino and Y. Nambu, "Black hole formation in the grazing collision of high-energy particles," Physical Review D 67 (2003) .

[21] H. Yoshino and V. S. Rychkov, "Improved analysis of black hole formation in high-energy particle collisions," Physical Review D 71 (2005) .

[22] S. B. Giddings and S. Thomas, "High energy colliders as black hole factories: The end of short distance physics," Physical Review D 65 (2002) .

[23] S. W. Hawking, "Particle creation by black holes," Communications in Mathematical Physics 43 (1975) .

[24] J. A. Frost, J. R. Gaunt, M. O. P. Sampaio, M. Casals, S. R. Dolan, M. A. Parker, and B. R. Webber, "Phenomenology of Production and Decay of Spinning Extra-Dimensional Black Holes at Hadron Colliders," Journal of High Enegry Physics 10 (2009) .

[25] D. M. Gingrich, "Missing energy in black hole production and decay at the Large Hadron Collider," Journal of High Energy Physics (2007) .

[26] D. N. Page, "Particle emission rates from a black hole. II. Massless particles from a rotating hole," Physical Review D 14 (1976) .

[27] P. Kanti and J. March-Russell, "Calculable corrections to brane black hole decay: The scalar case," Physical Review D 66 (2002) .

[28] P. Kanti and J. March-Russell, "Calculable corrections to brane black hole decay. II. Greybody factors for spin 1/2 and 1,"
Physical Review D 67 (2003) .

[29] C. M. Harris and P. Kanti, "Hawking Radiation from a (4+ n)-dimensional Black Hole: Exact Results for the Schwarzschild Phase,"
Journal of High Energy Physics (2003) .

[30] D. Ida, K.-y. Oda, and S. C. Park, "Erratum: Rotating black holes at future colliders: Greybody factors for brane fields,"
Physical Review D 69 (2004) .

[31] V. Cardoso, M. Cavaglia, and L. Gualtieri, "Hawking emission of gravitons in higher dimensions: non-rotating black holes,"
Journal of High Energy Physics (2006) .

[32] T. Banks and W. Fischler, "A model for high energy scattering in quantum gravity,"
arXiv:hep-th/9906038 [hep-th].

[33] T. J. Humanic, B. Koch, and H. Stöcker, "Signatures for Black Hole production from hadronic observables at the Large Hadron Collider,"
International Journal of Modern Physics E 16 (2007) .

[34] B. Koch, M. Bleicher, and H. Stöcker, "Black holes at LHC?,"
Journal of Physics G: Nuclear and Particle Physics 34 (2007) .

[35] D. M. Gingrich, "Experimental limits on the fundamental Planck scale in large extra dimensions,"
arXiv:1210.5923v4 [hep-ex].

[36] L. Evans and P. Bryant, "LHC Machine,"
Journal of Instrumentation 3 (2008) .

[37] ATLAS Collaboration, "The ATLAS Experiment at the CERN Large Hadron Collider,"
Journal of Instrumentation 3 (2008) .

[38] CMS Collaboration, "The CMS experiment at the CERN LHC,"
Journal of Instrumentation 3 (2008) .

[39] LHCb Collaboration, "The LHCb Detector at the LHC,"
Journal of Instrumentation 3 (2008) .

[40] LHCf Collaboration, "The LHCf experiment,"
AIP Conf. Proc. 1492 (2012) .

[41] TOTEM Collaboration, "The TOTEM experiment at the LHC and its physics results,"
Nuclear Physics Proceedings Supplements 245 (2013) .

[42] R. Schicker, "The ALICE detector at LHC,"
arXiv:hep-ph/0509259v2 [hep-ph].

[43] J. J. Goodson and R. McCarthy, "Search for Supersymmetry in States with Large Missing Transverse Momentum and Three Leptons including a Z-Boson,"
PhD Thesis, Stony Brook U. (2012) . http://cds.cern.ch/record/1449722.

[44] W. Buttinger, "The ATLAS Level-1 Trigger System,".
http://iopscience.iop.org/1742-6596/396/1/012010.

[45] "ATLAS Internal Note: Search for low-scale gravity signatures in multi-jet final states with the ATLAS detector at $\sqrt{s} = 8$ TeV,".

[46] N. Arkani-Hamed, S. Dimopoulos, and G. Dvali, "Phenomenology, astrophysics and cosmology of theories with submillimeter dimensions and TeV scale quantum gravity,"
Physical Review D 59 (1999) , arXiv:hep-ph/9807344 [hep-ph].

[47] W. Lampl, S. Laplace, D. Lelas, P. Loch, H. Ma, S. Menke, S. Rajagopalan, D. Rousseau, S. Snyder, and G. Unal, "Calorimeter clustering algorithms: Description and performance,"
ATL-COM-LARG-2008-003 (2008) . http://cds.cern.ch/record/1099735.

[48] M. Cacciari, G. P. Salam, and G. Soyez, "The Anti-k$_t$ jet clustering algorithm,"
Journal of High Energy Physics 0804 (2008) .

[49] ATLAS Collaboration, "Jet mass and substructure of inclusive jets in $\sqrt{s} = 7$ TeV pp collisions with the ATLAS experiment,"
Journal of High Energy Physics 1205 (2012) .

[50] V. Lendermann, J. Haller, M. Herbst, K. Kruger, H.-C. Schultz-Coulon, *et al.*, "Combining Triggers in HEP Data Analysis,"
Nuclear Instrumentation Methods A 604 (2009) .

[51] T. Sjostrand, S. Mrenna, and P. Z. Skands, "A Brief Introduction to PYTHIA 8.1,"
Computer Physics Communications 178 (2008) .

[52] M. Bahr, S. Gieseke, M. Gigg, D. Grellscheid, K. Hamilton, *et al.*, "Herwig++ Physics and Manual,"
European Physical Journal C 58 (2008) .

[53] B. Andersson, G. Gustafson, G. Ingelman, and T. Sjöstrand, "Parton fragmentation and string dynamics,"
Physics Reports 97 (1983) .

[54] T. Sjöstrand, "Jet fragmentation of multiparton configurations in a string framework,"
Nuclear Physics B 248 (1984) .

[55] B. R. Webber, "A QCD model for jet fragmentation including soft gluon interference,"
Nuclear Physics B 238 (1984) .

[56] ATLAS Collaboration, "Summary of ATLAS Pythia 8 tunes,"
ATL-PHYS-PUB-2012-003 (2012) . http://cds.cern.ch/record/1474107.

[57] H.-L. Lai, M. Guzzi, J. Huston, Z. Li, P. M. Nadolsky, J. Pumplin, and C.-P. Yuan, "New parton distributions for collider physics,"
Physics Review D 82 (2010) .

[58] S. Gieseke, C. Rhr, and A. Sidmok, "Colour reconnections in Herwig++,"
The European Physical Journal C 72 (2012) .

[59] J. Pumplin, D. R. Stump, J. Huston, H.-L. Lai, P. Nadolsky, and W.-K. Tung, "New Generation of Parton Distributions with Uncertainties from Global QCD Analysis,"
Journal of High Energy Physics (2002) .

[60] T. Gleisberg, S. Hoeche, F. Krauss, M. Schoenherr, S. Schumann, F. Siegert, and J. Winter, "Event generation with SHERPA 1.1,"
arXiv:0811.4622.

[61] T. Ježo and P. Nason, "On the Treatment of Resonances in Next-to-Leading Order Calculations Matched to a Parton Shower,"
arXiv:1509.09071.

[62] J. Alwall, R. Frederix, S. Frixione, V. Hirschi, F. Maltoni, O. Mattelaer, H.-S. Shao, T. Stelzer, P. Torrielli, and M. Zaro, "The automated computation of tree-level and next-to-leading order differential cross sections, and their matching to parton shower simulations,"
arXiv:1405.0301.

[63] M. Mangano, M. Moretti, F. Piccinini, R. Pittau, and A. Polosa, "ALPGEN, a generator for hard multiparton processes in hadronic collisions,"
arXiv:hep-ph/0206293.

[64] ATLAS Collaboration, "The ATLAS Simulation Infrastructure,"
European Physical Journal C 70 (2010) .

[65] GEANT4 Collaboration, S. Agostinelli *et al.*, "GEANT4: A Simulation toolkit,"
Nuclear Instrumentation Methods A 506 (2003) .

[66] ATLAS Collaboration, "Jet energy measurement with the ATLAS detector in proton-proton collisions at $\sqrt{s} = 7$ TeV,"
European Physical Journal C 73 (2013) .

[67] A. Saddique and D. Gingrich, "Search for Microscopic Black Holes in Multijet Final States with the ATLAS Detector using 8 TeV Proton-Proton Collisions at the Large Hadron Collider,"
PhD Thesis, Alberta U. (2014) . http://cds.cern.ch/record/1755267".

[68] A. L. Read, "Presentation of search results: The CL(s) technique,"
Journal of Physics G 28 (2002) .

[69] ATLAS Collaboration, "Improved luminosity determination in pp collisions at $\sqrt{s} = 7$ TeV using the ATLAS detector at the LHC,"
arXiv:1302.4393v2 [hep-ex].

[70] CMS Collaboration, "Search for microscopic black holes in pp collisions at $\sqrt{s} = 8$ TeV,"
Journal of High Energy Physics (2013) .

[71] ATLAS Collaboration, "Search for low-scale gravity signatures in multi-jet final states with the ATLAS detector at $\sqrt{s} = 8$ TeV,"
arXiv:1503.08988v2 [hep-ex].

[72] ATLAS Collaboration, "Search for strong gravity in multijet final states produced in pp collisions at $\sqrt{s} = 13$ TeV using the ATLAS detector at the LHC,"
arXiv:1512.02586 [hep-ex].

Appendices

Appendix A

Plots for Systematic Uncertainties due to JES and JER

In this appendix, plots for JES and JER are shown for all SRs for all triggers to estimate associated systematic uncertainties in this study.

A set of 100 pseudo-experiments are performed to estimate the systematic uncertainty due to JES in QCD predictions for PYTHIA8 and HERWIG++. The experiments which yield the maximum difference in QCD predictions from nominal QCD prediction on either sides for PYTHIA8 and HERWIG++ in a given SR are considered as the systematic uncertainty due to JES. Figures A.1, A.2 and A.3 show percent relative differences in QCD predictions of all pseudo-experiments from nominal QCD predictions for PYTHIA8 and HERWIG++ in red and blue, respectively for all SRs for all triggers.

A set of 500 samples are generated by randomly fluctuating p_T and E_T of reconstructed jets in an event to study the effect of JER in M and H_T distributions for PYTHIA8 and HERWIG++ for all triggers. Figures A.4 and A.5 show average deviation of these samples for M and H_T distributions from corresponding nominal distributions, respectively for all triggers. The region between solid and broken green lines is used to normalize PYTHIA8 and HERWIG++ distributions with respect to ATLAS data. Figures A.6, A.7 and A.8 show relative change in SR QCD predictions for MC JER samples with respect to normalized nominal MC events for each SR. The distributions in red and blue represent PYTHIA8 and HERWIG++, respectively. The maximum for each distribution along with $\pm 1\sigma$ are also mentioned in individual plots.

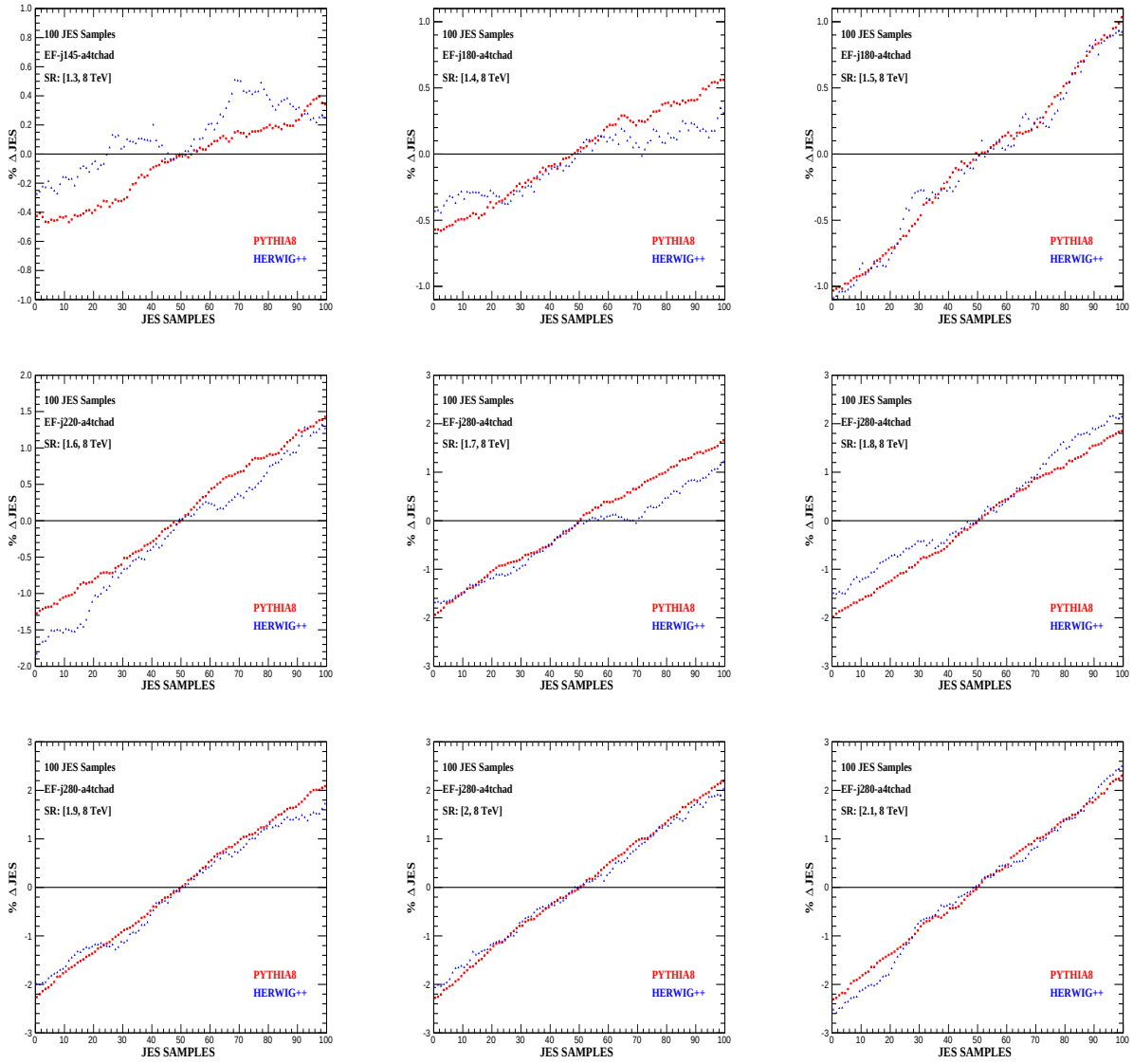

Figure A.1: ΔJES is percent relative change in SR QCD prediction for each pseudo-experiment with respect to normalized nominal MC events in each SR. 100 pesudo-experiments are performed. The distributions in red and blue represent PYTHIA8 and HERWIG++, respectively for EF-j145-a4tchad, EF-j180-a4tchad, EF-j220-a4tchad and EF-j280-a4tchad.

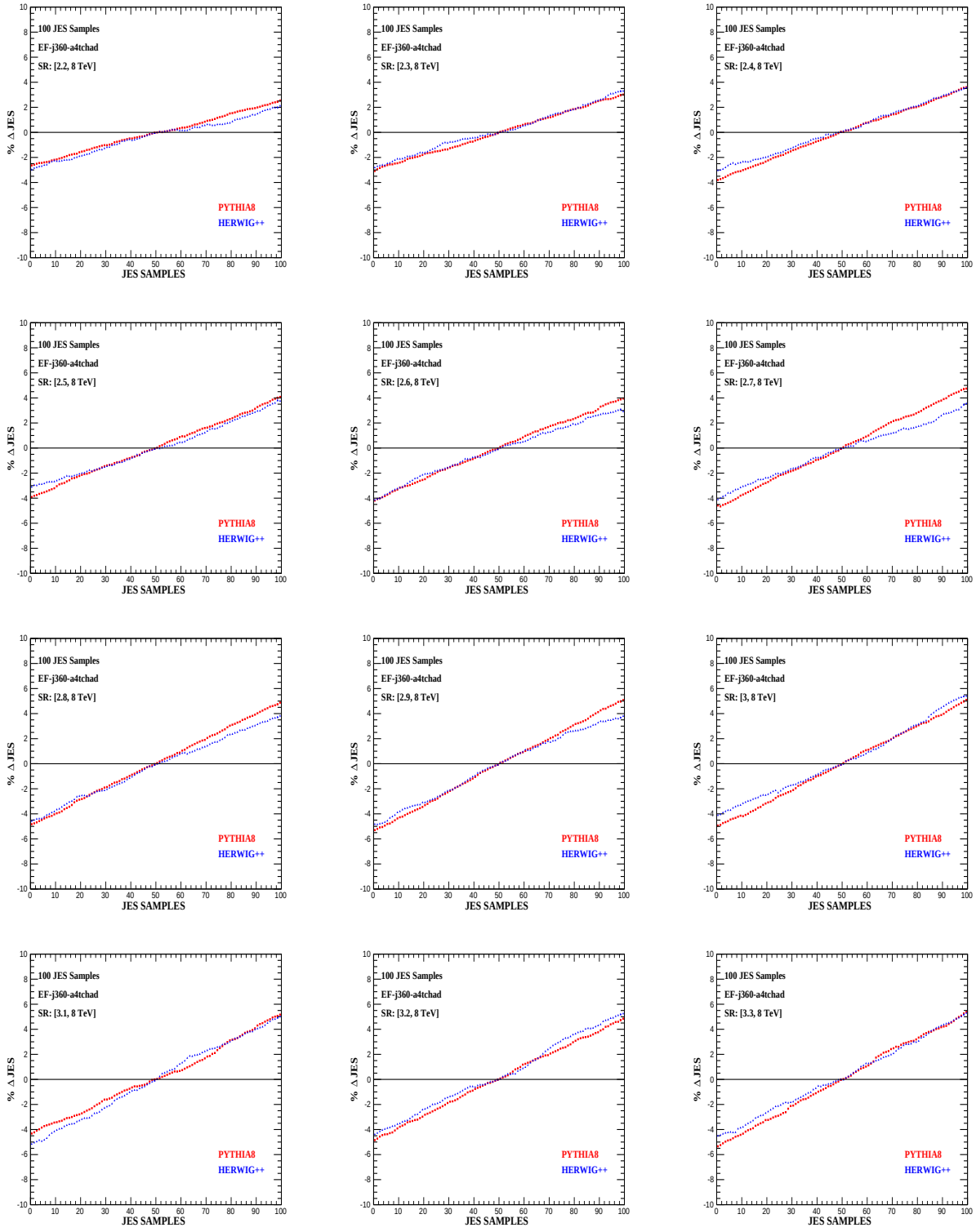

Figure A.2: ΔJES is percent relative change in SR QCD prediction for each pseudo-experiment with respect to normalized nominal MC events in each SR. 100 pesudo-experiments are performed. The distributions in red and blue represent PYTHIA8 and HERWIG++, respectively for EF-j360-a4tchad for first 12 SRs.

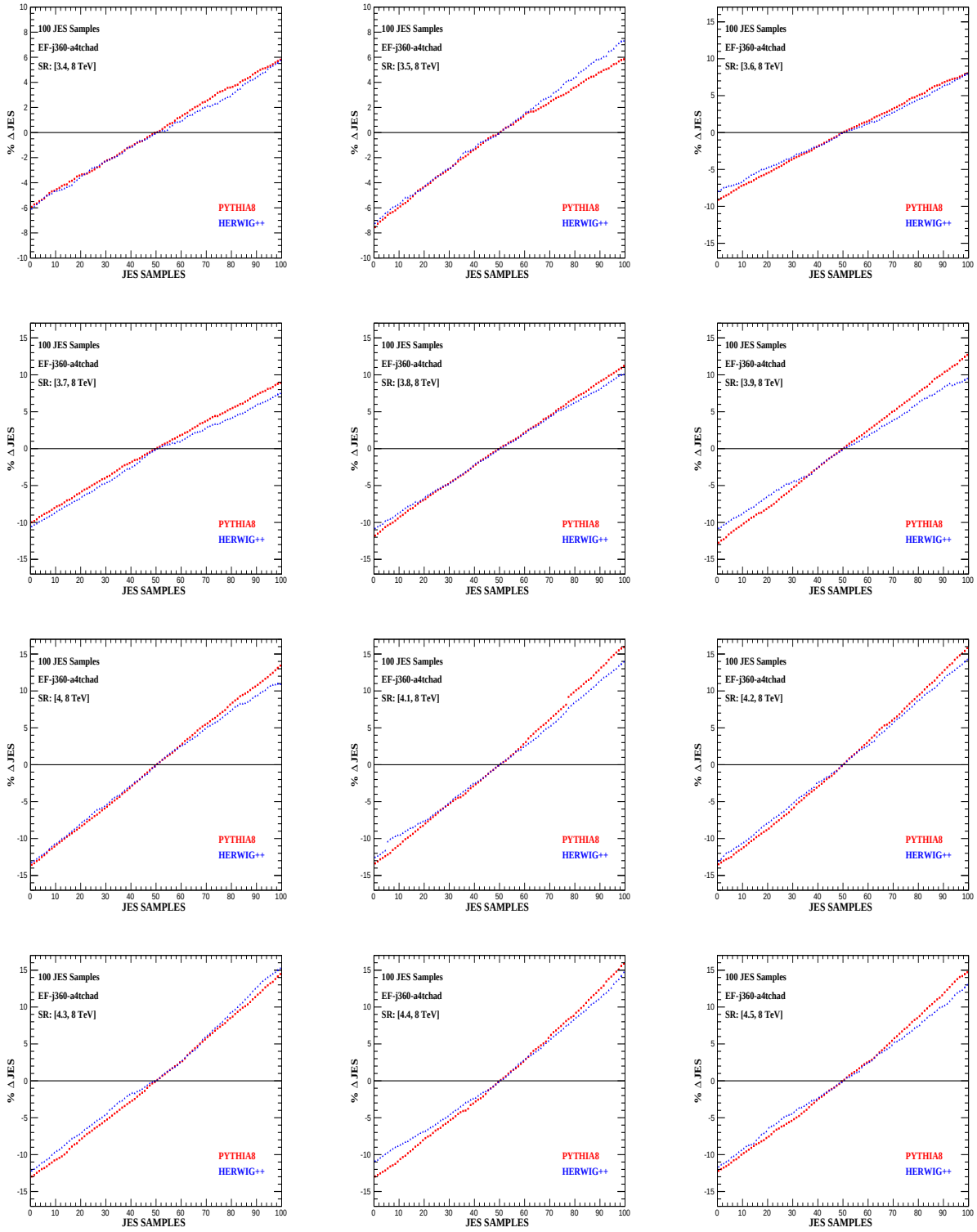

Figure A.3: ΔJES is percent relative change in SR QCD prediction for each pseudo-experiment with respect to normalized nominal MC events in each SR. 100 pesudo-experiments are performed. The distributions in red and blue represent PYTHIA8 and HERWIG++, respectively for EF-j360-a4tchad for last 12 SRs.

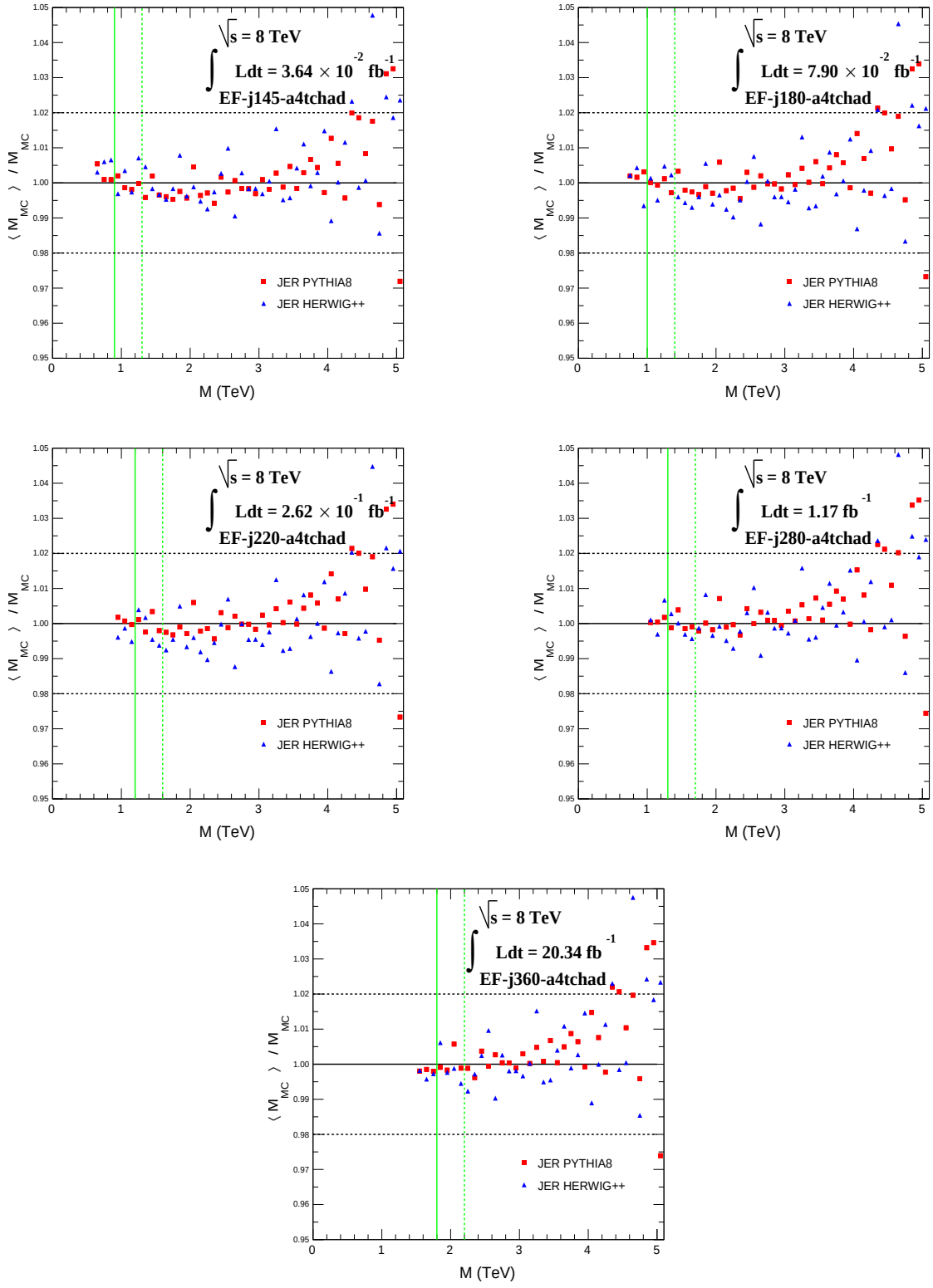

Figure A.4: Simple average of 500 M distributions is plotted relative to the nominal M distributions for 500 JER samples for PYTHIA8 and HERWIG++ in red and blue colours respectively, for each trigger. Dotted black lines mark $\pm 2\%$ difference from nominal M distributions.

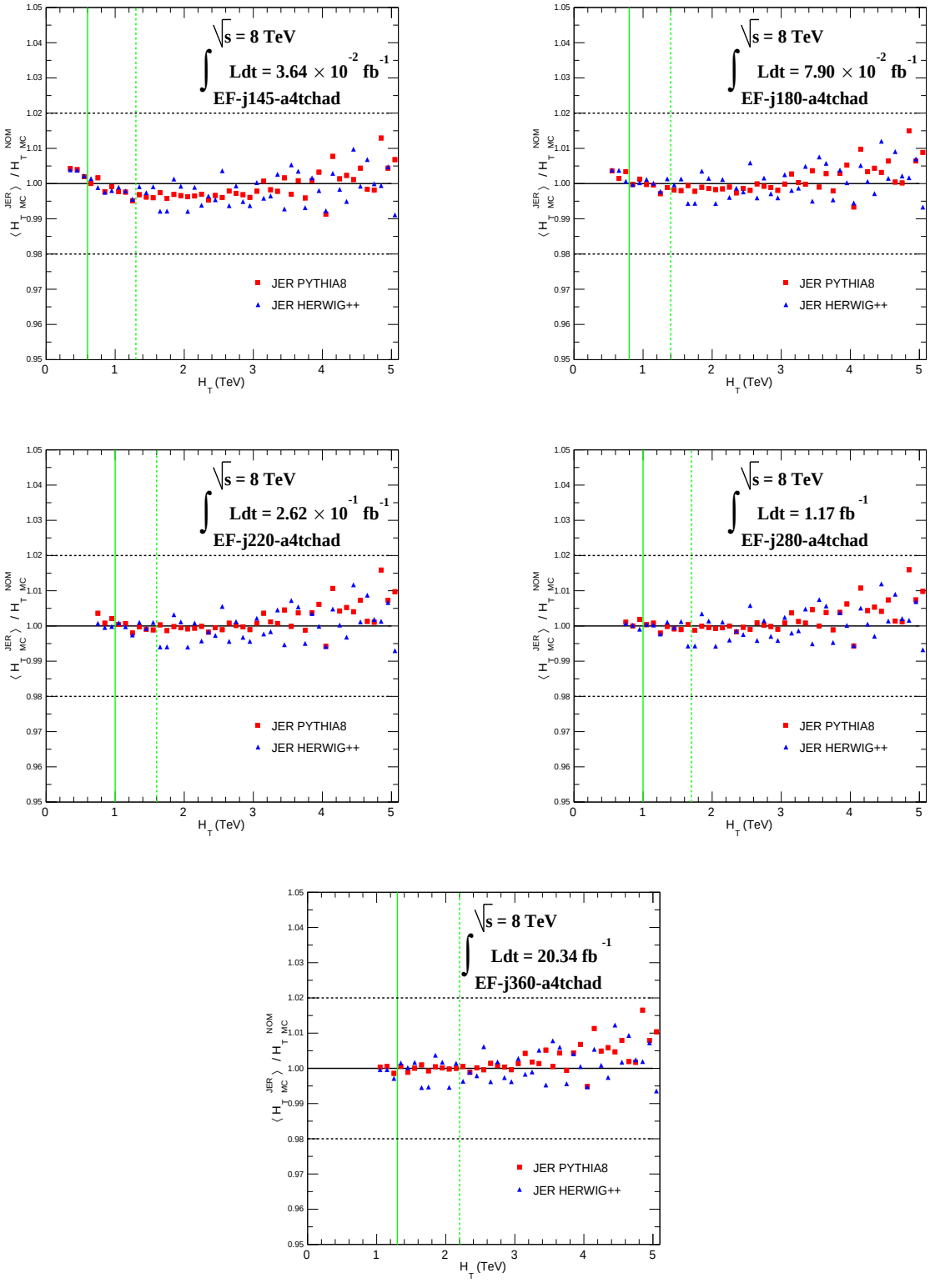

Figure A.5: Simple average of 500 H_T distributions is plotted relative to the nominal H_T distributions for for 500 JER samples for PYTHIA8 and HERWIG++ in red and blue colours respectively, for each trigger. Dotted black lines mark $\pm 2\%$ difference from nominal H_T distributions.

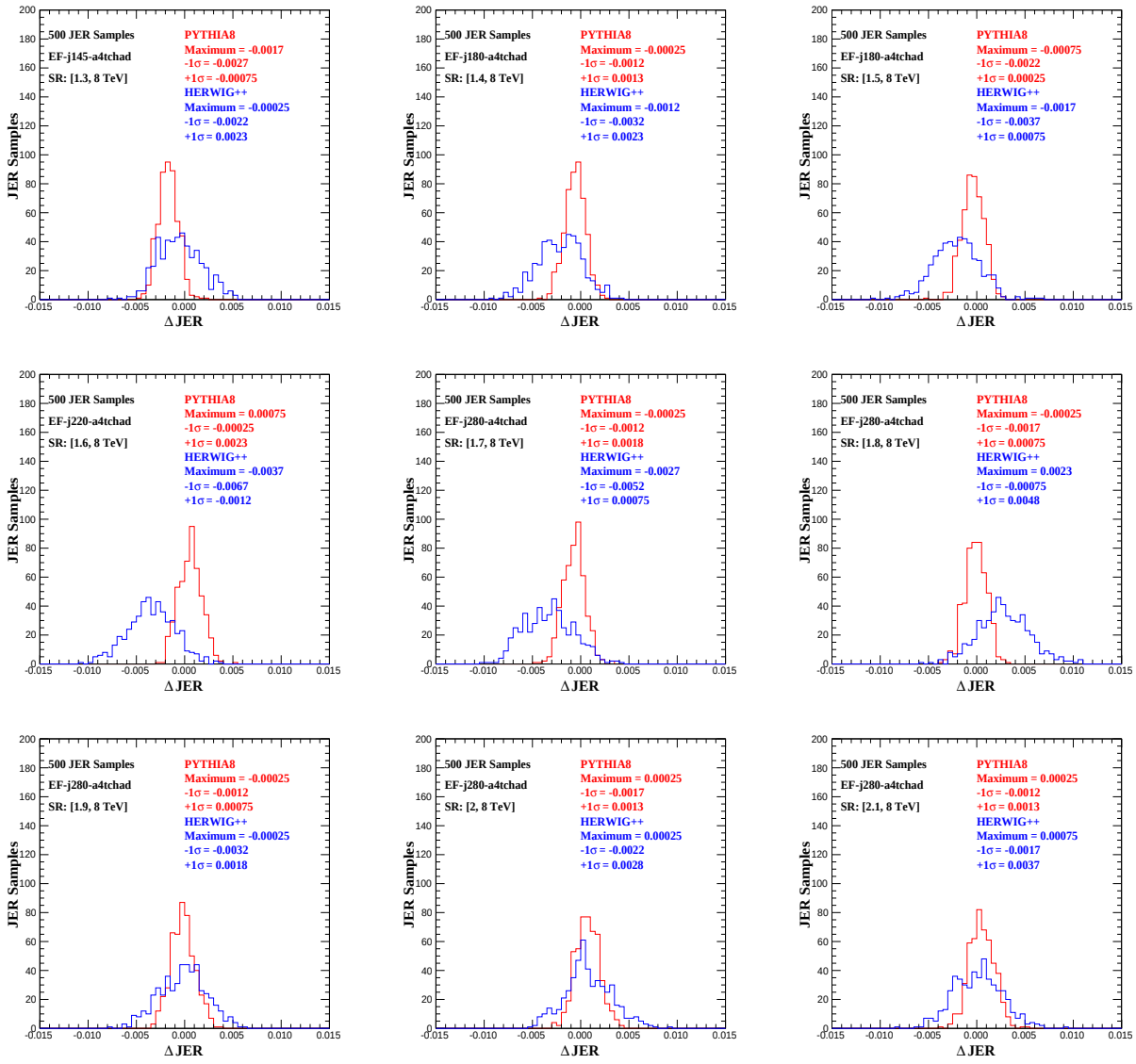

Figure A.6: ΔJER_i is the relative change in SR predictions for MC JER samples with respect to normalized nominal MC events for each SR. The distributions in red and blue represent PYTHIA8 and HERWIG++, respectively for EF-j145-a4tchad, EF-j180-a4tchad, EF-j220-a4tchad and EF-j280-a4tchad. The maximum for each distribution along with $\pm 1\sigma$ are also mentioned in individual plots.

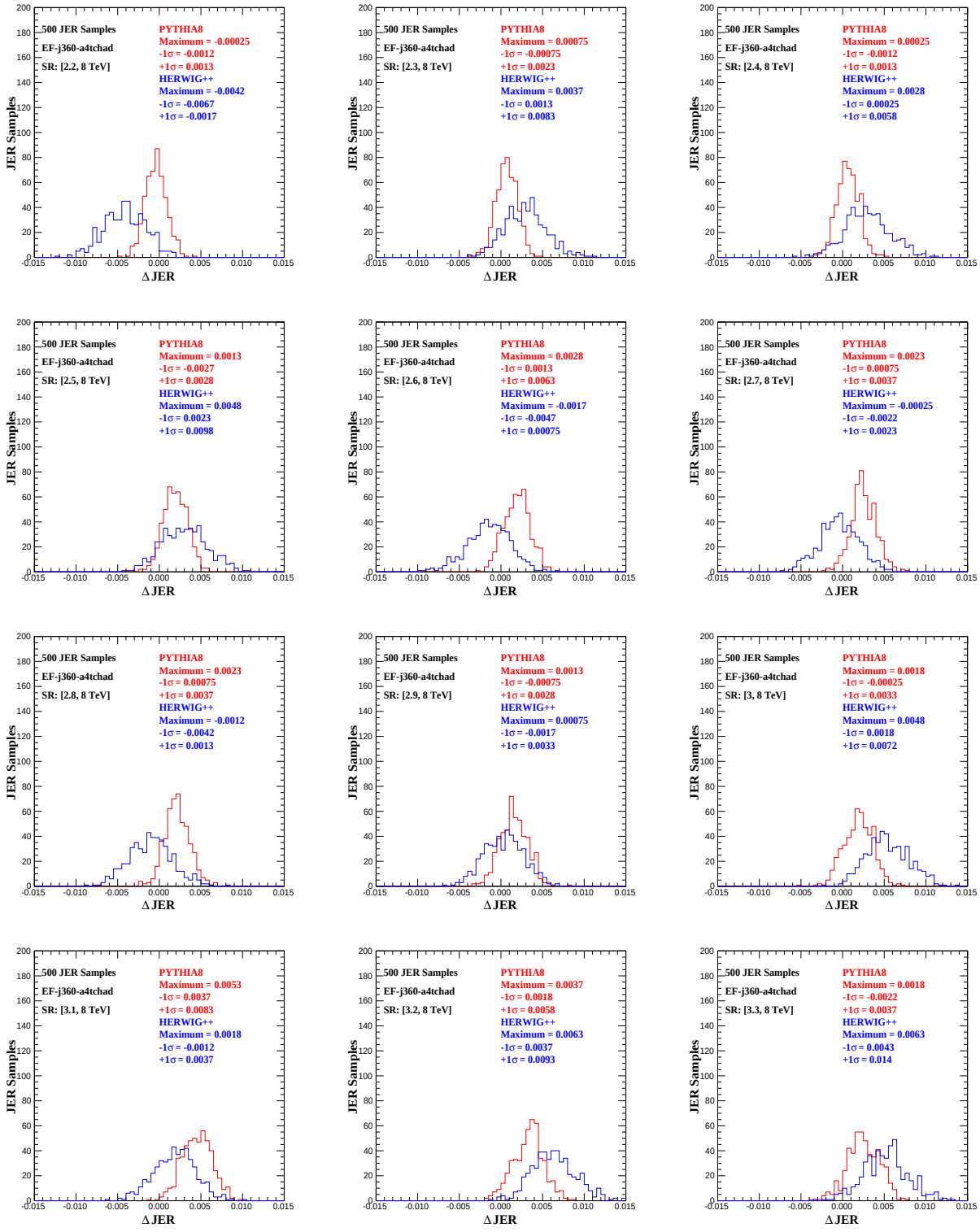

Figure A.7: ΔJER_i is the relative change in SR predictions for MC JER samples with respect to normalized nominal MC events for each SR. The distributions in red and blue represent PYTHIA8 and HERWIG++, respectively for EF-j360-a4tchad for first 12 SRs. The maximum for each distribution along with $\pm 1\sigma$ are also mentioned in individual plots.

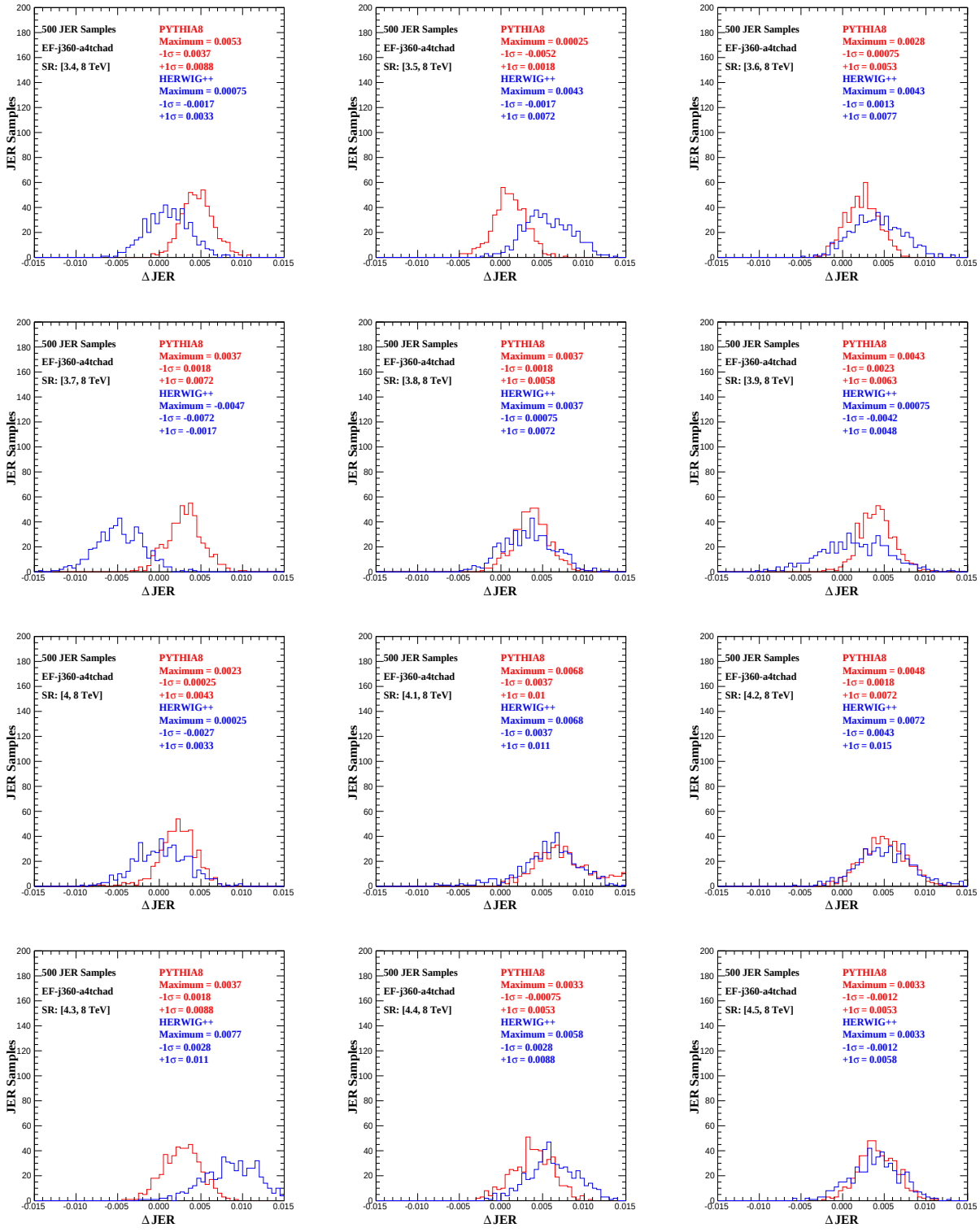

Figure A.8: ΔJER_i is the relative change in SR predictions for MC JER samples with respect to normalized nominal MC events for each SR. The distributions in red and blue represent PYTHIA8 and HERWIG++, respectively for EF-j360-a4tchad for last 12 SRs. The maximum for each distribution along with $\pm 1\sigma$ are also mentioned in individual plots.

Appendix B

CHARYBDIS2 Generator Parameters Listing for Non-Rotating and Rotating Black Holes

The lists of parameters used with the CHARYBDIS2 generator to produce non-rotating and rotating black holes are given here. The non-rotating and rotating black hole samples used in this thesis are known as BH1 and BH2 samples, respectively within the ATLAS community. The sample input given in Appendix B.1 corresponds to a non-rotating black hole sample with $n = 2$, $M_D = 1.5$ TeV and $M_{th} = 5.0$ TeV. The sample input given in Appendix B.2 corresponds to a rotating black hole sample with $n = 2$, $M_D = 1.5$ TeV and $M_{th} = 5.0$ TeV.

SAMPLE INPUT CONDITIONS FOR NON-ROTATING BLACK HOLES ALSO KNOWN AS BH1 SAMPLES WITHIN THE ATLAS COMMUNITY	
BEAM 1 ENERGY	4000.00
BEAM 2 ENERGY	4000.00
MINIMUN PARTONIC CM ENERGY	5000.00
MAXIMUM PARTONIC CM ENERGY	8000.00
PLANCK MASS	1500.00
STRING SCALE	1000.00
STRING COUPLING	0.30
MAXIMUM HAWKING TEMPERATURE	1000.00
MINIMUM REMNANT MASS	5000.00
DEFINITION OF PLANCK MASS	3
NUMBER OF TOTAL DIMENSIONS	6
RECOIL OPTION	2
STRING BALLS	F
YOSHINO-RYCHKOV C-S	F
TIME VARIATION	T
GREY BODY EFFECTS	T
KINEMATIC CUT	F
BOILING REMNANT MODEL	F
STABLE REMNANT MODEL	F
BH SPIN INCLUDED	F
TOTAL NLEPTON CONSERVATION	F
NELECTLEPTON CONSERVATION	F
NTAULEPTON CONSERVATION	F
NMULEPTON CONSERVATION	F
MASS AND ANGULAR MOMEMTUM LOST	F
MINIMUM MASS TO MBH THRESHOLD	T
CONST. V. BIAS	F
NBODY VARIABLE	T
NBODY PHASE	T
FMLOST	0.99
SKIP TO REMNANT	F
BRANE TENSION	0.1000E+04
ALL SM PARTICLES PRODUCED	T

Table B.1: List of CHARYBDIS2 generator parameters for the production of non-rotating black holes. These are also known as BH1 samples within the ATLAS community.

SAMPLE INPUT CONDITIONS FOR ROTATING BLACK HOLES ALSO KNOWN AS BH2 SAMPLES WITHIN THE ATLAS COMMUNITY	
BEAM 1 ENERGY	4000.00
BEAM 2 ENERGY	4000.00
MINIMUN PARTONIC CM ENERGY	5000.00
MAXIMUM PARTONIC CM ENERGY	8000.00
PLANCK MASS	1500.00
STRING SCALE	1000.00
STRING COUPLING	0.30
MAXIMUM HAWKING TEMPERATURE	1000.00
MINIMUM REMNANT MASS	5000.00
DEFINITION OF PLANCK MASS	3
NUMBER OF TOTAL DIMENSIONS	6
RECOIL OPTION	2
STRING BALLS	F
YOSHINO-RYCHKOV C-S	F
TIME VARIATION	T
GREY BODY EFFECTS	T
KINEMATIC CUT	F
BOILING REMNANT MODEL	F
STABLE REMNANT MODEL	F
BH SPIN INCLUDED	T
TOTAL NLEPTON CONSERVATION	F
NELECTLEPTON CONSERVATION	F
NTAULEPTON CONSERVATION	F
NMULEPTON CONSERVATION	F
MASS AND ANGULAR MOMEMTUM LOST	F
MINIMUM MASS TO MBH THRESHOLD	T
CONST. V. BIAS	F
NBODY VARIABLE	T
NBODY PHASE	T
FMLOST	0.99
SKIP TO REMNANT	F
BRANE TENSION	0.1000E+04
RECOILING BH SPIN	T
ANISOTROPIC DECAY	T
ALL SM PARTICLES PRODUCED	T

Table B.2: List of CHARYBDIS2 generator parameters for the production of rotating black holes. These are also known as BH2 samples within the ATLAS community.

Appendix C

Plots for Non-Rotating Black Hole Samples

The M and H_T distributions for non-rotating black hole signal samples added on top of the SM background PYTHIA8 prediction for $n = \{2, 4, 6\}$ and $M_D = \{1.5, 2.0, 2.5, 3.0, 3.5, 4.0\}$ are shown in Figures C.1, C.2, C.3, C.4, C.5 and C.6, respectively, for different values of M_D. The reconstruction efficiencies per 0.1 TeV bin for M and H_T distributions for all 52 AltFast-II signal samples in corresponding fully efficient regions of EF-j360-a4tchad trigger are shown in Figures C.7, C.8, C.9, C.10, C.11 and C.12. Figures C.13, C.15 and C.15 show separate plots of the upper limit on observed and expected production cross sections for each set of (n, M_D)−values.

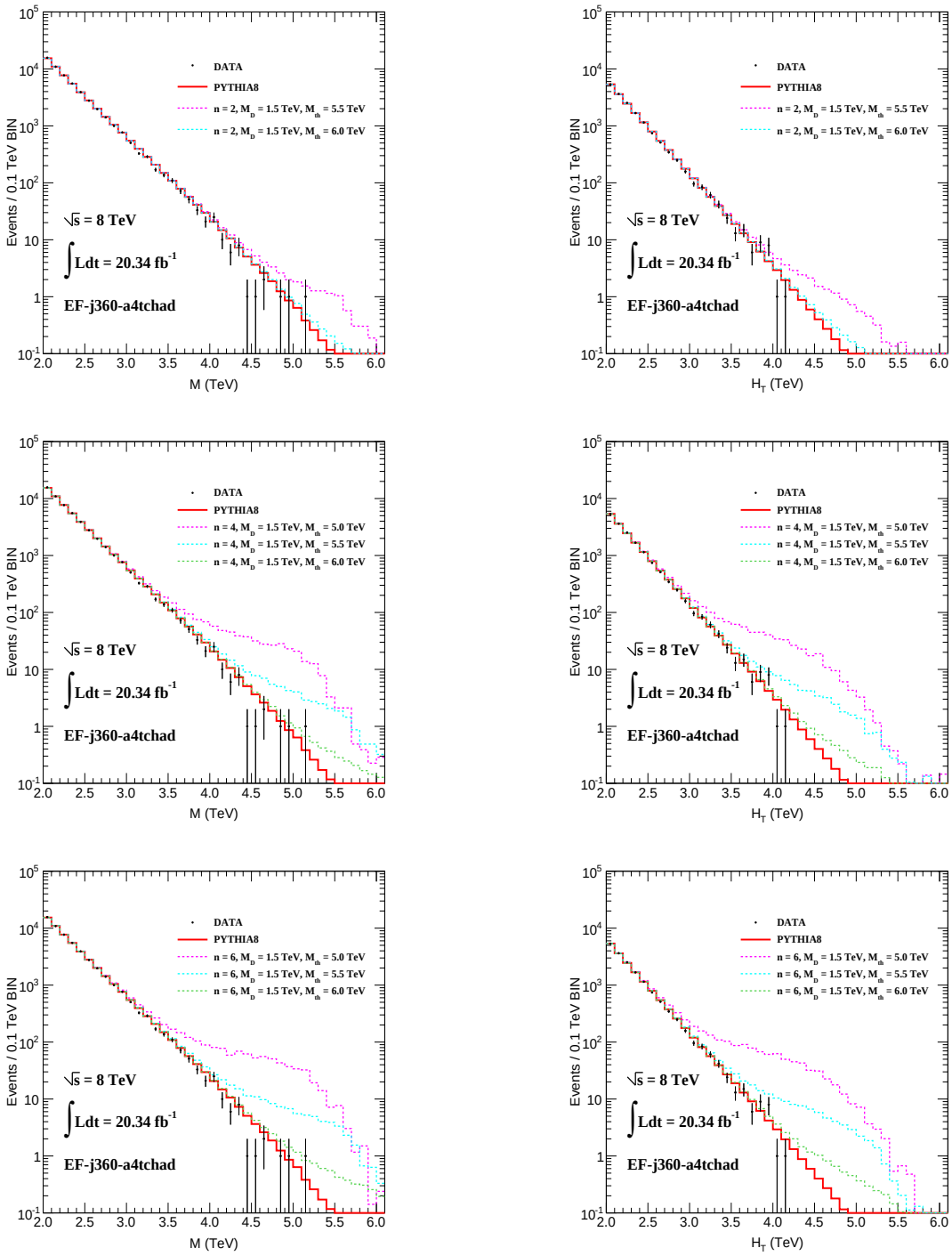

Figure C.1: M and H_T distributions for CHARYBDIS2 non-rotating black hole samples with no graviton emission are shown for extra dimensions $n = \{2, 4, 6\}$, fundamental Planck scale $M_D = 1.5$ TeV and different values of production mass threshold M_{th}. ATLAS data and PYTHIA8 M and H_T distributions are also shown.

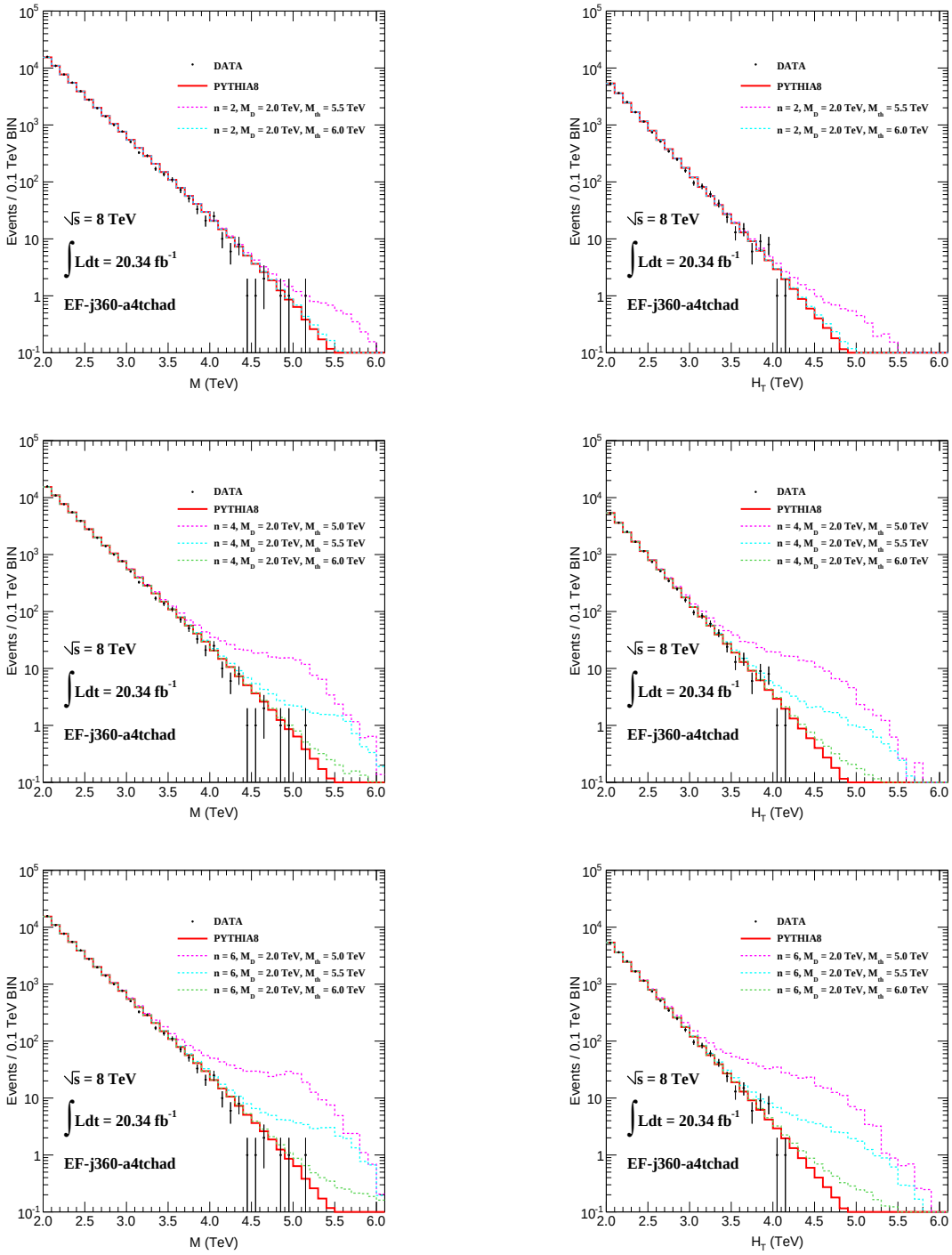

Figure C.2: M and H_T distributions for CHARYBDIS2 non-rotating black hole samples with no graviton emission are shown for extra dimensions $n = \{2, 4, 6\}$, fundamental Planck scale $M_D = 2.0$ TeV and different values of production mass threshold M_{th}. ATLAS data and PYTHIA8 M and H_T distributions are also shown.

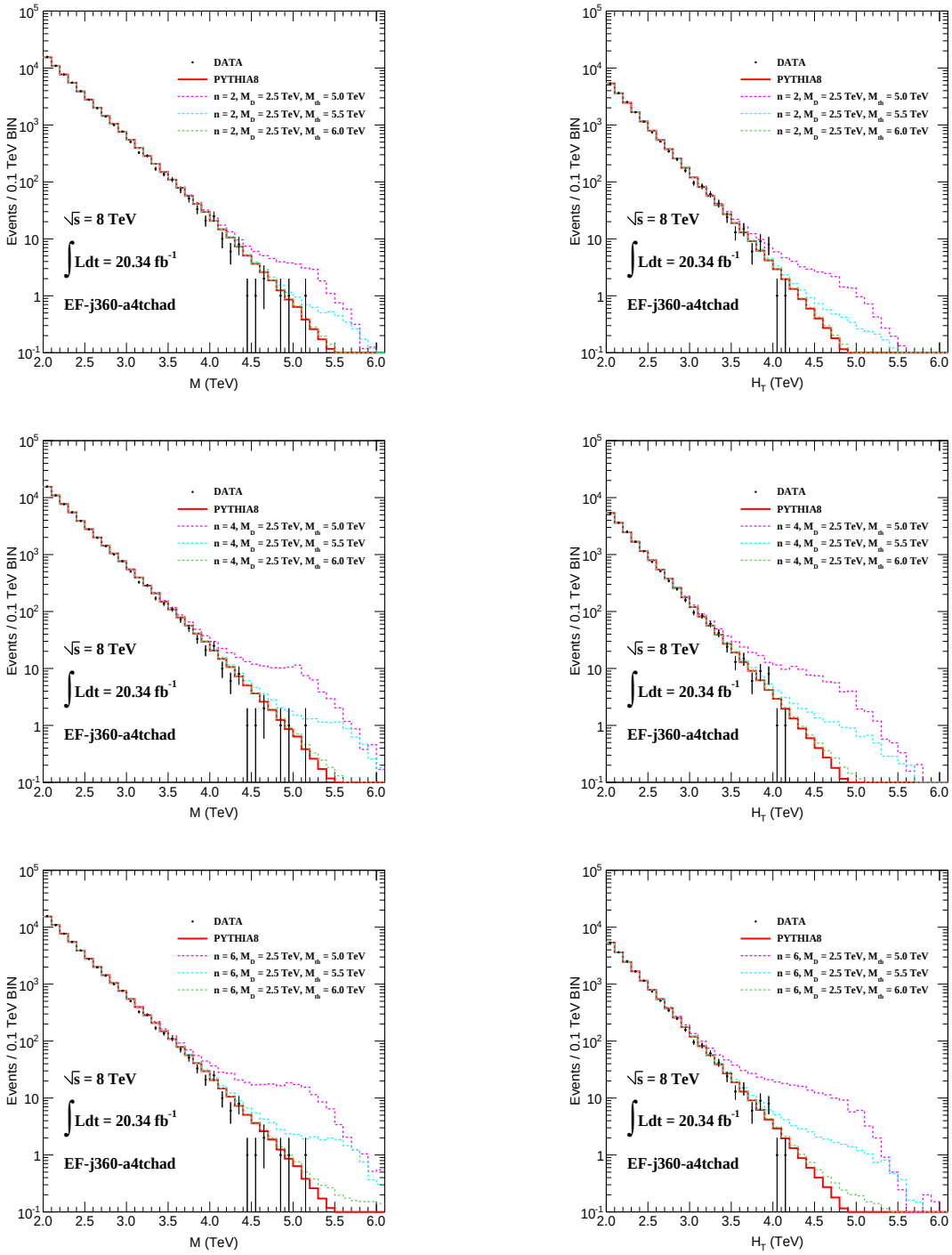

Figure C.3: M and H_T distributions for CHARYBDIS2 non-rotating black hole samples with no graviton emission are shown for extra dimensions $n = \{2, 4, 6\}$, fundamental Planck scale $M_D = 2.5$ TeV and different values of production mass threshold M_{th}. ATLAS data and PYTHIA8 M and H_T distributions are also shown.

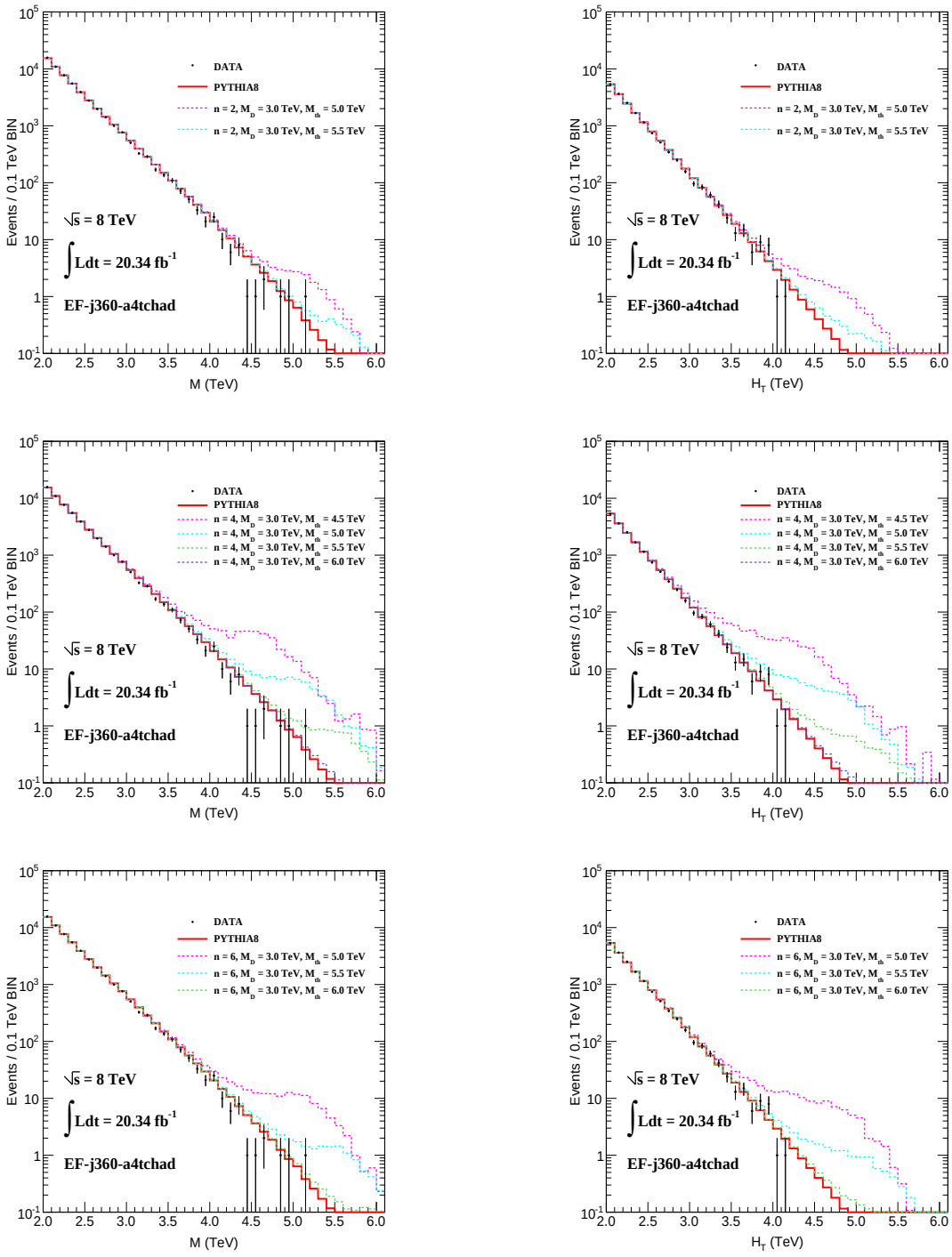

Figure C.4: M and H_T distributions for CHARYBDIS2 non-rotating black hole samples with no graviton emission are shown for extra dimensions $n = \{2, 4, 6\}$, fundamental Planck scale $M_D = 3.0$ TeV and different values of production mass threshold M_{th}. ATLAS data and PYTHIA8 M and H_T distributions are also shown.

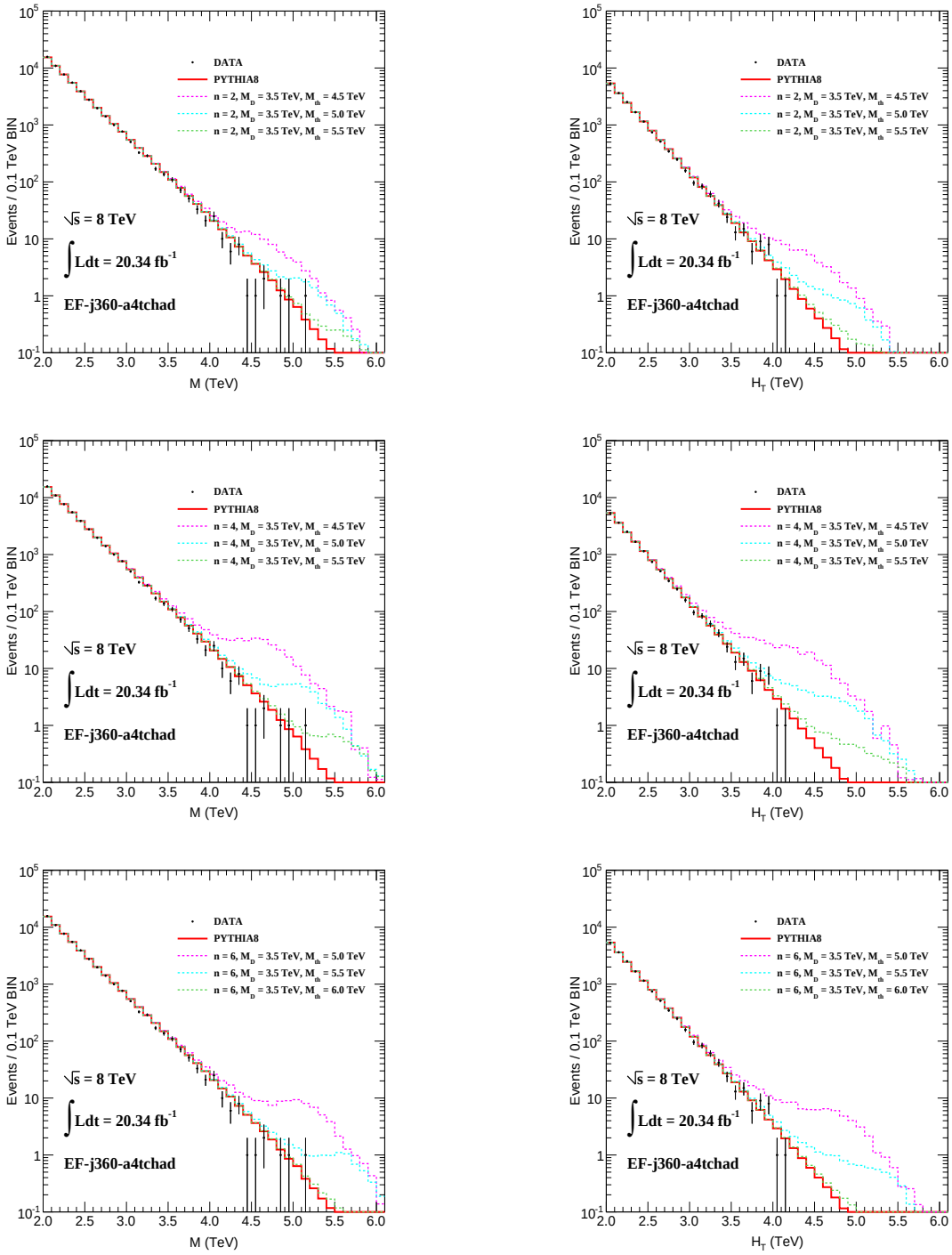

Figure C.5: M and H_T distributions for CHARYBDIS2 non-rotating black hole samples with no graviton emission are shown for extra dimensions $n = \{2, 4, 6\}$, fundamental Planck scale $M_D = 3.5$ TeV and different values of production mass threshold M_{th}. ATLAS data and PYTHIA8 M and H_T distributions are also shown.

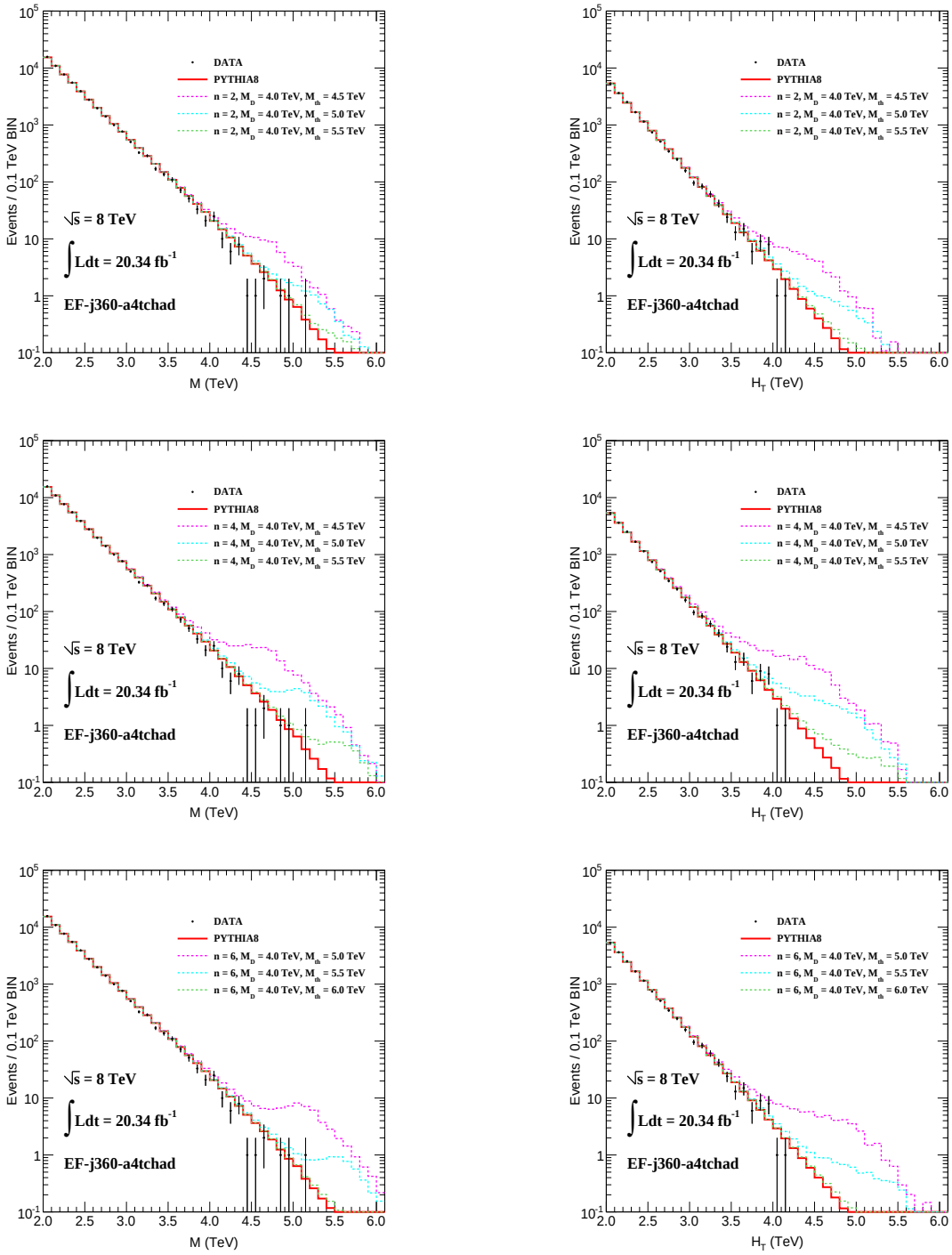

Figure C.6: M and H_T distributions for CHARYBDIS2 non-rotating black hole samples with no graviton emission are shown for extra dimensions $n = \{2, 4, 6\}$, fundamental Planck scale $M_D = 4.0$ TeV and different values of production mass threshold M_{th}. ATLAS data and PYTHIA8 M and H_T distributions are also shown.

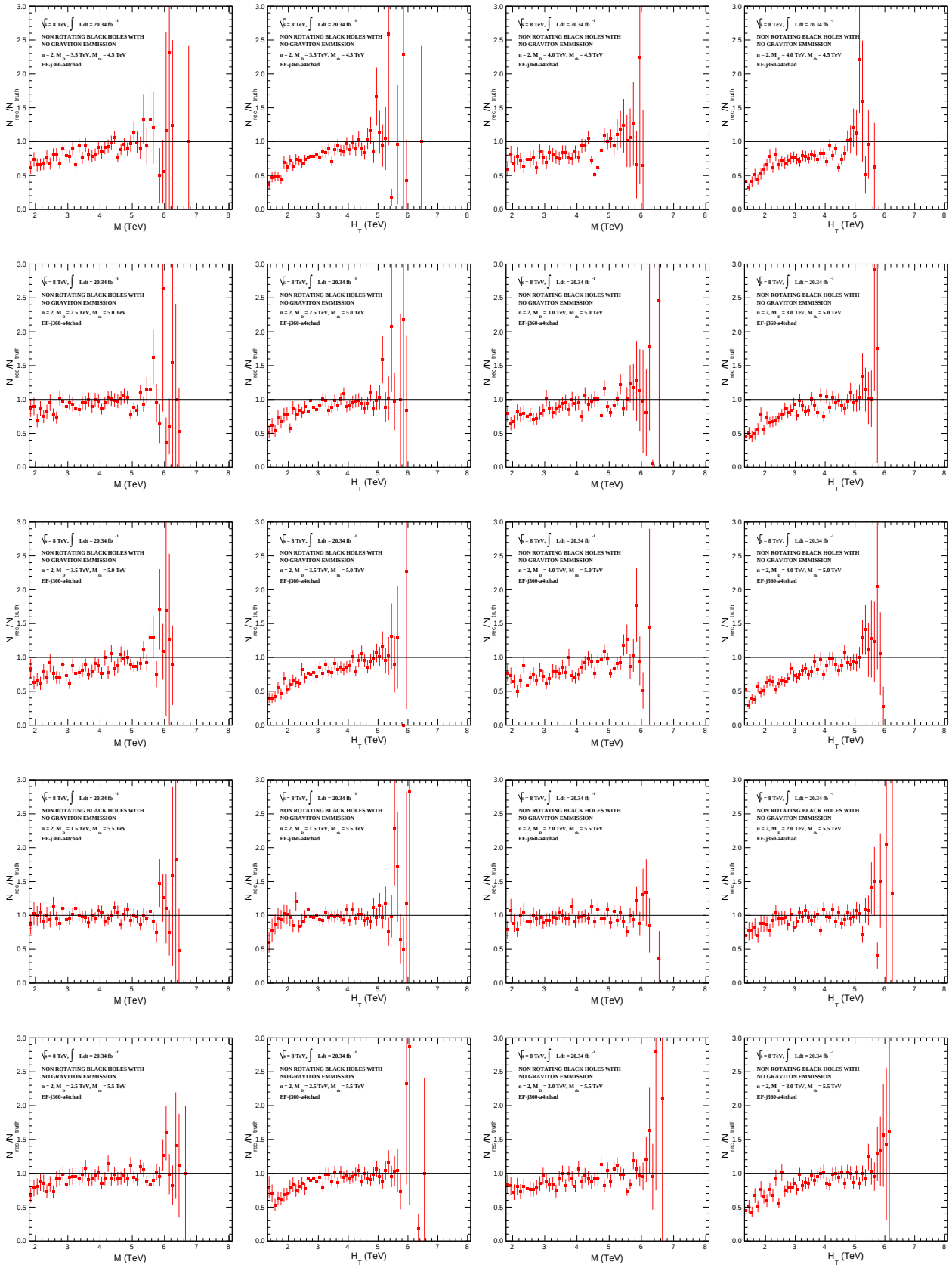

Figure C.7: Reconstruction efficiencies per 0.1 TeV bin for M and H_T distributions for non-rotating black hole samples.

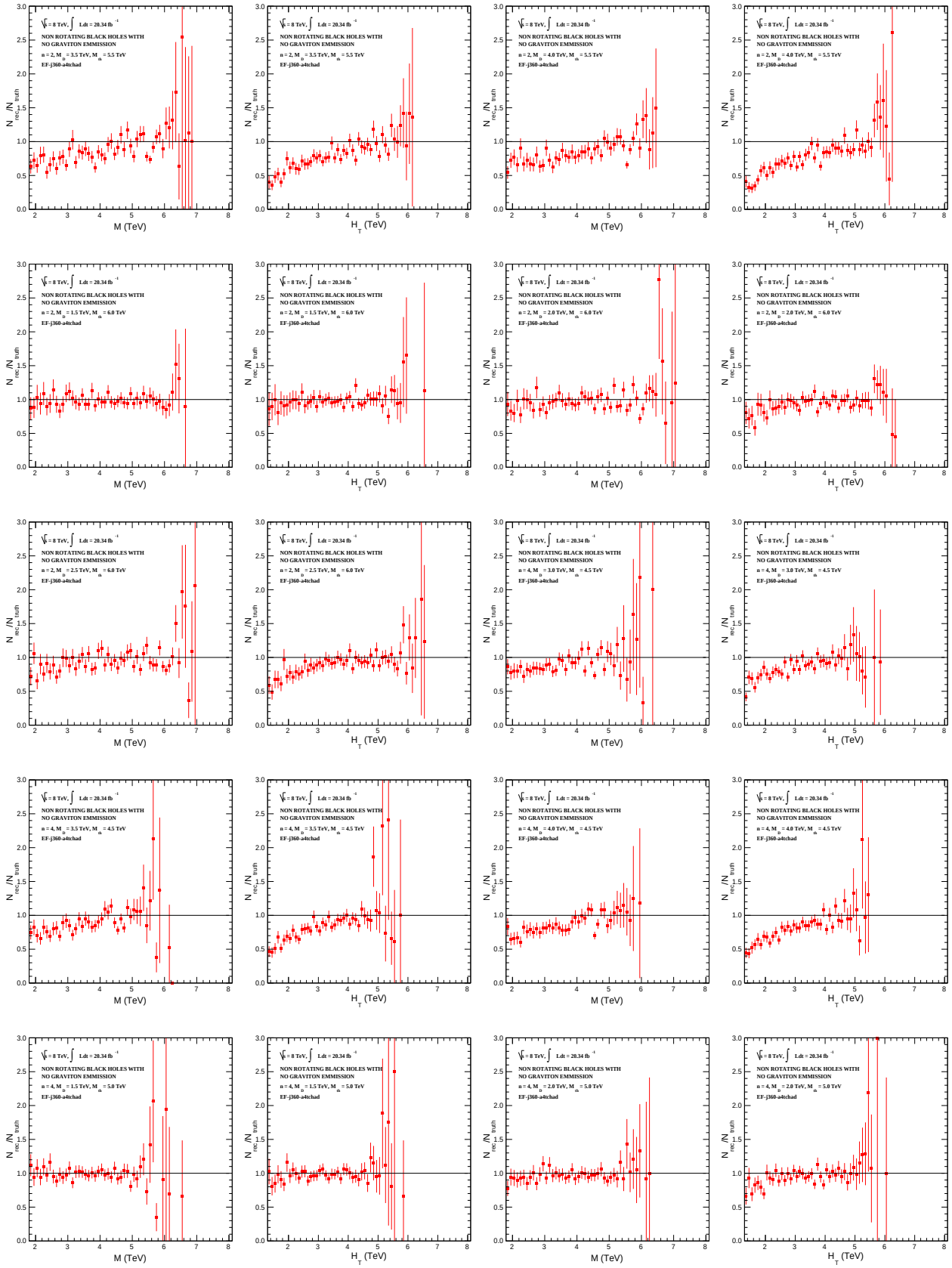

Figure C.8: Reconstruction efficiencies per 0.1 TeV bin for M and H_T distributions for non-rotating black hole samples.

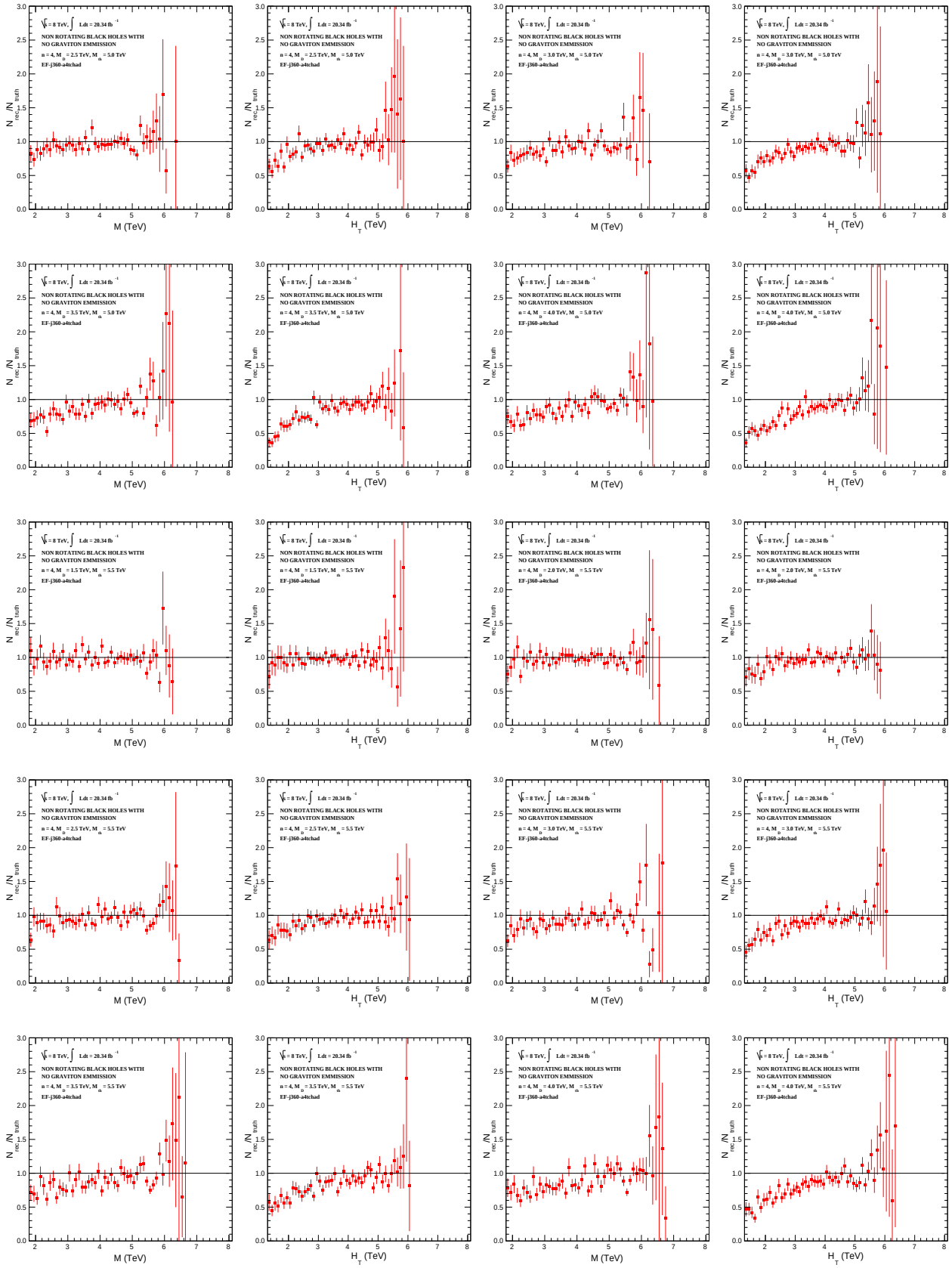

Figure C.9: Reconstruction efficiencies per 0.1 TeV bin for M and H_T distributions for non-rotating black hole samples.

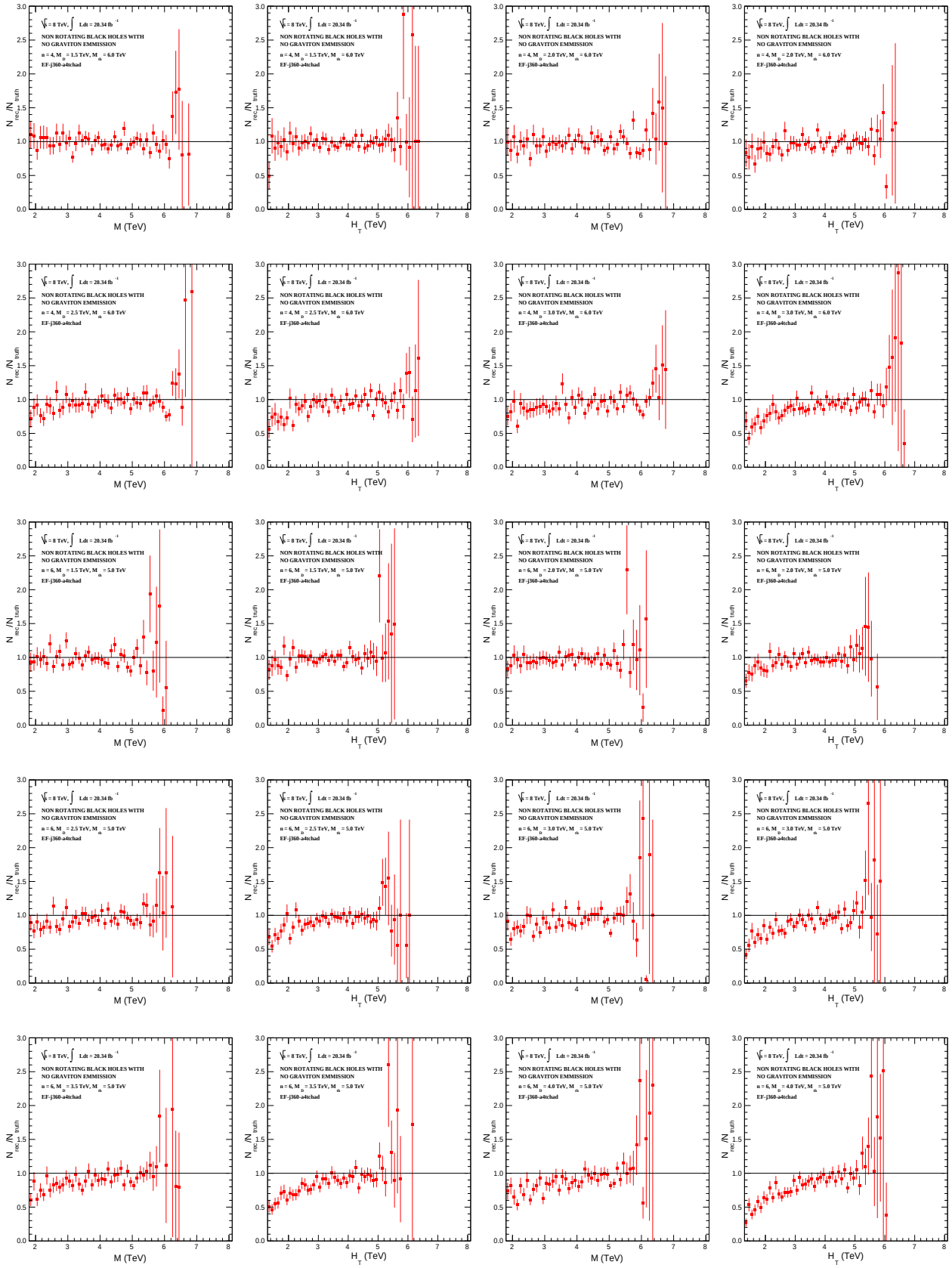

Figure C.10: Reconstruction efficiencies per 0.1 TeV bin for M and H_T distributions for non-rotating black hole samples.

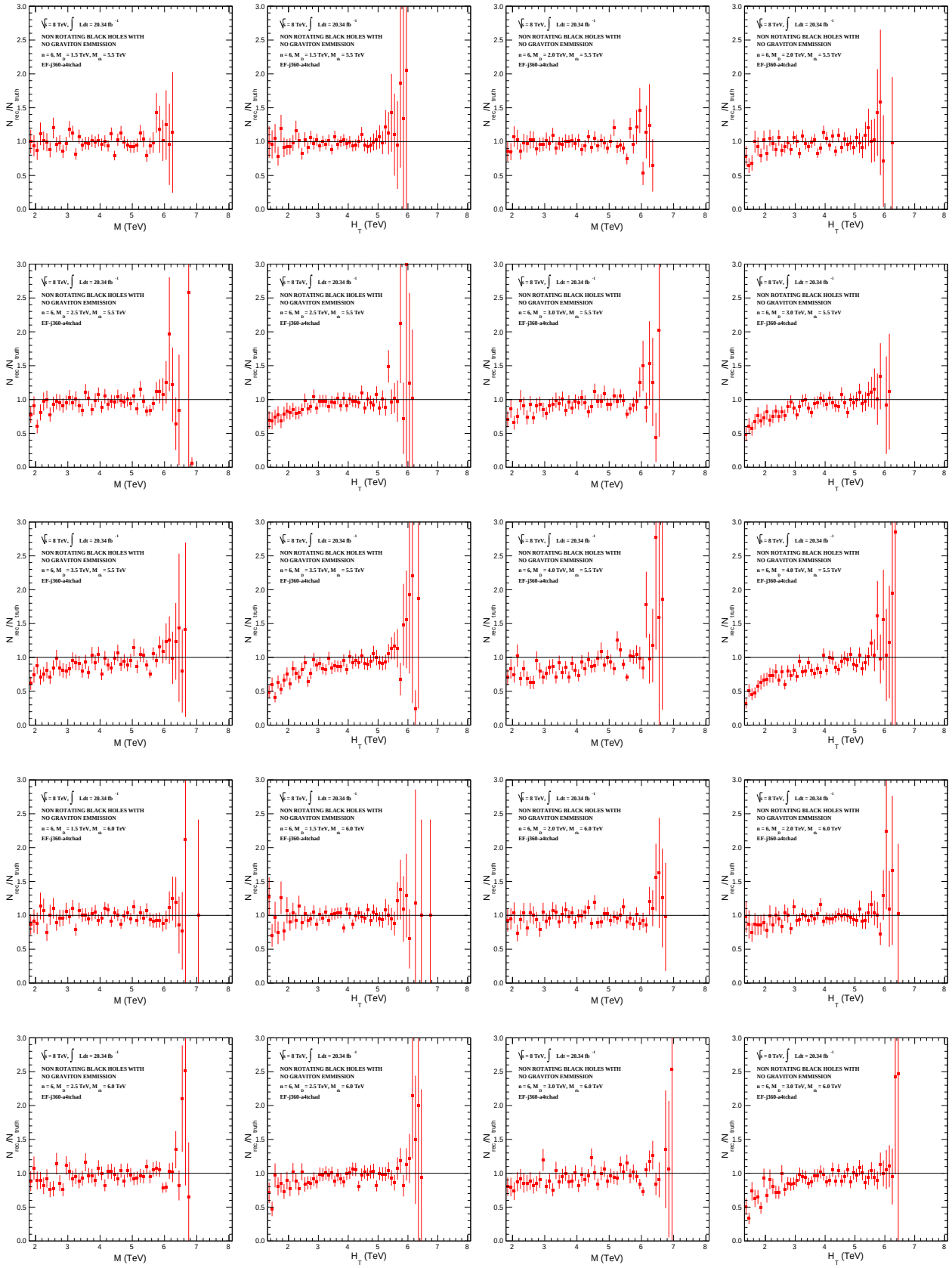

Figure C.11: Reconstruction efficiencies per 0.1 TeV bin for M and H_T distributions for non-rotating black hole samples.

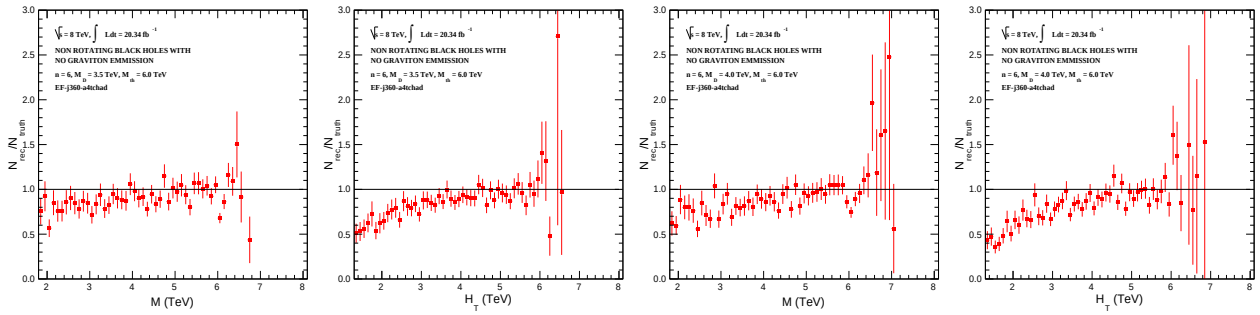

Figure C.12: Reconstruction efficiencies per 0.1 TeV bin for M and H_T distributions for non-rotating black hole samples.

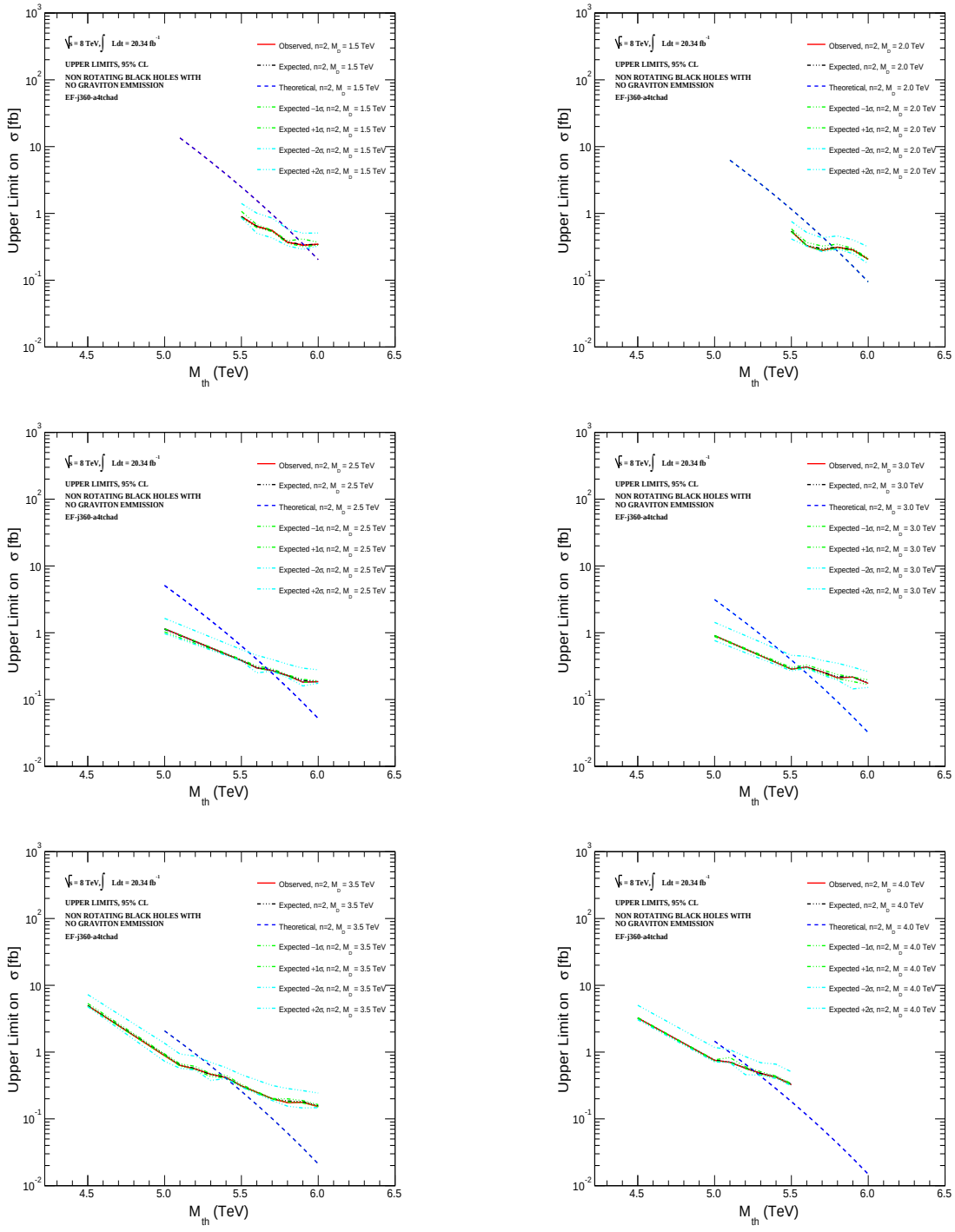

Figure C.13: Upper limits on the observed and expected production cross sections (σ) at the 95% confidence level (CL) (solid line and dotted-broken line, respectively) for two extra dimensions and fundamental Planck scale M_D={1.5,2.0,2.5,3.0,3.5,4.0} are compared with theoretical production cross sections from CHARYBDIS2 black hole generator (broken line), as a function of threshold mass M_{th} for non-rotating black hole with no graviton emission. The $\pm1\sigma$ and $\pm2\sigma$ curves represent 68% and 95% confidence intervals on either sides of the expected limit.

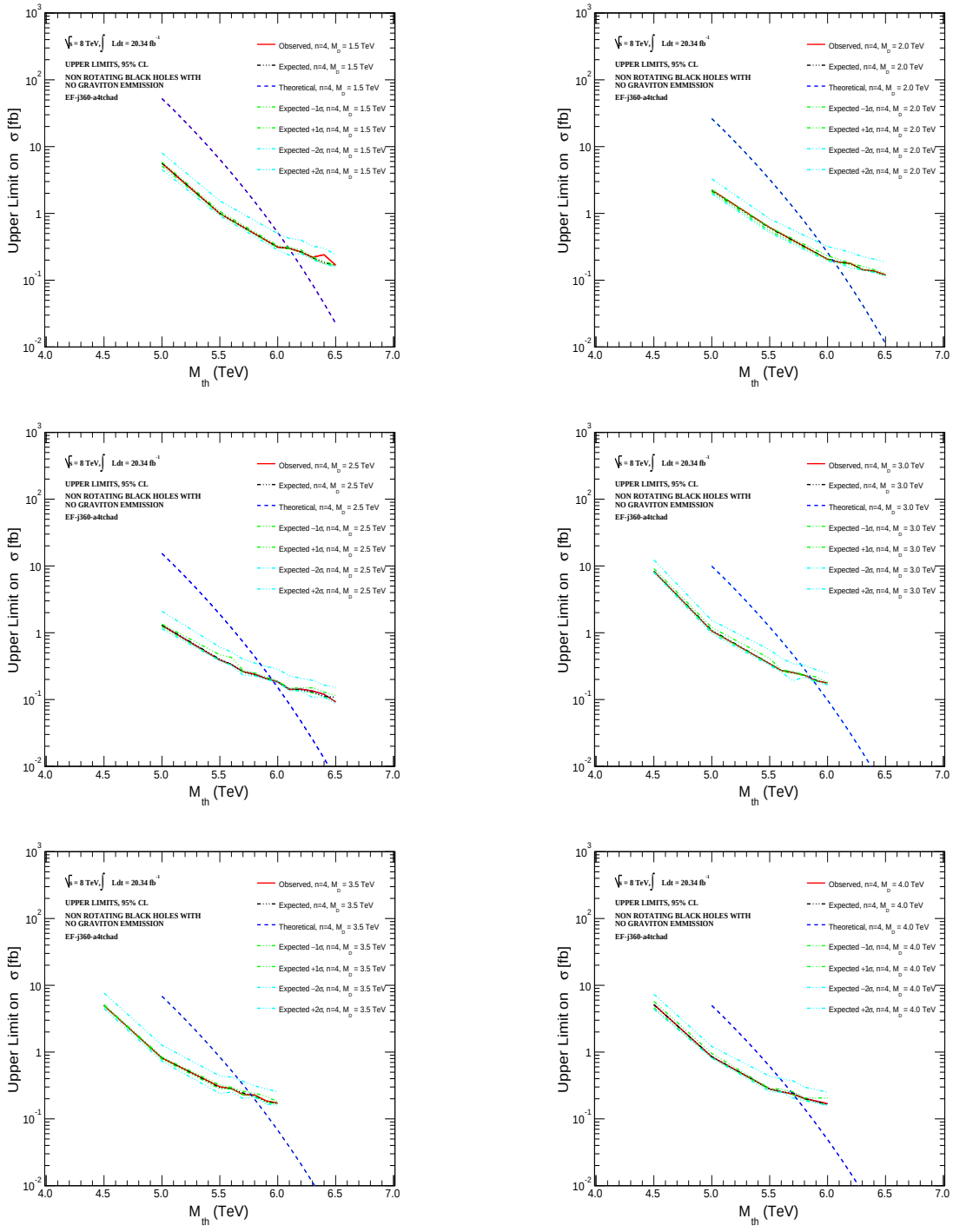

Figure C.14: Upper limits on the observed and expected production cross sections (σ) at the 95% confidence level (CL) (solid line and dotted-broken line, respectively) for four extra dimensions and fundamental Planck scale M_D={1.5,2.0,2.5,3.0,3.5,4.0} are compared with theoretical production cross sections from CHARYBDIS2 black hole generator (broken line), as a function of threshold mass M_{th} for non-rotating black hole with no graviton emission. The $\pm1\sigma$ and $\pm2\sigma$ curves represent 68% and 95% confidence intervals on either sides of the expected limit.

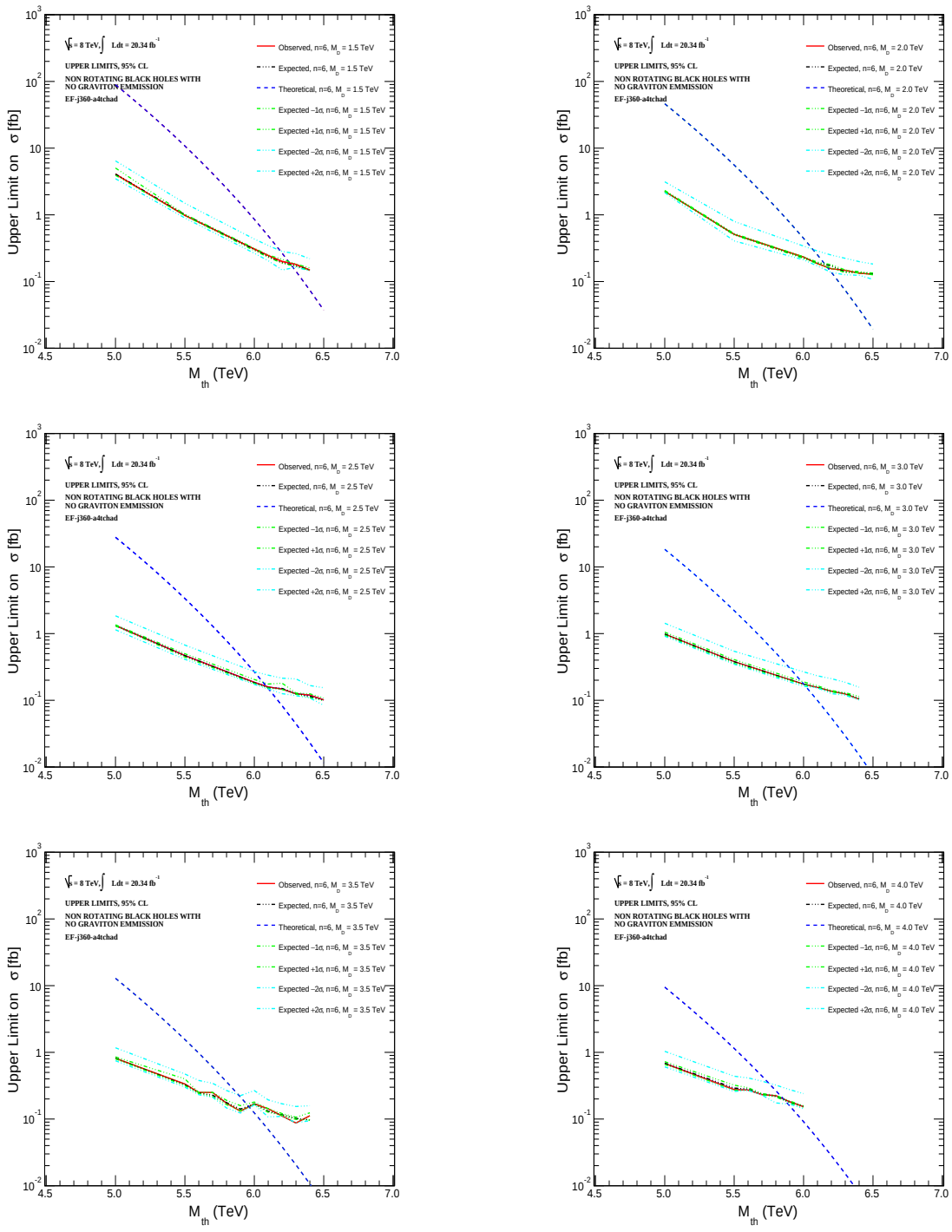

Figure C.15: Upper limits on the observed and expected production cross sections (σ) at the 95% confidence level (CL) (solid line and dotted-broken line, respectively) for six extra dimensions and fundamental Planck scale M_D={1.5,2.0,2.5,3.0,3.5,4.0} are compared with theoretical production cross sections from CHARYBDIS2 black hole generator (broken line), as a function of threshold mass M_{th} for non-rotating black hole with no graviton emission. The $\pm1\sigma$ and $\pm2\sigma$ curves represent 68% and 95% confidence intervals on either sides of the expected limit.

Appendix D

Plots for Rotating Black Hole Samples

The M and H_T distributions for rotating black hole signal samples added on top of the SM background PYTHIA8 prediction for $n = \{2, 4, 6\}$ and $M_D = \{1.5, 2.0, 2.5, 3.0, 3.5, 4.0\}$ are shown in Figures D.1, D.2, D.3, D.4, D.5 and D.6, respectively, for different values of M_D. The reconstruction efficiencies per 0.1 TeV bin for M and H_T distributions for all 49 AltFast-II signal samples in corresponding fully efficient regions of EF-j360-a4tchad trigger are shown in Figures D.7, D.8, D.9, D.10 and D.11. Figures D.12, D.14 and D.14 show separate plots of the upper limit on observed and expected production cross sections for each set of (n, M_D)−values.

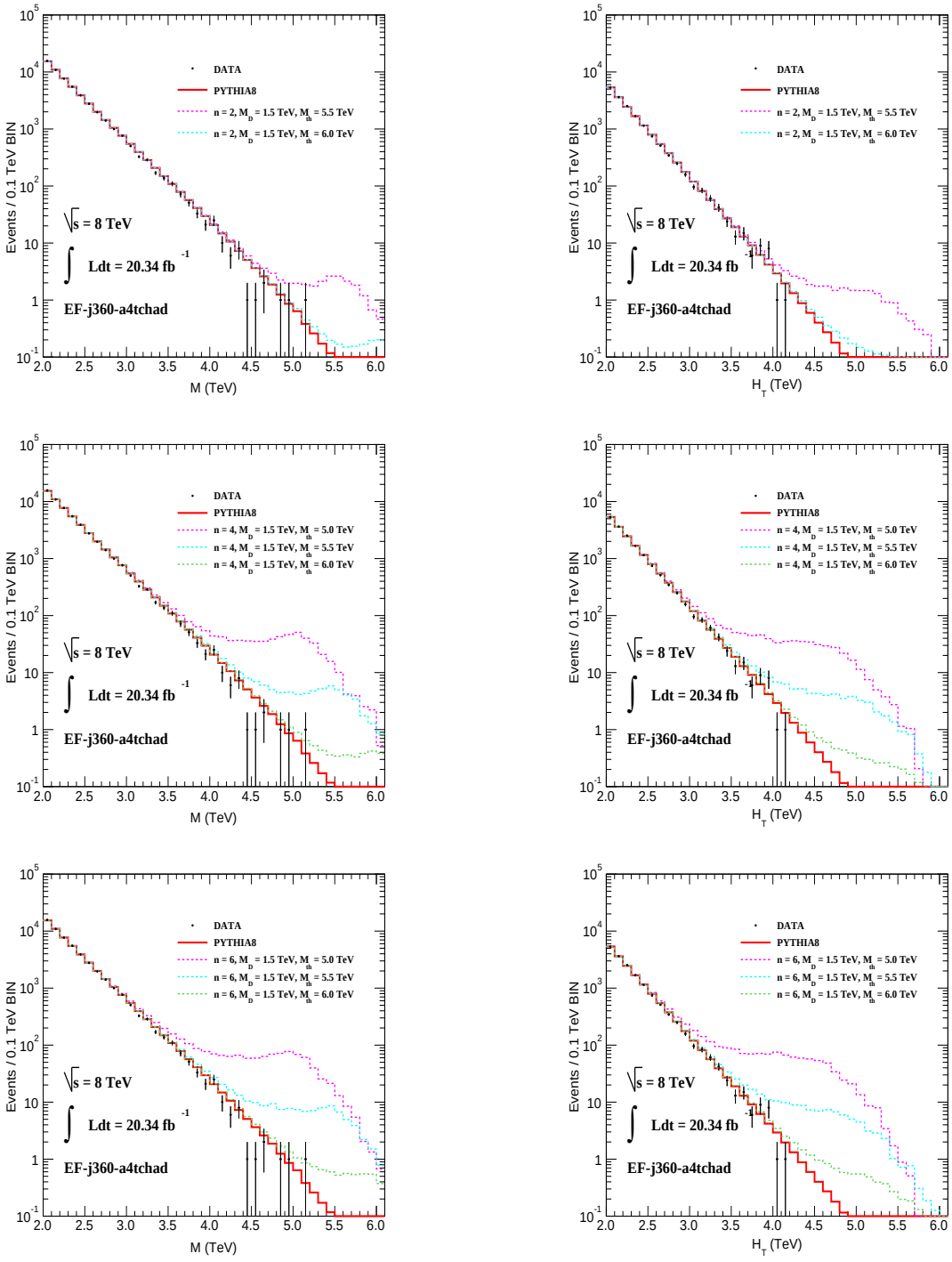

Figure D.1: M and H_T distributions for CHARYBDIS2 rotating black hole samples with no graviton emission are shown for extra dimensions $n = \{2, 4, 6\}$, fundamental Planck scale $M_D = 1.5$ TeV and different values of production mass threshold M_{th}. ATLAS data and PYTHIA8 M and H_T distributions are also shown.

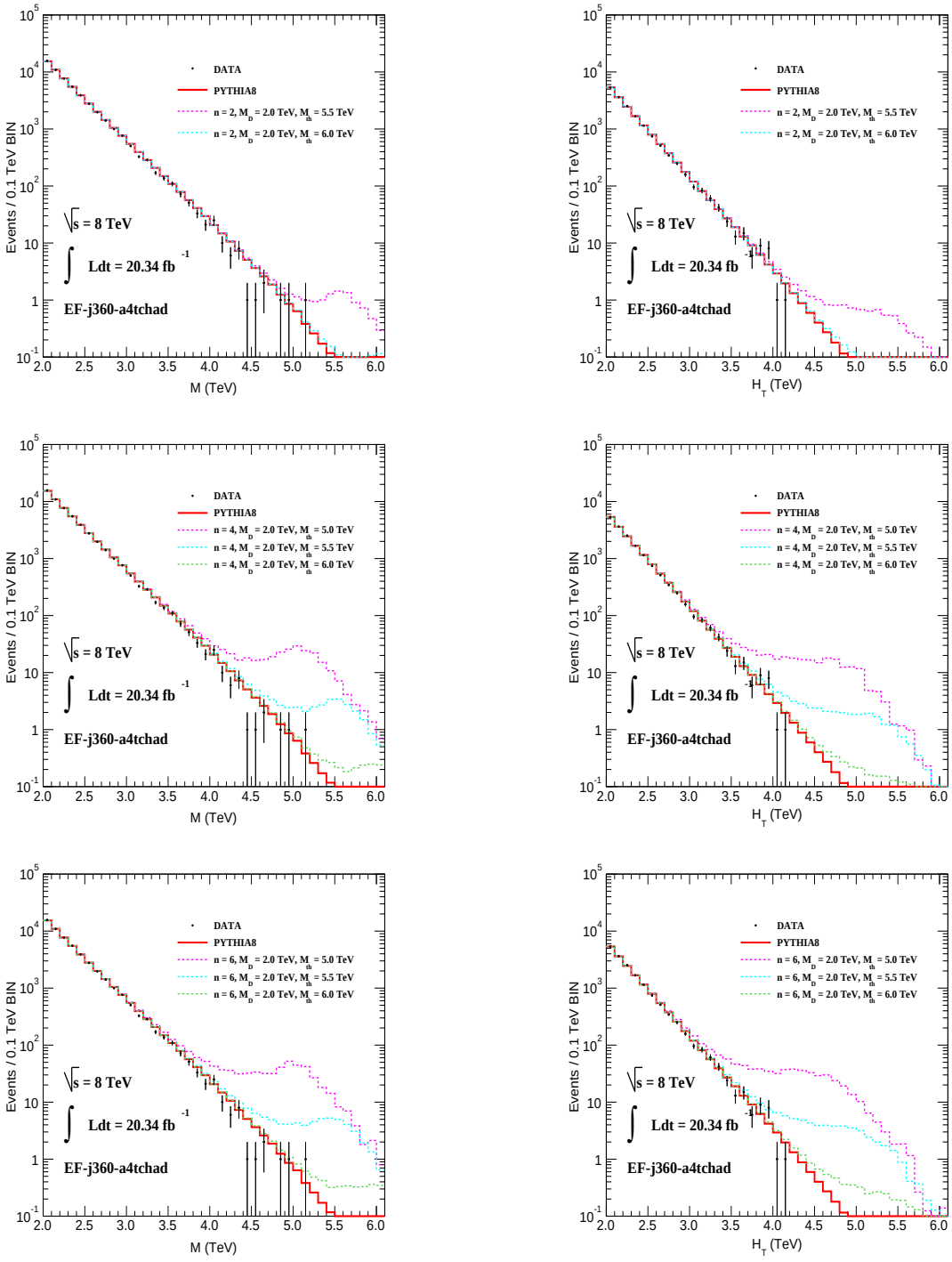

Figure D.2: M and H_T distributions for CHARYBDIS2 rotating black hole samples with no graviton emission are shown for extra dimensions $n = \{2, 4, 6\}$, fundamental Planck scale $M_D = 2.0$ TeV and different values of production mass threshold M_{th}. ATLAS data and PYTHIA8 M and H_T distributions are also shown.

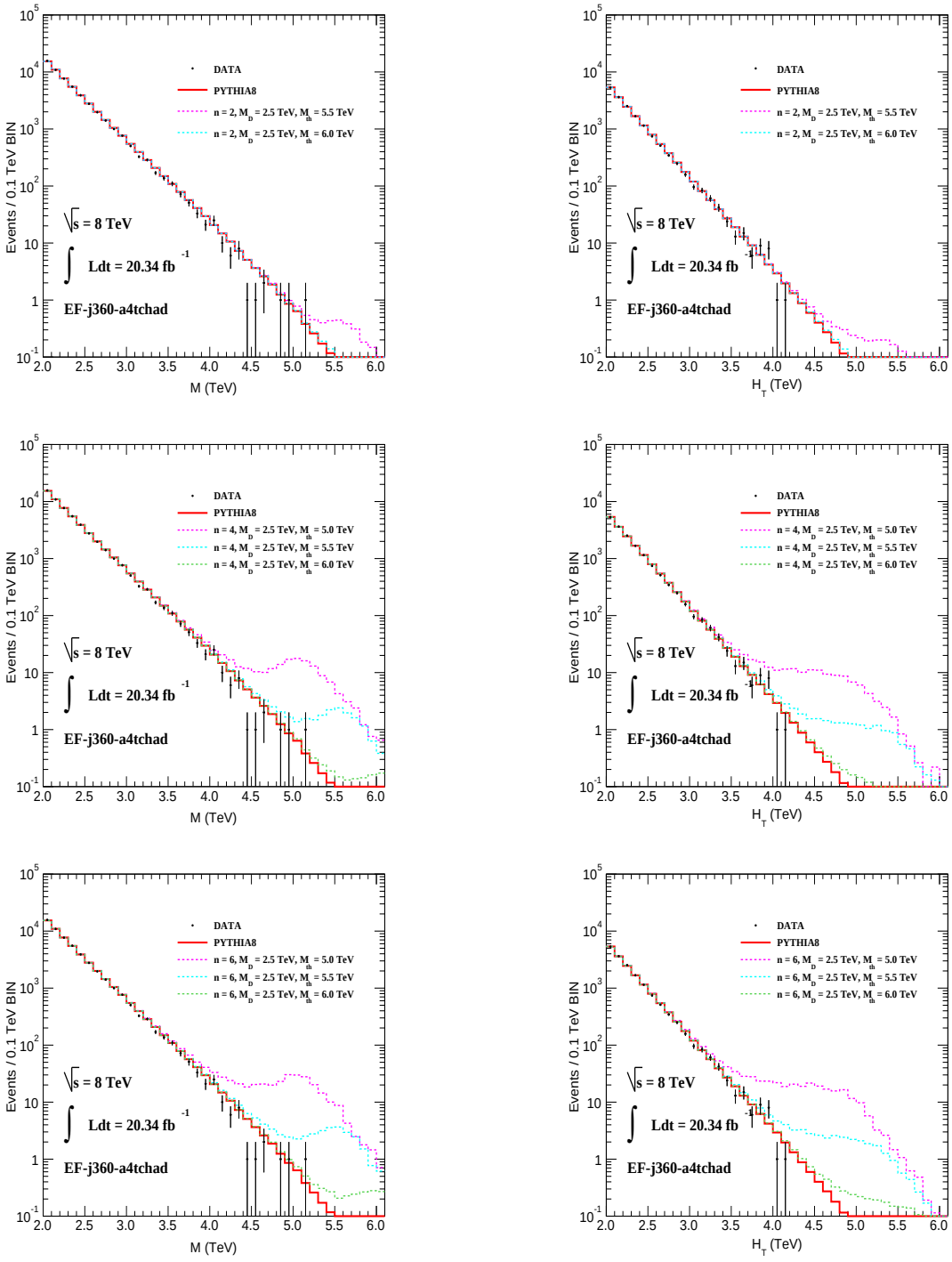

Figure D.3: M and H_T distributions for CHARYBDIS2 rotating black hole samples with no graviton emission are shown for extra dimensions $n = \{2, 4, 6\}$, fundamental Planck scale $M_D = 2.5$ TeV and different values of production mass threshold M_{th}. ATLAS data and PYTHIA8 M and H_T distributions are also shown.

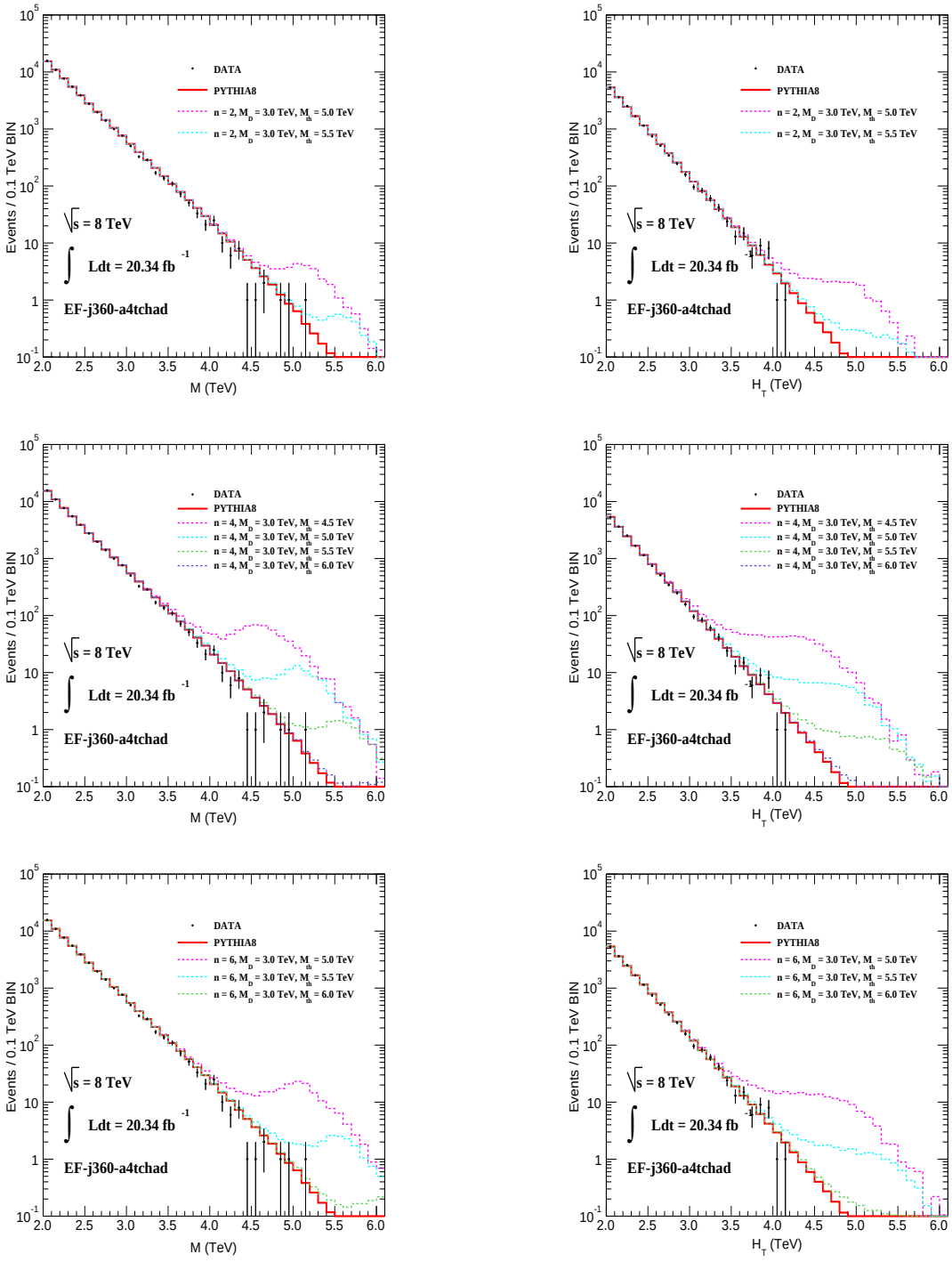

Figure D.4: M and H_T distributions for CHARYBDIS2 rotating black hole samples with no graviton emission are shown for extra dimensions $n = \{2, 4, 6\}$, fundamental Planck scale $M_D = 3.0$ TeV and different values of production mass threshold M_{th}. ATLAS data and PYTHIA8 M and H_T distributions are also shown.

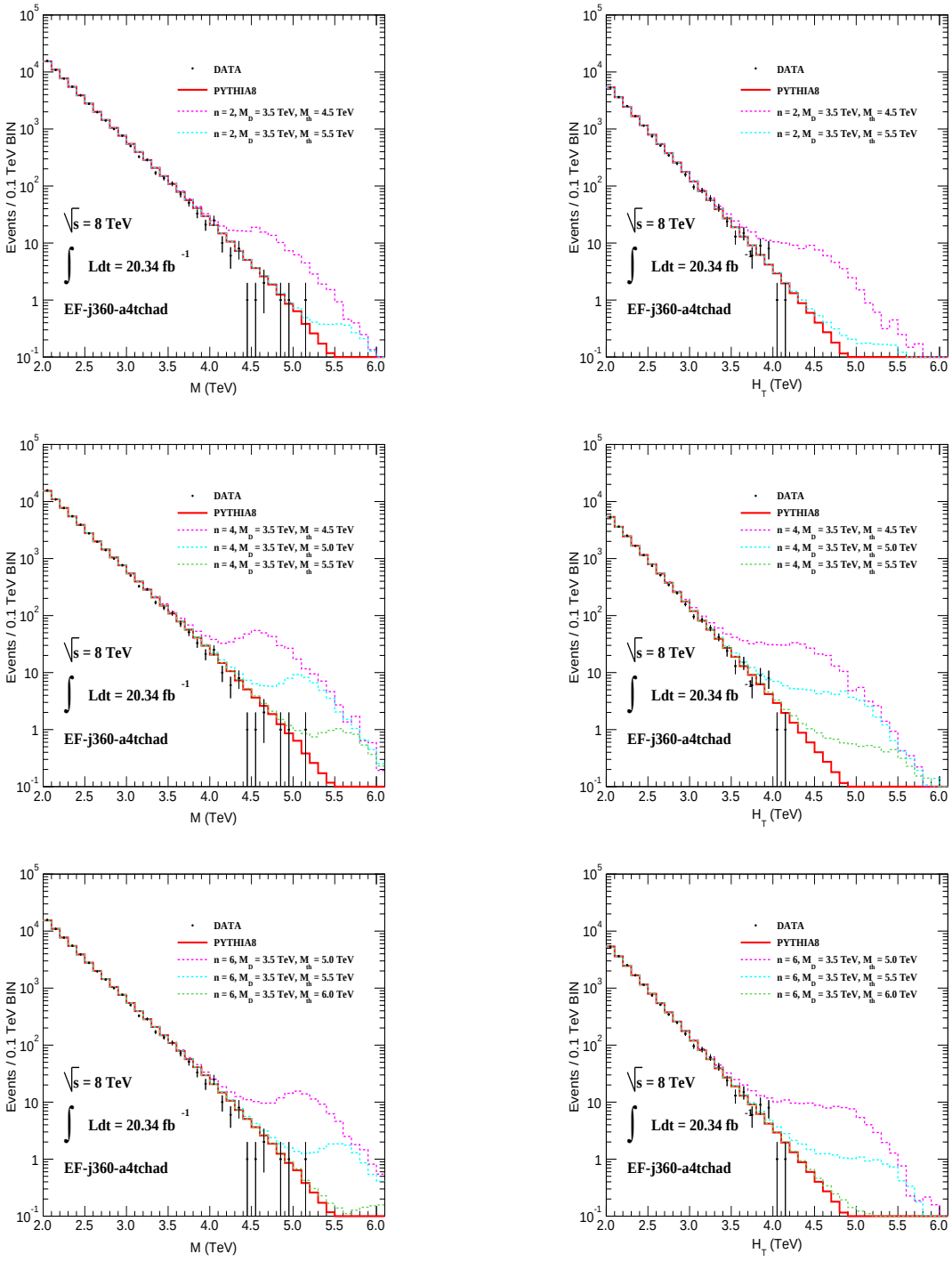

Figure D.5: M and H_T distributions for CHARYBDIS2 rotating black hole samples with no graviton emission are shown for extra dimensions $n = \{2, 4, 6\}$, fundamental Planck scale $M_D = 3.5$ TeV and different values of production mass threshold M_{th}. ATLAS data and PYTHIA8 M and H_T distributions are also shown.

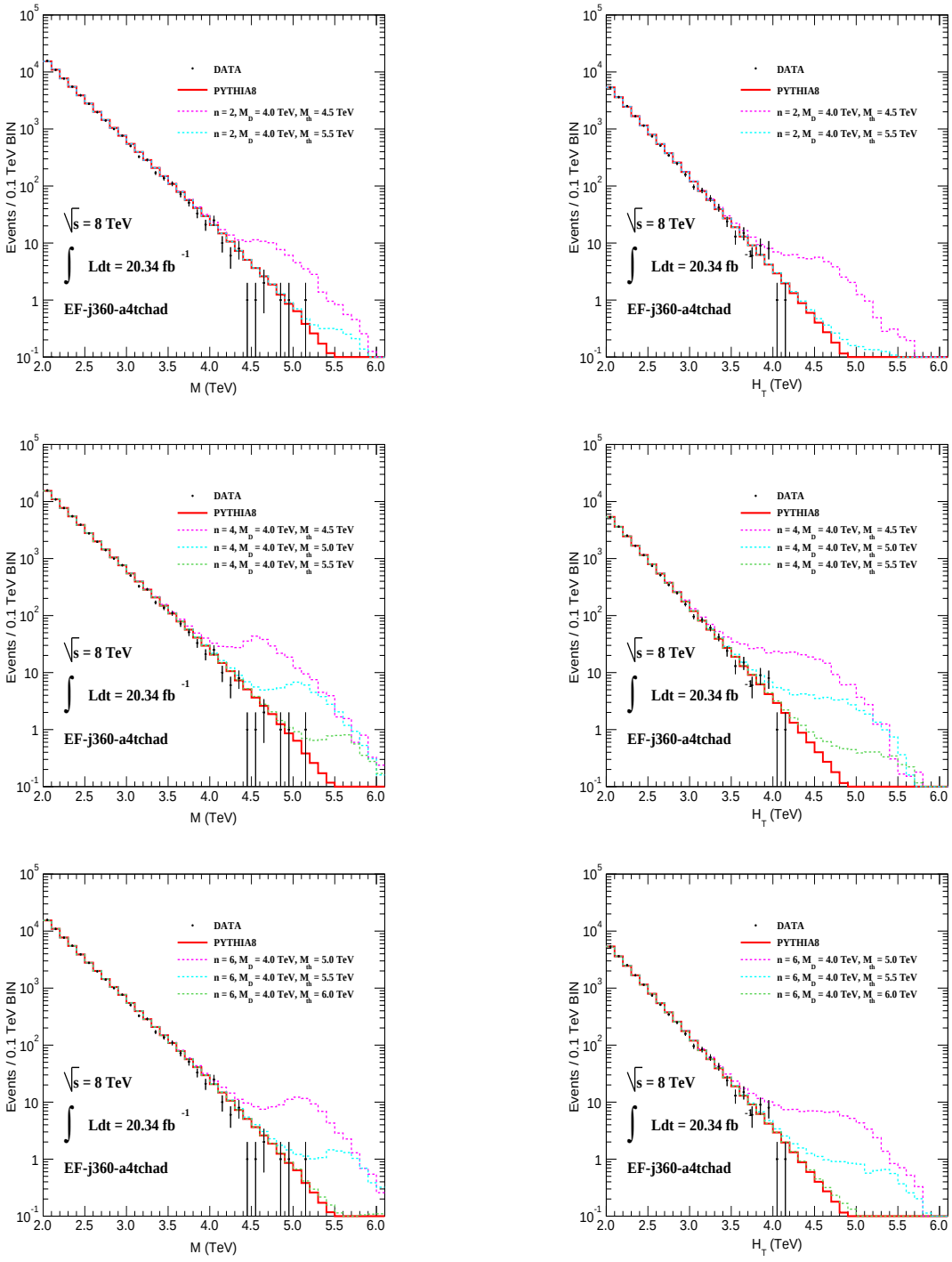

Figure D.6: M and H_T distributions for CHARYBDIS2 rotating black hole samples with no graviton emission are shown for extra dimensions $n = \{2, 4, 6\}$, fundamental Planck scale $M_D = 4.0$ TeV and different values of production mass threshold M_{th}. ATLAS data and PYTHIA8 M and H_T distributions are also shown.

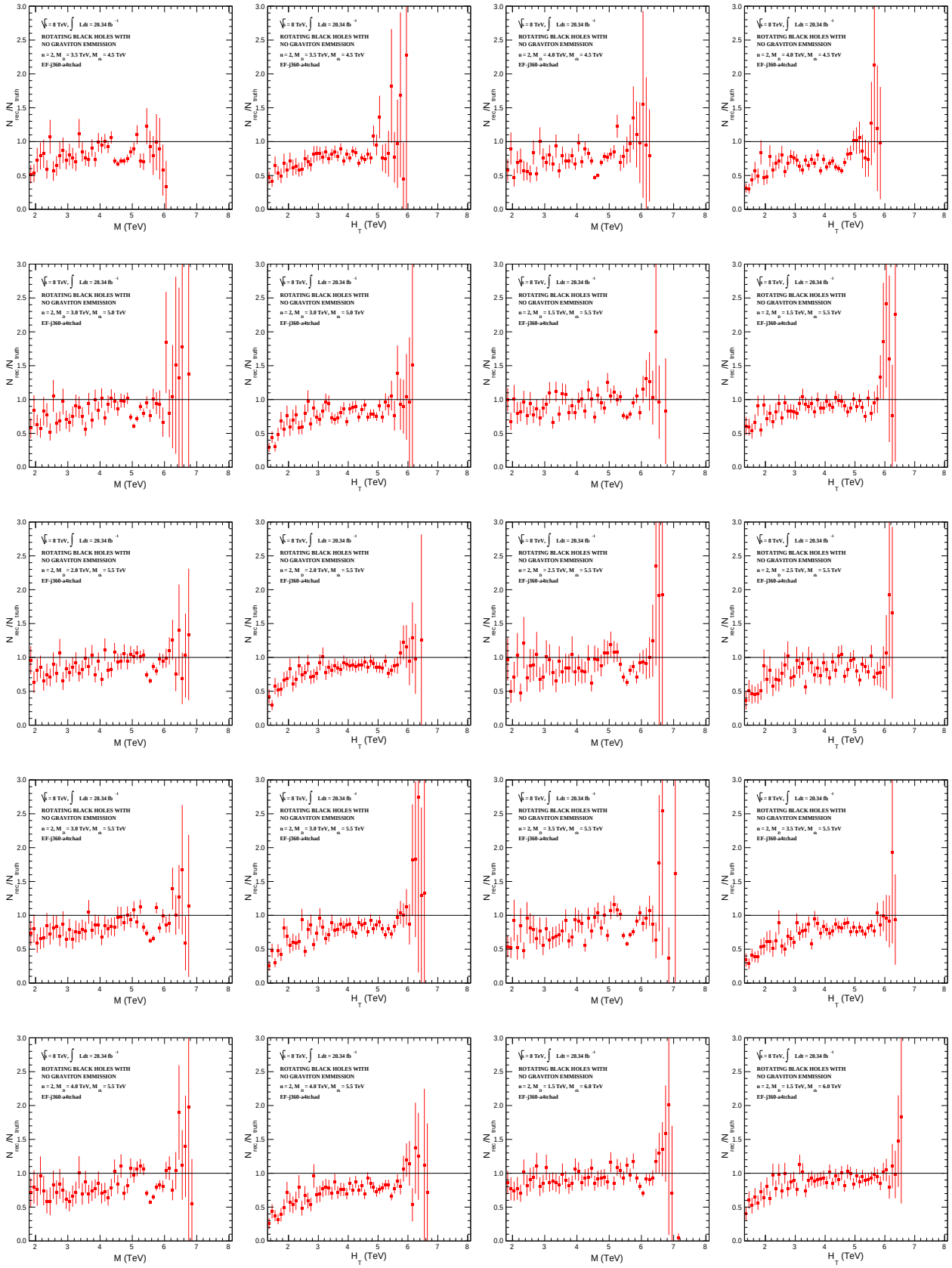

Figure D.7: Reconstruction efficiencies per 0.1 TeV bin for M and H_T distributions for rotating black hole samples.

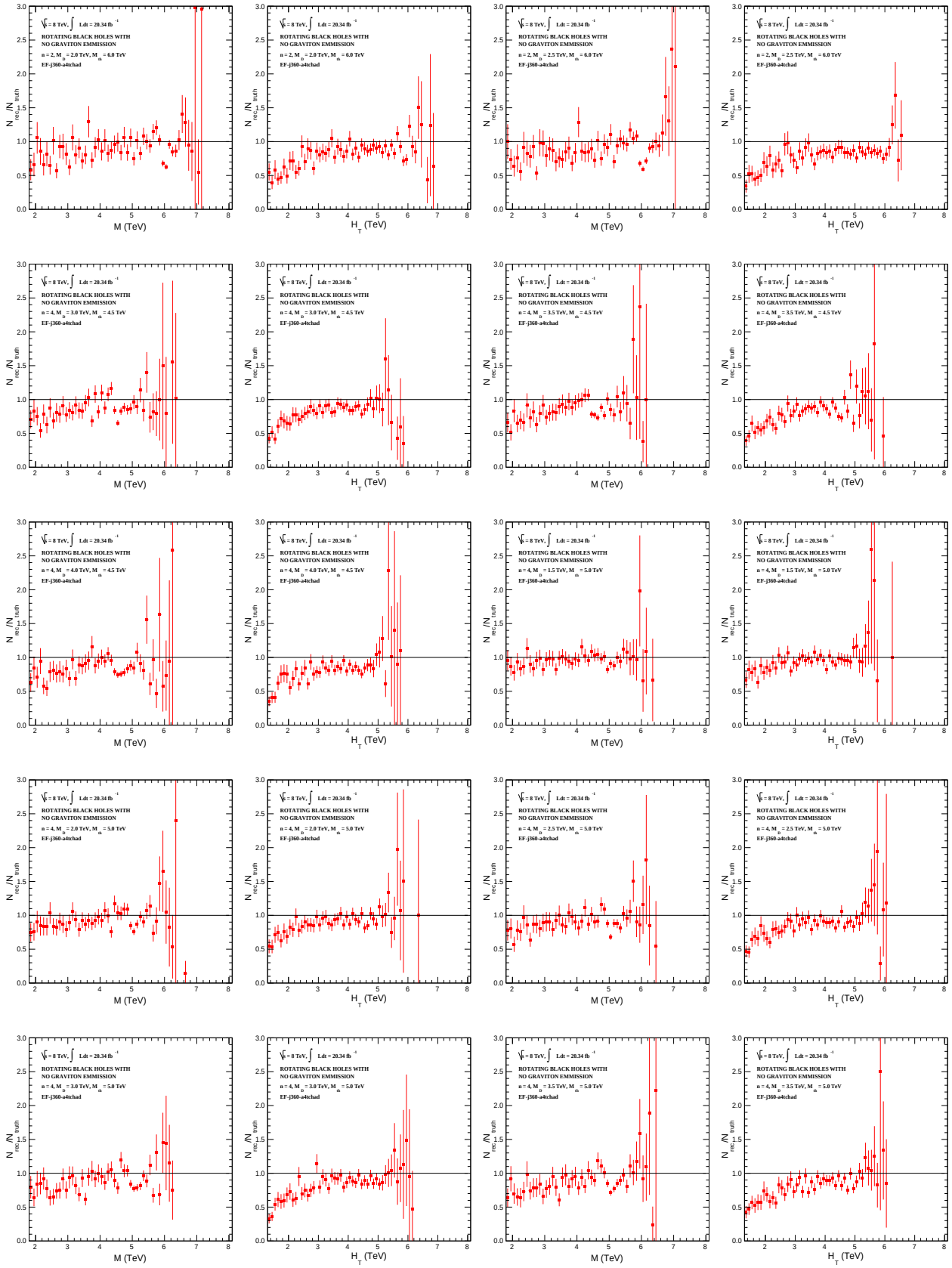

Figure D.8: Reconstruction efficiencies per 0.1 TeV bin for M and H_T distributions for rotating black hole samples.

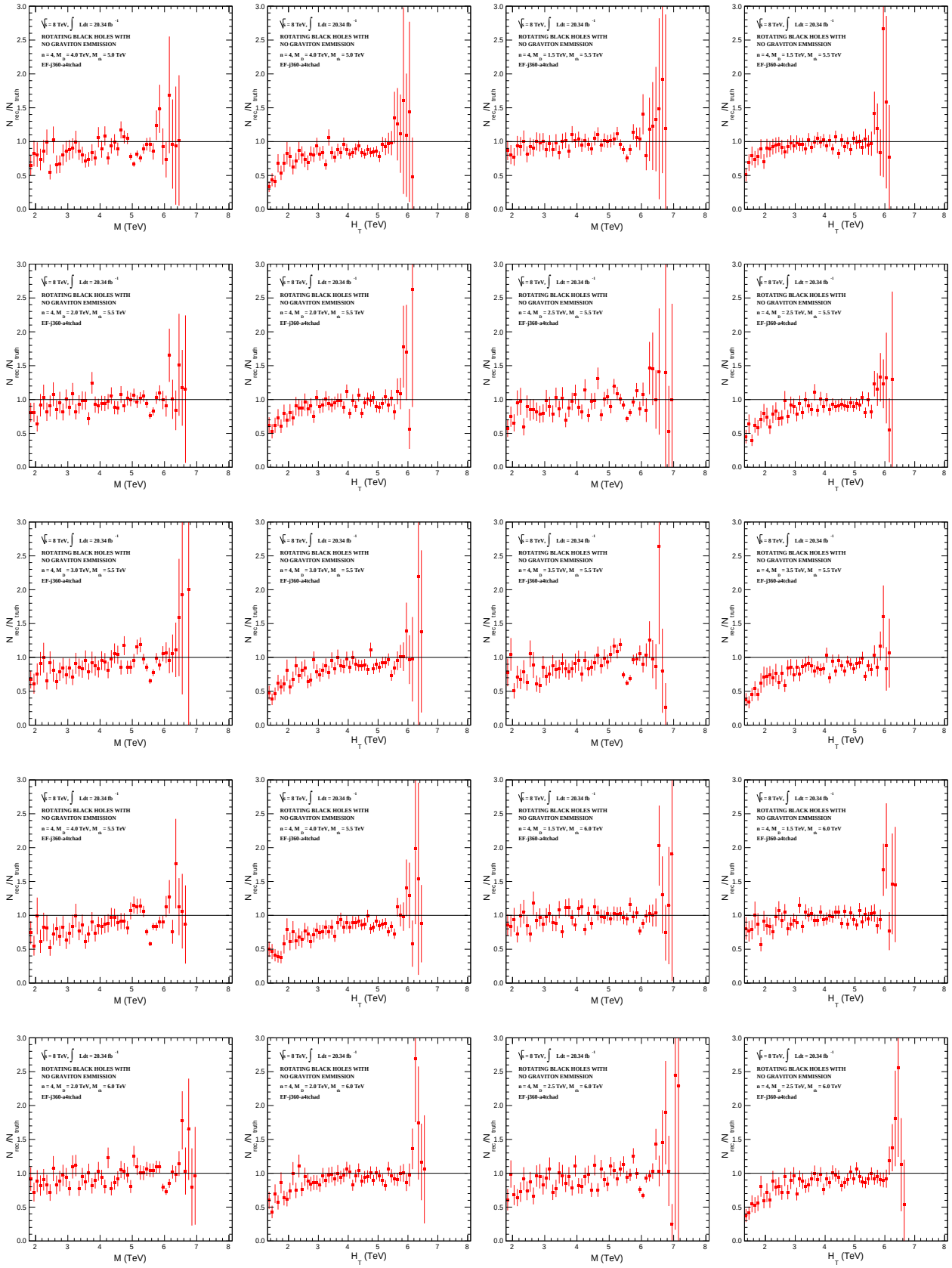

Figure D.9: Reconstruction efficiencies per 0.1 TeV bin for M and H_T distributions for rotating black hole samples.

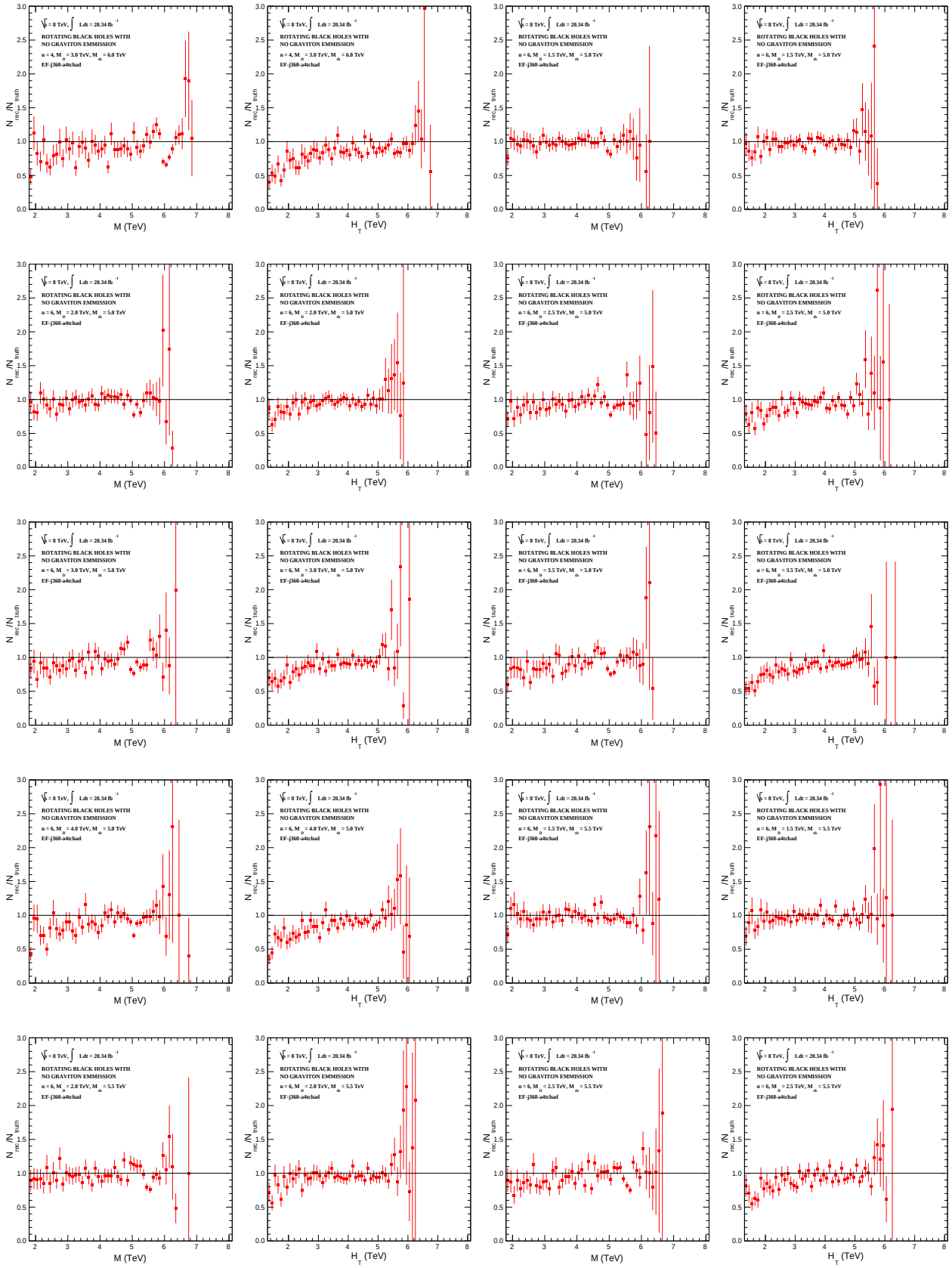

Figure D.10: Reconstruction efficiencies per 0.1 TeV bin for M and H_T distributions for rotating black hole samples.

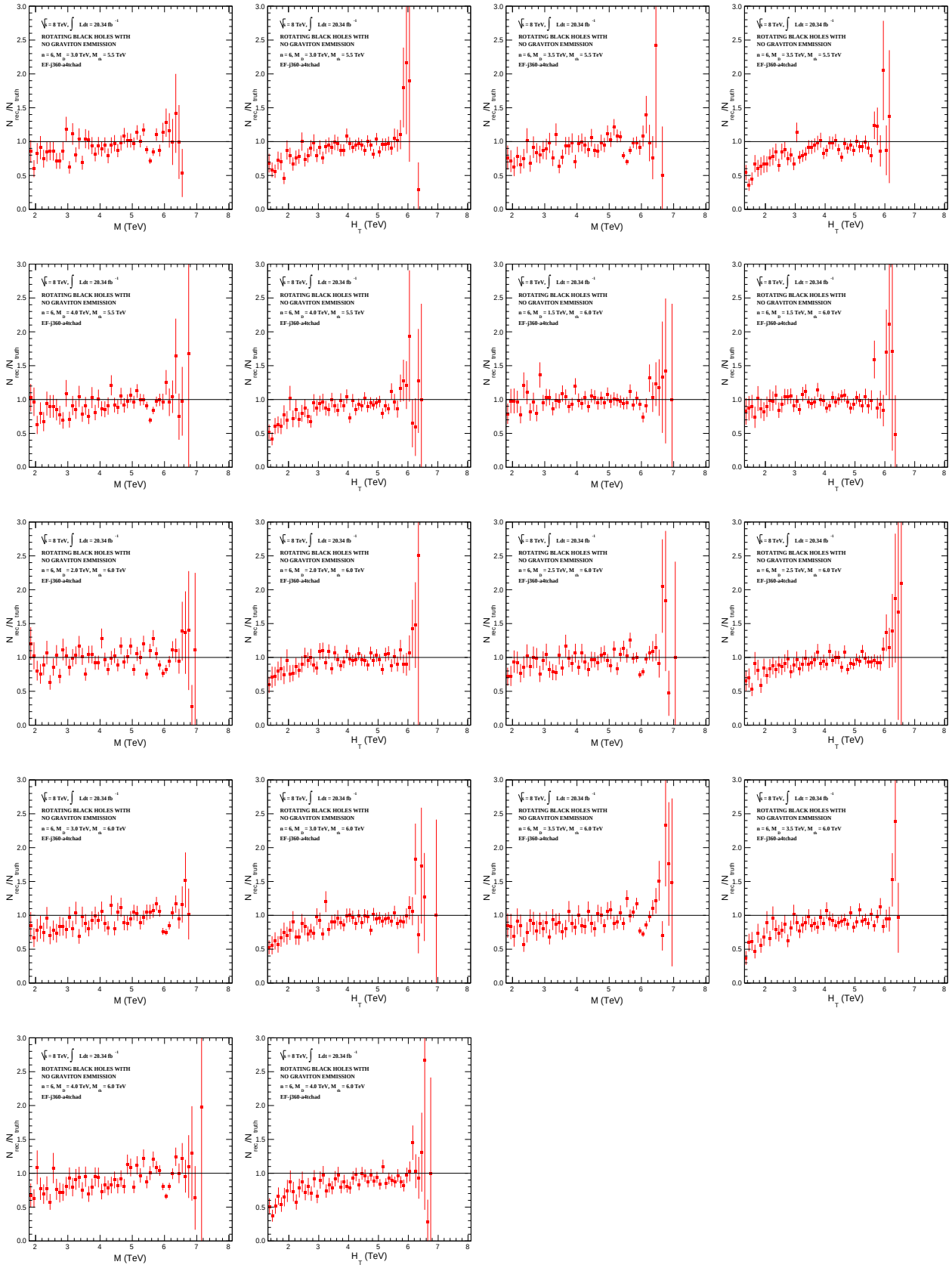

Figure D.11: Reconstruction efficiencies per 0.1 TeV bin for M and H_T distributions for rotating black hole samples.

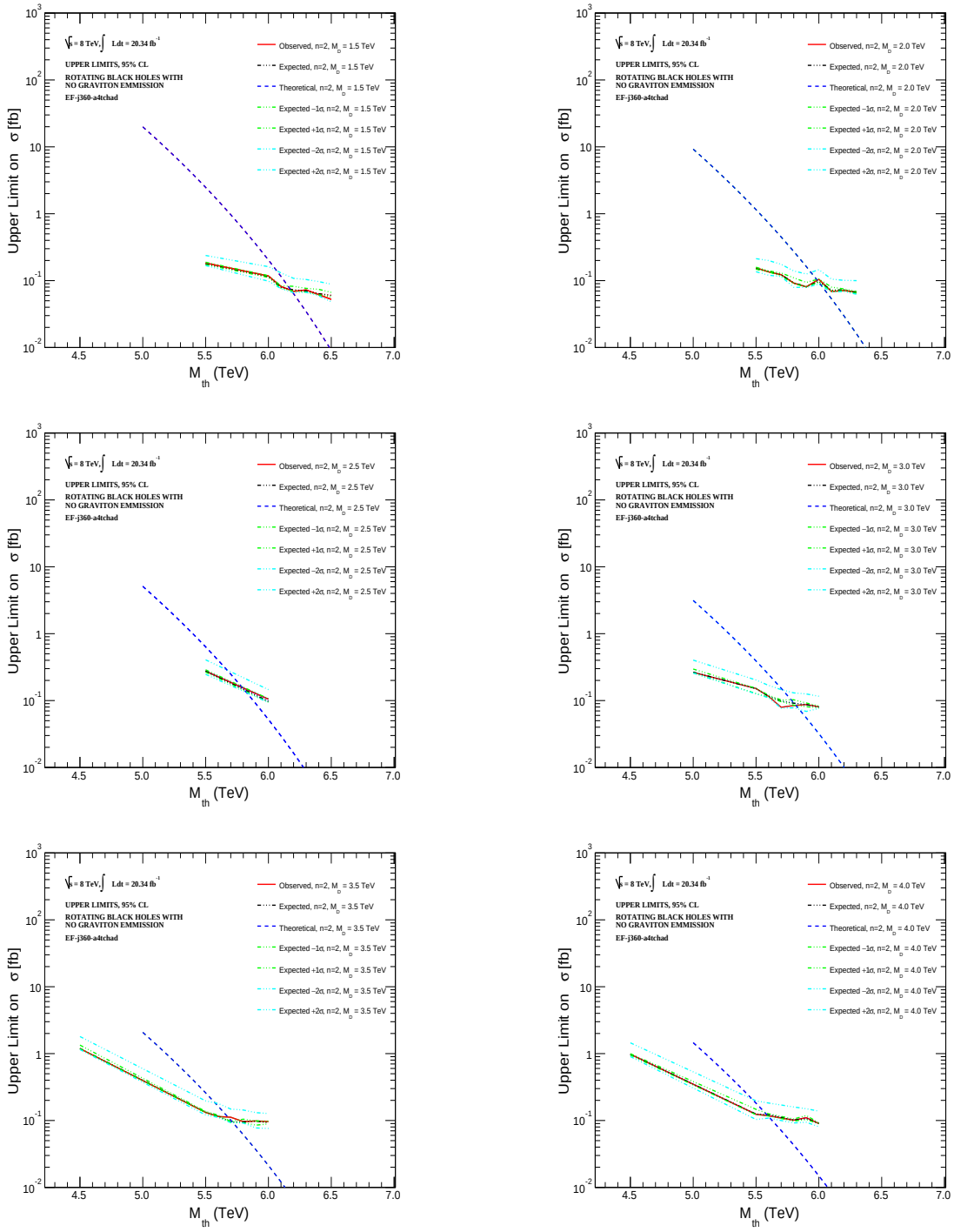

Figure D.12: Upper limits on the observed and expected production cross sections (σ) at the 95% confidence level (CL) (solid line and dotted-broken line, respectively) for two extra dimensions and fundamental Planck scale M_D=$\{$1.5,2.0,2.5,3.0,3.5,4.0$\}$ are compared with theoretical production cross sections from CHARYBDIS2 black hole generator (broken line), as a function of threshold mass M_{th} for rotating black hole with no graviton emission. The $\pm1\sigma$ and $\pm2\sigma$ curves represent 68% and 95% confidence intervals on either sides of the expected limit.

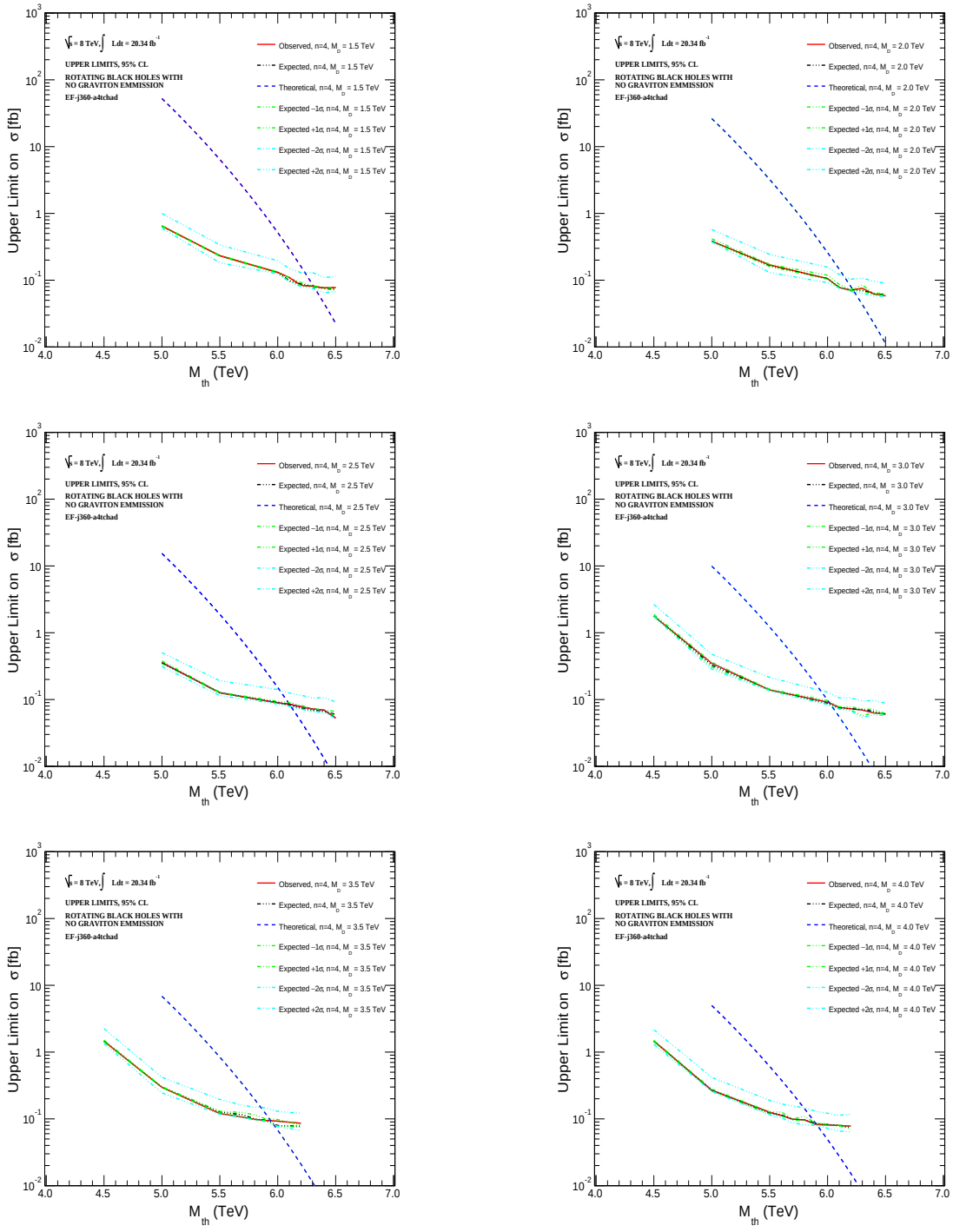

Figure D.13: Upper limits on the observed and expected production cross sections (σ) at the 95% confidence level (CL) (solid line and dotted-broken line, respectively) for four extra dimensions and fundamental Planck scale M_D={1.5,2.0,2.5,3.0,3.5,4.0} are compared with theoretical production cross sections from CHARYBDIS2 black hole generator (broken line), as a function of threshold mass M_{th} for rotating black hole with no graviton emission. The $\pm1\sigma$ and $\pm2\sigma$ curves represent 68% and 95% confidence intervals on either sides of the expected limit.

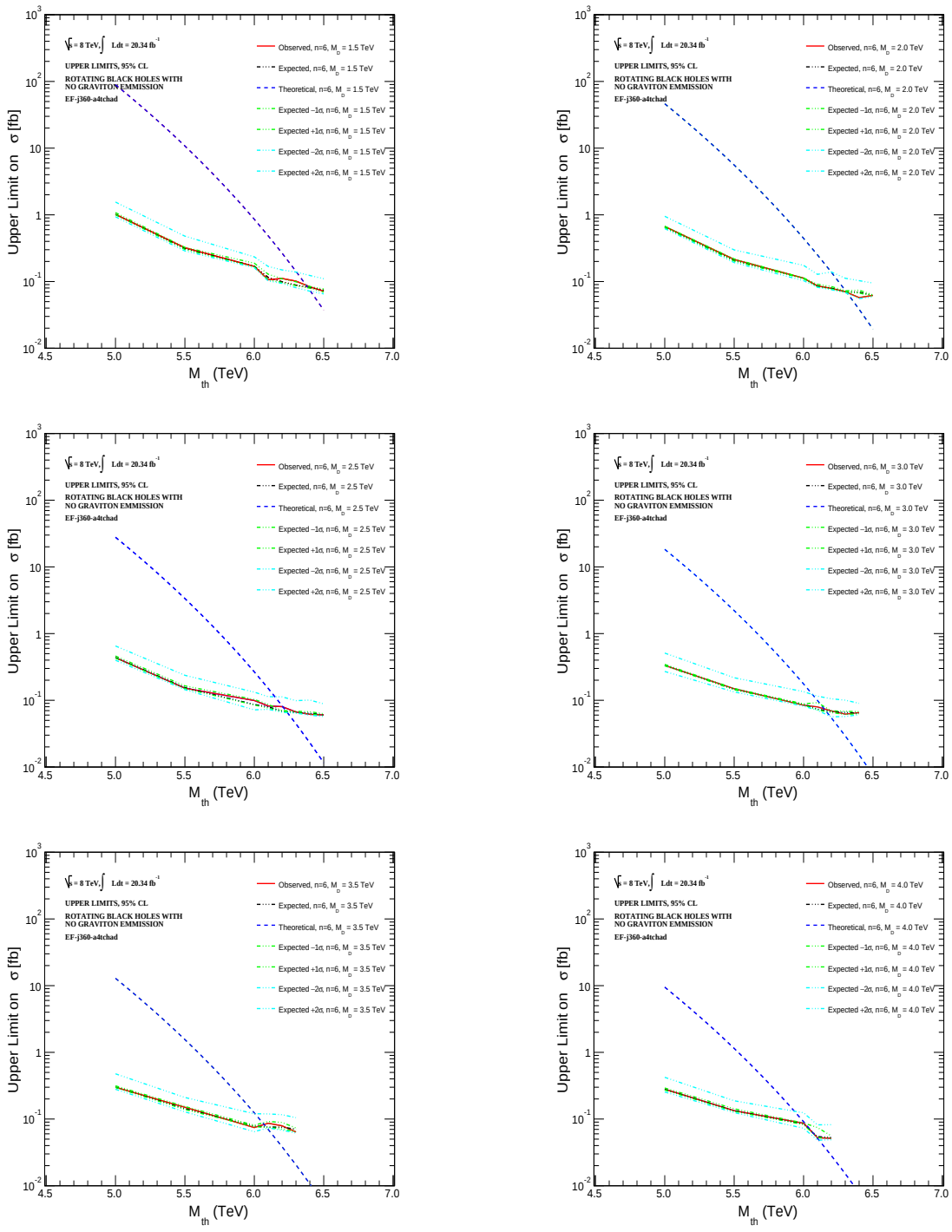

Figure D.14: Upper limits on the observed and expected production cross sections (σ) at the 95% confidence level (CL) (solid line and dotted-broken line, respectively) for six extra dimensions and fundamental Planck scale M_D={1.5,2.0,2.5,3.0,3.5,4.0} are compared with theoretical production cross sections from CHARYBDIS2 black hole generator (broken line), as a function of threshold mass M_{th} for rotating black hole with no graviton emission. The $\pm1\sigma$ and $\pm2\sigma$ curves represent 68% and 95% confidence intervals on either sides of the expected limit.

Appendix E

Data and MC Tags and ATLAS Packages

The following ATLAS data, MC samples and packages are used in this study:

Good Run List

data12_8TeV.periodAllYear_HEAD_DQDefects−00−00−33_PHYS_StandardGRL_All_Good.xml

D3PDs

JetTauEtmiss_NTUP_SUSYSKIM_p1328_p1329

Monte Carlo Samples

Pythia8_AU2CT10_jetjet_JZXW.merge.NTUP_SUSY.e1126_s1469_s1470_r3542_r3549_p1328
Herwigpp_EE3CTEQ6L1_jetjet_JZXW.merge.NTUP_SUSY.e1373_s1499_s1504_r3658_r3549_p1328

ATLAS Packages

ApplyJetCalibration−00−03−02 with JES_Full2012dataset_Preliminary_Jan13.config
PileupReweighting−00−02−09 with MC12a Pileup Reweighing by averageIntPerXing
JetUncertainties−00−08−05
JetResolution−r482618

Appendix F

Contribution to ATLAS Experiment

The ATLAS-Alberta group plays an important role in providing trained manpower and general services to the ATLAS experiment. Services provided can be categorized in three classes. Class-I services require least skills. ATLAS control room shift is one such example of class-I services where a person monitors the performance of different ATLAS sub-detectors during data taking phase. Class-II services are a level up. Ensuring data integrity during data taking phase requires expert skills and is one example of class-II work. Class-III work is a relatively long-term project that is required to earn authorship rights with ATLAS collaboration. Class-III work helps to understand the detector response to frequently changing operating conditions at the LHC during data taking phase, and during up-gradation phases of the LHC and the ATLAS detector.

I was stationed at CERN from January 2012 to August 2012 and from January 2013 to April 2013 during which I took numerous ATLAS control room shifts. I contributed as offline JetEtmiss data quality expert from April 2012 to November 2012 which is considered class-II service work.

I performed "Monte Carlo and Data Overlay Validation for LAr Calorimeter with Athena Release 17" for over a year to qualify for ATLAS authorship on May 27, 2013. One realistic way of modelling backgrounds is the process of combining raw data acquired with a special zerobias trigger, also called zerobias data, with Monte Carlo signal events to create a realistic Monte Carlo which would resemble the actual data collected for physics analysis. The process of combining the MC signal event with the zerobias event is called Background Overlay. The combined event is called the overlay event. The overlay events may be used to study how to remove fake jets and MET due to cosmics and beam backgrounds from the real physics QCD jets and MET. The Background Overlay has some advantages over Pileup Digitization as well as some disadvantages. Validation of overlay process is performed by comparing energies of the three samples at LAr cell level. We found that the energy difference in some LAr cells was considerably huge i.e. 20+ GeV, although the energy difference in most cells was in reasonable agreement. We noticed large discrepancies in the energy difference in FCAL and Inner Wheel only. We also noticed that the PulseShape for MC events is different from that of Overlay events. It is because the PulseShape we use for Overlay contains residual correction. After residual correction, $\Sigma(\text{OFC}(i) \times \text{PulseShape}(i)) \neq 1$ and there is a certain % bias on Overlay energy of the cells. We suggested that we should use the PulseShape for Overlay before any residual correction is applied and added two job options in preExec and postExec for overlay_bs_trf transformation job to address this problem. We also noticed that the large energy discrepancy in cells with medium and low gain is due to the fact that pulse reconstruction code uses ramp intercept whereas digitization code doesn't. Changes were made by Guillaume Unal to LArDigitization package to take into account the ramp intercept. As a result, compiling LArDigitization$-03-08-23$ and LArROD$-02-17-21$ before running overlay_bs_trf transformation job

significantly reduces large energy discrepancy in cells with medium and low gain. We made validation plots at each step, i.e., after opting new sample production scheme, after fixing PulseShape bug and after fixing ramp intercept.